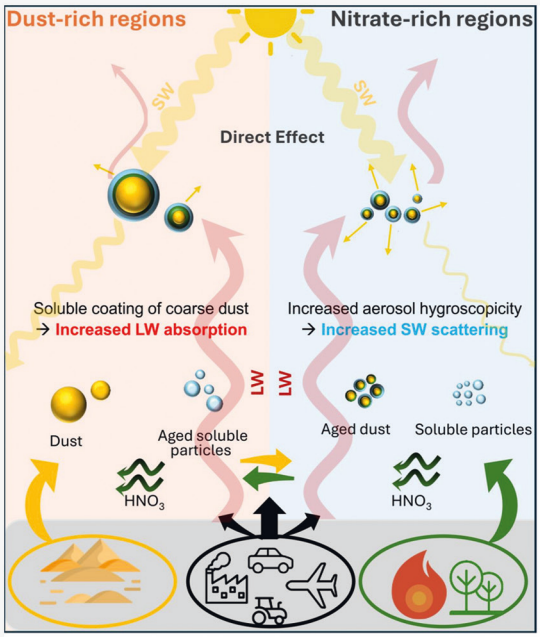

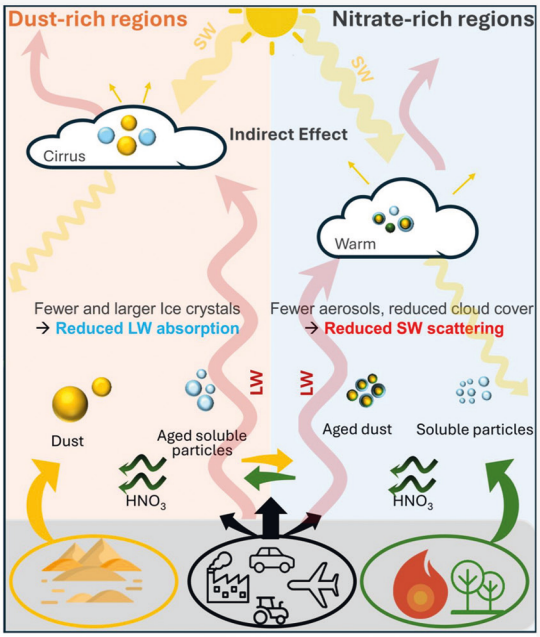

Advances in Understanding Nitrate Aerosol Formation and the Implications for Atmospheric Radiative Balance

Alexandros Milousis

Energie & Umwelt / Energy & Environment
Band / Volume 663
ISBN 978-3-95806-823-0

Mitglied der Helmholtz-Gemeinschaft

JÜLICH
Forschungszentrum

Schriften des Forschungszentrums Jülich
Reihe Energie & Umwelt / Energy & Environment Band / Volume 663

Forschungszentrum Jülich GmbH
Institute of Climate and Energy Systems (ICE)
Troposphäre (ICE-3)

Advances in Understanding Nitrate Aerosol Formation and the Implications for Atmospheric Radiative Balance

Alexandros Milousis

Schriften des Forschungszentrums Jülich
Reihe Energie & Umwelt / Energy & Environment Band / Volume 663

ISSN 1866-1793 ISBN 978-3-95806-823-0

Bibliografische Information der Deutschen Nationalbibliothek.
Die Deutsche Nationalbibliothek verzeichnet diese Publikation in der
Deutschen Nationalbibliografie; detaillierte Bibliografische Daten
sind im Internet über http://dnb.d-nb.de abrufbar.

Herausgeber und Vertrieb:	Forschungszentrum Jülich GmbH Zentralbibliothek, Verlag 52425 Jülich Tel.: +49 2461 61-5368 Fax: +49 2461 61-6103 zb-publikation@fz-juelich.de www.fz-juelich.de/zb
Umschlaggestaltung:	Grafische Medien, Forschungszentrum Jülich GmbH
Druck:	Grafische Medien, Forschungszentrum Jülich GmbH
Copyright:	Forschungszentrum Jülich 2025

Schriften des Forschungszentrums Jülich
Reihe Energie & Umwelt / Energy & Environment, Band / Volume 663

D 38 (Diss. Köln, Univ., 2025)

ISSN 1866-1793
ISBN 978-3-95806-823-0

Vollständig frei verfügbar über das Publikationsportal des Forschungszentrums Jülich (JuSER)
unter www.fz-juelich.de/zb/openaccess.

Abstract

Recent decades have highlighted the profound consequences of air pollution on air quality and human health, resulting in millions of deaths worldwide and contributing to the intensification of the Earth's climate due to ongoing anthropogenic emissions. These emissions, originating from densely populated and industrialized regions, lead to the release of gaseous pollutants that undergo chemical transformations in the atmosphere, producing secondary particulate pollutants. Atmospheric modeling is a valuable tool that facilitates a more profound comprehension of physicochemical processes, thereby providing guidelines for mitigating air pollution and enhancing our understanding of climatic feedback mechanisms.

Recent policies aimed at reducing emissions from anthropogenic activities have predominantly focused on specific species, including carbon dioxide (CO_2), methane (CH_4), sulfur dioxide (SO_2), and nitrogen oxides (NOx). This is expected to cause a change in the landscape of secondary aerosol population characteristics as the abundancy of their precursors will also change. For example, the observed historical increase in ammonia (NH_3) emissions is expected to enhance the importance of certain inorganic aerosol species at the expense of others. A substantial body of research conducted in the most heavily polluted regions of the Northern Hemisphere has already demonstrated that the average concentration of aerosol nitrate is comparable to, if not greater than, the respective concentration of aerosol sulfate. Sulfate is currently recognized as the most substantial contributor to the total inorganic aerosol mass on a global scale. Consequently, the estimation of aerosol nitrate by atmospheric models has become increasingly crucial, and the number of models that include this species in their calculations is steadily rising, despite not being the norm in the past. This thesis aims to address a key assumption that can influence the estimation of nitrate aerosols (NO_3^-) by models. This assumption is their physical state (i.e., solid or liquid). Aerosols typically crystallize and form solids when exposed to decreasing ambient relative humidity, though this process is often complex due to various aerosol compositions and the hysteresis effect .In thermodynamics, particles that form solids are considered to be in a stable state; however, aerosol water can exist even in very low humidity values, leaving particles in a supersaturated aqueous state called metastable. Utilizing a state-of-the-art chemistry and climate model (EMAC) and a recently developed version of a thermodynamic equilibrium model (ISORROPIA-lite), the study explores the hypothesis that the state assumption significantly impacts inorganic aerosol estimations. Additionally, it examines the impact of the aerosol physical state on the estimated particle acidity, as this is another quantity that influences the aerosol partitioning process. Furthermore, the thesis investigates a number of factors that are known to influence the model's ability to accurately estimate NO_3^- concentrations in regions of high anthropogenic activity, with a particular focus on the polluted North Hemisphere (East Asia, India, Europe, and North America). The objective is to ascertain the most significant factors that contribute to the best replication of observations of NO_3^- in sizes less than 1 μm and 2.5 μm in diameter (PM_1 and $PM_{2.5}$, respectively). The analysis is further expanded to encompass the recognition of any seasonal patterns as well as measurement location patterns. Finally, the study

examines the interactions between nitrate aerosol and mineral dust, thereby investigating the climatic impact of NO_3^- with respect to its radiative effect from both aerosol-radiation interactions (direct effect) and aerosol-cloud interactions (indirect effect).The importance of considering dust-nitrate interactions when examining such metrics is also quantified.

The study found that the physical state assumption has a minimal impact on the global budget of key inorganic aerosol species, including NO_3^-, SO_4^{2-}, and NH_4^+, as well as non-volatile cations, with overall differences being less than 10%. Consequently, for the purposes of climatic or air quality simulations that cover a long time period and consider a global scale, that choice is not expected to have a significant impact. However, the metastable assumption has been shown to yield faster simulation times, with an average increase of approximately 4-5%.In regions characterized by consistently low relative humidity values and/or mid-range temperatures, the assumption of considering only liquid particles has been found to result in lower concentration estimates, with NO_3^- concentrations being reduced by up to 40%, and slightly more acidic particles by up to 1 unit. Consequently, for analyses that consider specific regions, the aerosol physical state assumption assumes greater importance.

Concerning the factors influencing the accuracy of NO_3^- estimations, it was ascertained that, on average, a high model grid resolution and a low dinitrogen pentoxide (N_2O_5) hydrolysis coefficient tend to yield better agreement with observations in both sizes. The employment of disparate anthropogenic emissions databases emerged as a significant factor influencing model estimations, particularly in replicating PM_1 NO_3^- concentrations across diverse regions. In general, there is no 'perfect' model setup capable of best capturing both PM_1 and $PM_{2.5}$ NO_3^- concentrations across all regions simultaneously. Depending on the area of interest, different parameterizations yield superior rates of agreement.

Furthermore, it was determined that nitrate aerosols induce a net cooling direct radiative effect of -0.11 W/m^2, primarily attributable to the scattering of SW radiation by smaller size modes, accounting for 85% of this estimate. Conversely, nitrate aerosols have been observed to induce a net warming indirect radiative effect of +0.17 W/m^2, which is attributed to the depletion of smaller-sized particles (i.e., anthropogenic pollution) through coagulation with larger particles (i.e., dust). This depletion results in the formation of less low-level warm clouds, which decreases the amount of SW radiation that is reflected back to space. The efficacy of this mechanism is further augmented by nitrate-dust interactions, which augment the size of dust particles through adsorption and coating processes. The incorporation of dust chemistry is of paramount importance when compared to assumptions for dust composition or dust loading, as its omission engenders an underestimation of the aforementioned estimates by up to 45%.

Contents

1 Introduction

1.1 Aerosols in the atmosphere

Aerosols are particles that exist in either a solid or liquid state and are suspended in the atmosphere. Their size distribution exhibits a considerable range, spanning from a diameter of a few nanometers (nm) to hundreds of micrometers (μm). A standard categorization system divides aerosols into four size mode categories, namely nucleation, Aitken, accumulation, and coarse modes, with size ranges typical of these categories illustrated in Figure 1.1. Typically, aerosols are observed in the nucleation mode when new particles are formed via the nucleation process, which refers to the formation of new particles from clusters of gas molecules (Seinfeld and Pandis, 2016). The occurrence of this process necessitates atmospheric conditions characterized by supersaturation, defined as a relative humidity exceeding 100%. In such conditions, the continuous collisions between gas molecules and the clusters that serve as the particle formation sites initiate the process of agglomeration, subsequently transferring particles from the gaseous state to the liquid phase. With regard to the three larger size categories, an aerosol can be emitted directly or transferred from one mode to another via the processes of condensation and coagulation (Fig. 1.1). In general, aerosol particles can be classified as either soluble (hydrophilic/able to absorb water) or insoluble (hydrophobic/unable to absorb water) based on their physicochemical properties. Aerosols are further classified based on their diameter, with categories such as PM_{10}, $PM_{2.5}$, and PM_1 representing particles with diameters of 10, 2.5, and 1 micrometers, respectively. The atmospheric trajectory of aerosols is influenced by gravity, with larger particles typically having a shorter range of travel. Consequently, aerosols can be found in remote areas, even in altitudes that reach up to the upper stratosphere. However, it should be noted that nano particles, which are formed by nucleation, undergo rapid transfer to a larger size mode through coagulation with larger particles, resulting in limited travel distances.

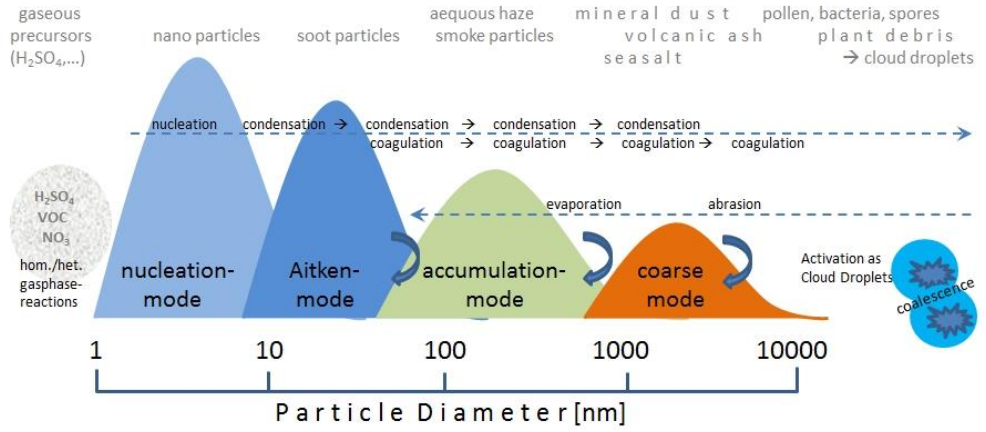

Figure 1.1: Depiction of aerosol multi-modal size distribution along with examples of aerosol types, typical of each mode. Also depicted are processes through which an aerosol particle can be transferred between the size modes. Figure taken from the Deutscher Wetterdienst webpage 'Particle Size Distribution' (https://www.dwd.de/EN/research/observing_atmosphere/composition_atmosphere/aerosol/cont_nav/particle_size_distribution_node.html).

Aerosols that are directly emitted into the atmosphere are designated as primary pollutants, with their sources encompassing a wide range of natural and anthropogenic origins. Notable instances of primary natural aerosols include sea salt particles, which are produced by the bursting of air bubbles entrained by wind stress over oceans (Monahan, 1986). These particles contain chloride anions (Cl^-) and sodium cations (Na^+). Dust particles, originating from the suspension of soil and wind erosion in desert regions (Marticorena and Bergametti, 1995), contain cations such as calcium (Ca^{2+}), magnesium (Mg^{2+}), potassium (K^+), and sodium (Sposito, 1989). In addition, organic carbon (OC), black carbon (BC), brown carbon (BrC), and soot particles are typically emitted from wildfires (Andreae and Gelencsér, 2006). Anthropogenic aerosols are typically emitted from activities related to power generation, materials production, transportation, and agricultural activities (IPCC, 2013). These aerosols can be either directly emitted as primary pollutants or formed later in the atmosphere from chemical reactions of precursor gases. In this case, they are deemed secondary pollutants. Natural aerosols can also be secondary pollutants from natural emissions of precursor gases such as ammonia (NH_3), nitrogen monoxide (NO), or dimethyl sulfide (DMS), for example. In general, primary aerosols tend to be emitted in larger sizes compared to secondary aerosols (Myhre et al., 2013). The classification of anthropogenic aerosols is predominantly determined by the presence of carbon-related compounds. In the first category, organic aerosols are distinguished by their carbon content, while in the second category, inorganic aerosols are defined by the absence of carbon. The three predominant species in the latter category are the anions sulfate (SO_4^{2-}), nitrate (NO_3^-), and ammonium (NH_4^+), which are all secondary aerosols originating from emissions of precursor gases such as SO_2, NOx, and NH_3 (Arias et al., 2021). Conversely, organic aerosols can be classified into two distinct categories: primary organic aerosols (POA), originating from biomass burning or fossil fuel combustion emissions, and secondary organic aerosols (SOA), arising from precursor volatile organic compound (VOC) emissions (Kanakidou et al., 2005). Organic aerosols can be further categorized based on their volatility and oxygenation levels (Jiménez et al., 2009).

Aerosols are removed from the atmosphere by various processes that can act either independently or in combination. These processes are divided into two categories: dry and wet removal. The process of dry removal is characterized by gravitational sedimentation, turbulent mixing, and Brownian motion, with removal rates depending on the size of the aerosol, the surface type on which they are deposited, and wind speed (Carslaw, 2022). Conversely, wet removal is characterized by the process of scavenging aerosols through rainfall or snowfall, followed by their subsequent deposition. This process is further categorized into two distinct mechanisms: rainout,

which occurs within the cloud, and washout, which transpires beneath the cloud (Kajino and Aikawa, 2015). During rainout, aerosols are removed by precipitation above the cloud base height, while during washout, they are removed when colliding with falling precipitation below the cloud base height.

Aerosols, in addition to their involvement in gas and liquid phase chemistry, play a significant role in dynamic atmospheric processes, as illustrated in Figure 1.2. These processes often lead to an enhancement in the size of aerosols. For instance, new particles can be formed by the nucleation of supersaturated gas compounds when their molecules cluster together (Laaksonen et al., 1995; Curtius, 2006). The newly formed aerosol particles then typically undergo a process of coagulation, in which particle clusters collide with each other due to Brownian motion, leading to an increase in their size through a process of coalescence (Fuks and Davies, 1964). A particularly notable aerosol process is their capacity to activate and form cloud droplets through the condensation of supersaturated water vapor on their surface (Andreae and Rosenfeld, 2008). These particles are designated as cloud condensation nuclei (CCN), while others possess the capacity to function as ice nucleating particles (INP), whereby droplets undergo freezing on their surface, leading to the formation of ice crystals (INP) (Suslick, 2001). The size and type of aerosols have been demonstrated to have a substantial impact on the characteristics of the resulting clouds and their climatic effects.

Aerosols have been shown to exert an impact on the Earth's climate through interactions with incoming short-wave (SW) and outgoing long-wave (LW) radiation (IPCC, 2013). These interactions constitute the aerosol direct radiative effect. Broadly speaking, aerosol types such as black carbon, brown carbon, and dust mostly contribute to a net direct warming through absorption (Kanakidou et al., 2005), while organic aerosols and the major anthropogenic inorganic particles contribute to a net direct cooling through scattering (Myhre et al., 2013). However, aerosols also impact the climate via interactions with clouds and more specifically by altering their optical characteristics (Twomey, 1977) and lifetimes (Albrecht, 1989). Figure 1.3 illustrates the various mechanisms through which aerosols modify the radiative equilibrium of the climate, encompassing both direct effects with radiation interactions and indirect effects with cloud interactions. The direct effect can be either positive (climate warming) due to the absorption of radiation or negative (climate cooling) due to the scattering of radiation. The indirect effect pertains to the aerosol-induced alterations in cloud reflectivity, which can also manifest as either positive or negative. It is widely acknowledged that aerosols of anthropogenic origin contribute to a net cooling of the planet (Myhre et al., 2014), a crucial aspect of which is the masking of the overall net warming that is induced by greenhouse gases globally (Urdiales-Flores et al., 2023). A more extensive discussion of the impacts of aerosols on climate is presented in Section 3.1.

Finally, it is widely acknowledged that aerosols, irrespective of their type or size, have a detrimental effect on human health, contributing to an increase in all-cause mortality, particularly due to heart attack and stroke-related deaths, as well as respiratory system infections (Pope, 2000; Pope and Dockery, 2006). Additionally, a recent correlation between exposure to $PM_{2.5}$ levels of pollution and an increased risk in developing Parkinson's Disease has been discovered

(Krzyzanowski et al., 2024). The collective impact of exposure to air pollution is marked by its profound global consequences, leading to over eight million premature deaths worldwide annually (WHO, 2022).

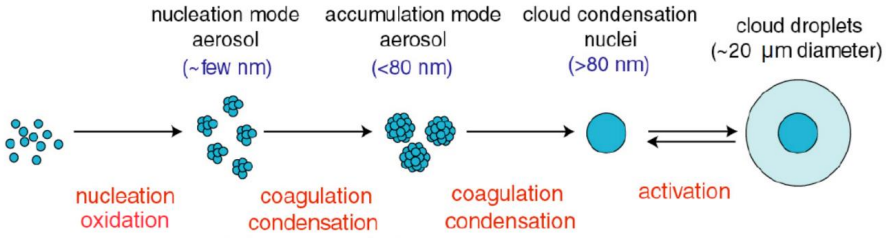

Figure 1.2: Schematic diagram of basic aerosol dynamic processes in the atmosphere, from the new particle formation (nucleation) to growth via coagulation and condensation to their eventual activation into cloud droplets. Figure is adopted under the Creative Commons Attribution 4.0 License (https://creativecommons.org/licenses/by/4.0/deed.en) from the 'An Introduction to Aerosol-Climate Interactions' presentation by François Dulac during the 'Workshop on Aerosol-Climate Interactions: Mechanisms, Monitoring, and Impacts in Tropical Regions' held by 'The Abdus Salam International Centre for Theoretical Physics' in Hurghada, Egypt during 11 – 15 February 2008 (https://indico.ictp.it/event/a07185/session/3/contribution/1/material/1/0.pdf).

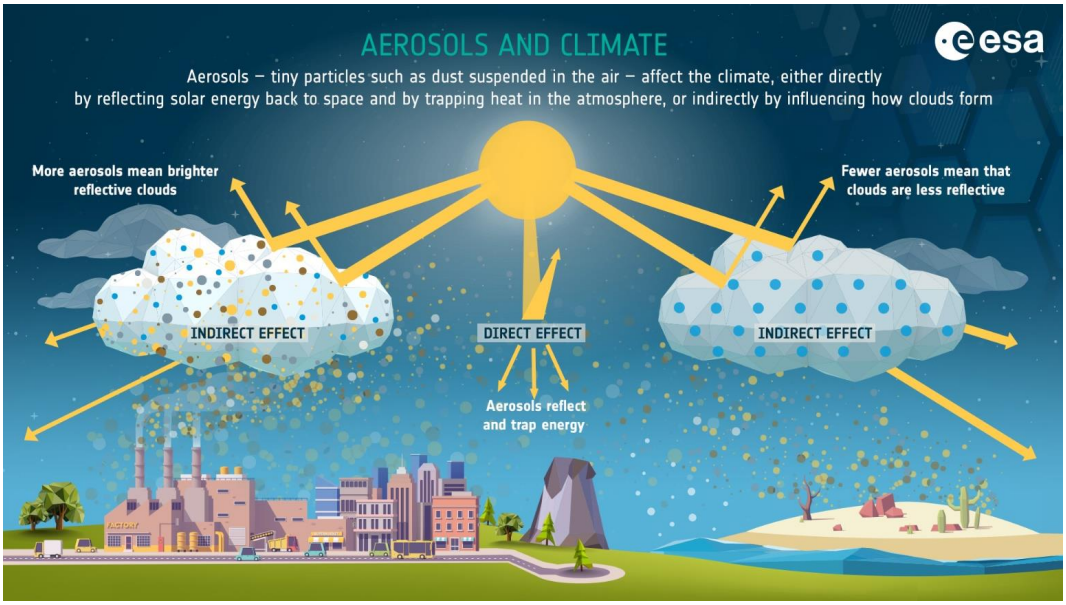

Figure 1.3: How aerosols impact the radiative budget of the climate through interactions with radiation (direct effect) and clouds (indirect effect). Figure taken from the European Space Agency webpage 'Clouds and aerosols in the climate system' (https://www.esa.int/Applications/Observing_the_Earth/FutureEO/EarthCARE/Clouds_and_aerosols_in_the_climate_system).

1.2 Modelling of aerosol processes

In the context of accurately representing aerosol processes within climate and chemistry models, it is imperative to address the fundamental aspect of aerosol microphysics. The size distribution of aerosols plays a pivotal role in determining this treatment, as the various processes previously discussed are characterized by substantial size dependency. Many models commonly employ a lognormal distribution to parameterize the four size ranges (Fig. 1.1). The equation that describes this distribution, giving the normalized number concentration n of aerosols in the size bin with a midpoint radius r, is the following :

$$n(\ln r) = \sum \frac{N_i}{\sqrt{2\pi}\ln\sigma_i} e^{\left(-\frac{(\ln r - \ln \overline{r_i})^2}{2\ln^2 \sigma_i}\right)} \quad (1.1)$$

Where i refers to each individual size mode, N_i to the number concentration of particles, $\overline{r_i}$ the geometric mean radius and σ_i the geometric standard deviation of the particle radius. In models that adopt the lognormal aerosol size distribution, as opposed to a sectional distribution approach, the radius limits of the different bins are not distinctly separated and there is some degree of overlap.

New particle formation is defined as the process of the nucleation of gas molecule clusters, which results in the formation of new aerosols that exist in the smallest size mode. The process of nucleation can occur in two distinct ways: homogeneous and heterogeneous. In the former, the process occurs without the presence of a foreign surface to assist it, whereas in the latter, a foreign surface is present. Nucleation can also occur with a single species present (homomolecular) or more (heteromolecular) (Seinfeld and Pandis, 2016), with the latter being most commonly present in chemistry models as species are well mixed with each other. The nucleation rate for new particles is typically contingent upon the concentrations of gas molecules, as well as the prevailing ambient conditions (e.g., temperature, relative humidity). The existence of supersaturation conditions is a necessary prerequisite for nucleation. The formation of new particles occurs through the process of agglomeration, where individual gas molecules collide with gas molecule clusters, resulting in a phase transition from gas to liquid. A very popular parameterization that is used by models to describe this process is that of Vehkamäki et al. (2002) which is relevant for temperatures in the range of 230.15 K until 305.15 K, relative humidities between 0.01 % and 100 % and gas molecule concentrations between 10^4 and 10^{11} cm^{-3}. It gives the nucleation rate J of new particles per cm^3 , as an exponential of a third order polynomial of the relative humidity RH and the total gas phase concentration N_a of a cluster of gas molecules :

$$\begin{aligned} J = \ & \exp\left[a(T,x^*) + b(T,x^*)\ln\left({}^{RH}/_{100}\right) + c(T,x^*)\left[\ln\left({}^{RH}/_{100}\right)\right]^2 + \right. \\ & d(T,x^*)\left[\ln\left({}^{RH}/_{100}\right)\right]^3 + e(T,x^*)\ln(N_a) + f(T,x^*)\ln\left({}^{RH}/_{100}\right)\ln(N_a) + \\ & g(T,x^*)\left[\ln\left({}^{RH}/_{100}\right)\right]^2\ln(N_a) + h(T,x^*)[\ln(N_a)]^2 + \\ & \left. i(T,x^*)\ln\left({}^{RH}/_{100}\right)[\ln(N_a)]^2 + j(T,x^*)[\ln(N_a)]^3\right] \end{aligned} \quad (1.2)$$

Where the coefficients $a(T,x^*)$ until $j(T,x^*)$ are conversely dependent on the mole fraction x^* of an individual gas species (e.g. sulfuric acid) present in the gas molecule cluster. Additionally, these functions are themselves third-order polynomial functions of temperature.

Following the process of nucleation, one way that the growth of aerosol particles in size is facilitated, is the condensation of gas species onto their surface. This process of condensation is a universal phenomenon, affecting all aerosol size modes. For aerosols in the nucleation mode, the change in mass A in molecules/cm^3 is given by the following equation :

$$\frac{d[A]}{dt} = \frac{N_1 C_1}{\sum_{i=1,7} N_i C_i} \left(\sum_{i=1,7} N_i C_i [A]\right) \quad (1.3)$$

Where i corresponds to the respective size mode with $i = 1$ denoting the nucleation mode. The case of $i = 2,4$ represents the soluble fraction of the three larger size modes (Fig. 1.1) and the case of $i = 5,7$ represents the insoluble fraction of the three larger size modes. However, precisely because these have an insoluble as well as a soluble fraction (unlike the nucleation size mode), there is an additional source of nucleated mass that condenses on them. Consequently, equation (1.3) is slightly altered into :

$$\frac{d[A]}{dt} = \frac{N_j C_j + N_{j+3} C_{j+3}}{\sum_{i=1,7} N_i C_i} \left(\sum_{i=1,7} N_i C_i [A]\right) \quad (1.4)$$

Here i represents all seven size modes, while $j = 2,4$ and refers to the soluble fractions of the three larger ones. Therefore the subscripts $(j + 3) = 5,7$ and refer to the insoluble fractions only. N denotes the particle number concentration in each specific size mode while C is the condensation coefficient for each size mode, and describes the diffusive flux of gas on a single particle surface. The condensable amount of gas on a particle, given by the diffusive flux, has a strong dependence on the particle size, the ambient atmospheric conditions to facilitate condensation as well as the gas phase species considered and time limitations for kinetic condensation. The condensation coefficient is given according to Fuks and Davies (1964) as follows :

$$C_i = \frac{4\pi D r_{gi}}{\frac{4D}{s v r_{gi}} + \frac{r_{gi}}{r_{gi} + \Delta}} \quad (1.5)$$

Where r_{gi} is the geometric mean radius of the size mode i, D is the diffusion coefficient (see Eq. 1.8), s is an accommodation coefficient for each gas species treated ranging from 0.03 to 1, v is the mean thermal velocity of the gas molecule and Δ is the mean free path length of the gas molecule. The physical meaning of Δ is that it denotes the distance from which the kinetic regime applies with respect to the particle, i.e. the distance from which the gas molecule is able to kinetically condense in the time frame of one model time step.

The process of particle coagulation is of paramount importance in the subsequent growth of aerosol size. This process occurs when particles of the same or different size modes collide and adhere to one another. Commonly this process is described by the following equation which gives the change in aerosol number concentration N_i in each size mode i describing both intermodal and intramodal coagulation :

$$\frac{dN_i}{dt} = \frac{1}{2} K_{ii} N_i^2 - \sum_j K_{ij} N_i N_j \tag{1.6}$$

Where j can be the respective size mode with which size mode i undergoes intermodal coagulation. K is the coagulation coefficient that acts as a metric for the frequency of collisions between particles. The smallest values of K , indicating less frequent collisions, occur for similarly sized aerosols. That is because small aerosols tend to move faster and more freely but have small available collision surface (cross section), while large aerosols even though having higher cross sections, tend to move slower requiring more time for a collision to take place. K is therefore heavily dependent on aerosol size, which inherently affects the moving speed and the number of collisions, and it is determined from the following equation according to Fuks and Davies (1964) :

$$K_{ij} = \frac{16\pi \bar{D} \bar{r}}{\frac{4\bar{D}}{\bar{v}\bar{r}} + \frac{\bar{r}}{\bar{r}+\Delta'}} \tag{1.7}$$

Where $\bar{r}$ is the mean geometric radius of the radii of modes i and j given as : $\bar{r} = \frac{\bar{r}_i + \bar{r}_j}{2}$ while $\bar{v}$ and Δ' correspond to the thermal velocity and the mean free path length of an aerosol with radius $\bar{r}$. Finally $\bar{D}$ is the diffusion coefficient which can be estimates as :

$$\bar{D} = 0.073 * \frac{1000}{P/100} * \left(\frac{T}{298.15}\right)^{1.5} \tag{1.8}$$

Where P and T are the atmospheric pressure in hPa and the atmospheric temperature in Kelvin units respectively. The diffusion coefficient is a metric of the rate that indicates the prevalence of Brownian motion that particles undergo compared to their gravitational settling. For example, a particle with a diameter of 0.1 μm will travel a longer distance in the atmosphere due to its diffusion rather than its sedimentation by gravity, owing to its miniscule mass. Conversely, for a particle with a diameter of 10 μm, this relation is the opposite. While the coagulation process does change the aerosol number concentrations among the different size modes, since intermodal coagulation will result in the aerosol residing in the bigger size, it ensures the total conservation of mass.

Aerosol thermodynamics is a critical process that governs the partitioning of particles between their gaseous and aerosol phases. This process also determines their physical state (liquid/solid), composition, and water content. Typically, organic and inorganic gas phase species are dissolved into their liquid form in the presence of solvents, with atmospheric water being the most abundant. These species are then subsequently dissociated into their ions to form aerosols. The extent of dissociation is dependent on the pH of the solvent and the acidic strength of the electrolyte (gas species) dissolved (Jacobson, 1999; Seinfeld and Pandis, 2016). It is important to note that aerosol formation can also originate from solid dissolved species. The resulting products can exist in either liquid or solid state and have a pure organic or inorganic composition or a mixture of both. The transition of an aerosol particle from a solid to a liquid state is termed deliquescence, and from liquid to solid state efflorescence. These transitions are dependent on ambient relative humidity. A solid particle exposed to increasing RH will begin to dissolve at a threshold known as Deliquescence Relative Humidity (DRH). However, the reverse phase transition rarely occurs at the same RH threshold, as a hysteresis effect comes into action during the process. Conversely, a liquid particle subjected to decreasing RH will undergo crystallization at a lower value, known as the Crystallization Relative Humidity (CRH). In multicomponent mixtures, the transition is governed by a different threshold, called Mutual Deliquescence Relative Humidity (MDRH), which depends on the particle composition. Typically, the MDRH is lower than the DRH of the pure solids in the mixture. This approach was first developed by Wexler and Seinfeld (1991) and has become a prevalent method for treating phase state transitions in thermodynamic equilibrium models. It is imperative to note that the DRH, CRH, and MDRH are all functions of ambient temperature.

In general, the computational demands associated with solving equilibrium equations are significant, prompting most models to employ diverse techniques to optimize their efficiency. These techniques are designed to facilitate incorporation into regional and global climate-chemistry models. A more detailed discussion regarding these approaches can be found in Section 2.1. It is noteworthy that all thermodynamic equilibrium models are reliant on the utilization of activity coefficients for the species under consideration. These coefficients represent the deviation of a species from ideal behavior (where a value of 1 indicates total ideality) and are typically dependent on ambient temperature. The determination of these activity coefficients can be achieved through either direct calculation by the model or through laboratory studies. However, given the impossibility of isolating individual ions in a solution, the calculations or measurements obtained typically correspond to the activity coefficients of specific ionic pairs. Finally, the most common parameterization for estimating the liquid water content of an aerosol particle is the Zdanovskii-Stokes-Robinson method (Zdanovskii, 1948; Stokes and Robinson, 1966), which only considers pure organic or inorganic compositions and is described by the following equation :

$$W = \sum_i \frac{C_i}{m_{i,0}(a_w)} \tag{1.9}$$

Where W is the aerosol water mass given in kg of water per m^3 of air, C_i is the concentration of an electrolyte i given in moles/m^3 of air in the aqueous phase and $m_{i,0}(a_w)$ is the molality of a single component aqueous solution of the electrolyte i that has a water activity equal to $a_w = {}^{RH}/_{100}$, given in mol/kg. More extensive information regarding the thermodynamic treatment that was followed throughout the thesis research and is relevant to all results that will be presented, can be found in Sections 2.1, 2.2.2, 3.2.2 and 4.2.2.

One of the most fundamental aspects of aerosol particles is their ability to act as cloud condensation nuclei (CCN) and activate into cloud droplets. The activation of aerosols occurs when their equilibrium supersaturation reaches (or exceeds) the critical supersaturation threshold necessary for activation, a process that is governed by their size. The activation of soluble particles, that have the capacity for water absorption, is most often described by the Köhler theory (Köhler, 1936). This theory attributes a Köhler curve to each individual particle, which is a curve that shows the radius at which the particle will activate (called the critical radius) in relation to the critical supersaturation for activation and its own equilibrium supersaturation. The equation most frequently employed to describe this theory is as follows :

$$s = \frac{A}{D_p} - \frac{B}{D_p^3} \tag{1.10}$$

This theoretical framework encompasses the interplay among two distinct phenomena, denoted as effects. The first term refers to the Kelvin (curvature) effect, which states that intermolecular forces over a curved surface are weaker than those over a flat surface. Consequently, any given molecule can more readily escape and transition to the vapor phase. The second term refers to the Raoult (solute) effect, which states that the supersaturation vapor pressure of a solvent (e.g., water) will be decreased in the presence of a solute (e.g., a species dissolved in water). Here s is the particle's equilibrium supersaturation, D_p is its diameter while $A = \frac{4\sigma M_w}{RT\rho_w}$ and $B = \frac{6n_s M_w v}{\pi\rho_w}$. M_w and ρ_w are the molar mass and density of water respectively, R is the universal gas constant, T is the temperature, σ is the surface tension of the gas-particle interphase, n_s are the number of moles of the solute substance (soluble material) in the aerosol particle and v is the Van't Hoff factor of said solute. A typical Köhler curve is depicted in Figure 1.4. Recently the Köhler theory has been expanded by Petters and Kreidenweis (2007) to include the aerosol's hygroscopicity parameter κ (which is a metric of its water absorption ability) slightly modifying the equation as :

$$s = \frac{4\sigma M_w}{RT\rho_w D_p} - \frac{D_d^3 \kappa}{D_p^3} \tag{1.11}$$

where D_d is the dry diameter of the aerosol particle.

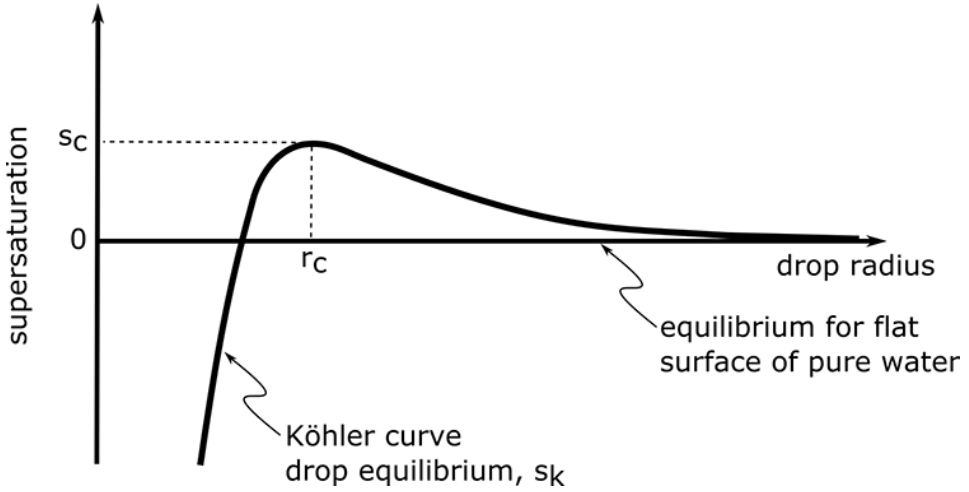

Figure 1.4: A typical example of a Köhler curve depicting the equilibrium supersaturation of a particle s_k as a function of its radius. If the ambient supersaturation is bigger that the critical supersaturation required for activation s_c then the particle will activate when it reaches its critical radius r_c and start increasing in size as it absorbs water. Generally larger particles exhibit smaller s_c and bigger r_c thresholds. Figure is adopted from W. Brunne © Penn State, and is licensed under the Creative Commons Attribution 4.0 License (https://creativecommons.org/licenses/by/4.0/deed.en).

The activation process is not exclusively limited to aerosol particles containing a solute (i.e., soluble material); insoluble particles can also activate into cloud droplets owing to the adsorption of soluble material on their surface. However, the dynamics of such particles are governed by a distinct theory, namely the Frenkel-Halsey-Hill (FHH) adsorption model, which involves the adsorption of multiple layers of soluble material. In such instances, the equilibrium supersaturation of the aerosol particle is determined by the following equation :

$$s = \frac{4\sigma M_w}{RT\rho_w D_p} - A_{FHH}\left(\frac{D_p - D_d}{2D_w}\right)^{-B_{FHH}} \tag{1.12}$$

The above is a parameterization developed by Sorjamaa and Laaksonen (2007) and Kumar et al. (2009). Here D_w is the diameter of a water molecule, while A_{FHH} and B_{FHH} are empirical constants that describe the interactions of the aerosol surface with the adsorbed molecules in the first layer and all subsequent layers respectively. These constants differ depending on the composition of the insoluble particle and are generally determined experimentally. Sorjamaa and Laaksonen (2007)

suggest a range of 0.1 to 3 for A_{FHH} and 0.5 to 3 for B_{FHH}. Recently, Kumar et al. (2011) developed a unified activation framework (UAF) to account for soluble coatings over particles with an insoluble core. In such instances, the equilibrium supersaturation of the particle is expressed as :

$$s = \frac{4\sigma M_w}{RT\rho_w D_p} - \frac{\varepsilon_s D_d^3 \kappa}{\left(D_p^3 - \varepsilon_i D_d^3\right)} - A_{FHH}\left(\frac{D_p - \varepsilon_i^{1/3} D_d}{2D_w}\right)^{-B_{FHH}} \quad (1.13)$$

Where ε_s and ε_i are the volume fractions of soluble and insoluble material respectively. Note that for a completely soluble aerosol particle ($\varepsilon_s = 1$ and $\varepsilon_i = 0$), equation (1.13) becomes equation (1.11), while for a complete insoluble particle ($\varepsilon_s = 0$ and $\varepsilon_i = 1$), equation (1.13) becomes equation (1.12).

As previously stated, aerosol particles can be removed from the atmosphere through a variety of processes, including gravitational sedimentation, dry deposition, and wet deposition. The latter process is further subdivided into two categories, depending on whether the particle will be scavenged within the cloud or below it, through washout. Comprehensive details concerning the parameterization of all depositional processes within chemistry and climate models can be found in Appendix A.1.

1.3 Importance and representation of particulate nitrate (NO_3^-)

Despite the fact that the majority of global and regional scale climate-chemistry models tend to address most, if not all, of the physical processes described in the previous section, their chemical representation of aerosol species is not always so explicit. Approximately two decades ago, models predominantly treated aerosol particles as bulk species and frequently incorporated simplifying assumptions for both organic and inorganic species, largely due to limitations in computational cost. It was not uncommon for most models to employ a simplified chemical speciation, representing the entire ensemble of their aerosol populations by a limited number of species (e.g., sea salt, dust, organic and black carbon, sulfate). However, significant advancements have been made since then, with most models now having detailed parameterizations and chemical treatments while simultaneously expanding their aerosol speciation. Noteworthy advancements include the expansion of the inorganic species to encompass other significant constituents, such as nitrate and ammonium, as well as chloride and mineral cations. A similar enhancement has been observed in the representation of organic species, which now offer a more sophisticated speciation based on their emission source characteristics (i.e., fossil fuel or biomass-related) and oxidation levels. This enhancement in the intricacy of chemical representation of aerosol species in numerical models has coincided with the transformation in emission trends over the past two decades, which was undertaken to address the concerns related to climate change.

A notable development pertains to the inorganic precursors, with substantial measures having been implemented for the reduction of SO_2 emissions, though less extensively for NOx emissions, while concurrently NH_3 emissions have exhibited an increase. This phenomenon is corroborated by the respective modeled and observed trends in the concentrations of these compounds (Bellouin et al., 2011; Hauglustaine et al., 2014; Ciarelli et al., 2019), with their projected future course simulated under different socioeconomic scenarios anticipated to follow a similar trajectory. This behavior is further illustrated in Figure 1.5. Such a change in the global reactive gases emissions landscape is also likely to bring about alterations in the inorganic aerosol composition regime. In the atmosphere, sulfuric acid (H_2SO_4) and nitric acid (HNO_3) compete with each other to react with the available ammonia (NH_3), leading to the formation of particulate sulfate (SO_4^{2-}) and particulate nitrate (NO_3^-), respectively. Since SO_2 is a key precursor for H_2SO_4 and NOx a key precursor for HNO_3, it is anticipated that the availability of HNO_3 to react with NH_3 will increase. This phenomenon, when considered in conjunction with the observed increase in global NH_3 levels, suggests a potential enhancement in the formation of particulate nitrate within the atmosphere, at the expense of particulate sulfate formation.

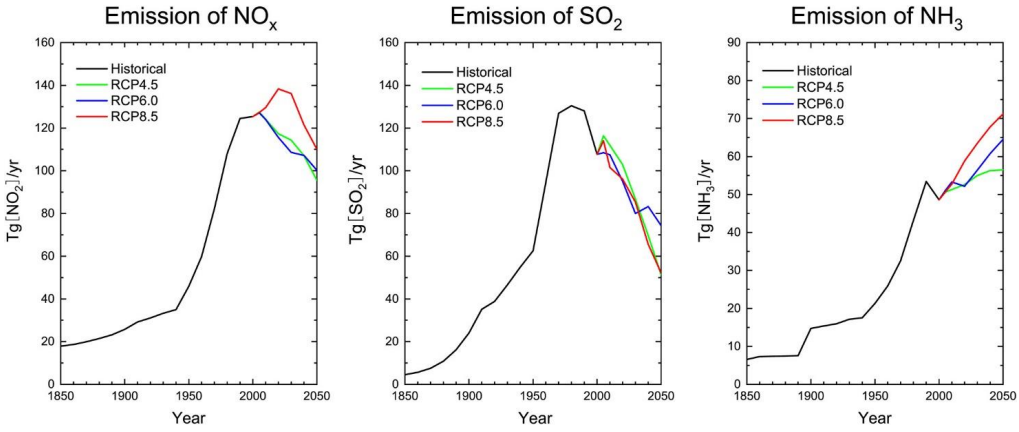

Figure 1.5: Global and annual averaged evolution (black line) of NO_x, SO_2, and NH_3 emissions. Also shown are the future projections among the three socioeconomic scenario pathways RCP4.5 (green line), RCP6.0 (blue line) and RCP8.5 (red line). The historical data for SO_2 are from Smith et al. (2004), while for NO_x and NH_3 are from Lamarque et al. (2010). The socioeconomic scenario data are described by Moss et al. (2010) and Van Vuuren et al. (2011). Figure is adopted from the open access publication by An et al. (2019) under the Creative Commons Attribution 4.0 License (https://creativecommons.org/licenses/by/4.0/deed.en).

Indeed, sulfate aerosols, which are the most significant contributor to inorganic mass concentrations on a global scale, have exhibited analogous declining trends in recent years, particularly in the U.S. (Hand et al., 2012; Leibensperger et al., 2012; Lajtha and Jones, 2013) and Europe (Lajtha and Jones, 2013; Ciarelli et al., 2019; Yang et al., 2020). This phenomenon is gradually and consistently contributing to an increase in the nitrate aerosol component's share of the total inorganic mass. Numerous studies have identified concentration levels that are comparable to or favor the nitrate species in the U.S. (Walker et al., 2012; Shah et al., 2018), Europe (Schaap et al., 2004; Galindo et al., 2008; Lanz et al., 2010; Aksoyoglu et al., 2017), and more strongly over the East Asian region (Kai et al., 2007; Lin et al., 2010; Wang et al., 2013; Wen et al., 2018; Li et al., 2020) as well as on the general global scale (Hauglustaine et al., 2014). A transition from a sulfate-dominated atmosphere to one dominated by nitrate is expected to affect not only the atmospheric acidity levels but also the behavior of dust particles, a major natural aerosol species. Specifically, a decrease in sulfate levels is predicted to result in an increase in the pH of particles, thereby affecting the process of aerosol thermodynamic partitioning between the gas and particle phases. This, in turn, is expected to influence the overall atmospheric oxidation capacity (Pye et al., 2020; Nenes et al., 2020). In regard to the second impact, the interactions between nitrate and dust particles are expected to result in a shift in the latter's optical characteristics, manifesting in an accelerated manner. However, these changes do not necessarily result in a straightforward climatic response, exhibiting either warming or cooling radiative effects for dust particles (Klingmüller et al., 2020; Kok et al., 2023). Consequently, studies have identified nitrate aerosols as a primary inorganic component of both air quality and climatic impact in both the long and near future (Bauer et al., 2007a; Bellouin et al., 2011; Li et al., 2015). Consequently, a comprehensive representation of nitrate aerosols, particularly their formation and chemical evolution, is imperative for air quality and climate models..

However, this is not a simple task, as the semi-volatile nature of nitrate aerosols poses significant challenges in predicting their partitioning between the gas and particle phases. This task is typically reserved for thermodynamic equilibrium models. An examination of the production of nitrate aerosol in the atmosphere is crucial, as it is a secondary pollutant, meaning it is not directly emitted. The primary precursor of nitrate aerosol is nitric acid (HNO_3), which, notably, does not itself constitute a primary pollutant. Nitrate aerosol formation involves two predominant pathways, which vary with the diurnal cycle (Jacobson, 1999; Seinfeld and Pandis, 2016). Specifically, during daytime, the predominant source of HNO_3 is the oxidation of NO2 by the hydroxyl radical (OH). Atmospheric oxidation is regarded as the chemical transformation of trace gases by certain species, with OH being one of the most significant, along with ozone (O3) and the nitrate radical (NO_3). This process generally leads to the removal of primary gaseous pollutants. The oxidation of NO_2 is represented by the following gas phase reaction :

$$NO_2 + OH \rightarrow HNO_3 \qquad \text{(R1.1)}$$

During daytime, the reaction of NO2 with sunlight (i.e., photolysis) reduces its availability, as it "breaks down" NO_2 into nitrogen monoxide (NO) and an oxygen atom. However, during nocturnal periods, the absence of sunlight and subsequent photolysis of NO_2 results in a shift in this regime, leading to a significant increase in NO_2 abundance compared to daytime levels. Consequently, NO_2 reacts with ozone to produce the nitrate radical as follows :

$$NO_2 + O_3 \rightarrow NO_3 + O_2 \qquad \text{(R1.2)}$$

As with NO_2, the absence of photolysis of the nitrate radical during the night results in its increased concentrations. Consequently, the nitrate radical reacts with NO_2 to produce dinitrogen pentoxide (N_2O_5) via the following reaction :

$$NO_3 + NO_2 \leftrightarrows N_2O_5 \qquad \text{(R1.3)}$$

The aforementioned reaction is reversible and governed by a thermal equilibrium, the scale of which is measured in minutes. The final link in the chain of reactions that occur during nighttime is the hydrolysis of N_2O_5, a heterogeneous reaction that takes place on a particle surface with an adequate amount of water, resulting in the production of HNO_3 as follows :

$$N_2O_5 + H_2O(aq,s) \rightarrow 2HNO_3 \qquad \text{(R1.4)}$$

Subsequently, HNO_3 can lead to the production of nitrate aerosols via equilibrium partitioning between the gas and particle phases, gas phase chemistry, and heterogeneous chemistry (Jacobson, 1999; Seinfeld and Pandis, 2016). A concise overview of the pivotal reactions associated with nitrate aerosol formation is presented in Table 1.1.

The solubility of HNO_3 in the gas phase allows for its dissolution into the ions H+ and NO_3^- within cloud water. Furthermore, the formation of particulate nitrate originates from the reaction of HNO_3 with NH_3 to produce the ammonium nitrate species (NH_4NO_3). Depending on the ambient relative humidity, this can exist either in solid form as a salt or in liquid form (deliquesced into the NH_4^+ and NO_3^- ions). A typical value for the DRH of ammonium nitrate at 25°C is 62% (Hidy, 2012). The formation of ammonium nitrate through this pathway is predominantly observed in urban and polluted regions, leading to the presence of aerosol nitrate primarily in the fine mode. The formation of ammonium nitrate is found to be highly dependent on the availability of NH_3. Specifically, in low concentrations where there is not enough NH_3 to react with H_2SO_4 in order to neutralize the available sulfate, the production of ammonium sulfate ($(NH_4)_2SO_4$) overpowers that of ammonium nitrate. Conversely, under conditions of elevated ammonia concentrations, sufficient to counteract sulfate, a surplus ammonia is produced that is more readily available to react with nitric acid (HNO_3) to form ammonium nitrate. In the context of heterogeneous chemistry, nitrate aerosols are produced through the adsorption of HNO_3 on the surface of sea salt

particles and mineral dust particles. In the initial instance, HNO_3 reacts with NaCl, yielding the salt $NaNO_3$, with hydrochloric acid (HCl) as a by-product. In the second case, HNO_3 reacts with the carbonates present in mineral dust to produce the salts $Ca(NO_3)_2$, $Mg(NO_3)_2$, KNO_3, and also $NaNO_3$. These salts, akin to ammonium nitrate, can exist in their solid form or undergo deliquescence to become individual ions (see Table 1.1). The formation of these salts through this pathway occurs predominantly in more remote regions, resulting in aerosol nitrate primarily in the coarse mode. Finally, the equilibrium gas-to-particle partitioning of the nitrate aerosol species is anti-correlated with ambient temperature, with colder conditions favoring the transition towards the particle phase.

Table 1.1 : Summary of most common chemical reactions resulting in aerosol nitrate formation

Reaction	Conditions
Gas Phase with Aqueous Products	
$HNO_3(g) \rightarrow H^+ + NO_3^-$	Dissolution in cloud water
$NH_3(g) + HNO_3(g) \rightarrow NH_4^+ + NO_3^-$	Ambient RH > DRH of Ammonium Nitrate
Gas Phase with Solid Products	
$NH_3(g) + HNO_3(g) \rightarrow NH_4NO_3(s)$	Ambient RH < DRH of Ammonium Nitrate
Heterogeneous	
$NaCl(s) + HNO_3(g) \rightarrow NaNO_3(s) + HCl\ (g)$	Sea Salt surface
$CaCO_3(s) + 2HNO_3(g) \rightarrow Ca(NO_3)_2(s) + CO_2(g) + H_2O(aq)$	Mineral Dust surface
$MgCO_3(s) + 2HNO_3(g) \rightarrow Mg(NO_3)_2(s) + CO_2(g) + H_2O(aq)$	Mineral Dust surface
$K_2\ CO_3(s) + 2HNO_3(g) \rightarrow 2KNO_3(s) + CO_2(g) + H_2O(aq)$	Mineral Dust surface
$(Na)_2\ CO_3(s) + 2HNO_3(g) \rightarrow 2NaNO_3(s) + CO_2(g) + H_2O(aq)$	Mineral Dust surface
Equilibrium Partitioning	
$HNO_3(g) \leftrightarrow HNO_3(aq)$	
$HNO_3(g) \leftrightarrow H^+ + NO_3^-$	
$NaNO_3(s) \leftrightarrow Na^+ + NO_3^-$	
$Ca(NO_3)_2(s) \leftrightarrow Ca^{2+} + 2NO_3^-$	
$Mg(NO_3)_2(s) \leftrightarrow Mg^{2+} + 2NO_3^-$	
$KNO_3(s) \leftrightarrow K^+ + NO_3^-$	

1.4 Research approach – Thesis objectives

A prevalent hypothesis among atmospheric models concerning the precise estimation of inorganic aerosol concentrations concerns the assumption of their thermodynamic physical state. This involves the inquiry of whether the particles will enable the process of crystallization when the ambient relative humidity (RH) is sufficiently low, thereby forming solid salts, or if they will be characterized by a supersaturated aqueous state even in conditions of extremely low ambient RH. The former state is designated as stable, while the latter is referred to as metastable. Evidence of aerosol water existing in this supersaturated form in the low end of the RH spectrum has been found (Brooks et al., 2003; Parsons et al., 2004), and the existence of aerosols in the metastable state in RH ranges as low as 40% has also been observed by field campaigns (Guo et al., 2015; Bougiatioti et al., 2016; Guo et al., 2018). Furthermore, it has been argued that treating the aerosol physical state as metastable is a more appropriate approach for models that tend to ignore the crystallization hysteresis effect (Adams et al., 1999; Metzger et al., 2002). However, it would be erroneous to consider the aerosol physical state an obvious choice for simulating inorganic aerosol concentrations, especially on a global scale. For instance, the consideration of a stable state is believed to yield a more accurate agreement with observations under conditions where the ambient RH consistently falls below 50% (Fountoukis et al., 2009; Karydis et al., 2010). Conversely, under conditions of intermediate ambient RH, the metastable approach has been shown to offer a more substantial agreement with observations for low aerosol concentrations (Ansari and Pandis, 2000). However, under comparable conditions and at higher aerosol concentrations, the two approaches yield insignificant differences (Ansari and Pandis, 2000). Furthermore, in scenarios where ambient RH is comparatively low (< 60%), yet ambient temperature is relatively high (> 10°C), the metastable assumption generally exhibits stronger agreement with observations. Conversely, for lower temperatures (< 5°C), this is true for the stable assumption, with both treatments demonstrating insignificant differences for high RH values (> 83%) (Cheng et al., 2022). Therefore, it is evident that the assumption choice is significantly influenced by the region and the prevailing atmospheric conditions, particularly in the context of a global model. Finally, the consideration of the aerosol physical state, apart from its implications for ambient concentrations, also has an impact on aerosol acidity, which in turn affects the gas/particle partitioning process (Guo et al., 2016; Nenes et al., 2020; Pye et al., 2020). This is of particular importance for the particular nitrate species, as its phase partitioning is sensitive to the aerosol pH. Specifically, at pH values of ~1 all nitrate exists practically in the gas phase, while when pH exhibits values of ~4 then it is found almost exclusively is the particle phase (Tilgner et al., 2021). Therefore, it is evident how even small discrepancies in the model estimated aerosol acidity can result in unwanted uncertainties in the estimates of such species.

In consideration of the aforementioned information, the initial objective of the present thesis, as outlined in Section 2, is to meticulously examine the disparities between the two approaches, which have been integrated within a global atmospheric model, with respect to their respective applications in the simulation of inorganic aerosols. The central objective is to address

the most significant geographical regions and ambient conditions under which such discrepancies arise. This will enable future users to make informed decisions regarding the strengths and weaknesses of each assumption. To that end, the following central research questions have been developed and addressed :

- Does the aerosol physical state consideration lead to significant differences in inorganic aerosol concentrations on a global scale ?
- Under what conditions and over which regions do the two approaches exhibit the highest discrepancies ?
- How is the inorganic aerosol acidity affected by their physical state assumption ?
- Does one consideration result in any measurable computational speed-up in global scale simulations ?

To this end, a global scale climate-chemistry model is employed to conduct simulations that will compare both approaches. Comprehensive information regarding the model can be found in Sections 2.2.1, 3.2.1, and 4.2.1. The model has been utilized to conduct simulations that compare the estimations of the two thermodynamical approaches with observations from the most polluted regions and with each other. Additionally, the simulations examine the key differences in estimated aerosol pH values. Furthermore, the changes in computational cost required by both approaches has been thoroughly investigated.

Another central focus of this thesis is the aim to take a step towards a more accurate estimation of nitrate aerosols by a global atmospheric model. In addition to the examples that demonstrate the growing significance of nitrate aerosols within the category of inorganic aerosols, as discussed in the preceding section, it is crucial to note the projected future increase in NH_3 emissions (Fu et al., 2017; Chen et al., 2019b; Xu et al., 2020), a primary precursor. This increase will contribute to an elevated presence of fine-mode nitrate aerosols in regions affected to a greater extent by anthropogenic pollution. This is particularly relevant given the established role of nitrate aerosols as a significant component of the overall aerosol population in today's environment (He et al., 2001; Silva et al., 2007; Weagle et al., 2018; Tang et al., 2021). The rationale behind striving for a more precise nitrate aerosol representation is that a prevalent bias in many regional and global models is the overprediction of concentration levels. Specifically, this feat is reported by modeling studies that were conducted in the most heavily polluted regions of the planet, such as Europe (Fountoukis et al., 2011; Tuccella et al., 2012; Ciarelli et al., 2016; Chen et al., 2018; Jones et al., 2021), USA (Yu et al., 2005; Heald et al., 2012; Zakoura and Pandis, 2018, 2019; Jones et al., 2021) and especially East Asia (Kim et al., 2006; Li and Han, 2016; Bian et al., 2017; Chen et al., 2019a; Tan et al., 2020; Miao et al., 2020).

In light of such model biases, Section 3 endeavors to investigate a range of configurations and parameterizations associated with the estimation of fine mode nitrate aerosol in the global model. The objective is to pinpoint the most crucial aspects to bridge the disparities between simulated and observed concentrations of PM_1 and $PM_{2.5}$ nitrate particles. The regions with the highest levels of anthropogenic activity across the Northern Hemisphere, namely East Asia, India, Europe, and North America, were examined. The primary objective of this section is to derive model setup recommendations for future users, tailored to the specific region and size mode of interest. The aspects that are examined include the impacts of :

- Utilizing different grid resolutions.
- Using different databases for anthropogenic emissions of trace gases and aerosols.
- The thermodynamic aerosol physical state assumption.
- Considering a lower uptake coefficient for the N_2O_5 hydrolysis.
- Considering a more simplified mechanism regarding aerosol wet deposition.

The model estimations resulting from all considerations above are extensively compared with observations from both filter measurement networks regarding the $PM_{2.5}$ size, as well as field campaigns of AMS measurements regarding the PM_1 size in the aforementioned regions. The time span of the comparisons extends over a decade, with all seasons being taken into account.

Finally, this thesis thoroughly investigates the climate impact of nitrate aerosols in both coarse and fine modes, in regard to their present-day global direct and indirect radiative effect. The investigation is further expanded by considering the implications of the interactions between nitrate aerosols and mineral dust particles. The significance of these interactions stems from the promotion of nitrate aerosol production on dust surfaces through HNO_3 adsorption (Trump et al., 2015; Karydis et al., 2016) and the subsequent heterogeneous reactions described in the previous section. The implications of dust-pollution interactions on the radiative effects of anthropogenic aerosols have been the focus of recent studies (Klingmüller et al., 2019; Klingmüller et al., 2020; Kok et al., 2023). However, the specific focus on the implications of dust-nitrate interactions on the latter's radiative effects has not been a primary research area. Furthermore, the direct radiative effect (linked to interactions with radiation) of nitrate aerosol has been estimated by numerous studies previously (Adams et al., 2001; Liao et al., 2004; Bauer et al., 2007a; Bauer et al., 2007b; Bellouin et al., 2011; Xu and Penner, 2012; Heald et al., 2014). However, the same cannot be said for the indirect radiative effect (linked to interactions with clouds) of the species, which is of particular importance as nitrate aerosols are not only very effective cloud condensation nuclei themselves, but they also result in the increased activation into cloud droplets of dust aerosols through physicochemical interactions with them (Karydis et al., 2011, 2017). Apart from this fact,

the indirect radiative effect is generally the largest source of uncertainty in the total radiative effect (Myhre et al., 2014; Seinfeld et al., 2016).

Beyond the examination of dust-nitrate interactions and their impact on the radiative effects of nitrate aerosols, this thesis aspires to address two additional research queries. The first is the extent to which the chemical composition and the emitted amount of mineral dust in the atmosphere will impact the loading of nitrate aerosols on a global scale, and whether a linear relationship exists. Secondly, the study will examine the impact of these two factors on the estimated radiative effects of NO_3^-. In order to address these research queries, the study proposes the following research questions, which will be explored in Section 4 :

- What is the present-day global direct radiative effect of coarse and fine nitrate aerosols ?
- What is the present-day global indirect radiative effect of total nitrate aerosols ?
- What is the impact of dust-nitrate interactions on both these estimates ?
- Is the consideration of dust composition or dust aerosol loading most important ?

The global model has simulated multiple scenarios concerning various chemical compositions and dust loadings in the atmosphere. Each scenario encompassed a 11-year time period to calculate radiative effect estimations. Details regarding the aspects examined are presented in section 4.2.1. Finally, all details about the representation of dust-nitrate interactions in the global model are found in section 4.2.2.

2 Impact of thermodynamic treatment consideration in global inorganic aerosol estimations and acidity

The content of this chapter was published as : “Implementation of the ISORROPIA-lite Aerosol Thermodynamics Model into the EMAC Chemistry Climate Model 2.55.2: Implications for Aerosol Composition and Acidity” by A. Milousis, A. P. Tsimpidi, H. Tost, S. N. Pandis, A. Nenes, A. Kiendler-Scharr and V. A. Karydis in Geoscientific Model Development, 2024, DOI: https://doi.org/10.5194/gmd-17-1111-2024 under the Creative Commons 4.0 License (https://creativecommons.org/licenses/by/4.0/deed.en).

The supplementary material is provided in Appendix A.2. The data produced in the study are available from the authors upon request. The authors contributed to the article as follows:

AM and VAK wrote the paper with contributions from all coauthors. VAK planned the research with contributions from AKS, SNP and AN. AN and SNP provided the ISORROPIA-lite model. AM and HT performed the implementation in EMAC. AM performed the simulations and analyzed the results assisted by VAK and APT. APT provided the observations and performed the model evaluation. All the authors discussed the results and contributed to the manuscript.

Geosci. Model Dev., 17, 1111–1131, 2024
https://doi.org/10.5194/gmd-17-1111-2024

Geoscientific Model Development
Open Access
EGU

Implementation of the ISORROPIA-lite aerosol thermodynamics model into the EMAC chemistry climate model (based on MESSy v2.55): implications for aerosol composition and acidity

Alexandros Milousis[1], Alexandra P. Tsimpidi[1], Holger Tost[2], Spyros N. Pandis[3,4], Athanasios Nenes[3,5], Astrid Kiendler-Scharr[1,†], and Vlassis A. Karydis[1]

[1]Institute for Energy and Climate Research, IEK-8 Troposphere, Forschungszentrum Jülich GmbH, Jülich, Germany
[2]Institute of Atmospheric Physics, Johannes Gutenberg University Mainz, Mainz, Germany
[3]Institute of Chemical Engineering Sciences, FORTH ICE HT, Patras 26504, Greece
[4]Department of Chemical Engineering, University of Patras, Patras 26500, Greece
[5]School of Architecture, Civil and Environmental Engineering, Laboratory of atmospheric processes and their impacts, École Polytechnique Fédérale de Lausanne, 1015 Lausanne, Switzerland
[†]deceased

Correspondence: Vlassis A. Karydis (v.karydis@fz-juelich.de)

Received: 23 August 2023 – Discussion started: 7 September 2023
Revised: 4 December 2023 – Accepted: 19 December 2023 – Published: 12 February 2024

Abstract. This study explores the differences in performance and results by various versions of the ISORROPIA thermodynamic module implemented within the ECHAM/MESSy Atmospheric Chemistry (EMAC) model. Three different versions of the module were used, ISORROPIA II v1, ISORROPIA II v2.3, and ISORROPIA-lite. First, ISORROPIA II v2.3 replaced ISORROPIA II v1 in EMAC to improve pH predictions close to neutral conditions. The newly developed ISORROPIA-lite has been added to EMAC alongside ISORROPIA II v2.3. ISORROPIA-lite is more computationally efficient and assumes that atmospheric aerosols exist always as supersaturated aqueous (metastable) solutions, while ISORROPIA II includes the option to allow for the formation of solid salts at low RH conditions (stable state). The predictions of EMAC by employing all three aerosol thermodynamic models were compared to each other and evaluated against surface measurements from three regional observational networks in the polluted Northern Hemisphere (Interagency Monitoring of Protected Visual Environments (IMPROVE), European Monitoring and Evaluation Programme (EMEP), and Acid Deposition Monitoring Network of East Asia (EANET)). The differences between ISORROPIA II v2.3 and ISORROPIA-lite were minimal in all comparisons with the normalized mean absolute difference for the concentrations of all major aerosol components being less than 11 % even when different phase state assumptions were used. The most notable differences were lower aerosol concentrations predicted by ISORROPIA-lite in regions with relative humidity in the range of 20 % to 60 % compared to the predictions of ISORROPIA II v2.3 in stable mode. The comparison against observations yielded satisfactory agreement especially over the USA and Europe but higher deviations over East Asia, where the overprediction of EMAC for nitrate was as high as 4 $\mu g\,m^{-3}$ ($\sim$ 20 %). The mean annual aerosol pH predicted by ISORROPIA-lite was on average less than a unit lower than ISORROPIA II v2.3 in stable mode, mainly for coarse-mode aerosols over the Middle East. The use of ISORROPIA-lite accelerated EMAC by nearly 5 % compared to the use of ISORROPIA II v2.3 even if the aerosol thermodynamic calculations consume a relatively small fraction of the EMAC computational time. ISORROPIA-lite can therefore be a reliable and computationally efficient alternative to the previous thermodynamic module in EMAC.

Published by Copernicus Publications on behalf of the European Geosciences Union.

1 Introduction

Aerosols in the atmosphere have a significant impact on climate and air pollution. They contribute to the deterioration of air quality, especially in heavily industrialized regions, leading to increased mortality rates and decreased life expectancy (Héroux et al., 2015). Particulate matter with diameter less than 2.5 µm ($PM_{2.5}$) is the largest contributor to stroke, cancer, heart conditions and chronic obstructive pulmonary diseases (Brook et al., 2010; Pope et al., 2011), with ambient pollution causing approximately 4.2 million premature deaths in 2019 alone (WHO, 2022). Tarin-Carrasco et al. (2021) predicted that mortality rates in Europe due to air pollution could increase in the next 30 years in the more extreme emission scenarios (e.g., RCP8.5). In addition to the direct threat aerosols pose to humans and ecosystems through their effects on air quality, they can also affect other climate-related processes. For example, they can act as cloud condensation nuclei and modify cloud lifetime and optical properties (Andreae et al., 2005; Klingmüller et al., 2020). Aerosols also affect the energy balance of our planet by reflecting additional solar radiation back to space and thus cooling the atmosphere or by absorbing solar radiation and thus warming the atmosphere (Klingmüller et al., 2019; Miinalainen et al., 2021). Some major inorganic aerosol components also affect various ecosystems. For example, nitrates and sulfates can harm flora by lessening its lifetime and variety (Honour et al., 2009; Manisalidis et al., 2020) and can affect wildlife by causing water eutrophication (Doney et al., 2007). A critical property of atmospheric particles that regulates their impacts on clouds and ecosystems is their acidity (Karydis et al., 2021). Depending on its levels, acidity can affect air quality and human health (Lelieveld et al., 2015) but also the aerosols' hygroscopic characteristics (Karydis et al., 2016). The aerosol pH also drives the partitioning of semivolatile inorganic components between the gas and aerosol phases (Nenes et al., 2020). Finally, aerosol acidity plays a role in the activation of halogens in aerosols (Saiz-Lopez and von Glasow, 2012), their toxicity (Fang et al., 2017) and also in secondary organic aerosol formation (Marais et al., 2016).

Sulfate is the most important component of $PM_{2.5}$ inorganic aerosol, since it contributes the most in terms of global mass burden (Szopa et al., 2021) and aerosol optical depth (AOD) (Myhre et al., 2013). The nitrate contribution to the $PM_{2.5}$ aerosol composition is also important in several areas (e.g., Europe, North America, East Asia) and seasons (He et al., 2001; Silva et al., 2007; Weagle et al., 2018; Tang et al., 2021). The quantification of nitrate partitioning between the gas and particulate phases is challenging partly because it is affected by meteorology (temperature, relative humidity) and all ionic aerosol components but also due to the lack of observations to constrain the composition of the gas-phase components and the size distribution of the particulate phase. Nitrate in the form of ammonium nitrate is mainly found in the fine mode (e.g., $PM_{2.5}$) (Putaud et al., 2010). This is especially the case over polluted regions where there is enough ammonia remaining after the neutralization of sulfate (Karydis et al., 2011, 2016). In coastal and desert areas, nitrate is formed mainly by reactions of HNO_3 with sea salt and dust particles (Savoie and Prospero, 1982; Wolff, 1984; Karydis et al., 2016) and therefore is found mainly in the coarse particles. The importance of nitrate in the troposphere is expected to increase in the following decades, because SO_2 emissions are anticipated to drop, while NH_3 emissions are anticipated to increase (Fu et al., 2017; Chen et al., 2019; Xu et al., 2020). With decreased SO_2 concentrations, less ammonia is required to neutralize the sulfates and therefore more is available for ammonium nitrate formation (Tsimpidi et al., 2007).

There have been several thermodynamic models developed in the last decades to calculate the inorganic aerosol concentrations and composition in the atmosphere. Two of the first were EQUIL and KEQUIL, developed by Bassett and Seinfeld (1983). Then the MARS model was developed by Saxena et al. (1986) with the aim of reducing the computational time required in order to be incorporated into larger-scale chemical transport models. MARS was the first model to divide the composition domain into smaller subdomains, aiming to reduce the number of equations needed to be solved. Then the SEQUILIB model by Pilinis and Seinfeld (1987) was the first to incorporate sodium and chloride as well as the corresponding salts in the simulated aerosol system. Further developments included EQUISOLV by Jacobson et al. (1996) as well as SCAPE by Kim et al. (1993), which simulated temperature-dependent deliquescence following Wexler and Seinfeld (1991) and predicted the presence of liquid-phase aerosols even at low relative humidity (RH). E-AIM is another benchmark thermodynamic model which instead of solving algebraic equations for equilibrium uses the minimization of the Gibbs free energy approach (Wexler and Clegg, 2002). Later versions of E-AIM also include selected organic aerosol components (Clegg et al., 2003). Furthermore, AIOMFAC is a model that utilizes organic–inorganic interactions in aqueous solutions in order to calculate activity coefficients up to high ionic strengths (Zuend et al., 2008) and is based on the LIFAC model by Yan et al. (1999). Further developments in AIOMFAC include a wider variety of organic compounds (Zuend et al., 2011). The EQSAM thermodynamic model was developed by Metzger et al. (2002) with the basic concept that aerosol activities in equilibrium are controlled by RH, and solute activity is a function of RH. The model uses a domain structure based on sulfate availability to increase computational efficiency by solving fewer thermodynamic equations, similar to Nenes et al. (1998). EQSAM and ISORROPIA are the two available options for aerosol thermodynamics in the EMAC model.

Nenes et al. (1998) developed the ISORROPIA model in an effort to increase computational efficiency while maintaining the accuracy of the calculations. The system simulated by ISORROPIA included NH_4^+, Na^+, Cl^-, NO_3^-,

SO_4^{2-} and H_2O. ISORROPIA also contains the temperature-dependent equations for deliquescence by Wexler and Seinfeld (1991) and is computationally efficient so that it can be incorporated into 3D atmospheric models. In ISORROPIA, the aerosol state is predicted as a weighted mean value of the dry and wet states. The weighting factors depend on ambient RH, the mutual deliquescence relative humidity (MDRH) and the deliquescence relative humidity (DRH) of the most hygroscopic salt in the mixture. An improved version of ISORROPIA including the mineral ions K^+, Ca^{2+} and Mg^+, called ISORROPIA II, was developed by Fountoukis and Nenes (2007). The addition of the above crustal ions resulted in the inclusion of 10 more salts and 3 more ions in the solid and aqueous phases, respectively. The model gained in computational efficiency by performing different calculations for different atmospheric chemical composition regimes, which are determined by the abundance of each aerosol precursor as well as the ambient temperature and relative humidity. Depending on the values of the so-called "sulfate ratio", the "crustal species and sodium ratio" and the "crustal species ratio", five aerosol composition regimes are determined in order to calculate the necessary equilibrium equations for the species present in each regime. Furthermore, the use of pre-calculated look-up tables for the activity coefficients (see Sect. 2.2), including their temperature dependence, is another factor for the gain in computational efficiency. Like E-AIM, ISORROPIA II can solve the thermodynamic equilibrium problem under stable or metastable conditions. In the second case, aerosols are assumed to exist only as supersaturated aqueous solutions even at low RH, while in the first case the aerosols are able to form solid salts. A very slightly updated version, called ISORROPIA II v2.3, was introduced to improve aerosol pH predictions close to neutral conditions (Song et al., 2018). More specifically, in some subcases of the ISORROPIA II regime, NH_3 evaporation was not taken into account in the aerosol pH calculations, leading to unrealistic estimates close to neutrality (pH $\sim$ 7). This error had a minimal effect on the predicted gas-phase NH_3 levels and consequently on the inorganic aerosol concentrations. Moreover, it only affected a few subcases and only when the stable mode was used. More details on these differences can be found in Song et al. (2018). The newest development of ISORROPIA II, called ISORROPIA-lite, was designed to be even more computationally efficient than its predecessor and to also include the effects that organic aerosol components have on particle water and the semivolatile inorganic aerosol species partitioning (Kakavas et al., 2022).

This study aims to evaluate the newly developed ISORROPIA-lite thermodynamic module within the EMAC global climate and chemistry model and to explore any discrepancies on a global scale, by utilizing different aerosol phase states. For this reason, our analysis explores the differences in the results between ISORROPIA-lite and ISORROPIA II over diverse conditions and environments. In Sect. 2, the model configuration and the treatment of inorganic aerosol thermodynamics is presented. In Sects. 3 and 4, the results and comparisons between the simulations are analyzed, and in Sect. 5 the major conclusions are presented.

2 Model configuration

2.1 EMAC model setup

The EMAC (ECHAM5/MESSy) model is a global atmospheric chemistry and climate model (Jöckel et al., 2006). It includes a series of submodels and links them via the Modular Earth Submodel System (Jöckel et al., 2005) to the base model (core) that is the fifth-generation European Center Hamburg general circulation model (Roeckner et al., 2006). Gas-phase chemistry is simulated by MECCA (Sander et al., 2019) with a simplified scheme similar to the one used in CCMI (Chemistry-Climate Model Initiative), like in Jöckel et al. (2016). Aerosol microphysics along with gas–aerosol partitioning are treated by GMXe in which the aerosols are differentiated between soluble and insoluble modes with a total of seven lognormal modes (Pringle et al., 2010a, b). The soluble mode contains the nucleation, Aitken, accumulation and coarse size ranges, while the insoluble mode lacks only the nucleation size range. Transfer of material between the insoluble and soluble modes is calculated in two processes. After coagulation, when a hydrophobic and a hydrophilic particle coagulate, the resulting mass is assumed to reside in the hydrophilic mode and also when soluble material condenses onto a hydrophobic particle (after gas–aerosol partitioning) it is again transferred to the hydrophilic mode (Pringle et al., 2010a, b). Wet deposition of gases and aerosols is described by SCAV (Tost et al., 2006, 2007), dry deposition is described via DRYDEP (Kerkweg et al., 2006) and gravitational sedimentation of aerosols is described by SEDI (Kerkweg et al., 2006). Cloud properties and microphysics are calculated by the CLOUD submodel (Roeckner et al., 2006), utilizing the detailed two-moment liquid and ice-cloud microphysical scheme of Lohmann and Ferrachat (2010) and considering a physically based treatment of the processes of liquid (Karydis et al., 2017) and ice crystal (Bacer et al., 2018) activation. The organic aerosol composition and evolution in the atmosphere is calculated by the ORACLE submodel (Tsimpidi et al., 2014, 2018).

The model simulations in this work were nudged towards actual meteorology using ERA5 data (Hersbach et al., 2020). For the purposes of this study, the spectral resolution applied within EMAC was T63L31, which corresponds to a grid resolution of 1.875° × 1.875°, covering vertical altitudes up to 25 km with a total of 31 layers. The simulations were all done for the period 2009–2010, with 2009 representing the model spin-up period.

Anthropogenic emissions of aerosols and aerosol precursors were based on the EDGARv4.3.2 inventory (Crippa et al., 2018). Open biomass burning emissions were derived by

the GFEDv3.1 database (van der Werf et al., 2010), and natural emissions of NH_3 (volatilization from soils and oceans) were based on the GEIA database (Bouwman et al., 1997). SO_2 emissions by volcanic eruptions are based on the AEROCOM dataset (Dentener et al., 2006), as are emissions of sea spray aerosols using the chemical composition proposed by Seinfeld and Pandis (2016). Biogenic emissions of NO from soils are calculated online according to the algorithm of Yienger and Levy (1995), while NO_x produced by lightning is also calculated online based on the parameterization of Grewe et al. (2001). Oceanic emissions of dimethyl sulfide (DMS) are calculated online by the AIRSEA submodel (Pozzer et al., 2006). Finally, the dust emission fluxes are calculated online according to Astitha et al. (2012), by taking into account the meteorological information for each grid cell (i.e., temperature and relative humidity) as well as the different thresholds of friction velocities above which suspension of dust particles takes place. The emissions of crustal ions (Ca^{2+}, Mg^{+}, K^{+} and Na^{+}) are estimated as a fraction of the total dust flux based on the soil chemical composition of each individual grid cell (Karydis et al., 2016; Klingmüller et al., 2018). These ions are emitted in the insoluble accumulation and coarse size modes and are subsequently transferred to the soluble aerosols by the processes described above.

2.2 Inorganic aerosol thermodynamics treatment

In this study, the ISORROPIA-lite aerosol thermodynamic model has been implemented in EMAC as part of the GMXe submodel, not as a replacement but as an alternative to the previous version, in order to efficiently calculate the equilibrium partitioning of the inorganic species between gas and aerosol phases. Furthermore, ISORROPIA II v2.3 is used to replace ISORROPIA II v1 in the model.

Kinetic limitations in the partitioning need to be taken into consideration, because only fine aerosols are able to achieve equilibrium within the time frame of one model time step, which in this study equals to 10 min. Therefore, the partitioning calculation is done in two stages according to Pringle et al. (2010a, b). First the amount of the gas-phase species that is able to kinetically condense onto the aerosol phase within the model time step is calculated by assuming diffusion-limited condensation (Vignati et al., 2004). Then, in the second stage, the partitioning between this gas-phase material and the aerosol phase is performed. The partitioning calculation is performed for all seven size modes (i.e., in each model time step, ISORROPIA is called separately for each of them).

According to Kakavas et al. (2022), ISORROPIA-lite features two main modifications in its code, with regard to ISORROPIA II v2.3 (Song et al., 2018) and ISORROPIA II v1 (Fountoukis and Nenes, 2007). First, the routines related to the stable case have been removed, since only the metastable case is considered and all salts formed are deliquesced. However, $CaSO_4$ is the only solid salt allowed to form, as it is considered insoluble for most atmospherically relevant RH values and precipitates spontaneously. Furthermore, for the calculation of binary activity coefficients, ISORROPIA-lite uses the tabulated binary activity coefficient data for each salt from Kusik-Meissner (Kusik and Meissner, 1978) instead of calculating them online, and it includes their temperature dependence according to Meissner and Peppas (1973). This is done by combining the Kusik and Meissner (1978) model for specific ionic pairs with the Bromley (1973) activity coefficient mixing rule for multicomponent mixtures. More information on this procedure can be found in Fountoukis and Nenes (2007). This second modification is the major contributor to the computational speed-up provided by ISORROPIA-lite, which in an offline estimation was reported to be around 35 % (Kakavas et al., 2022). Furthermore, this feature could explain differences in inorganic aerosol estimates with the previous version of ISORROPIA using the same aerosol state assumption (metastable case). Another important modification is that the effect of organic aerosol water on the inorganic semivolatile aerosol components is included. This consideration slightly increases the aerosol pH but more significantly drives the phase partitioning towards the aerosol phase in order to satisfy equilibrium conditions (Kakavas et al., 2022). However, this feature of ISORROPIA-lite was not used in the present study, as the water uptake by organics is treated by other parts of the GMXe aerosol microphysics submodel in the EMAC global model. The effects of the secondary organic aerosol on aerosol water and nitrate partitioning are discussed by Kakavas et al. (2023).

In the updated version of the GMXe submodel, users have the option to select between ISORROPIA-lite and ISORROPIA II v2.3 to perform EMAC simulations depending on the application and the desired phase state assumption. While ISORROPIA-lite utilizes the metastable approach exclusively, ISORROPIA II v2.3 utilizes both and has the stable approach as default.

3 Evaluation of new aerosol thermodynamic modules within EMAC

For reasons of clarity, from this point forward both in the main text as well as in any figure captions, whenever different aerosol sizes are mentioned, total suspended particles (denoted TSP) refer to the sum of the four lognormal size modes of the aerosol microphysics submodel (i.e., nucleation, Aitken, accumulation and coarse modes), fine aerosols refer to the sum of the three smaller size modes (i.e., nucleation, Aitken and accumulation modes) and coarse aerosols refer to the largest size mode of the model exclusively.

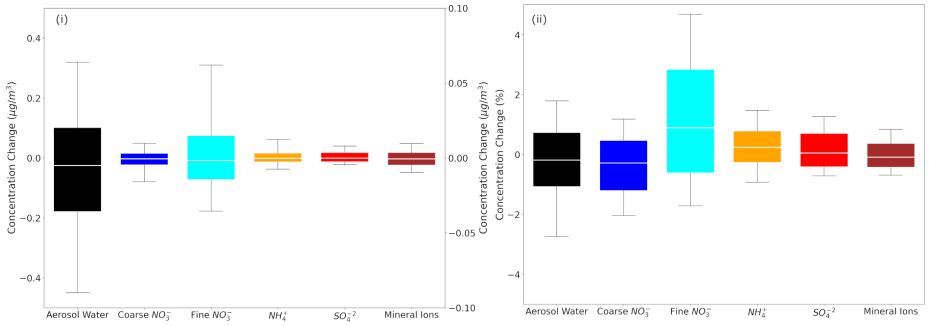

Figure 1. Box plots depicting the 25th, 50th and 75th percentiles (box) of the **(i)** difference and **(ii)** fractional difference in global daily mean surface concentrations of aerosol water (left y axis), mineral ions, NH_4^+ and SO_4^{2-} in TSP as well as coarse and fine aerosol NO_3^- (right y axis), as predicted by EMAC using ISORROPIA II v1 and ISORROPIA II v2.3. The 10th and 90th percentiles (whiskers) for each aerosol component are also shown. Both models assume that the aerosol is at its stable state at low RH and that a positive change corresponds to higher concentrations by ISORROPIA II v1.

Table 1. Statistical analysis of EMAC-simulated mean daily surface concentrations by employing ISORROPIA II v1 versus ISORROPIA II v2.3, both in stable mode. Deviations are given as ISORROPIA II v1 minus ISORROPIA II v2.3.

	Mean difference ($\mu g\,m^{-3}$)	Normalized mean absolute difference (%)
Coarse NO_3^-	-8×10^{-4}	1.8
Fine NO_3^-	-0.011	2.6
HNO_3	-3.1×10^{-4}	0.7
NH_4^+	-1.6×10^{-4}	2.0
SO_4^{2-}	-0.009	1.2
Na^+	0.007	1.6
Ca^{2+}	1.7×10^{-4}	0.4
K^+	1.1×10^{-4}	0.4
Mg^+	1.5×10^{-4}	0.4
Cl^-	0.040	2.3
H_2O	0.046	1.1
H^+	-2.9×10^{-5}	1.5

3.1 Comparison of ISORROPIA II v1 against ISORROPIA II v2.3 in stable mode

The first comparison aims to examine how ISORROPIA II v2.3 fares against ISORROPIA II v1 when considering solely the stable assumption, after the latter's replacement in the newer version of the EMAC model.

The differences in global daily mean surface concentrations of NH_4^+, SO_4^{2-}, mineral ions (sum of Ca^{2+}, K^+, Mg^{2+}) and aerosol water in TSP as well as fine and coarse aerosol NO_3^- as predicted by the two versions can be seen in Fig. 1. The 25th and 75th percentiles of concentration differences between the two versions for the aerosol water are below $0.2\,\mu g\,m^{-3}$, and for the remaining species they are an order of magnitude less, which translates to differences mostly below 1 % for all species. Therefore, the predictions of inorganic aerosol composition of the two versions agree exceptionally well.

In order to investigate potential differences arising in specific areas, regions affected by high nitrate concentrations were selected, i.e., Europe, the Tibetan Plateau, East Asia, North America and the Middle East. The differences in daily mean coarse and fine NO_3^- over these regions are shown in Fig. S1 in the Supplement. The comparison showed that the differences regarding the 25th and 75th percentiles are less than $0.05\,\mu g\,m^{-3}$ (or less than 2.5 %) between the results of the two ISORROPIA II versions for both size modes. A statistical analysis of the results reveals that all differences between the aforementioned species are on average below 3 % (Table 1). Therefore, the replacement of ISORROPIA II v1 by v2.3 in the EMAC model yields only trivial differences in the predicted aerosol ionic composition and water. The following sections focus on the comparison between the results of ISORROPIA-lite against ISORROPIA II v2.3 (called ISORROPIA II hereafter for simplicity), both in stable and metastable states.

3.2 Comparison of ISORROPIA-lite against ISORROPIA II in metastable mode

The model results using ISORROPIA-lite are compared first against those using ISORROPIA II in metastable mode in order to determine whether the ISORROPIA-lite version can produce similar results with the more detailed module in EMAC, under the same conditions. Figure 2 depicts the differences of the global daily mean surface concentrations of the same species that were examined before. The comparison yields differences for the 25th and 75th percentiles that

Table 2. Statistical analysis of EMAC-simulated mean daily surface concentrations by employing ISORROPIA-lite versus ISORROPIA II, both in metastable mode. Bias is given as ISORROPIA-lite minus ISORROPIA II.

	Mean difference ($\mu g\,m^{-3}$)	Normalized mean absolute difference (%)
Coarse NO_3^-	-6.2×10^{-4}	3.5
Fine NO_3^-	-3.1×10^{-4}	3.9
HNO_3	-2.7×10^{-4}	2.0
NH_4^+	-1.4×10^{-5}	3.8
SO_4^{2-}	2.5×10^{-3}	4.0
Na^+	0.011	6.7
Ca^{2+}	2.9×10^{-4}	1.9
K^+	1.8×10^{-4}	2.4
Mg^+	5.8×10^{-4}	3.5
Cl^-	0.017	7.0
H_2O	0.035	1.8
H^+	-8.3×10^{-4}	4.6

are less than $0.5\,\mu g\,m^{-3}$ for the aerosol water and mostly less than $0.05\,\mu g\,m^{-3}$ for the remaining inorganic aerosol components, which translates into differences of less than 2 % for all species most of the time.

Figure S2 shows the comparison between predicted global daily mean coarse and fine aerosol nitrate concentrations, focusing on the regions with the higher simulated mean annual concentrations. Across all regions, the concentration differences for both size modes are typically lower than $0.1\,\mu g\,m^{-3}$ (or less than 3 %) and are mostly found over the Himalayan and East Asian regions.

In Table 2, the statistics of the results for the global surface concentrations for all examined aerosol components reveal differences that are on average less than 7 %. Therefore, ISORROPIA-lite does provide quite similar predictions with ISORROPIA II in the EMAC model for simulations using the metastable state assumption.

3.3 Evaluation of inorganic aerosol predictions

EMAC predictions using both ISORROPIA-lite and ISORROPIA II in stable mode for $PM_{2.5}$ ammonium, sulfate and nitrate were compared against measurements from three observational networks. The networks cover some of the most polluted areas in the Northern Hemisphere. The EPA CASTNET network (U.S. Environmental Protection Agency Clean Air Status and Trends Network, 2024) and the IMPROVE network (Interagency Monitoring of Protected Visual Environments) with 152 stations for nitrate and sulfate and 143 stations for ammonium cover the USA, with IMPROVE concerning mostly rural and/or remote areas. The EMEP network (European Monitoring and Evaluation Programme) includes nine stations for nitrate and sulfate and seven for ammonium covering the European region. Finally, the EANET network (Acid Deposition Monitoring Network in East Asia, 2024) with 33 stations measuring all three major aerosol components covers parts of East Asia. The number of stations refers to the year 2010, which is simulated in this work.

Figure 3 depicts the differences between the model-predicted and the observed mean annual concentration values for SO_4^{2-}, NH_4^+ and NO_3^- aerosols, while Tables 3, 4 and 5 contain the overall statistics for the same comparisons. Here, the mean bias (MB), mean absolute gross error (MAGE), normalized mean bias (NMB), normalized mean error (NME) and the root-mean-square error (RMSE) are calculated to assess the model performance. Starting with SO_4^{2-}, the model tends to underpredict the observations but with a mean bias (MB) of less than $-0.5\,\mu g\,m^{-3}$ for Europe and less than $-1\,\mu g\,m^{-3}$ for the USA, capturing both the higher values of the eastern USA and the lower values of the western USA. Its normalized mean error (NME) ranges from 40 % to 60 %, being highest for the East Asian region, which also has the highest MB of $-1.65\,\mu g\,m^{-3}$ (Table 3). Seasonally, the largest biases are found during summertime over Europe and the USA and during wintertime over East Asia (Table S4), while the same is true for the predictions of ISORROPIA II in stable mode, exhibiting quite similar metrics (Table S1). NH_4^+ is much better simulated by the model over the three regions, where the agreement with observations is high with MB values of less than $0.4\,\mu g\,m^{-3}$ but with slightly higher NME values (Table 4). Over East Asia, the only important disparity is a slight underprediction of about $2\,\mu g\,m^{-3}$ around Hong Kong following the underprediction of SO_4^{2-} over the same area (Fig. 3). Seasonally, spring is the worst period for the predictions of both versions, while there does not seem to be a consistent pattern of behavior for all three regions which perform best over different periods (Tables S5 and S2). Finally, the model tends to overpredict NO_3^- concentrations over the three regions with MB values of less than $1\,\mu g\,m^{-3}$, albeit with high NME values (Table 5). Over East Asia, with the exception of Hong Kong, the model overestimates the NO_3^- concentrations by about $3\,\mu g\,m^{-3}$, especially in the Wuhan and Guangzhou areas and also around Beijing (Fig. 3). In general, besides Hong Kong, the model overpredicts the concentrations of all three aerosol components examined here in the East Asian region. For all regions, the best seasonal agreement between the predictions of both versions in terms of MB values is found during the summer period, while the worst agreement occurs around the winter/spring period (Tables S6 and S3). The NME values are lowest in the summer for the USA and, surprisingly, in the winter for Europe and East Asia, even though this is the period with the worst MB values for these regions. Potential explanations include the coarse grid resolution used in this work as well as issues related to emissions (Zakoura and Pandis, 2018). It should be noted that even though the two versions perform similarly, better performance on certain statistical metrics should not be taken as an indication that one state as-

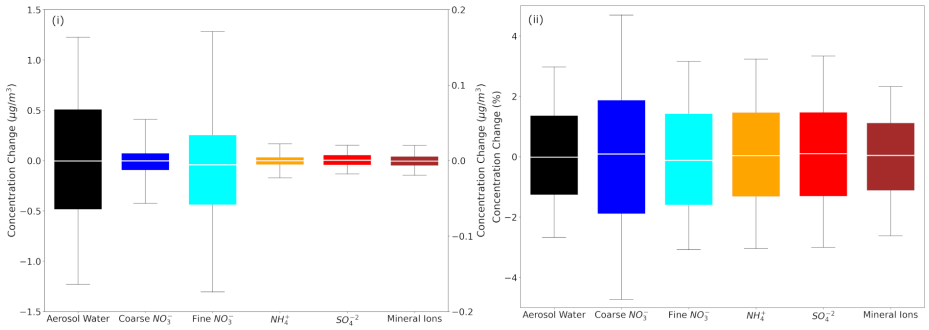

Figure 2. Box plots depicting the 25th, 50th and 75th percentiles (box) of the **(i)** difference and **(ii)** fractional difference in global daily mean surface concentrations of aerosol water (left y axis), mineral ions, NH_4^+ and SO_4^{2-} in TSP as well as coarse and fine aerosol NO_3^- (right y axis), as predicted by EMAC using ISORROPIA-lite and ISORROPIA II. The 10th and 90th percentiles (whiskers) for each aerosol component are also shown. Both models assume that the aerosol is at its metastable state at low RH and that a positive change corresponds to higher concentrations by ISORROPIA-lite.

Table 3. Statistical evaluation of EMAC-predicted surface concentrations of $PM_{2.5}$ SO_4^{2-} using ISORROPIA-lite against observations during 2010.

Network	Number of of datasets	Mean observed ($\mu g\,m^{-3}$)	Mean predicted ($\mu g\,m^{-3}$)	MAGE ($\mu g\,m^{-3}$)	MB ($\mu g\,m^{-3}$)	NME (%)	NMB (%)	RMSE ($\mu g\,m^{-3}$)
EPA	1791	2.18	1.28	0.92	−0.90	42	−38	0.93
IMPROVE	1526	1.02	0.92	0.47	−0.10	46	−11	0.73
EMEP	108	1.71	1.27	0.75	−0.44	44	−26	0.91
EANET	353	3.19	1.54	1.95	−1.65	61	−51	2.46

sumption is more scientifically valid than the other. While a stable state could be considered more accurate under very low humidity conditions (e.g., over remote deserts; Karydis et al., 2016), in regions such as those with intermediate RH and low nitrate concentration (e.g., northeastern USA), particles are mostly in the metastable state (Guo et al., 2016). However, the two state assumptions produce very similar results in most cases, as shown here.

3.4 Computational speed-up metrics

The computational efficiency and speed-up that ISORROPIA-lite provides compared to ISORROPIA II in both stable and metastable modes were quantified. Table 6 contains the total number of time steps that the EMAC model performed for the same simulation period (i.e., 24 h of CPU time using 16 nodes), as well as the real time that was needed per individual time step, for each ISORROPIA version. The metrics shown in Table 6 concern the average value of each quantity, along with the corresponding standard deviation, resulting from a total of 18 simulations (6 for each version). From the difference in the real time required by the model to execute each individual time step, the speed-up of ISORROPIA-lite was found to be just above 3 % compared to ISORROPIA II in metastable mode and almost 5 % compared to ISORROPIA II in stable mode. These values are, as expected, lower than the improvement in the computational efficiency that the ISORROPIA-lite version provides compared to the original version, as found in the offline evaluation, because EMAC contains several other modules that are quite computationally expensive. For example, the gas-phase chemistry (MECCA submodel) as well as wet deposition and liquid-phase chemistry (SCAV submodel) are responsible for two-thirds of the total computational cost of the global model. As a comparison, the offline speed-up that ISORROPIA-lite provided was calculated to be 35 % and when utilized in the regional model PMCAMx 3D it was found to be 10 % (Kakavas et al., 2022).

4 Comparison of ISORROPIA-lite against ISORROPIA II in stable mode

In this section, we present a comparison of the ISORROPIA-lite results in metastable mode against those of the ISORROPIA II results in stable mode. Both versions are now available in the latest version of the EMAC model, and the

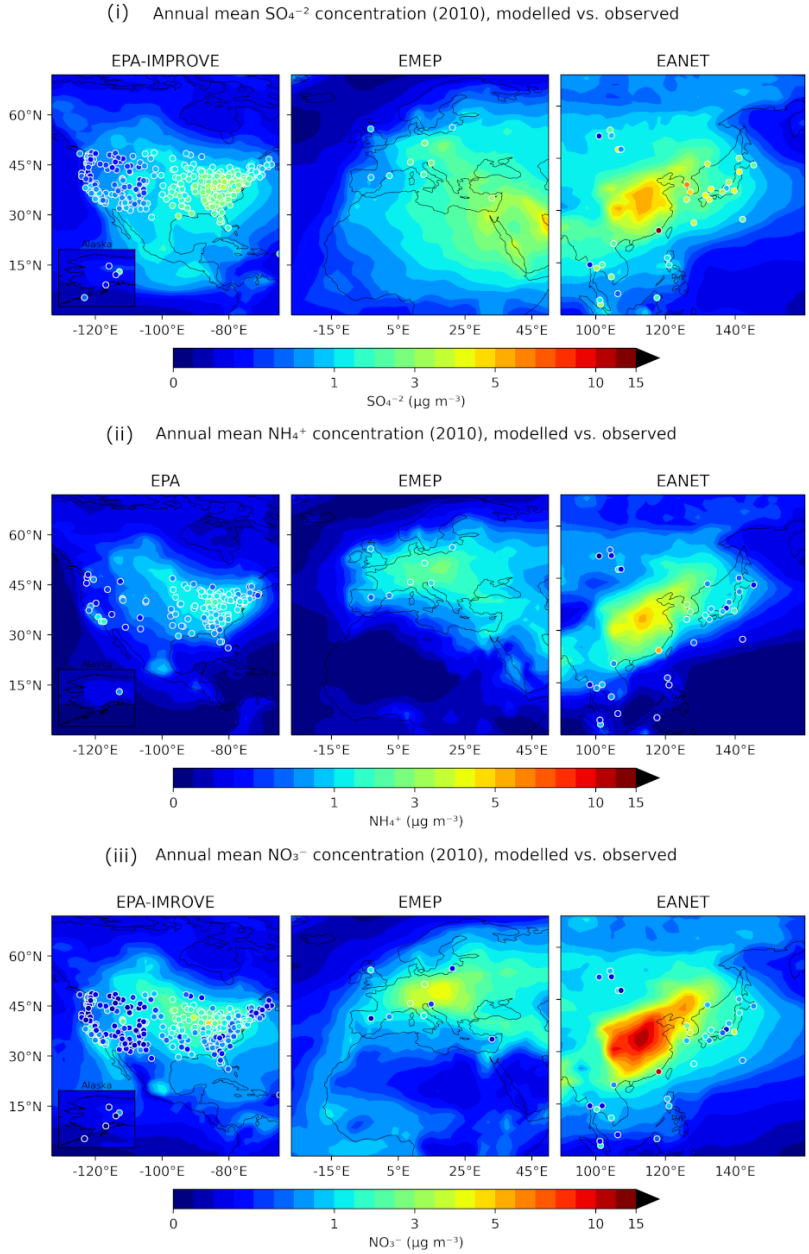

Figure 3. Annual mean surface concentrations of $PM_{2.5}$ for **(i)** SO_4^{2-}, **(ii)** NH_4^+ and **(iii)** NO_3^- as simulated by EMAC using ISORROPIA-lite (shaded contours) versus observations of the same species from the IMPROVE, EMEP and EANET networks (colored circles).

Table 4. Statistical evaluation of EMAC-predicted surface concentrations of $PM_{2.5}$ NH_4^+ using ISORROPIA-lite against observations during 2010.

Network	Number of of datasets	Mean observed ($\mu g\,m^{-3}$)	Mean predicted ($\mu g\,m^{-3}$)	MAGE ($\mu g\,m^{-3}$)	MB ($\mu g\,m^{-3}$)	NME (%)	NMB (%)	RMSE ($\mu g\,m^{-3}$)
EPA	1660	1.01	1.01	0.50	0.00	49	0	0.72
IMPROVE	–	–	–	–	–	–	–	–
EMEP	84	1.08	1.44	0.63	0.36	59	34	0.75
EANET	360	0.93	1.25	0.69	0.32	74	34	1.25

Table 5. Statistical evaluation of EMAC-predicted surface concentrations of $PM_{2.5}$ for NO_3^- using ISORROPIA-lite against observations during 2010.

Network	Number of datasets	Mean observed ($\mu g\,m^{-3}$)	Mean predicted ($\mu g\,m^{-3}$)	MAGE ($\mu g\,m^{-3}$)	MB ($\mu g\,m^{-3}$)	NME (%)	NMB (%)	RMSE ($\mu g\,m^{-3}$)
EPA	1762	1.39	1.87	1.06	0.48	76	42	1.65
IMPROVE	1526	0.42	1.18	0.82	0.76	194	175	1.15
EMEP	108	1.15	1.91	1.25	0.76	109	66	1.66
EANET	372	1.32	2.27	1.33	0.95	101	72	2.17

user has the option to utilize either one. While ISORROPIA-lite always assumes metastable aerosols, ISORROPIA II assumes stable aerosols by default. This comparison is done in an attempt to quantify the effects of using the metastable case in global atmospheric simulations and to identify the regions and conditions under which the two assumptions have any significant differences. Some discrepancies are expected due to the different physical states of aerosols at low RH; however, the choice between a stable state and a metastable state should not be considered obvious. For example, Fountoukis et al. (2009) and Karydis et al. (2010) have shown that the stable assumption is in better agreement with observations under conditions where RH is consistently below 50 %. On the other hand, Ansari and Pandis (2000) emphasize that the metastable assumption must be considered for regions characterized by intermediate RH and low pollutant concentrations (in this case of NO_3^-), while there are no significant differences between the two assumptions over regions with high concentrations. Here, differences in the calculated aerosol acidity by the two modules are also investigated.

4.1 Spatial variability of mean annual aerosol concentrations

For sulfate in TSP, the predicted maximum annual average concentration was $7\,\mu g\,m^{-3}$ over East Asia, highlighting the large anthropogenic impact over that region, while it was also high ($> 5\,\mu g\,m^{-3}$) in India, Europe and the Middle East in both simulations (Fig. 4i). Absolute differences for sulfate in TSP were lower than $0.15\,\mu g\,m^{-3}$ ($< 3\,\%$) and found mainly over the polluted Northern Hemisphere (mainly eastern USA and Europe) with slightly higher values simulated by ISORROPIA II (Fig. 4ii). This is most likely related to the also higher NO_3^- aerosol predictions by ISORROPIA-lite over the same regions (see below and Fig. 4viii). The higher SO_4^{2-} aerosol concentrations estimated by ISORROPIA II over the Middle East region are mainly due to changes in wet deposition induced by the different physical states of the aerosol due to the higher water content by ISORROPIA-lite. The simulated concentrations of NH_4^+ in TSP had maximum annual average values of $6\,\mu g\,m^{-3}$ and were found mainly over East Asia, especially around the greater Beijing and Wuhan areas, while India and Europe also exhibited high mean annual values for TSP NH_4^+ ($> 3\,\mu g\,m^{-3}$) (Fig. 4iii). The absolute differences for NH_4^+ in TSP between the two model versions are higher over the Himalayan and East Asian regions (in favor of ISORROPIA II) but apparently weaker over the USA, the Middle East and Africa (ISORROPIA-lite predicts higher values), although never higher than $0.5\,\mu g\,m^{-3}$ ($< 5\,\%$) (Fig. 4iv). Regarding aerosol NO_3^- concentrations in the coarse mode, the maximum annual average of $6\,\mu g\,m^{-3}$ was predicted at the Arabian Peninsula (Fig. 4v), while in the fine mode the maximum annual average value of $11\,\mu g\,m^{-3}$ was predicted over the metropolitan areas of Wuhan and Guangzhou (Fig. 4vii). Other high annual average concentrations of fine aerosol NO_3^- are found in the Tibetan Plateau and most prominently in heavy industrial regions such as eastern USA, East Asia and Europe (exceeding $4\,\mu g\,m^{-3}$ in most of these areas), with the latter two regions contributing high annual average concentrations in the coarse mode as well. The absolute differences for coarse NO_3^- were similar in magnitude to those of NH_4^+ in TSP with the Middle East yielding higher values by ISORROPIA-lite, while the opposite is true for Europe and the eastern USA (Fig. 4vi). The absolute differences for fine NO_3^- are higher than those

Table 6. Total number of time steps that EMAC executed in 24 h of running time and number of seconds needed for each time step, utilizing ISORROPIA-lite and ISORROPIA II (both in stable and metastable). The computational speed-up refers to how much quicker (in %) the process is executed by ISORROPIA-lite in comparison to the previous version in both modes.

Simulation	No. of time steps	No. of seconds per time step	Computational speed-up (%)
ISORROPIA-lite	$78\,193 \pm 116$	1.10 ± 0.002	–
ISORROPIA II v2.3 (metastable)	$75\,720 \pm 242$	1.14 ± 0.003	3.3 ± 0.3
ISORROPIA II v2.3 (stable)	$74\,599 \pm 169$	1.16 ± 0.003	4.8 ± 0.3

for coarse NO_3^-, reaching up to $1.75\,\mu g\,m^{-3}$ mainly over the Tibetan Plateau ($\sim 30\,\%$) with ISORROPIA II predicting the higher values (Fig. 4vii). Higher nitrate concentrations were also predicted by ISORROPIA II mainly close to the west coast of South America and north of the Atacama Desert. Around those regions as well as the Tibetan Plateau, the relative humidity is often below 50 % and 30 %, respectively (see Fig. 8), and the metastable assumption results in lower nitrate concentrations, in agreement with the findings of Ansari and Pandis (2000). At the same time, ISORROPIA II predicts a higher aerosol fraction for NO_3^- (up to 10 %) for the west coast of South America and the Tibetan Plateau. This is not the case for East Asia (Fig. 5ii), although the low sulfate-to-nitrate ratio of that region results in an excess of available NH_3 to react with HNO_3 and form ammonium nitrate that would justify the higher fine-mode nitrate concentrations by the stable case of ISORROPIA II (Ansari and Pandis, 2000). A higher NO_3^- aerosol fraction (up to 10 %) in the Middle East was exhibited by ISORROPIA-lite (Fig. 5ii). This area is characterized by increased mineral ion concentrations and high sulfate to nitrate ratios (Karydis et al., 2016), which led to higher coarse-mode nitrate predictions by the metastable case (Ansari and Pandis, 2000), although the maximum difference was only $0.6\,\mu g\,m^{-3}$ (Fig. 4vi, viii). The differences in coarse and fine NO_3^- among the two versions did not display any strong seasonality as they were only slightly higher during autumn (for East Asia) and winter (for India-Himalaya) (not shown). A comparison of the simulated aerosol concentrations at higher altitudes can be found in Fig. S3, where the zonal mean annual average concentrations as well as their absolute differences between the two model versions are depicted. The deviations between the results of the two ISORROPIA versions become smaller as the air masses move higher in the atmosphere, until they are practically identical at altitudes above 700 hPa. Regarding the behavior of,the mineral ions of Ca^{2+}, K^+ and Mg^{2+}, the majority of high concentrations are found around the largest desert regions of the Sahara, Gobi, Atacama and Namib deserts (Fig. S4), with Ca^{2+} being evidently the most dominant across all minerals. Furthermore, the absolute difference maps (Fig. S4) show minimal differences in mean annual surface concentrations (mostly less than $0.5\,\mu g\,m^{-3}$) between the simulations from the two model versions. This is also reflected in the comparison of zonal mean annual average concentrations and their differences, as shown in Fig. S5.

In the heavily polluted regions (particularly eastern USA, Europe and East Asia), the particulate NO_3^- dominates compared to the gas-phase HNO_3 (Fig. 5i). The fine-mode fraction of the particulate nitrate burden is higher than the coarse-mode fraction over East Asia, India, Europe or the eastern USA, while in the large desert areas of the Middle East and the Sahara most of the particulate NO_3^- exists in the coarse mode (Fig. 5iii). The aerosol water fraction is low ($< 30\,\%$) across the most arid regions of Sahara, Atacama, Namib and Gobi, while Europe has the highest continental average aerosol water content in the Northern Hemisphere polluted regions (Fig. 5v). ISORROPIA-lite predicts higher average aerosol water concentration globally since the particles cannot form solids because the salts remain in a supersaturated metastable solution (Fig. 5vi).

The absolute differences in global daily mean concentrations are mostly less than $0.3\,\mu g\,m^{-3}$ for all species (NH_4^+, SO_4^{2-} and mineral cations in TSP as well as coarse and fine aerosol NO_3^-) except aerosol water in TSP (Fig. 6). In that case, the absolute differences for the 25th and 75th percentiles are less than $5\,\mu g\,m^{-3}$. This translates to fractional differences for the 25th and 75th percentiles mostly below 20 % for aerosol water in TSP and coarse NO_3^- aerosol and mostly below 5 % for all the remaining species.

The model results in the regions with the highest mean annual loads of fine and coarse aerosol NO_3^- concentrations (see Sect. 3.1) as well as the most significant differences in estimated aerosol water and aerosol acidity (see Sect. 4.3) were further analyzed to determine whether the phase state assumption has a large effect on simulated aerosol nitrate formation (Fig. 7). For both coarse and fine daily mean NO_3^- concentrations, Europe and North America are clearly the regions with the smallest differences between the two versions. On the other hand, East Asia and especially the India-Himalaya region are areas where the differences are the highest; ISORROPIA II is predicting higher fine aerosol NO_3^- concentrations, while in the Middle East ISORROPIA-lite is predicting higher coarse-mode aerosol NO_3^- concentrations. However, even for these areas the differences are typically below $0.25\,\mu g\,m^{-3}$ (25th and 75th percentiles) with the higher differences not exceeding $0.8\,\mu g\,m^{-3}$ (10th and 90th

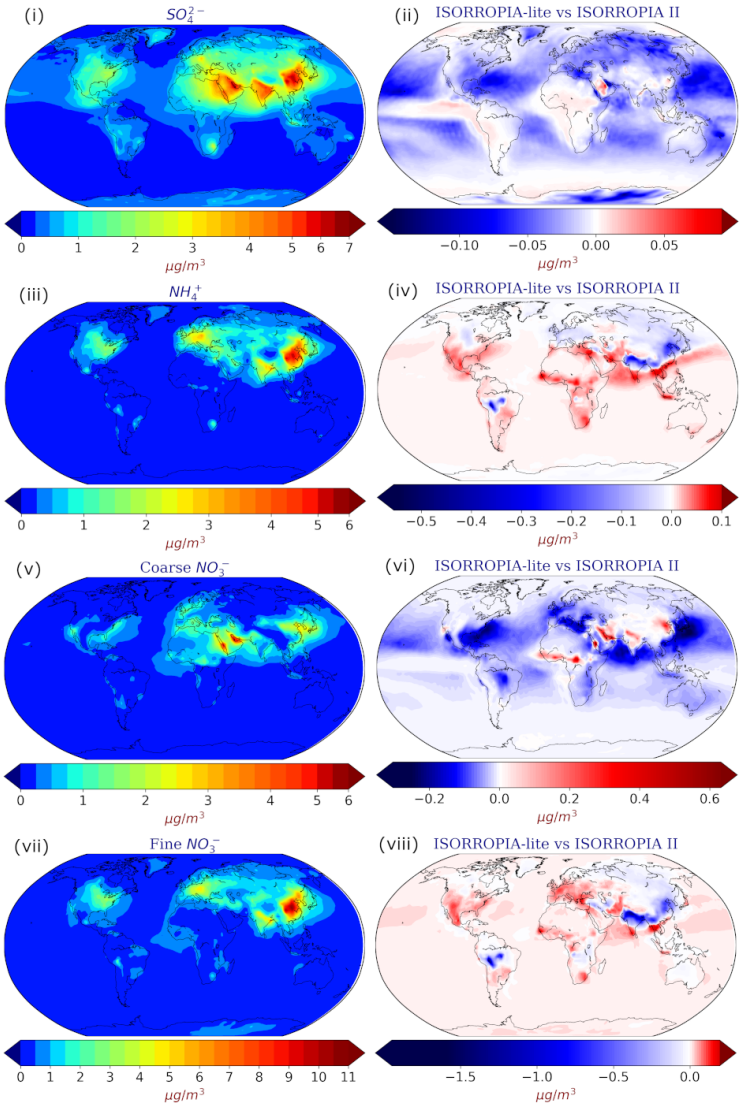

Figure 4. Annual mean surface concentrations of **(i)** SO_4^{2-} and **(iii)** NH_4^+ in TSP as well as **(v)** coarse and **(vii)** fine aerosol NO_3^- as predicted by EMAC using ISORROPIA-lite. Change of the annual mean EMAC-simulated surface concentration of **(ii)** SO_4^{2-} and **(iv)** NH_4^+ in TSP as well as **(vi)** coarse and **(viii)** fine aerosol NO_3^- after employing ISORROPIA II. Positive values in red indicate higher concentrations by ISORROPIA-lite. The models assume different aerosol states.

percentiles). This translates to fractional differences below 25 % (25th and 75th percentiles) for all regions, reaching up to 30 % (10th and 90th percentiles) mainly in the Tibetan Plateau and the Middle East.

Table 7 contains the statistics for the comparisons of the global daily average surface concentrations calculated by the two simulations. While all the aerosol component concentrations, except for aerosol water, are higher for ISORROPIA II, the differences are still quite low. Furthermore, de-

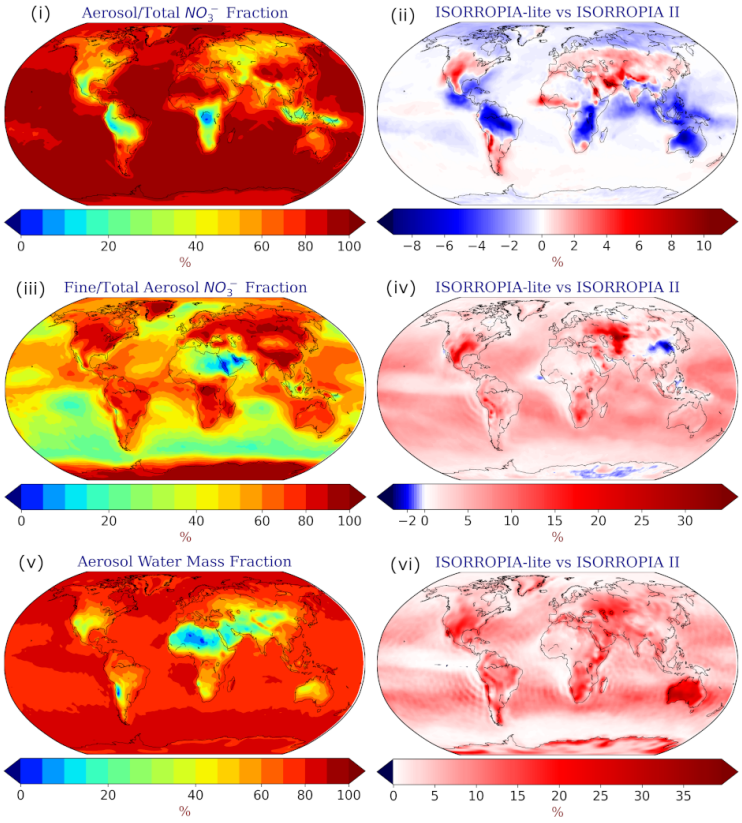

Figure 5. Annual mean surface fractions of **(i)** aerosol/total NO_3^-, **(iii)** fine/total-aerosol NO_3^- and **(v)** aerosol water mass as calculated by EMAC using ISORROPIA-lite. Change of the annual mean EMAC-simulated surface fractions of aerosol/total **(ii)** NO_3^-, **(iv)** fine/total-aerosol NO_3^- and **(vi)** aerosol water mass after employing ISORROPIA II. Positive values in red indicate higher fractions by ISORROPIA-lite. The models assume different aerosol states.

spite the different aerosol phase state assumptions by the two versions, the normalized mean absolute difference remains low for all species (on average $< 11\,\%$) except HNO_3. The overall statistics support the conclusion that, on the global scale, the phase state assumption for low RH does not have a significant impact on the predicted tropospheric aerosol load. More specifically, ISORROPIA-lite produces a slightly higher tropospheric burden for aerosol NO_3^- than ISORROPIA II (0.875 Tg versus 0.861 Tg, respectively), while the opposite was the case for HNO_3 (0.921 Tg versus 0.935 Tg). The higher burden of ISORROPIA-lite is due to the fact that the higher aerosol water content favors the partitioning of HNO_3 to the particulate phase.

4.2 Relative-humidity-dependent behavior of NO_3^- aerosols

The dependence of the differences in nitrate predictions on relative humidity was examined for both fine and coarse mode particles (Fig. 8). The differences between ISORROPIA II and ISORROPIA-lite are higher at intermediate RH ranging from 20 % to 60 %, being more evident in the fine-mode aerosol NO_3^- and for high annual mean concentrations of coarse-mode aerosol NO_3^- ($> 4\,\mu g\,m^{-3}$). In this RH range, solid salts can precipitate when the stable equilibrium state is assumed (Seinfeld and Pandis, 2016), while in the metastable state all these salts remain dissolved in water. A region that often has RH in the 20 %–60 % range is the Tibetan Plateau, which leads to discrepancies in the fine-mode particulate nitrate predictions of the two models in this area, while higher coarse-mode particulate nitrate concentra-

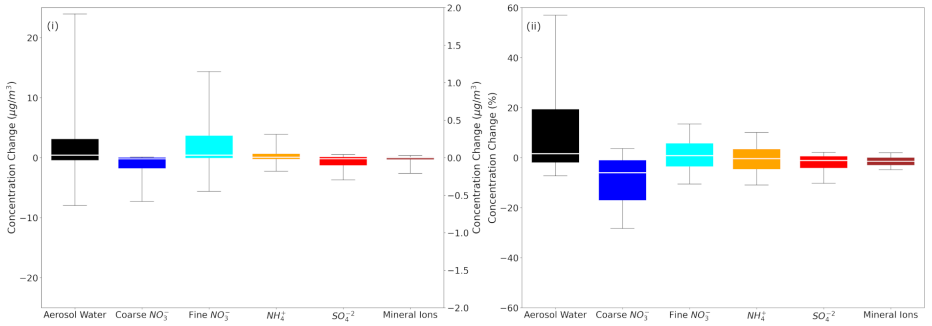

Figure 6. Box plots depicting the 25th, 50th and 75th percentiles (box) of the **(i)** difference and **(ii)** fractional difference in global daily mean surface concentrations of aerosol water (left y axis), mineral ions, NH_4^+ and SO_4^{2-} in TSP as well as coarse and fine aerosol NO_3^- (right y axis), as predicted by EMAC using ISORROPIA-lite and ISORROPIA II. The models assume different aerosol states at low RH and that a positive change corresponds to higher concentrations by ISORROPIA-lite.

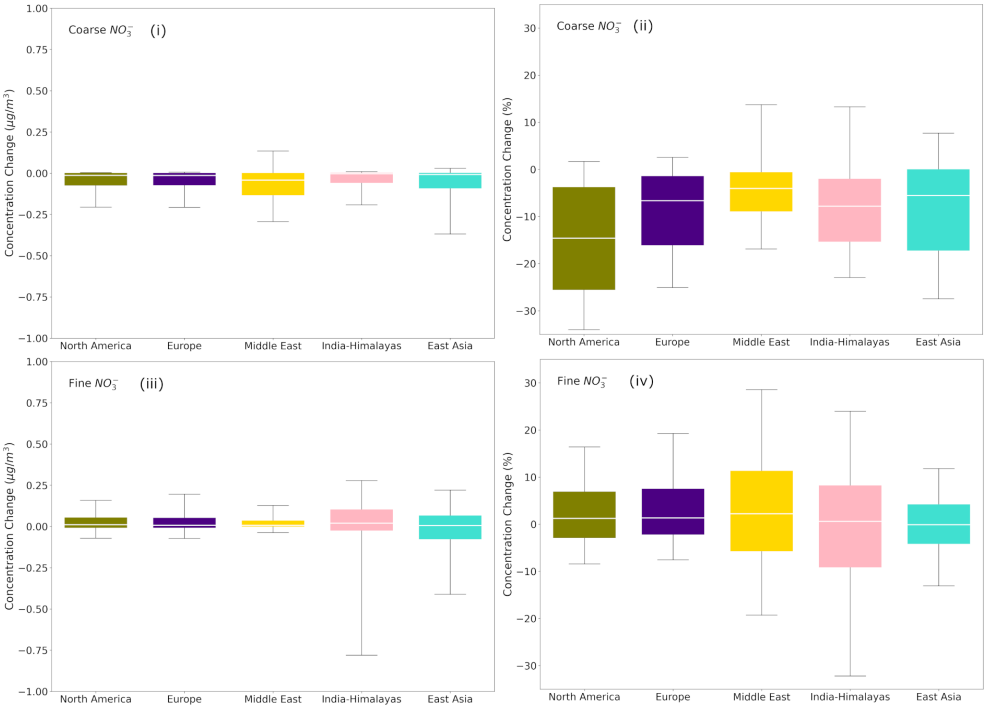

Figure 7. Box plots depicting the 25th, 50th and 75th percentiles (box) of the difference in the global daily mean surface concentrations of **(i)** coarse and **(iii)** fine aerosol NO_3^- for the regions of North America, Europe, the Middle East, India-Himalaya and East Asia, as predicted by EMAC using ISORROPIA-lite and ISORROPIA II. The fractional differences in global daily mean surface concentrations of **(ii)** coarse and **(iv)** fine aerosol NO_3^- for the same regions are also shown. The models assume different aerosol states at low RH and that a positive change corresponds to higher concentrations by ISORROPIA-lite.

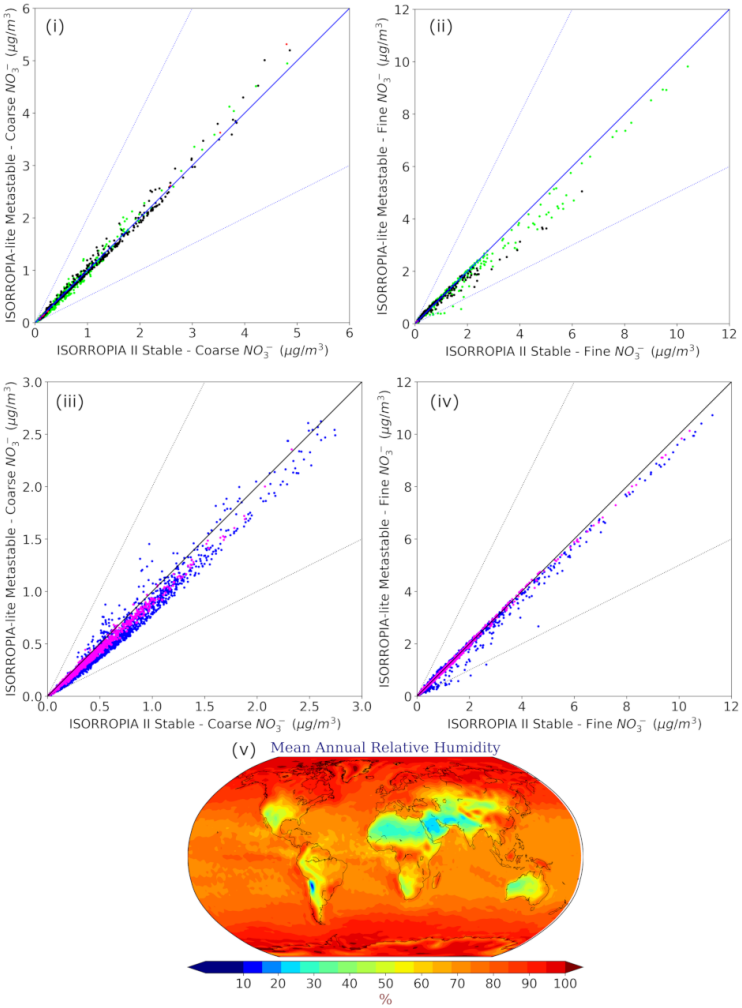

Figure 8. Scatterplots comparing the annual mean surface concentrations of coarse **(i, iii)** and fine aerosol NO_3^- **(ii, iv)** for relative humidity ranges of 20 %–60 % **(i, ii)** and 60 %–100 % **(iii, iv)** as predicted by EMAC using ISORROPIA-lite versus ISORROPIA II. The models assume different aerosol states at low RH. Black points represent the 20 %–40 % RH range, green points represent the 40 %–60 % range, blue points represent the 60 %–80 % range and pink points represent the 80 %–100 % range. **(v)** Mean annual relative humidity as calculated by EMAC using ISORROPIA-lite.

tions are predicted by ISORROPIA-lite in the Middle East, which is an area that is also often characterized by intermediate RH. The differences found for coarse-mode particulate nitrate in the higher RH range of 60 %–100 % can account for the respective differences that occurred in areas characterized by such RH values (eastern USA, Europe and East Asia) but concern lower annual mean concentration values ($< 3\,\mu g\,m^{-3}$).

4.3 Comparison of the estimated aerosol acidity

The estimated aerosol acidity by the two model versions was compared separately for the accumulation and coarse size modes. This comparison aims at verifying the credibility of the estimated inorganic aerosol acidity of ISORROPIA-lite, as the first results of its implementation in the EMAC model are presented here. Since this capability is well established

Table 7. Statistical analysis of EMAC-simulated mean daily surface concentrations by employing ISORROPIA-lite in metastable mode versus ISORROPIA II in stable mode. Bias is given as ISORROPIA-lite minus ISORROPIA II.

	Mean difference ($\mu g\,m^{-3}$)	Normalized mean absolute difference (%)
Coarse NO_3^-	−0.026	9.1
Fine NO_3^-	−0.044	9.8
HNO_3	−0.002	10.3
NH_4^+	-1.8×10^{-4}	8.0
SO_4^{2-}	−0.020	4.8
Na^+	−0.081	8.6
Ca^{2+}	−0.005	1.7
K^+	−0.002	1.8
Mg^+	−0.002	1.7
Cl^-	−0.120	9.4
H_2O	2.717	10.8
H^+	-4.7×10^{-4}	6.1
pH accumulation	−0.06 (pH)	2.3
pH coarse	0.03 (pH)	2.3

for ISORROPIA II (Karydis et al., 2021), it is of interest to examine any potential, but otherwise expected, differences between the two versions. The pH was computed for the fine- and coarse-mode particles:

$$\mathrm{pH} = -\log_{10}\left(\frac{[H^+]}{[H_2O]}\right). \quad (1)$$

The calculations were performed neglecting the water associated with the organic fraction of aerosols, as they are handled by other parts of the aerosol microphysics submodel GMXe. The average pH was calculated based on the instantaneous H^+ and H_2O values estimated every 5 h. This is because utilizing daily average values for H^+ and H_2O can result in a low-biased predicted pH of ~ 2 units globally (Karydis et al., 2021). The 5 h interval provides a frequent output of values at different times of the day to account for the diurnal variability of pH, since a selection of 6 or 8 h intervals would result in instantaneous H^+ and H_2O values at identical times on different days; pH calculations are performed only in cases where there is enough water in the aerosol (instantaneous values exceeding $0.05\,\mu g\,m^{-3}$).

ISORROPIA-lite predicts slightly more acidic particles mainly in the coarse mode (Fig. 9iv). The most significant differences (up to 1 unit) in that size range are located over the Middle East and the Arabian Peninsula, while smaller differences can be found in limited parts of the Himalayan and the East Asian regions as well as the western USA and the Amazon Basin. These regions are characterized by high mineral cation concentrations and/or low RH. Therefore, the stable state results in increased pH values due to the precipitation of insoluble salts out of the aqueous phase. On the other hand, in the metastable state all anions remain in the aqueous phase, lowering the particle pH. Differences in accumulation mode particle acidity are not as high (Fig. 9ii). ISORROPIA-lite predicts that accumulation mode particles over heavily industrialized regions such as Southeast Asia, Europe and the eastern USA are moderately acidic with mean pH values in the range of 4–5, while exhibiting alkaline behavior in desert areas where the increased levels of mineral ions elevate the pH above 7 (Fig. 9i). Coarse-mode particles are in general more alkaline than those in the accumulation mode, with a few exceptions over the eastern USA, central Europe, north India and Southeast Asia (Fig. 9iii). These regions are characterized by high NH_3 concentrations from agricultural activities.

A sensitivity test was performed by reducing all NH_3 emissions by half to investigate if there would be a buffering mechanism that controls the pH of the accumulation mode particles more than in the coarse mode. Figure 10 shows the difference in the mean annual calculated aerosol pH between the base case (NH_3 emissions present) and the sensitivity case (half NH_3 emissions). When NH_3 emissions are switched off, the pH of fine PM decreases by up to 3 units, and the particles become a lot more acidic (Fig. 10i). For the coarse mode, this effect is not that strong (pH reduction of up to 1.5 units) (Fig. 10ii). As expected, this buffering mechanism is mainly observed across the aforementioned regions where NH_3 concentrations are high, but it is also observed over areas affected by natural NH_3 emissions. This is consistent with the results of Karydis et al. (2021), who found that, in the absence of NH_3, aerosol particles would be extremely acidic in most of the world.

The differences in the accumulation mode pH calculated by ISORROPIA-lite and ISORROPIA II are extremely small (i.e., mean difference of 0.06 pH units or 2.3 %) and even smaller for coarse-mode pH (Table 7), indicating an overall good agreement between the two model versions.

5 Conclusions

This study presents the first results of the implementation of the ISORROPIA-lite thermodynamic module in the EMAC global chemistry and climate model, and it is compared to the previous version, ISORROPIA II v2.3, after the latter has successfully replaced ISORROPIA II v1 to improve pH predictions close to neutral conditions.

The results of ISORROPIA II versions 1 and 2.3 both in stable mode had insignificant differences ($< 3\,\%$) concerning the global predictions of NH_4^+, SO_4^{2-}, mineral ions and aerosol water in TSP concentrations as well as fine- and coarse-mode aerosol NO_3^-. The comparison of results from ISORROPIA-lite against ISORROPIA II v2.3 in metastable mode showed also negligible differences ($< 7\,\%$) between all the examined aerosol components on a global scale. The comparison of the ISORROPIA-lite results for $PM_{2.5}$

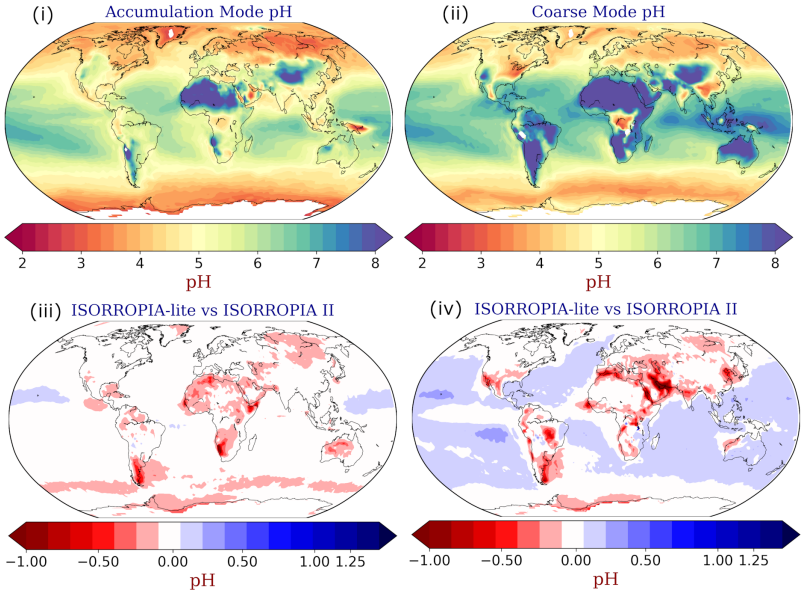

Figure 9. Annual mean EMAC-simulated **(i)** accumulation and **(ii)** coarse-mode aerosol pH using ISORROPIA-lite. Change of the annual mean EMAC-simulated **(iii)** accumulation and **(iv)** coarse-mode aerosol pH after using ISORROPIA II, with negative values in red indicating lower pH by ISORROPIA-lite. The models assume different aerosol states.

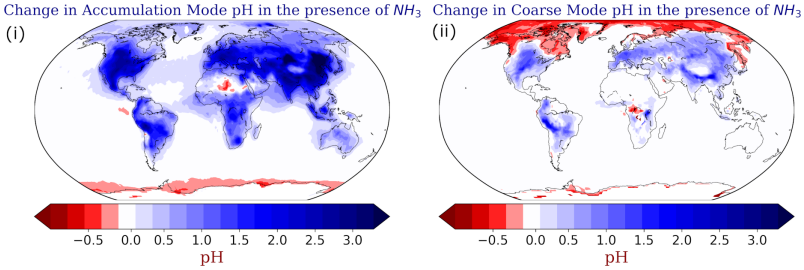

Figure 10. Absolute change of the annual mean EMAC-simulated **(i)** accumulation and **(ii)** coarse-mode aerosol pH using ISORROPIA-lite after reducing the NH_3 emissions by half. Positive values in blue indicate higher aerosol pH when NH_3 is present.

NH_4^+, SO_4^{2-} and NO_3^- versus observations from the IMPROVE, EMEP and EANET networks reveals that East Asia is the area with the largest discrepancies. There was satisfactory agreement in Europe and over the USA for NH_4^+ and SO_4^{2-}, while ISORROPIA-lite predicted lower concentrations around Hong Kong with a maximum difference of $1.5\,\mu g\,m^{-3}$ ($\sim 20\,\%$) for these two species. For NO_3^-, the discrepancy was up to $3\,\mu g\,m^{-3}$ ($\sim 30\,\%$) in the same region, while a difference of about $1.5\,\mu g\,m^{-3}$ ($\sim 25\,\%$) was found over central Europe with ISORROPIA-lite predicting the higher values. With the exception of Hong Kong, the model in general overpredicted the concentrations of all three aerosol components over the East Asian region.

A comparison between ISORROPIA-lite in the metastable state and ISORROPIA II in the stable state was performed to identify potential discrepancies in the inorganic aerosol concentrations simulated by EMAC. Although differences between the two model versions are to be expected due to the different physical state of aerosols at low RH, it is of interest to examine under which conditions these differences occur so that potential users are informed of the strengths and weaknesses of using either model version depending on the application. Both modules are now available as differ-

ent options in the EMAC model. The agreement between the two versions was generally quite good for global daily mean surface concentrations of inorganic aerosols, mineral ions and aerosol water. More specifically, mineral ions, SO_4^{2-} and NH_4^+ in TSP had the smallest differences overall, less than $0.5\,\mu g\,m^{-3}$ even in localized extreme cases but in the vast majority less than $0.1\,\mu g\,m^{-3}$ (or less than 5 %). For coarse NO_3^- aerosols, the absolute differences were of similar magnitude, with the higher concentrations simulated by ISORROPIA-lite in the Middle East being the most notable. In the case of fine NO_3^- aerosols, the differences were larger (up to $\sim 1.75\,\mu g\,m^{-3}$ in local extremes), mainly over the west coast of South America (north of the Atacama Desert), the Tibetan Plateau and East Asian regions, with higher concentrations simulated by ISORROPIA II but still within ∼ 30 %. In Europe and the USA, the corresponding differences were less than $0.25\,\mu g\,m^{-3}$. The most important difference was the higher aerosol water calculated by ISORROPIA-lite, especially for relative humidity in the 20 % to 60 % range. However, this was less than $5\,\mu g\,m^{-3}$ or 20 % in most cases. Therefore, even though local differences are expected in regions where the relative humidity is often in this range, on a global scale choosing a different physical state of the aerosol at lower RH does not have such a big impact.

When the relative humidity ranged from 20 % to 60 %, differences in coarse and fine NO_3^- concentration predictions among the two versions increased. The highest discrepancies were found in the Tibetan Plateau and the Middle East regions, both of which are dominated by such RH values during most of the year. In the first region, the combination of those RH values with mid-range temperatures does not favor nitrate aerosol formation if the aerosol is in the metastable state (ISORROPIA-lite). In the second region, the low RH values result in very low aerosol water predictions for the stable state assumed by ISORROPIA II, which hinder the condensation of HNO_3 into the aerosol phase.

Investigation of the differences in the estimated inorganic aerosol acidity between the two versions, due to the different assumed aerosol phase states, is of great interest for potential future use of ISORROPIA-lite in global climate simulations. ISORROPIA-lite produces slightly more acidic coarse-mode aerosols (in comparison to ISORROPIA II) but by less than 1 pH unit on average. The most important differences were found mainly in the Middle East and the Arabian Peninsula due to the presence of high mineral cation concentrations. The stable state considered by ISORROPIA II allows for the precipitation of insoluble salts and removes anions from the aqueous phase that would otherwise deplete the pH, while this is not the case for the metastable aerosol state considered by ISORROPIA-lite. Furthermore, NH_3 is found to control the aerosol acidity of both fine and coarse mode particles; however, it provides a significantly larger buffering capacity to the accumulation mode than to the coarse mode. This results in slightly more basic accumulation particles than coarse in regions with high NH_3 from agricultural activities and low mineral cation concentrations (e.g., Europe).

Finally, concerning the computational efficiency that ISORROPIA-lite provides when used by the EMAC global model, a speed-up of more than 3 % was achieved compared to ISORROPIA II in metastable state and nearly 5 % compared to ISORROPIA II in stable state.

Code and data availability. The usage of MESSy (Modular Earth Submodel System) and access to the source code is licensed to all affiliates of institutions which are members of the MESSy Consortium. Institutions can become a member of the MESSy Consortium by signing the "MESSy Memorandum of Understanding". More information can be found on the MESSy Consortium website: http://www.messy-interface.org (last access: 8 February 2024). The code developed in this study and all relevant features, including the ISORROPIA II v2.3 and ISORROPIA-lite v1.0 thermodynamic equilibrium codes as part of MESSy, are archived with a restricted-access DOI (https://doi.org/10.5281/zenodo.8379120, The MESSy Consortium, 2023) and have already been incorporated into the official development branch of the EMAC modeling system and will therefore be part of all future released versions. The data produced in the study are available from the author upon request.

Supplement. The supplement related to this article is available online at: https://doi.org/10.5194/gmd-17-1111-2024-supplement.

Author contributions. AM and VAK wrote the paper with contributions from all coauthors. VAK planned the research with contributions from AKS, SNP and AN. AN and SNP provided the ISORROPIA-lite model. AM and HT performed the implementation in EMAC. AM performed the simulations and analyzed the results, assisted by VAK and APT. APT provided the observations and performed the model evaluation. All the authors discussed the results and contributed to the paper.

Competing interests. At least one of the (co-)authors is a member of the editorial board of *Geoscientific Model Development*. The peer-review process was guided by an independent editor, and the authors also have no other competing interests to declare.

Disclaimer. Publisher's note: Copernicus Publications remains neutral with regard to jurisdictional claims made in the text, published maps, institutional affiliations, or any other geographical representation in this paper. While Copernicus Publications makes every effort to include appropriate place names, the final responsibility lies with the authors.

Acknowledgements. The work described in this paper has received funding from the Initiative and Networking Fund of the Helmholtz Association through the project "Advanced Earth System Modelling Capacity (ESM)". The authors gratefully acknowledge the

Earth System Modelling Project (ESM) for funding this work by providing computing time on the ESM partition of the supercomputer JUWELS (Alvarez, 2021) at the Jülich Supercomputing Centre (JSC).

Financial support. This research has been supported by the project FORCeS funded from the European Union's Horizon 2020 research and innovation program under grant agreement no. 821205.

The article processing charges for this open-access publication were covered by the Forschungszentrum Jülich.

Review statement. This paper was edited by Samuel Remy and reviewed by two anonymous referees.

References

Alvarez, D.: JUWELS cluster and booster: Exascale pathfinder with modular supercomputing architecture at juelich supercomputing Centre, Journal of large-scale research facilities JLSRF, 7, A183, https://doi.org/10.17815/jlsrf-7-183, 2021.

Andreae, M. O., Jones, C. D., and Cox, P. M.: Strong present-day aerosol cooling implies a hot future, Nature, 435, 1187–1190, https://doi.org/10.1038/nature03671, 2005.

Ansari, A. S. and Pandis, S. N.: The effect of metastable equilibrium states on the partitioning of nitrate between the gas and aerosol phases, Atmos. Environ., 34, 157–168, https://doi.org/10.1016/S1352-2310(99)00242-3, 2000.

Astitha, M., Lelieveld, J., Abdel Kader, M., Pozzer, A., and de Meij, A.: Parameterization of dust emissions in the global atmospheric chemistry-climate model EMAC: impact of nudging and soil properties, Atmos. Chem. Phys., 12, 11057–11083, https://doi.org/10.5194/acp-12-11057-2012, 2012.

Bacer, S., Sullivan, S. C., Karydis, V. A., Barahona, D., Krämer, M., Nenes, A., Tost, H., Tsimpidi, A. P., Lelieveld, J., and Pozzer, A.: Implementation of a comprehensive ice crystal formation parameterization for cirrus and mixed-phase clouds in the EMAC model (based on MESSy 2.53), Geosci. Model Dev., 11, 4021–4041, https://doi.org/10.5194/gmd-11-4021-2018, 2018.

Bassett, M. and Seinfeld, J. H.: Atmospheric equilibrium model of sulfate and nitrate aerosols, Atmos. Environ., 17, 2237–2252, https://doi.org/10.1016/0004-6981(83)90221-4, 1983.

Bouwman, A. F., Lee, D. S., Asman, W. A., Dentener, F. J., Van Der Hoek, K. W., and Olivier, J. G. J.: A global high-resolution emission inventory for ammonia, Global Biogeochem. Cy., 11, 561–587, https://doi.org/10.1029/97GB02266, 1997.

Bromley, L. A.: Thermodynamic properties of strong electrolytes in aqueous solutions, AICHE J., 19, 313–320, https://doi.org/10.1002/aic.690190216, 1973.

Brook, R. D., Rajagopalan, S., Pope, C. A., Brook, J. R., Bhatnagar, A., Diez-Roux, A. V., Holguin, F., Hong, Y., Luepker, R. V., Mittleman, M. A., and Peters, A.: Particulate matter air pollution and cardiovascular disease: an update to the scientific statement from the American Heart Association, Circulation, 121, 2331–2378, https://doi.org/10.1161/CIR.0b013e3181dbece1, 2010.

Chen, Y., Shen, H., and Russell, A. G.: Current and future responses of aerosol pH and composition in the US to declining SO_2 emissions and increasing NH_3 emissions, Environ. Sci. Technol., 53, 9646–9655, https://doi.org/10.1021/acs.est.9b02005, 2019.

Clegg, S. L., Seinfeld, J. H., and Edney, E. O.: Thermodynamic modelling of aqueous aerosols containing electrolytes and dissolved organic compounds. II. An extended Zdanovskii–Stokes–Robinson approach, J. Aerosol Sci., 34, 667–690, https://doi.org/10.1016/S0021-8502(03)00019-3, 2003.

Crippa, M., Guizzardi, D., Muntean, M., Schaaf, E., Dentener, F., van Aardenne, J. A., Monni, S., Doering, U., Olivier, J. G. J., Pagliari, V., and Janssens-Maenhout, G.: Gridded emissions of air pollutants for the period 1970–2012 within EDGAR v4.3.2, Earth Syst. Sci. Data, 10, 1987–2013, https://doi.org/10.5194/essd-10-1987-2018, 2018.

Dentener, F., Kinne, S., Bond, T., Boucher, O., Cofala, J., Generoso, S., Ginoux, P., Gong, S., Hoelzemann, J. J., Ito, A., Marelli, L., Penner, J. E., Putaud, J.-P., Textor, C., Schulz, M., van der Werf, G. R., and Wilson, J.: Emissions of primary aerosol and precursor gases in the years 2000 and 1750 prescribed data-sets for AeroCom, Atmos. Chem. Phys., 6, 4321–4344, https://doi.org/10.5194/acp-6-4321-2006, 2006.

Doney, S. C., Mahowald, N., Lima, I., Feely, R. A., Mackenzie, F. T., Lamarque, J. F., and Rasch, P. J.: Impact of anthropogenic atmospheric nitrogen and sulfur deposition on ocean acidification and the inorganic carbon system, P. Natl. Acad. Sci. USA, 104, 14580–14585, https://doi.org/10.1073/pnas.0702218104, 2007.

European Monitoring and Evaluation Programme (EMEP): EBAS database online, https://projects.nilu.no/ccc/index.html, last access: 5 February 2024.

Fang, T., Guo, H., Zeng, L., Verma, V., Nenes, A., and Weber, R. J.: Highly acidic ambient particles, soluble metals, and oxidative potential: a link between sulfate and aerosol toxicity, Environ. Sci. Technol., 51, 2611–2620, https://doi.org/10.1021/acs.est.6b06151, 2017.

Fountoukis, C. and Nenes, A.: ISORROPIA II: a computationally efficient thermodynamic equilibrium model for K^+–Ca^{2+}–Mg^{2+}–NH_4^+–Na^+–SO_4^{2-}–NO_3^-–Cl^-–H_2O aerosols, Atmos. Chem. Phys., 7, 4639–4659, https://doi.org/10.5194/acp-7-4639-2007, 2007.

Fountoukis, C., Nenes, A., Sullivan, A., Weber, R., Van Reken, T., Fischer, M., Matías, E., Moya, M., Farmer, D., and Cohen, R. C.: Thermodynamic characterization of Mexico City aerosol during MILAGRO 2006, Atmos. Chem. Phys., 9, 2141–2156, https://doi.org/10.5194/acp-9-2141-2009, 2009.

Fu, X., Wang, S., Xing, J., Zhang, X., Wang, T., and Hao, J.: Increasing ammonia concentrations reduce the effectiveness of particle pollution control achieved via SO_2 and NO_X emissions reduction in east China, Environ. Sci. Tech. Let., 4, 221–227, https://doi.org/10.1021/acs.estlett.7b00143, 2017.

Grewe, V., Brunner, D., Dameris, M., Grenfell, J. L., Hein, R., Shindell, D., and Staehelin, J.: Origin and variability of upper tropospheric nitrogen oxides and ozone at northern mid-latitudes, Atmos. Environ., 35, 3421–3433, https://doi.org/10.1016/S1352-2310(01)00134-0, 2001.

Guo, H., Sullivan, A. P., Campuzano-Jost, P., Schroder, J. C., Lopez-Hilfiker, F. D., Dibb, J. E., Jimenez, J. L., Thornton, J. A., Brown, S. S., Nenes, A., and Weber, R. J.: Fine particle pH and the partitioning of nitric acid during winter in the north-

eastern United States, J. Geophys. Res.-Atmos., 121, 355–310, https://doi.org/10.1002/2016JD025311, 2016.

He, K., Yang, F., Ma, Y., Zhang, Q., Yao, X., Chan, C. K., Cadle, S., Chan, T., and Mulawa, P.: The characteristics of $PM_{2.5}$ in Beijing, China, Atmos. Environ., 35, 4959–4970, https://doi.org/10.1016/S1352-2310(01)00301-6, 2001.

Héroux, M. E., Anderson, H. R., Atkinson, R., Brunekreef, B., Cohen, A., Forastiere, F., Hurley, F., Katsouyanni, K., Krewski, D., Krzyzanowski, M., and Künzli, N.: Quantifying the health impacts of ambient air pollutants: recommendations of a WHO/Europe project, Int. J. Public Health, 60, 619–627, https://doi.org/10.1007/s00038-015-0690-y, 2015.

Hersbach, H., Bell, B., Berrisford, P., Hirahara, S., Horanyi, A., Muñoz-Sabater, J., Nicolas, J., Peubey, C., Radu, R., Schepers, D., and Simmons, A.: The ERA5 global reanalysis, Q. J. Roy. Meteor. Soc., 146, 1999–2049, https://doi.org/10.1002/qj.3803, 2020.

Honour, S. L., Bell, J. N. B., Ashenden, T. W., Cape, J. N., and Power, S. A.: Responses of herbaceous plants to urban air pollution: effects on growth, phenology and leaf surface characteristics, Environ. Pollut., 157, 1279–1286, https://doi.org/10.1016/j.envpol.2008.11.049, 2009.

Interagency Monitoring of Protected Visual Environment (IMPROVE): Federal Land Manager Environmental Database, http://vista.cira.colostate.edu/Improve/improve-data/, last access: 5 February 2024.

Jacobson, M. Z., Tabazadeh, A., and Turco, R. P.: Simulating equilibrium within aerosols and nonequilibrium between gases and aerosols, J. Geophys. Res.-Atmos., 101, 9079–9091, https://doi.org/10.1029/96JD00348, 1996.

Jöckel, P., Sander, R., Kerkweg, A., Tost, H., and Lelieveld, J.: Technical Note: The Modular Earth Submodel System (MESSy) - a new approach towards Earth System Modeling, Atmos. Chem. Phys., 5, 433–444, https://doi.org/10.5194/acp-5-433-2005, 2005.

Jöckel, P., Tost, H., Pozzer, A., Brühl, C., Buchholz, J., Ganzeveld, L., Hoor, P., Kerkweg, A., Lawrence, M. G., Sander, R., Steil, B., Stiller, G., Tanarhte, M., Taraborrelli, D., van Aardenne, J., and Lelieveld, J.: The atmospheric chemistry general circulation model ECHAM5/MESSy1: consistent simulation of ozone from the surface to the mesosphere, Atmos. Chem. Phys., 6, 5067–5104, https://doi.org/10.5194/acp-6-5067-2006, 2006.

Jöckel, P., Tost, H., Pozzer, A., Kunze, M., Kirner, O., Brenninkmeijer, C. A. M., Brinkop, S., Cai, D. S., Dyroff, C., Eckstein, J., Frank, F., Garny, H., Gottschaldt, K.-D., Graf, P., Grewe, V., Kerkweg, A., Kern, B., Matthes, S., Mertens, M., Meul, S., Neumaier, M., Nützel, M., Oberländer-Hayn, S., Ruhnke, R., Runde, T., Sander, R., Scharffe, D., and Zahn, A.: Earth System Chemistry integrated Modelling (ESCiMo) with the Modular Earth Submodel System (MESSy) version 2.51, Geosci. Model Dev., 9, 1153–1200, https://doi.org/10.5194/gmd-9-1153-2016, 2016.

Kakavas, S., Pandis, S. N., and Nenes, A.: ISORROPIA-Lite: A Comprehensive Atmospheric Aerosol Thermodynamics Module for Earth System Models, Tellus B, 74, 1–23, https://doi.org/10.16993/tellusb.33, 2022.

Kakavas, S., Pandis, S. N., and Nenes, A.: Effects of simulated secondary organic aerosol water on PM_1 levels and composition over the US, Atmos. Chem. Phys., 23, 13555–13564, https://doi.org/10.5194/acp-23-13555-2023, 2023.

Karydis, V. A., Tsimpidi, A. P., Fountoukis, C., Nenes, A., Zavala, M., Lei, W. F., Molina, L. T., and Pandis, S. N.: Simulating the fine and coarse inorganic particulate matter concentrations in a polluted megacity, Atmos. Environ., 44, 608–620, https://doi.org/10.1016/j.atmosenv.2009.11.023, 2010.

Karydis, V. A., Tsimpidi, A. P., Lei, W., Molina, L. T., and Pandis, S. N.: Formation of semivolatile inorganic aerosols in the Mexico City Metropolitan Area during the MILAGRO campaign, Atmos. Chem. Phys., 11, 13305–13323, https://doi.org/10.5194/acp-11-13305-2011, 2011.

Karydis, V. A., Tsimpidi, A. P., Pozzer, A., Astitha, M., and Lelieveld, J.: Effects of mineral dust on global atmospheric nitrate concentrations, Atmos. Chem. Phys., 16, 1491–1509, https://doi.org/10.5194/acp-16-1491-2016, 2016.

Karydis, V. A., Tsimpidi, A. P., Bacer, S., Pozzer, A., Nenes, A., and Lelieveld, J.: Global impact of mineral dust on cloud droplet number concentration, Atmos. Chem. Phys., 17, 5601–5621, https://doi.org/10.5194/acp-17-5601-2017, 2017.

Karydis, V. A., Tsimpidi, A. P., Pozzer, A., and Lelieveld, J.: How alkaline compounds control atmospheric aerosol particle acidity, Atmos. Chem. Phys., 21, 14983–15001, https://doi.org/10.5194/acp-21-14983-2021, 2021.

Kerkweg, A., Buchholz, J., Ganzeveld, L., Pozzer, A., Tost, H., and Jöckel, P.: Technical Note: An implementation of the dry removal processes DRY DEPosition and SEDImentation in the Modular Earth Submodel System (MESSy), Atmos. Chem. Phys., 6, 4617–4632, https://doi.org/10.5194/acp-6-4617-2006, 2006.

Kim, Y. P., Seinfeld, J. H., and Saxena, P.: Atmospheric gas-aerosol equilibrium I. Thermodynamic model, Aerosol Sci. Technol., 19, 157–181, https://doi.org/10.1080/02786829308959628, 1993.

Klingmüller, K., Metzger, S., Abdelkader, M., Karydis, V. A., Stenchikov, G. L., Pozzer, A., and Lelieveld, J.: Revised mineral dust emissions in the atmospheric chemistry–climate model EMAC (MESSy 2.52 DU_Astitha1 KKDU2017 patch), Geosci. Model Dev., 11, 989–1008, https://doi.org/10.5194/gmd-11-989-2018, 2018.

Klingmüller, K., Lelieveld, J., Karydis, V. A., and Stenchikov, G. L.: Direct radiative effect of dust–pollution interactions, Atmos. Chem. Phys., 19, 7397–7408, https://doi.org/10.5194/acp-19-7397-2019, 2019.

Klingmüller, K., Karydis, V. A., Bacer, S., Stenchikov, G. L., and Lelieveld, J.: Weaker cooling by aerosols due to dust–pollution interactions, Atmos. Chem. Phys., 20, 15285–15295, https://doi.org/10.5194/acp-20-15285-2020, 2020.

Kusik, C. L. and Meissner H. P.: Electrolyte Activity Coefficients in Inorganic Processing, AICHE Sym. S., 173, 14–20, 1978.

Lelieveld, J., Evans, J. S., Fnais, M., Giannadaki, D., and Pozzer, A.: The contribution of outdoor air pollution sources to premature mortality on a global scale, Nature, 525, 367–371, https://doi.org/10.1038/nature15371, 2015.

Lohmann, U. and Ferrachat, S.: Impact of parametric uncertainties on the present-day climate and on the anthropogenic aerosol effect, Atmos. Chem. Phys., 10, 11373–11383, https://doi.org/10.5194/acp-10-11373-2010, 2010.

Manisalidis, I., Stavropoulou, E., Stavropoulos, A., and Bezirtzoglou, E.: Environmental and health impacts of air pollution: a review, Frontiers in Public Health, 14, 8–14, https://doi.org/10.3389/fpubh.2020.00014, 2020.

Marais, E. A., Jacob, D. J., Jimenez, J. L., Campuzano-Jost, P., Day, D. A., Hu, W., Krechmer, J., Zhu, L., Kim, P. S., Miller, C. C., Fisher, J. A., Travis, K., Yu, K., Hanisco, T. F., Wolfe, G. M., Arkinson, H. L., Pye, H. O. T., Froyd, K. D., Liao, J., and McNeill, V. F.: Aqueous-phase mechanism for secondary organic aerosol formation from isoprene: application to the southeast United States and co-benefit of SO2 emission controls, Atmos. Chem. Phys., 16, 1603–1618, https://doi.org/10.5194/acp-16-1603-2016, 2016.

Meissner, H. P. and Peppas, N. A.: Activity coefficients – aqueous solutions of polybasic acids and their salts, AICHE J., 19, 806–809, https://doi.org/10.1002/aic.690190419, 1973.

Metzger, S., Dentener, F., Pandis, S., and Lelieveld, J.: Gas/aerosol partitioning, 1, A computationally efficient model, J. Geophys. Res.-Atmos., 107, 16–24, https://doi.org/10.1029/2001JD001102, 2002.

Miinalainen, T., Kokkola, H., Lehtinen, K. E., and Kühn, T.: Comparing the radiative forcings of the anthropogenic aerosol emissions from Chile and Mexico, J. Geophys. Res.-Atmos., 126, 10, https://doi.org/10.1029/2020JD033364, 2021.

Myhre, G., Samset, B. H., Schulz, M., Balkanski, Y., Bauer, S., Berntsen, T. K., Bian, H., Bellouin, N., Chin, M., Diehl, T., Easter, R. C., Feichter, J., Ghan, S. J., Hauglustaine, D., Iversen, T., Kinne, S., Kirkevåg, A., Lamarque, J.-F., Lin, G., Liu, X., Lund, M. T., Luo, G., Ma, X., van Noije, T., Penner, J. E., Rasch, P. J., Ruiz, A., Seland, Ø., Skeie, R. B., Stier, P., Takemura, T., Tsigaridis, K., Wang, P., Wang, Z., Xu, L., Yu, H., Yu, F., Yoon, J.-H., Zhang, K., Zhang, H., and Zhou, C.: Radiative forcing of the direct aerosol effect from AeroCom Phase II simulations, Atmos. Chem. Phys., 13, 1853–1877, https://doi.org/10.5194/acp-13-1853-2013, 2013.

Nenes, A., Pandis, S. N., and Pilinis, C.: ISORROPIA: A new thermodynamic equilibrium model for multiphase multicomponent inorganic aerosols, Aquat. Geochem., 4, 123–152, https://doi.org/10.1023/A:1009604003981, 1998.

Nenes, A., Pandis, S. N., Weber, R. J., and Russell, A.: Aerosol pH and liquid water content determine when particulate matter is sensitive to ammonia and nitrate availability, Atmos. Chem. Phys., 20, 3249–3258, https://doi.org/10.5194/acp-20-3249-2020, 2020.

Pilinis, C. and Seinfeld, J. H.: Continued development of a general equilibrium model for inorganic multicomponent atmospheric aerosols, Atmos. Environ., 21, 2453–2466, https://doi.org/10.1016/0004-6981(87)90380-5, 1987.

Pope, C. A., Burnett, R. T., Turner, M. C., Cohen, A., Krewski, D., Jerrett, M., Gapstur, S. M., and Thun, M. J.: Lung cancer and cardiovascular disease mortality associated with ambient air pollution and cigarette smoke: shape of the exposure–response relationships, Environ. Health Persp., 119, 1616–1621, https://doi.org/10.1289/ehp.1103639, 2011.

Pozzer, A., Jöckel, P., Sander, R., Williams, J., Ganzeveld, L., and Lelieveld, J.: Technical Note: The MESSy-submodel AIRSEA calculating the air-sea exchange of chemical species, Atmos. Chem. Phys., 6, 5435–5444, https://doi.org/10.5194/acp-6-5435-2006, 2006.

Pringle, K. J., Tost, H., Message, S., Steil, B., Giannadaki, D., Nenes, A., Fountoukis, C., Stier, P., Vignati, E., and Lelieveld, J.: Description and evaluation of GMXe: a new aerosol submodel for global simulations (v1), Geosci. Model Dev., 3, 391–412, https://doi.org/10.5194/gmd-3-391-2010, 2010a.

Pringle, K. J., Tost, H., Metzger, S., Steil, B., Giannadaki, D., Nenes, A., Fountoukis, C., Stier, P., Vignati, E., and Lelieveld, J.: Corrigendum to "Description and evaluation of GMXe: a new aerosol submodel for global simulations (v1)" published in Geosci. Model Dev., 3, 391–412, 2010, Geosci. Model Dev., 3, 413–413, https://doi.org/10.5194/gmd-3-413-2010, 2010b.

Putaud, J. P., Van Dingenen, R., Alastuey, A., Bauer, H., Birmili, W., Cyrys, J., Flentje, H., Fuzzi, S., Gehrig, R., Hansson, H. C., and Harrison, R. M.: A European aerosol phenomenology–3: Physical and chemical characteristics of particulate matter from 60 rural, urban, and kerbside sites across Europe, Atmos. Environ., 44, 1308–1320, https://doi.org/10.1016/j.atmosenv.2009.12.011, 2010.

Roeckner, E., Brokopf, R., Esch, M., Giorgetta, M., Hagemann, S., Kornblueh, L., Manzini, E., Schlese, U., and Schulzweida, U.: Sensitivity of simulated climate to horizontal and vertical resolution in the ECHAM5 atmosphere model, J. Climate, 19, 3771–3791, https://doi.org/10.1175/JCLI3824.1, 2006.

Saiz-Lopez, A. and von Glasow, R.: Reactive halogen chemistry in the troposphere, Chem. Soc. Rev., 41, 6448–6472, https://doi.org/10.1039/C2CS35208G, 2012.

Sander, R., Baumgaertner, A., Cabrera-Perez, D., Frank, F., Gromov, S., Grooß, J.-U., Harder, H., Huijnen, V., Jöckel, P., Karydis, V. A., Niemeyer, K. E., Pozzer, A., Riede, H., Schultz, M. G., Taraborrelli, D., and Tauer, S.: The community atmospheric chemistry box model CAABA/MECCA-4.0, Geosci. Model Dev., 12, 1365–1385, https://doi.org/10.5194/gmd-12-1365-2019, 2019.

Savoie, D. L. and Prospero, J.: Particle size distribution of nitrate and sulfate in the marine atmosphere, Geophys. Res. Lett., 9, 1207–1210, https://doi.org/10.1029/GL009i010p01207, 1982.

Saxena, P., Hudischewskyj, A. B., Seigneur, C., and Seinfeld, J. H.: A comparative study of equilibrium approaches to the chemical characterization of secondary aerosols, Atmos. Environ., 20, 1471–1483, https://doi.org/10.1016/0004-6981(86)90019-3, 1986.

Seinfeld, J. H. and Pandis, S. N.: Atmospheric chemistry and physics: from air pollution to climate change, John Wiley & Sons, ISBN 1118947401, 2016.

Silva, P. J., Vawdrey, E. L., Corbett, M., and Erupe, M.: Fine particle concentrations and composition during wintertime inversions in Logan, Utah, USA, Atmos. Environ., 41, 5410–5422, https://doi.org/10.1016/j.atmosenv.2007.02.016, 2007.

Song, S., Gao, M., Xu, W., Shao, J., Shi, G., Wang, S., Wang, Y., Sun, Y., and McElroy, M. B.: Fine-particle pH for Beijing winter haze as inferred from different thermodynamic equilibrium models, Atmos. Chem. Phys., 18, 7423–7438, https://doi.org/10.5194/acp-18-7423-2018, 2018.

Szopa, S., Naik, V., Adhikary, B., Artaxo, P., Berntsen, T., Collins, W. D., Fuzzi, S., Gallardo, L., Kiendler-Scharr, A., Klimont, Z., Liao, H., Unger, N., and Zanis, P.: Short-Lived Climate Forcers. In Climate Change 2021: The Physical Science Basis, Contribution of Working Group I to the Sixth Assessment Report of the Intergovernmental Panel on Climate Change, edited by: Masson-Delmotte, V., Zhai, P., Pirani, A., Connors, S. L., Péan, C., Berger, S., Caud, N., Chen, Y., Goldfarb, L., Gomis, M. I., Huang, M., Leitzell, K., Lonnoy, E.,

Matthews, J. B. R., Maycock, T. K., Waterfield, T., Yelekçi, O., Yu, R., and Zhou, B., Cambridge University Press, Cambridge, United Kingdom and New York, NY, USA, 817–922, https://doi.org/10.1017/9781009157896.008, 2021.

Tang, Y. S., Flechard, C. R., Dämmgen, U., Vidic, S., Djuricic, V., Mitosinkova, M., Uggerud, H. T., Sanz, M. J., Simmons, I., Dragosits, U., Nemitz, E., Twigg, M., van Dijk, N., Fauvel, Y., Sanz, F., Ferm, M., Perrino, C., Catrambone, M., Leaver, D., Braban, C. F., Cape, J. N., Heal, M. R., and Sutton, M. A.: Pan-European rural monitoring network shows dominance of NH_3 gas and NH_4NO_3 aerosol in inorganic atmospheric pollution load, Atmos. Chem. Phys., 21, 875–914, https://doi.org/10.5194/acp-21-875-2021, 2021.

Tarin-Carrasco, P., Im, U., Geels, C., Palacios-Peña, L., and Jiménez-Guerrero, P.: Contribution of fine particulate matter to present and future premature mortality over Europe: A non-linear response, Environ. Int., 153, 106517, https://doi.org/10.1016/j.envint.2021.106517, 2021.

The Acid Deposition Monitoring Network in East Asia: EANET Data on the Acid Deposition in the East Asian Region, https://monitoring.eanet.asia/document/public/index, last access: 5 February 2024.

The MESSy Consortium: The Modular Earth Submodel System (2.55.2_842-isorropia-light), Zenodo [code], https://doi.org/10.5281/zenodo.8379120, 2023.

Tost, H., Jöckel, P., Kerkweg, A., Sander, R., and Lelieveld, J.: Technical note: A new comprehensive SCAVenging submodel for global atmospheric chemistry modelling, Atmos. Chem. Phys., 6, 565–574, https://doi.org/10.5194/acp-6-565-2006, 2006.

Tost, H., Jöckel, P., Kerkweg, A., Pozzer, A., Sander, R., and Lelieveld, J.: Global cloud and precipitation chemistry and wet deposition: tropospheric model simulations with ECHAM5/MESSy1, Atmos. Chem. Phys., 7, 2733–2757, https://doi.org/10.5194/acp-7-2733-2007, 2007.

Tsimpidi, A. P., Karydis, V. A., and Pandis, S. N.: Response of Inorganic Fine Particulate Matter to Emission Changes of Sulfur Dioxide and Ammonia: The Eastern United States as a Case Study, J. Air Waste Manage., 57, 1489–1498, https://doi.org/10.3155/1047-3289.57.12.1489, 2007.

Tsimpidi, A. P., Karydis, V. A., Pozzer, A., Pandis, S. N., and Lelieveld, J.: ORACLE (v1.0): module to simulate the organic aerosol composition and evolution in the atmosphere, Geosci. Model Dev., 7, 3153–3172, https://doi.org/10.5194/gmd-7-3153-2014, 2014.

Tsimpidi, A. P., Karydis, V. A., Pozzer, A., Pandis, S. N., and Lelieveld, J.: ORACLE 2-D (v2.0): an efficient module to compute the volatility and oxygen content of organic aerosol with a global chemistry–climate model, Geosci. Model Dev., 11, 3369–3389, https://doi.org/10.5194/gmd-11-3369-2018, 2018.

U.S. Environmental Protection Agency Clean Air Markets Division Clean Air Status and Trends Network (CASTNET): CASTNET Data, https://www.epa.gov/castnet, last access: 5 February 2024.

van der Werf, G. R., Randerson, J. T., Giglio, L., Collatz, G. J., Mu, M., Kasibhatla, P. S., Morton, D. C., DeFries, R. S., Jin, Y., and van Leeuwen, T. T.: Global fire emissions and the contribution of deforestation, savanna, forest, agricultural, and peat fires (1997–2009), Atmos. Chem. Phys., 10, 11707–11735, https://doi.org/10.5194/acp-10-11707-2010, 2010.

Vignati, E., Wilson, J., and Stier, P.: M7: An efficient size-resolved aerosol microphysics module for large-scale aerosol transport models, J. Geophys. Res.-Atmos., 109, D22, https://doi.org/10.1029/2003JD004485, 2004.

Weagle, C. L., Snider, G., Li, C., Van Donkelaar, A., Philip, S., Bissonnette, P., Burke, J., Jackson, J., Latimer, R., and Stone, E.: Global sources of fine particulate matter: interpretation of $PM_{2.5}$ chemical composition observed by SPARTAN using a global chemical transport model, Environ. Sci. Technol., 52, 11670–11681, https://doi.org/10.1021/acs.est.8b01658, 2018.

Wexler, A. S. and Clegg, S. L.: Atmospheric aerosol models for systems including the ions H^+, NH_4^+, Na^+, SO_4^{2-}, NO_3^-, Cl^-, Br^-, and H_2O, J. Geophys. Res.-Atmos., 107, ACH-14, https://doi.org/10.1029/2001JD000451, 2002.

Wexler, A. S. and Seinfeld, J. H.: Second-generation inorganic aerosol model, Atmos. Environ. A.-Gen., 25, 2731–2748, https://doi.org/10.1016/0960-1686(91)90203-J, 1991.

Wolff, G. T.: On the nature of nitrate in coarse continental aerosols, Atmos. Environ., 18, 977–981, https://doi.org/10.1016/0004-6981(84)90073-8, 1984.

World Health Organization: Ambient (outdoor) air pollution, https://www.who.int/news-room/fact-sheets/detail/ambient-(outdoor)-air-quality-and-health, last access: 19 December 2022.

Xu, G., Zhang, Q., Yao, Y., and Zhang, X.: Changes in $PM_{2.5}$ sensitivity to NO_x and NH_3 emissions due to a large decrease in SO_2 emissions from 2013 to 2018, Atmos. Ocean. Sc. Lett., 13, 210–215, https://doi.org/10.1080/16742834.2020.1738009, 2020.

Yan, W., Topphoff, M., Rose, C., and Gmehling, J.: Prediction of vapor–liquid equilibria in mixed-solvent electrolyte systems using the group contribution concept, Fluid Phase Equilibr., 162, 97–113, https://doi.org/10.1016/S0378-3812(99)00201-0, 1999.

Yienger, J. J. and Levy, H.: Empirical model of global soil-biogenic NOx emissions, J. Geophys. Res.-Atmos., 100, 11447–11464, https://doi.org/10.1029/95JD00370, 1995.

Zakoura, M. and Pandis, S. N.: Overprediction of aerosol nitrate by chemical transport models: The role of grid resolution Atmos. Environ., 187, 390–400, https://doi.org/10.1016/j.atmosenv.2018.05.066, 2018.

Zuend, A., Marcolli, C., Luo, B. P., and Peter, T.: A thermodynamic model of mixed organic-inorganic aerosols to predict activity coefficients, Atmos. Chem. Phys., 8, 4559–4593, https://doi.org/10.5194/acp-8-4559-2008, 2008.

Zuend, A., Marcolli, C., Booth, A. M., Lienhard, D. M., Soonsin, V., Krieger, U. K., Topping, D. O., McFiggans, G., Peter, T., and Seinfeld, J. H.: New and extended parameterization of the thermodynamic model AIOMFAC: calculation of activity coefficients for organic-inorganic mixtures containing carboxyl, hydroxyl, carbonyl, ether, ester, alkenyl, alkyl, and aromatic functional groups, Atmos. Chem. Phys., 11, 9155–9206, https://doi.org/10.5194/acp-11-9155-2011, 2011.

3 Exploring varieties of setups and parameterizations for accurate fine mode NO_3^- aerosol predictions

The content of this chapter is a manuscript with the title: “Global Perspectives on Nitrate Aerosol Dynamics: A Comprehensive Sensitivity Analysis” by A. Milousis, S. M.C. Scholz, H. Fuchs, A. P. Tsimpidi, and V. A. Karydis.

The supplementary material is provided in Appendix A.3. The data produced in the study are available from the authors upon request. The authors contributed to the article as follows:

AM and VAK wrote the paper with contributions from APT, HF and SS. VAK planned the research with contributions from APT. AM performed the simulations and analyzed the results, assisted by VAK and APT. APT and SS provided the observational data. All the authors discussed the results and contributed to the paper.

Global Perspectives on Nitrate Aerosol Dynamics: A Comprehensive Sensitivity Analysis

Alexandros Milousis[1], Susanne M.C. Scholz[1], Hendrik Fuchs[1,2], Alexandra P. Tsimpidi[1], and Vlassis A. Karydis[1]

[1]Institute of Climate and Energy Systems, ICE-3: Troposphere, Forschungszentrum Jülich GmbH, Jülich, Germany
[2]Department of Physics, University of Cologne, Cologne, Germany

Abstract

In recent decades, nitrate aerosols have gradually become a predominant component of atmospheric composition, outcompeting sulfate aerosols in terms of both abundance and climatic significance. Nevertheless, the accurate simulation of nitrate aerosols remains a persistent challenge for most global atmospheric models. The factors that influence the formation of nitrate aerosols are diverse and complex, further complicated by variations in conditions across different regions. This study aims to explore these factors to identify the most critical components for accurately simulating aerosol nitrate levels in the world's most polluted areas. To do so, the state-of-the-art EMAC atmospheric climate and chemistry model is employed to assess the impact of key parameters, including grid resolution, emission inventories, as well as the treatment of thermodynamic, chemical, and aerosol scavenging processes. The widely used ISORROPIA II thermodynamic equilibrium model is applied to simulate the formation and composition of inorganic aerosols. The model predictions are then compared with surface observations of particulate nitrate in the size ranges of smaller than 1 μm and 2.5 μm in diameter (PM_1 and $PM_{2.5}$). These include $PM_{2.5}$ data from routine filter-based measurement networks (EMEP, EPA, IMPROVE, and EANET) and PM_1 measurements obtained by aerosol mass spectrometer (AMS) in field campaigns conducted in Europe, North America, East Asia, and India. The findings indicate that the model consistently predicts higher nitrate concentrations of $PM_{2.5}$ in all regions, particularly in East Asia, with biases reaching up to a factor of 3. However, the model's performance is enhanced by increasing the grid resolution, decreasing the uptake coefficient for N_2O_5 hydrolysis, and utilizing an appropriate emission database (e.g., CMIP6). Notably, the region of East Asia exhibited enhanced prediction accuracy when a simplified aerosol scavenging treatment was employed. A comparison of model predictions and observations of $PM_{2.5}$ nitrate underscores a seasonal dependence in the model's ability to best replicate network observations across different regions. Conversely, the model exhibited a tendency to underpredict observations of PM_1 nitrate, contrasting with the observed patterns for $PM_{2.5}$ nitrate. This discrepancy is particularly pronounced at downwind sites, where the model and measurement discrepancies were most significant. The identification of a universal optimal model configuration for the representation of PM_1 presents a significant challenge. It was found that improvements in the model achieved using the aforementioned parameters did not necessarily result in enhanced agreement in this comparison. In general, modeling PM_1 nitrate aerosol in Europe and in locations downwind of emission sources poses the greatest challenges for the model. A comparison of the diurnal concentrations between model predictions and observations at selected European stations reveals that much of the model bias stems from an unrealistically sharp decrease in nitrate aerosol levels from morning maxima to evening minima, a pattern rarely reflected in the measurements. Finally, the predicted tropospheric burden of total nitrate aerosol demonstrates relatively minor variations across all sensitivity tests, with differences not exceeding 25%.

Keywords : Nitrate aerosol, model bias, seasonal variation, diurnal variation, tropospheric burden

1. Introduction

Aerosols represent a critical and intricate component of the Earth's climate system, attributable to the complexity of their chemical composition and the numerous alterations they undergo upon emission into the atmosphere. The composition of anthropogenic aerosols, influenced by the diverse precursor gases emitted by anthropogenic activities, plays a pivotal role in shaping climate and air quality. Of particular concern are aerosols with a diameter of less than 2.5 μm ($PM_{2.5}$), which have been linked to a significant global mortality rate, estimated to exceed four million deaths per year (Chowdhury et al., 2022; Im et al., 2023). Furthermore, anthropogenic aerosols have a significant impact on the Earth's energy balance by causing a net cooling effect that tends to mask the warming induced by greenhouse gases (Storelvmo et al., 2016; Glantz et al., 2022; Nair et al., 2023). Among the various types of anthropogenic aerosols, sulfates (SO_4^{2-}) have become the dominant type in terms of mass concentrations, with a tropospheric burden that is more than twice as high as that of nitrates (NO_3^-) (Bellouin et al., 2011; Myhre et al., 2013; Karydis et al., 2016). However, numerous studies have indicated a shift in this regime, with nitrates challenging the dominance of sulfates in several key regions of the polluted northern hemisphere, including Europe (Lanz et al., 2010; Aksoyoglu et al., 2017), the USA (Walker et al., 2012), and East Asia (Wang et al., 2013; Li et al., 2020). This phenomenon can be attributed to the strict restrictions on sulfur dioxide (SO_2) emissions worldwide, which have not always been accompanied by a corresponding reduction in nitrogen oxide (NOx) emissions, and particularly ammonia (NH_3), which has increased in recent decades (Bellouin et al., 2011; Hauglustaine et al., 2014). Nitrate aerosols are of particular importance because they can influence atmospheric chemistry through heterogeneous reactions with dust and sea salt, which also lead to more acidic conditions in aerosols (Karydis et al., 2016; Karydis et al., 2021). Additionally, nitrate aerosols have been shown to affect climate through a direct radiative effect that leads to cooling (Myhre et al., 2013; Hauglustaine et al., 2014; Milousis et al., 2025). Furthermore, nitrate aerosols influence the properties of clouds and other aerosol species, resulting in a complex indirect radiative effect (Milousis et al., 2025). Consequently, the precise representation of nitrate aerosols in global chemistry climate models (CCM) is imperative, as they are projected to have the most substantial impact on climate and air quality by the end of the century.

However, this task presents a number of challenges. Concentrations of nitrate aerosols are highly sensitive to the levels of their precursors, making their accurate representation in models an essential starting point for their accurate prediction. Furthermore, nitrate aerosols are inherently semi-volatile, implying that partitioning between the gas and particle phases is an intricate process, as equilibrium conditions must be met, which in turn complicates calculations (Seinfeld and Pandis, 2016). To ensure the reliability of model predictions, it is imperative that they accurately represent the equilibrium between the gas and particle phases, which is contingent on various atmospheric conditions. For instance, humidity and temperature have been identified as pivotal factors in determining this equilibrium, while atmospheric acidity has been shown to play a crucial role in regulating partitioning processes (Ansari and Pandis, 2000; Guo et al., 2016; Pye et al., 2020). The complexity of the system is further compounded by the interaction of nitrate aerosols with other significant aerosol species, such as sea salt and mineral dust. The inclusion of these pathways is imperative for accurate predictions (Karydis et al., 2010; Karydis et al., 2016; Kakavas and Pandis, 2021). The intricate nature of nitrate aerosols often leads to discrepancies between model estimates and observations, with models frequently predicting higher mass concentrations. For instance, overestimations of approximately 2 $\mu g/m^3$ have been identified in Europe (Jones et al., 2021; Milousis et al., 2024), with biases reaching a factor of 5 or more in certain instances

(Chen et al., 2018). Analogous findings have been documented in the US (Walker et al., 2012; Zakoura and Pandis, 2018, 2019; Jones et al., 2021), while model projections in East Asia have been observed to exhibit amplified biases relative to other regions (Miao et al., 2020; Milousis et al., 2024), with Xie et al. (2022) noting that approximately 60% of studies modeling particle concentrations in China have overpredicted particulate nitrate levels. The potential causes of such biases can be categorized into several groups, encompassing a range of physicochemical processes and model characteristics.

A fundamental reason for discrepancies between model predictions and observations, as well as between predictions made by different models, is the grid resolution employed. A high spatial resolution (i.e., a substantial number of simulated grid cells with reduced size) facilitates the capture of chemical interactions that precursors undergo and their various removal processes with a high degree of precision. Conversely, a low spatial resolution may result in oversimplifications. It is important to note that the increased complexity of the representation is associated with higher computational costs. However, the use of high spatial resolution has been shown to reduce biases in predicted nitrate aerosol concentrations by 60-80% (Metzger et al., 2002; Zakoura and Pandis, 2018, 2019). Furthermore, Schaap et al. (2004) and Heald et al. (2012) posit that the employment of high resolution is, in certain instances, imperative to ensure the accurate comparison of model outcomes with observational data.

Another source of discrepancies between model and measurement results is the accuracy of the emission inventories in the model. Specifically in the case of nitrate aerosols, the presence of ammonia (NH_3) emissions is critical in determining their concentrations. In regions where there is an excess of ammonia, it forms ammonium nitrate (NH_4NO_3) after having neutralized sulfuric acid (H_2SO_4) and reacting with nitric acid (HNO_3) (Seinfeld and Pandis 2016). The primary sources of NH_3 emissions are associated with agricultural activities, and the accuracy of its representation in emission inventories is not always guaranteed (Nair and Yu, 2020). This is due to the influence of various factors. These include the variety of agricultural practices and management techniques used, as well as the land changes induced by agricultural activities in general (Sutton et al., 2013; Ge et al., 2020). These factors make it difficult to ensure consistent accuracy regarding NH_3 emissions. Additionally, the distinct characteristics of soil types and climates across different regions can substantially influence emission factors (Reis et al., 2009; Nair and Yu, 2020), a critical consideration in the development of a global inventory. For instance, Zhang et al. (2017) have highlighted that numerous prior NH_3 emission inventories in China employed emission factors determined for Europe. In addition, the diurnal and seasonal variability of NH_3 emissions must be considered in global inventories to ensure representability (Pinder et al., 2006; Hendriks et al., 2016). These considerations are equally relevant to the representation of other precursor gases, such as NOx and SO_2, which are also crucial for particulate nitrate formation.

The thermodynamic state of the aerosol is another factor that plays an important role in the accuracy of model predictions. Specifically, the assumption regarding the particle's ability to persist as a supersaturated aqueous solution throughout its lifetime (metastable conditions) or its potential to undergo deliquescence into a solid state as the ambient relative humidity declines (stable conditions) is of consequence. This assumption can lead to alterations in the aerosol's acidity, which, in turn, can influence the prediction of concentrations for species such as nitrate aerosols. These species are characterized as semi-volatile, and the partitioning to the aerosol phase is favored in more acidic conditions, and vice versa (Nenes et al., 2020). Previous studies have examined the impact of the thermodynamic state assumption on aerosol concentration predictions and have demonstrated that the choice is region-dependent. For instance, a stable state has been

shown to yield more realistic predictions when simulating arid and desert regions (Karydis et al., 2016). Furthermore, Fountoukis et al. (2009) and Karydis et al. (2010) found that stable thermodynamic conditions are more consistent with observations when the ambient relative humidity (RH) is below 50%. Conversely, Ansari and Pandis (2000) found that metastable thermodynamic conditions are more suitable for regions with intermediate relative humidity (RH) and low aerosol concentrations. However, no significant differences were observed between these two assumptions for high aerosol concentrations. Guo et al. (2016) determined that metastable thermodynamic conditions are more representative of areas exhibiting characteristics analogous to those observed in the Northeastern US. In contrast, Milousis et al. (2024) found minimal differences between the two assumptions for major inorganic pollutants (i.e., nitrate, sulfate, and ammonium aerosols, as well as mineral cations) on a global scale.

Another factor influencing model predictions of nitrate aerosols is the chemistry of dinitrogen pentoxide (N_2O_5), which is particularly important for the nocturnal production of nitrate particles. Specifically, N_2O_5, a compound derived from the oxidation of NOx species, undergoes heterogeneous hydrolysis on particle surfaces in the presence of sufficient amounts of water, resulting in the formation of HNO_3, a pivotal precursor of nitrate aerosols. This heterogeneous pathway has been shown to dominate the nighttime production of HNO_3, potentially accounting for up to 50% of particulate nitrate production in polluted areas during both winter (Liu et al., 2020) and summer (Qu et al., 2019). The hydrolysis reaction is predominantly governed by a corresponding uptake coefficient, with numerous models employing a single average value. However, the reaction exhibits a strong dependence on environmental quantities such as temperature and relative humidity. Consequently, some studies suggest the utilization of different values in models depending on the prevalent ambient conditions of the examined region. For instance, Wang et al. (2020) proposed a significantly lower value than the conventional value utilized in CCMs (0.02) to better align with conditions observed in Beijing. A similarly suggestion was made by Phillips et al. (2016) for semi-rural regions in Germany, with the intent of providing more precise estimates of particulate nitrate, and this is supported by a number of studies in various parts of the US as well (Bertram et al., 2009; Brown et al., 2009; Chang et al., 2011; Chang et al., 2016). The significance of N_2O_5 chemistry is particularly pronounced in regions exhibiting activities that contribute to elevated NOx concentrations. This effect is further exacerbated in areas characterized by intrusions of particles, such as mineral dust and/or sea salt, which facilitate heterogeneous reactions.

Furthermore, model predictions of nitrate aerosols can be strongly influenced by the model treatment of their wet deposition and, specifically, the manner in which cloud acidity affects the dissolution of HNO_3. Specifically, in less acidic conditions, elevated in-cloud dissolution of HNO_3 is observed to achieve overall electroneutrality, leading to increased particulate nitrate production (Seinfeld and Pandis, 2016; Tilgner et al., 2021). Consequently, it is imperative for a model to accurately represent in-cloud properties, as the nuances of pH conditions in regions with different characteristics will be more accurately captured. This, in turn, will facilitate a more comprehensive understanding of nitrate formation processes.

The present study aims to investigate the sensitivity of modelled nitrate aerosol predictions and how their modelled concentrations are influenced by a number of parameters on a global scale. To this purpose, the global atmospheric chemistry-climate model EMAC was employed, utilizing diverse configurations and parameterizations that encompass all the aforementioned aspects that influence the predictions of particulate nitrate concentrations. The model's performance was

evaluated against network and station observations of NO_3^- in the $PM_{2.5}$ and PM_1 size ranges, with the objective of identifying the parameters that are most significant over specific regions.

2. Methodology

2.1 Model setup

The model utilized in this study is the EMAC global chemistry and climate model (Jöckel et al., 2006). EMAC comprises a series of submodels, which are interconnected via the Modular Earth Submodel System (MESSy) (Jöckel et al., 2005) to the base (core) model, namely the fifth generation European Center Hamburg general circulation model (ECHAM5) (Roeckner et al., 2006). The gas phase chemistry is simulated by the submodel MECCA (Sander et al., 2019) with a simplified scheme similar to that used in the Chemistry Climate Model Initiative (CCMI), as described by Jöckel et al. (2016). The liquid phase chemistry is simulated by the submodel SCAV (Tost et al., 2006), which is also responsible for the wet deposition treatment of trace gases and aerosols. The submodel DRYDEP (Kerkweg et al., 2006b) addresses the dry deposition of trace gases and aerosols, while the submodel SEDI (Kerkweg et al., 2006b) handles the gravitational sedimentation of aerosols. The GMXe submodel (Pringle et al., 2010a; Pringle et al., 2010b) simulates aerosol microphysical processes and the gas-to-particle partitioning of inorganic species. For more detailed information on these particular processes, the reader is referred to Section 2.2. The ORACLE submodel (Tsimpidi et al., 2014; 2018) is responsible for simulating the composition and chemical evolution of all organic aerosol species. The microphysical processes of clouds are simulated by the CLOUD submodel (Roeckner et al., 2006), using the two-moment microphysical scheme for liquid and ice clouds of Lohmann and Ferrachat (2010), while considering a physically based treatment for the processes related to the activation of liquid droplets (Karydis et al., 2017) and ice crystals (Bacer et al., 2018). In this study, all simulations performed were nudged towards the actual meteorology using ERAI data (Dee et al., 2011), and concern the period 2009-2018, with the first year being used as the model spin-up period.

The spatial resolution used in all simulations, except for the sensitivity cases (Section 2.3), corresponds to T63L31, which has a grid resolution of $1.875^o \, x \, 1.875^o$ and covers vertical altitudes up to 25 km, divided into 31 layers. The database of anthropogenic emissions in terms of aerosols and their precursors, utilized by all simulations with the exception of the sensitivity cases where modifications were made (see Section 2.3), was derived from the CAMS inventory (Inness et al., 2019). The database pertaining to biomass burning emissions was derived from the GFEDv4.1 database (Randerson et al., 2017). The natural emissions of NH_3, originating from soil and oceanic volatilization, were obtained from the GEIA database (Bouwman et al., 1997). The biogenic soil emissions of NO were calculated online during runtime using the algorithm of Yienger and Levy (1995). Lightning production of NOx is also calculated online by the LNOx submodel (Tost et al., 2007a) based on the parameterization of Grewe et al. (2001). The emissions of SO_2 from volcanic eruptions are obtained from the AEROCOM database (Dentener et al., 2006). Sea salt emissions are calculated online according to the parameterization of Guelle et al. (2001), which utilizes precalculated lookup tables to determine the wind speed-dependent mass and particle number fluxes for the accumulation and coarse mode sizes, which applies for sea salt aerosols. For more detailed information on the calculation of the lookup tables, the reader is referred to Stier et al. (2005) and Kerkweg et al. (2006a). The AIRSEA submodel (Pozzer et al., 2006) calculates oceanic emissions of dimethyl sulfide (DMS) online. Additionally, dust emission fluxes are calculated online using the parameterization of Astitha et al. (2012). This method

considers both the meteorological information of each grid cell (temperature and relative humidity) and the various friction velocity thresholds above which dust particle suspension occurs. The mineral dust composition is determined by the bulk composition, and the mineral ions Na^+, Ca^{2+}, K^+ and Mg^{2+} are estimated as a fraction of the total dust emission flux based on the chemical composition of the soil in each grid cell (Karydis et al., 2016; Klingmüller et al., 2018).

2.2 Inorganic aerosol partitioning

In this study, all calculations related to the thermodynamics of inorganic aerosols, as well as their partitioning process, are performed by ISORROPIA II v2.3 (Fountoukis and Nenes, 2007), which is a thermodynamic module integrated into the GMXe submodel. ISORROPIA II v2.3 treats the chemical system of K^+–Ca^{2+}–Mg^{2+}–NH_4^+–Na^+–SO_4^{2-}–NO_3^-–Cl^-–H_2O aerosols and has the ability to simulate either a stable thermodynamic state, where aerosols are allowed to precipitate into solid salts, or a metastable state, where aerosols remain in a supersaturated aqueous solution even at low relative humidities. The initial case is employed as the fundamental assumption of this study, along with all other sensitivity simulations, with the exception of one (Section 2.3). ISORROPIA II v2.3 is a slightly updated version of ISORROPIA II that concerns more accurate predictions of aerosol pH near neutral conditions (Song et al., 2018). Nevertheless, its impact is confined to a limited subset of calculations within the diverse compositional sub-regimes of ISORROPIA II. Specifically, in certain instances, NH_3 evaporation was not taken into account in the aerosol pH calculations, resulting in values that approached neutrality. However, this had a negligible effect on both the predicted NH_3 and the inorganic aerosol concentrations. The ISORROPIA II v2.3 model utilizes Bromley's formula (Bromley, 1973) to calculate the binary activity coefficients for multicomponent mixtures. For specific component pairs, it employs the Kusik-Meissner relationship (Kusik and Meissner, 1978), which incorporates the temperature dependence of Meissner and Peppas (1973). Further insights can be found in the study by Fountoukis and Nenes (2007).

In the GMXe submodel, aerosol size is described by seven lognormal size modes, four of which are assigned to a soluble fraction and the remaining three to an insoluble fraction. The soluble fraction includes the nucleation, Aitken, accumulation, and coarse size modes, while the insoluble fraction includes only the latter three (Pringle et al., 2010a, 2010b). In the aerosol partitioning process, kinetic limitations must be considered, as only sizes smaller than coarse mode can reach equilibrium within the timeframe of one model time step (10 minutes for this study). Consequently, the partitioning calculations are performed in two stages. Initially, the amount of gas phase species that can kinetically condense to the particle phase within this timeframe is calculated according to the diffusion limited condensation theory of Vignati et al. (2004). Subsequently, the partitioning between the gas and particle phases is estimated by assuming instantaneous equilibrium for all aerosol size modes, as the ISORROPIA II v2.3 routines are called separately for each one. Finally, the transfer of material between the soluble and insoluble modes is calculated by GMXe after the partitioning calculations have been completed. This transfer can occur in two ways: by coagulation, where two particles of different modes collide and the resulting particle is in the soluble mode; or if substantial soluble material has condensed onto an insoluble particle when it is transferred back to the soluble mode (Pringle et al., 2010a, 2010b).

2.3 Sensitivity configuration details

A total of eight simulations were performed (base case and seven sensitivity cases) in an attempt to cover all aspects that influence the model predictions of particulate nitrate concentrations, as discussed in Section 1, and whose configurations are summarized in Table 1. The objective is to

ascertain whether a specific configuration can most accurately replicate the measurements of $PM_{2.5}$ and PM_1 concentrations in the most heavily polluted regions of the globe. The base case simulation was performed using the following combination of configurations. A T63L31 spatial resolution ($1.875^o\ x\ 1.875^o$ grid) with anthropogenic emissions provided by the CAMS database is used. The aerosols' thermodynamic state was assumed to be stable, i.e., it was permitted to precipitate into solid salts at low relative humidity (RH). Aerosol scavenging is addressed by a comprehensive mechanism encompassing over 150 chemical reactions for the liquid phase, in addition to the online calculation of the in-cloud and precipitation pH (Tost et al., 2006, 2007b). The uptake coefficient of N_2O_5 hydrolysis is 0.02 according to the parameterization proposed by Evans and Jacob (2005).

In the initial two sensitivity model iterations ('RES_low' and 'RES_high'), the sole modification implemented was an alteration in the spatial grid resolution. This alteration involved the adoption of a lower resolution, characterized by a reduction in the number of grid cells, and a higher resolution, marked by an increase in the number of grid cells. Notably, the vertical resolution was maintained at 31 layers, consistent with the base case. The lower spatial resolution is the T42L31 resolution, which corresponds to a $2.813^o\ x\ 2.813^o$ grid and the higher spatial resolution is the T106L31 resolution, which corresponds to a $1.125^o\ x\ 1.125^o$ grid. The other two sensitivity model runs ('CMIP' and 'HTAP') employed distinct emission inventories with regard to anthropogenic emissions of aerosols and trace gases, yet utilized the grid resolution of the base case. Specifically, the CMIP6 model run utilized the CMIP6 database (O'Neill et al., 2016), while the HTAP model run employed the HTAPv3 database (Crippa et al., 2023).

An additional sensitivity model run was performed in which the thermodynamic state of the aerosol was altered ('THERM'). In this run, the metastable assumption was implemented, meaning aerosols are prevented from forming solids, even at extremely low RH values, allowing them to persist in a supersaturated aqueous phase. Additionally, a sensitivity model run was conducted in which the scavenging treatment was modified ('SCAV'), employing a simplified mechanism where the gas-to-particle phase partitioning follows the effective Henry's Law coefficients approach. Furthermore, no aqueous phase chemistry was considered in the calculation of cloud acidity, as a constant value of 5 was assumed for in-cloud and precipitation pH (Tost et al., 2007b). Another sensitivity model run ('HYDRO') concerns the treatment of the uptake of N_2O_5 hydrolysis, and more specifically the uptake coefficient considered. Specifically, an uptake coefficient for hydrolysis of 0.002 was employed (one order of magnitude lower than in the base case) in an attempt to obtain more accurate predictions in certain regions (Section 1).

Table 1: Configurations used in the base case and all sensitivity simulations.

Simulation Name	Spatial Resolution			Anthropogenic Emissions			Thermodynamic State		Scavenging Treatment		N_2O_5 Uptake Coefficient	
	T42	T63	T106	CAMS	CMIP6	HTAP	Stable	Metast.	Simple	Complex	0.02	0.002
Base Case		X		X			X			X	X	
RES_low	X			X			X			X	X	
RES_high			X	X			X			X	X	
CMIP6		X			X		X			X	X	
HTAP		X				X	X			X	X	
THERM		X		X				X		X	X	
SCAV		X		X			X		X		X	
HYDRO		X		X			X			X		X

3. Evaluation of the Base Case Predictions for particulate NO_3^-

3.1 Surface concentrations and $PM_{2.5}$ size fraction

The mean surface concentrations of $PM_{2.5}$, NO_3^-, and the size fraction of $PM_{2.5}$ NO_3^- (i.e., the fraction of $PM_{2.5}$ NO_3^- mass in respect to the total aerosol NO_3^- mass) are shown in Figure 1 for the entire period from 2010 to 2018. The maximum values of 14 µg/m3 are predicted over the Indian subcontinent and the East Asian region, with Central Europe showing concentrations of ~5 µg/m^3 for the period average, while Turkey and Eastern USA show mostly concentrations of ~3 µg/m^3 (Fig. 1a). With respect to the size fraction, $PM_{2.5}$ accounts for more than 80% of the total particle

concentration over the polluted northern hemisphere and up to 70% over South America, the southern part of Africa, and Australia (Fig. 1b). The $PM_{2.5}$ size fraction also demonstrates a 60% contribution attributable to interactions of particulate nitrate with mineral dust particles originating from the Sahara and the dust outflow directed towards South America. A 30% contribution is also observed over the Southern Ocean due to interactions of particulate nitrate with sea salt particles. The Arabian Peninsula region exhibits the lowest predicted NO_3^- $PM_{2.5}$ fraction, with a value of less than 20%.

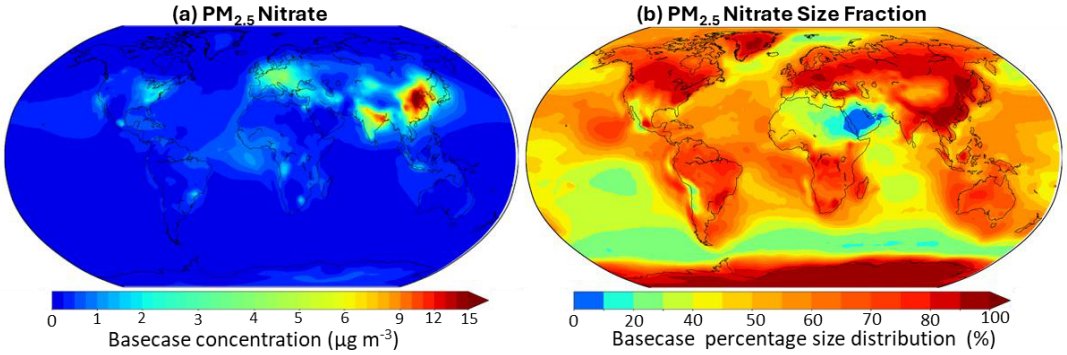

Figure 1: Annual mean (a) surface concentrations and (b) size fraction of $PM_{2.5}$ NO_3^- for the period 2010 – 2018 as simulated with EMAC from the base case.

3.2 Comparison of base case model results with $PM_{2.5}$ observations

The $PM_{2.5}$ aerosol observations are obtained from four networks that cover regions with the highest levels of anthropogenic activity in the polluted northern hemisphere. These networks include the EPA CASTNET network (U.S. Environmental Protection Agency Clean Air Status and Trends Network) and the IMPROVE network (Interagency Monitoring of Protected Visual Environments), which collectively encompass 152 stations for particulate nitrate across the United States. Notably, IMPROVE predominantly focuses on rural and remote regions, while EPA primarily covers urban areas. The EMEP network (European Monitoring and Evaluation Programme Air Pollutant Monitoring Data) includes nine stations for particulate nitrate, covering the European region. Additionally, the EANET network (The Acid Deposition Monitoring Network in East Asia) covers parts of East Asia with 33 stations. The locations of all stations can be found in Figure S1a. The aforementioned networks provide monthly measurements for the entire period under consideration in this study. Given the continuous nature of $PM_{2.5}$ measurements, a comparison with model predictions is presented in the form of surface concentration maps, where the observations from each station are overlaid on the model concentration maps (see Figure 2). A comparison in the form of scatter plots of seasonal means can be found in Figure S2. The seasonal statistical evaluation for the comparison of $PM_{2.5}$ nitrate is shown in Table 2. The metrics employed include Mean Absolute Gross Error (MAGE), Mean Bias (MB), Normalized Mean Error (NME), Normalized Mean Bias (NMB), and Root Mean Square Error (RMSE).

As illustrated in Figure 2a, the model demonstrates a notable capacity for reproducing the measurements for the majority of stations in the USA, particularly those situated in the Midwestern

region and along the Southern East Coast. However, discrepancies of approximately 1 μg/m^3 (model overprediction) are evident over the Central East stations, and discrepancies of approximately 2 μg/m^3 are observed for the larger areas of New York and Northern California. In Europe, the model's overprediction of low concentrations is evident in the Iberian Peninsula, the Baltic region, and Croatia (~3 μg/m^3 difference), while it more accurately represents the high concentrations observed in the UK and the Central and Western regions, with some exceptions in Germany and Switzerland (Fig. 3b). In East Asia, the discrepancy between model predictions and observations is particularly pronounced. The model values for the North China Plain, Japan, Vietnam, and Thailand exceed the observed concentrations by up to 2 μg/m^3, similar to the overprediction observed in Europe. However, the model values for Korea are three times higher than the observed concentrations (Fig. 3c). Conversely, the concentrations in the Zhangzhou region were underpredicted by the model, with discrepancies reaching up to 5 μg/m^3.

Statistically, the USA region demonstrates the most optimal model representation exhibiting differences to network observations that are less than 1 μg/m^3 across all seasons. However, elevated normalized error values were observed during the summer and autumn periods. While the model demonstrates higher overpredictions for East Asia, the mean bias and normalized error values appear to be relatively unaffected. However, the mean gross error and root square error metrics are notably larger compared to those observed for the USA. Notably, Europe exhibits the most significant discrepancies between model predictions and observations, with a mean bias exceeding 1 μg/m^3 and normalized error values particularly pronounced during the warm spring and summer periods, which are typically associated with low nitrate concentrations.

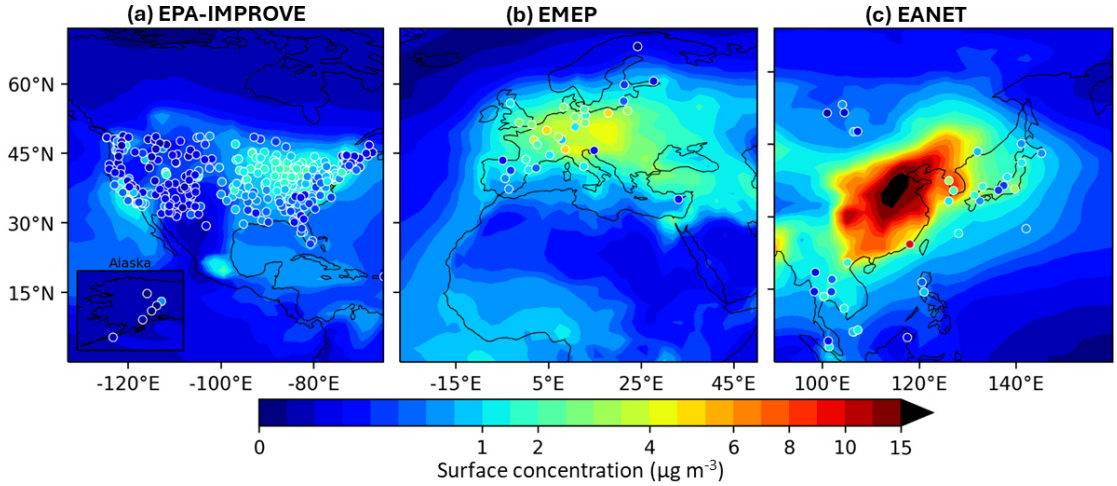

Figure 2: Annual mean surface concentrations of $PM_{2.5}$ NO_3^- for the period 2010 – 2018 as simulated by EMAC from the base case (shaded contours) versus observations of the same species from the (a) EPA-IMPROVE, (b) EMEP and (c) EANET networks (colored circles).

Table 2: Seasonal statistical evaluation of EMAC values for $PM_{2.5}$ NO_3^- surface concentrations from the base case against observations during 2010-2018. The used metrics include the Mean Absolute Gross Error (MAGE), Mean Bias (MB), Normalized Mean Error (NME), Normalized Mean Bias (NMB) and Root Mean Square Error (RMSE).

Network	Season	Number of datasets	Mean Observed (μg m^{-3})	Mean Predicted (μg m^{-3})	MAGE (μg m^{-3})	MB (μg m^{-3})	NME (%)	NMB (%)	RMSE (μg m^{-3})
EPA	Winter	144	2.8	2.4	1.4	-0.5	50	-16	2.2
	Spring	291	1.4	2.2	1.2	0.8	87	54	1.5
	Summer	280	0.5	0.8	0.5	0.3	103	59	0.9
	Autumn	290	0.7	0.9	0.6	0.2	89	37	0.9
IMPROVE	Winter	116	0.8	1.2	0.7	0.4	80	48	0.9
	Spring	233	0.5	1.1	0.7	0.6	131	112	0.9
	Summer	193	0.2	0.4	0.3	0.2	155	123	0.5
	Autumn	214	0.2	0.4	0.3	0.2	143	99	0.5
EMEP	Winter	7	3.4	3.9	2.5	0.6	74	16	3.3
	Spring	18	1.6	2.8	1.6	1.2	96	73	2.1
	Summer	18	0.3	1.5	1.3	1.2	461	451	1.8
	Autumn	17	0.8	2.7	1.9	1.9	241	233	2.8
EANET	Winter	30	2.0	2.5	1.6	0.4	80	21	2.6
	Spring	59	1.9	2.0	1.6	0.1	87	8	2.9
	Summer	59	0.6	1.6	1.4	0.9	217	147	2.6
	Autumn	59	0.8	0.8	0.7	0.0	85	3	1.1

3.3 Comparison of base case model results with PM_1 observations

The aerosol observations of PM_1 are derived from AMS measurements obtained during field campaigns in the Northern Hemisphere from 2010 to 2018. The measurement durations of these campaigns ranged from one to six months and encompassed rural, urban, and downwind locations. The campaign and types of locations can be seen in Figure S1b. Further details regarding the locations of the field campaigns, including their duration, can be found in Tsimpidi et al. (2016; 2024). As the field observations (in contrast to the network measurements) are not continuous but rather fragmented into different time periods for each field campaign location, the comparison is presented in the form of scatter plots that compare the model and the measured values depending on the location type (see Figure 3). A scatter plot comparison of the seasonal means is shown in Figure S3. The statistical evaluation involves the regions of the USA, East Asia, Europe, and India, employing the same metrics as previously outlined. The results are presented in Table 3.

As illustrated in Figure 3a, the model demonstrates a notable capacity to replicate the average PM_1 values over Europe with a high degree of accuracy, exhibiting an average bias of up to 50%,

despite manifesting substantial variations at specific locations. In North America, the observed underprediction of average values is slightly stronger for downwind and particularly for rural locations (Fig. 3b) with average values for urban sites showing better agreement. In East Asia, the model demonstrates a comparable degree of accuracy to that observed in Europe, although it exhibits a significantly lower prevalence of outliers (Fig. 3c). However, the average downwind values in this region exhibit an overprediction of slightly more than 50%. In India, the model's estimation of average urban values aligns closely with measurements, while the model significantly overestimates average rural values by a factor of 4 (Fig. 3d).

In contrast to the comparison of $PM_{2.5}$ concentrations, the majority of the metrics indicate that PM_1 aerosol observations in Europe are better reproduced. Conversely, the USA exhibited low mean bias values and high scatter, as evidenced by normalized bias and error metrics. Conversely, East Asia exhibits higher absolute differences. The model demonstrates suboptimal performance for India, particularly in rural areas where there is a substantial discrepancy between the modeled and observed values. Conversely, the model demonstrates a higher degree of accuracy in predicting PM_1 concentrations in both rural and urban locations as compared to downwind areas.

Table 3: Statistical evaluation of EMAC predicted PM_1 NO_3^- surface concentrations from the base case against observations during 2010-2018. The used metrics include the Mean Absolute Gross Error (MAGE), Mean Bias (MB), Normalized Mean Error (NME), Normalized Mean Bias (NMB) and Root Mean Square Error (RMSE).

Region	Type of location	Number of datasets	Mean Observed (μg m^{-3})	Mean Predicted (μg m^{-3})	MAGE (μg m^{-3})	MB (μg m^{-3})	NME (%)	NMB (%)	RMSE (μg m^{-3})
USA	Rural	31	1.1	0.7	1.0	-0.5	88	-42	1.5
	Urban	22	1.5	1.8	1.6	0.4	111	25	2.1
	Downwind	5	1.2	0.8	1.1	-0.5	87	-36	1.7
East Asia	Rural	40	6.8	7.8	4.7	1.0	68	15	6.0
	Urban	78	9.7	10.3	4.0	0.6	41	6	5.2
	Downwind	15	4.9	7.9	3.5	3.0	71	61	5.2
Europe	Rural	163	1.4	1.4	0.9	0.0	62	1	1.4
	Urban	28	1.8	1.5	1.0	-0.2	54	-13	1.5
	Downwind	99	3.2	2.4	1.5	-0.7	48	-23	2.2
India	Rural	5	0.4	2.1	1.8	1.7	439	412	2.6
	Urban	14	8.2	7.8	4.0	-0.4	49	-5	5.2

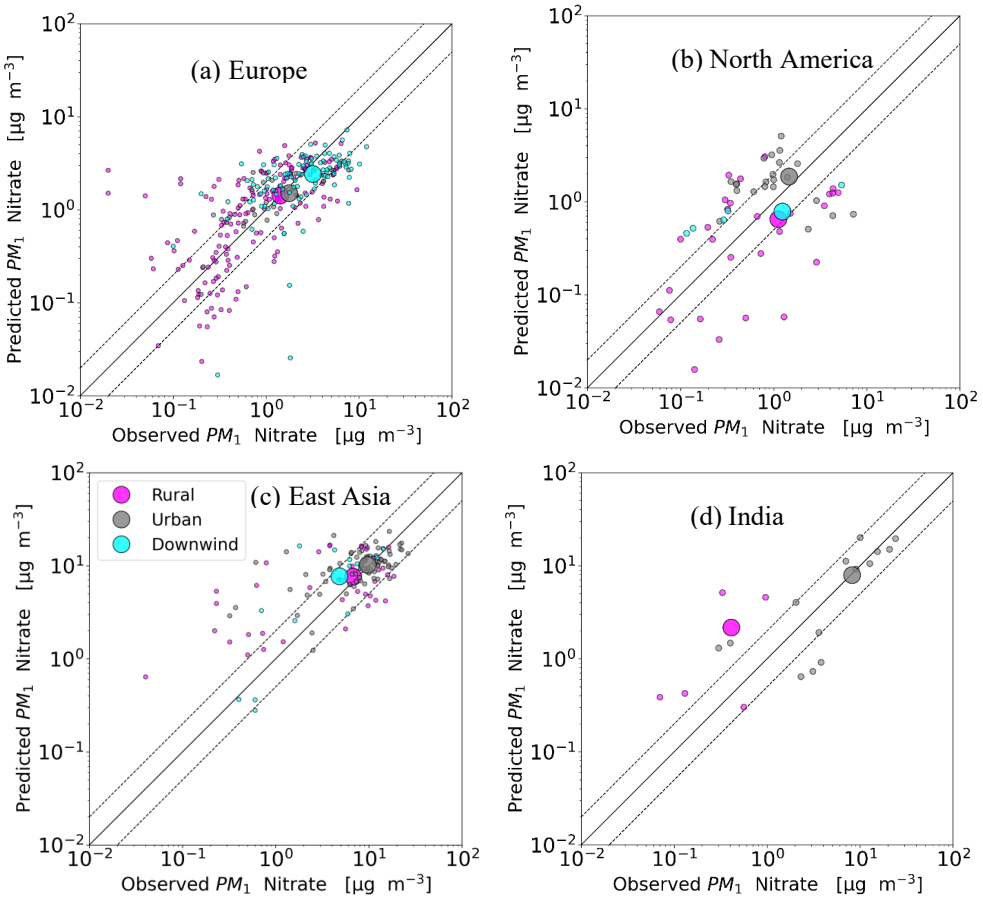

Figure 3: Scatterplots comparing mean surface concentrations of PM_1 NO_3^- as simulated by EMAC from the base case and AMS observations in campaigns in the regions of (a) Europe, (b) North America, (c) East Asia and (d) India. Enlarged dots indicate the 2008 – 2018 period averages from all locations. Also shown are the 1:1 lines (solid) as well as the 2:1 and 1:2 lines (dashed).

4. Differences between $PM_{2.5}$ and PM_1 NO_3^- concentrations in the sensitivity model runs

The differences in the predicted surface $PM_{2.5}$ nitrate concentrations across the sensitivity simulations in comparison to the base case, are illustrated in Figure 4. Furthermore, a comparison for $PM_{2.5}$ concentrations across different seasons can be seen in Figure 5 and a comparison of PM_1 concentrations for the different types of measurements sites in Figure 6, with detailed statistical metrics provided in Tables S1–S14.

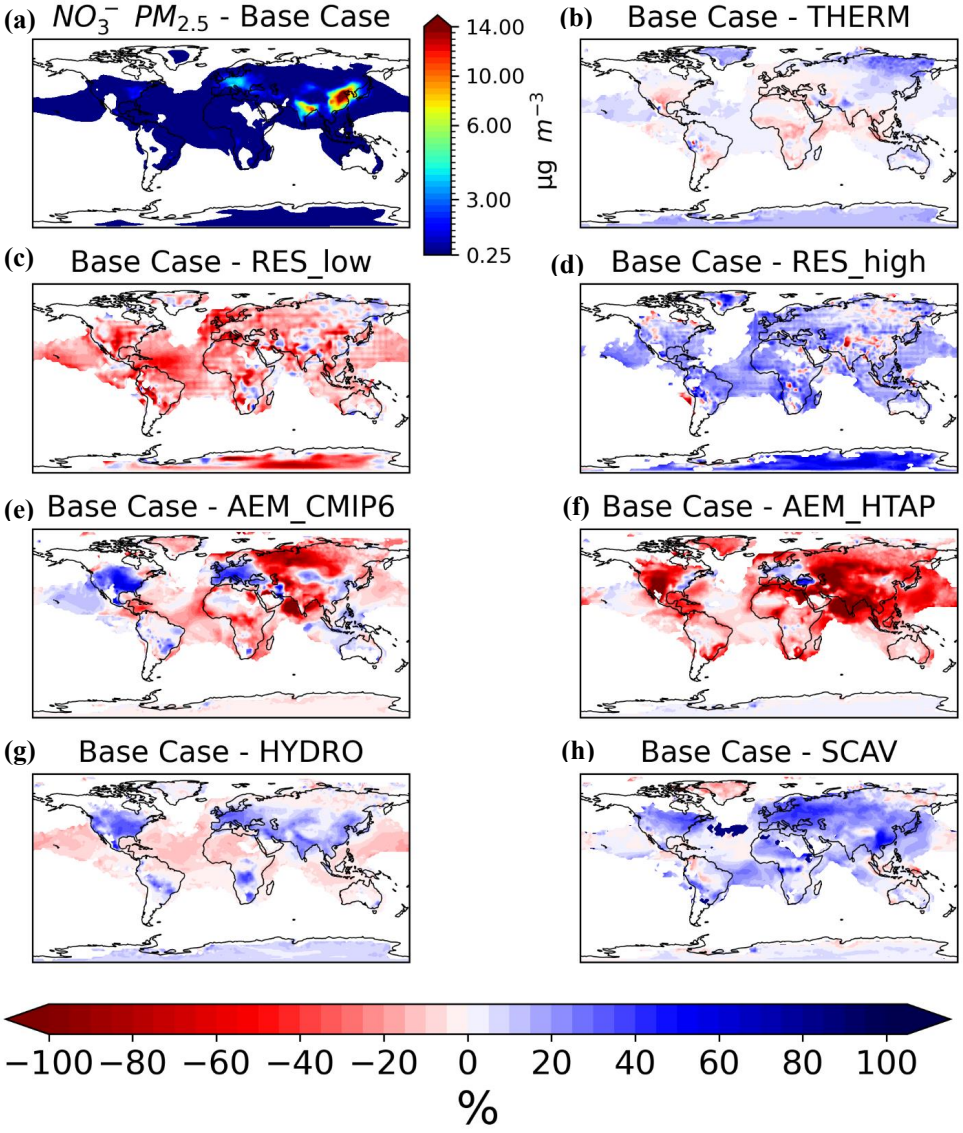

436 **Figure 4:** (a) Average surface concentrations of $PM_{2.5}$ NO_3^- for the period of 2008 – 2018 as
437 simulated by EMAC from the base case. White areas indicate average concentrations smaller than
438 0.25 µg/m^3 . Percentage changes of the EMAC-simulated average surface concentrations of $PM_{2.5}$
439 NO_3^- between the base case model run and the (b) 'THERM' case (c) 'RES_low' case, (d)
440 'RES_high' case, (e) 'CMIP' case, (f) 'HTAP' case, (g) 'HYDRO' case and (h) 'SCAV' case

model runs. Negative values in red indicate higher concentrations by the respective sensitivity case and positive values in blue indicate the opposite.

4.1 Sensitivity to the model spatial resolution

Lower Grid Resolution: Employing a coarser grid resolution generally predicts higher surface $PM_{2.5}$ nitrate concentrations than the base case (Fig. 4c). The most substantial disparities (reaching up to 80%) are evident in North America, followed by Europe (~30%). In East Asia, changes are more localized, with some areas exhibiting up to 15% lower values, while the Himalayan Plateau in India shows reductions of approximately 50%.

When evaluated against observational datasets, the 'RES_low' model run demonstrates a strong capacity for reproducing mean winter and spring nitrate concentrations in Europe, where nitrate levels typically peak during these seasons (Fig. 5). However, the model significantly overestimates summer and autumn concentrations, with biases reaching factors of 3 to 4 for EMEP observations. In North America, this model consistently overestimates nitrate levels, particularly during the warmer seasons, although winter concentrations are more in line with EPA observations. Conversely, the model's estimates for $PM_{2.5}$ nitrate levels in the IMPROVE network are elevated by up to threefold, exhibiting comparable overestimations to those observed in EANET data. According to the statistical metrics, the 'RES_low' model run does not outperform the base case, indicating that a coarser grid resolution does not increase the model's estimation accuracy.

For PM_1 nitrate concentrations, the 'RES_low' case slightly overpredicts rural values in Europe by approximately 13%, while urban values are slightly underpredicted (Fig. 6). At downwind locations, the underprediction is more pronounced, reaching around 25%. In North America, this tendency is nearly reversed, with rural sites exhibiting a substantial underprediction (~30%) and urban sites demonstrating an overprediction (~20%). Notably, downwind locations in this region are best represented by the 'RES_low' sensitivity model run. In East Asia, the 'RES_low' case shows very similar rural values to the base case, while urban sites display a moderate underprediction (~15%). However, at downwind locations, concentrations are significantly overpredicted, with nearly twice as high values as the observed values. In India, the 'RES_low' case exhibits a contrasting pattern. In this case, concentrations in rural areas are overpredicted, similar to the base case results, while concentrations in urban areas show the largest underprediction among all sensitivity model runs, with concentrations being approximately a factor of 2.5 lower. Statistically, the 'RES_low' case exhibits a marginal enhancement in accuracy for rural locations in North America and East Asia. However, it does not exceed the accuracy of the base case for Europe or India.

Higher Grid Resolution: Conversely, simulations employing a higher grid resolution have yielded reduced surface $PM_{2.5}$ nitrate concentrations in comparison to the base case (Fig. 4d). The disparities in nitrate concentrations can reach up to 50% across North America, Europe, and India, with less consistent patterns observed in East Asia.

A comparison of the 'RES_high' model run with the EMEP observations reveals that it underpredicts nitrate concentrations in winter and spring by approximately 20%, while demonstrating greater accuracy in summer and autumn, reducing the overestimation compared to the base case (Fig. 5). A similar pattern is observed in the prediction of EPA observations, with more accurate forecasts in most seasons, except in winter, where slight underestimations occur. For the IMPROVE network, the 'RES_high' model run demonstrates the strongest agreement with observations during summer, though its performance varies across other seasons.

For PM_1 nitrate, the 'RES_high' scenario reveals a modest underprediction across all European location types, with the most substantial discrepancy observed at downwind sites (~33%). In North America, rural and downwind sites exhibit a more pronounced underprediction, reaching up to a factor of 2, while urban locations show a modest overprediction (~12%). Conversely, the results for East Asia exhibit an opposing pattern, with all location types demonstrating a slight overprediction, particularly evident at downwind sites (~factor of 2). In India, the urban locations estimates by this sensitivity align closely with the base case results, while rural sites demonstrate a marginally higher overprediction. Statistically, the 'RES_high' case enhances the accuracy of model predictions for urban sites in North America and Europe while also improving rural predictions in East Asia, underscoring its effectiveness in capturing finer spatial variability.

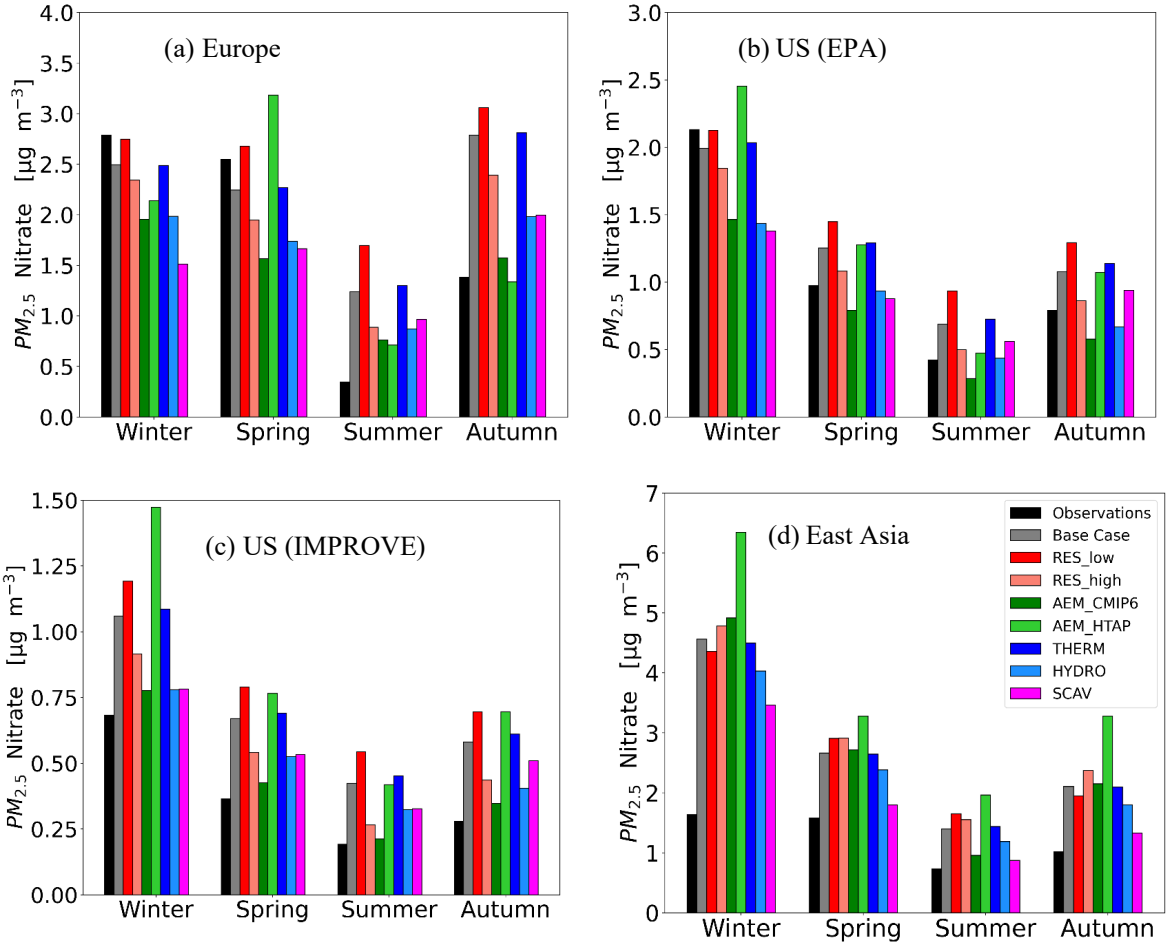

Figure 5: Average seasonal surface concentrations of $PM_{2.5}$ NO_3^- measured and predicted from the base case and all sensitivity cases for the networks of (a) EMEP, (b) EPA, (c) IMPROVE and (d) EANET during winter, spring, summer and autumn.

4.2 Sensitivity to anthropogenic emission inventories

CMIP6: The application of the CMIP6 anthropogenic emission inventory to the simulation of surface $PM_{2.5}$ nitrate concentrations reveals a pattern of lower concentrations in most regions, with the exception of India (Fig. 4e). The most significant reductions in surface $PM_{2.5}$ nitrate concentrations are observed in North America and Europe, with a range of 50% to 60%. In contrast, East Asia exhibits a comparatively smaller reduction, ranging from 10% to 20%. Conversely, India exhibits an increase in $PM_{2.5}$ nitrate levels ranging from 30% to 40%.

A comparison with observations reveals notable discrepancies (Fig. 5). For EMEP observations, the 'CMIP' model run underestimates winter and spring concentrations by up to 40%, while overestimating summer values (by twofold), although autumn values are well captured. For EPA observations, this case underestimates in all seasons except winter, yielding the lowest $PM_{2.5}$ nitrate predictions among all cases. Of particular interest is the observation that the underestimation during most seasons is analogous to the overestimation seen in the 'RES_high' case. In contrast, IMPROVE observations exhibited more precise model predictions, characterized by minor positive biases (less than 10%). In comparison, the IMPROVE observations exhibited minor positive biases (less than 10%), with summer values demonstrating enhancement over the base case. Conversely, EANET observations displayed overprediction tendencies in other seasons, aligning closely with the outcomes of the base case. Statistically, the 'CMIP' case demonstrates greater efficacy than the base case for most observational networks, with the exception of EANET, where comparable outputs are obtained.

A comparison of the 'CMIP' model run with observations of PM_1 nitrate concentrations measured by AMS instruments in field campaigns reveals the largest underprediction of all sensitivity model runs for all location types in Europe, with downwind sites exhibiting notable discrepancies (~factor of 2). A similar pattern is observed in North America, where rural sites show differences as high as 80%. In contrast, observations in East Asia are more closely aligned with this case. The observations from rural sites exhibited the strongest agreement with the model, while urban sites demonstrated a slight underprediction of less than 10%. In contrast, downwind locations demonstrate a moderate overprediction of approximately 25%. In India, the 'CMIP' simulation results in an overprediction of observations of around 20% in urban areas, with values in rural areas showing an even greater discrepancy, reaching approximately a factor of 10. Statistically, this particular case exhibits suboptimal performance in comparison to the base case for Europe and India. However, it demonstrates enhanced performance in East Asia and the USA, particularly for metrics other than MB and NMB.

HTAP: The simulation using the HTAPv3 anthropogenic emission inventory generally predicts higher $PM_{2.5}$ nitrate concentrations than the base case (Fig. 4f). Notably, Europe and the eastern United States constitute exceptions, exhibiting 20–30% lower concentrations compared to the base case model. In other regions, particularly western North America and India, the predicted concentrations are up to 100% higher than in the base case model, with values in East Asia showing increases of 60–80%.

A comparison of the model results with observations reveals significant variations. For EMEP observations, the 'HTAP' model run underestimates values in winter, similar to the 'CMIP' case, and overestimates concentrations in summer. Notably, the 'HTAP' model run exhibits the most

significant underestimation in spring, reaching approximately 60%. However, the model's performance is satisfactory in the autumn. In contrast, comparisons to EPA observations demonstrate a consistent overestimation in all seasons, contrasting with the results of the 'CMIP' case. A similar overestimation of values is observed when comparing the 'HTAP' simulation results to the IMPROVE data, particularly in winter, and this is consistent with the results of the 'RES_low' model run. For EANET observations, the 'HTAP' sensitivity demonstrates a high degree of overprediction of values, ranging from a factor of 2 in spring and summer to a factor of 4 in winter. From a statistical perspective, the 'HTAP' model run demonstrates stronger performance in comparison to the base case simulation for EMEP observations during summer and autumn, while model predictions are less accurate in winter and spring. Slight enhancements are evident for EPA observations, while the model's performance is suboptimal for IMPROVE observations, particularly for EANET observations.

When evaluated against PM_1 nitrate concentrations measured by AMS instruments in field campaigns, the 'HTAP' case demonstrates a 20% underprediction of values in rural sites in Europe, despite the fact that this particular sensitivity best captured average urban values among all others. However, in downwind locations, the model underpredicts concentrations by nearly 40%. The 'HTAP' model run demonstrates a notable degree of alignment with observations in North America, exhibiting the strongest agreement with measurements in both rural and urban locations. Conversely, in downwind locations, the model values are considerably lower than observations, akin to the base case estimates, exhibiting a model-measurement discrepancy of nearly 50%. In contrast, the modeling of observations in East Asia appears to be a challenging endeavor for this particular sensitivity model run, as predicted values show the highest overprediction among all model cases for all location types. The results for downwind sites exhibit a distinct overprediction of almost a factor of 2, while results for other locations show discrepancies of less than 20%. In India, concentrations as predicted by the 'HTAP' case demonstrate a substantial overprediction for both urban and rural locations, and the most significant model-measurement discrepancies among all sensitivity model runs. In rural areas, the overprediction can reach up to a factor of 15, while in urban areas, the predicted concentrations are approximately double the observed values. Statistically, the 'HTAP' case exhibits suboptimal performance relative to the base case in East Asia and India. However, it does yield enhanced predictions for rural sites in the USA and Europe, with the exception of downwind locations.

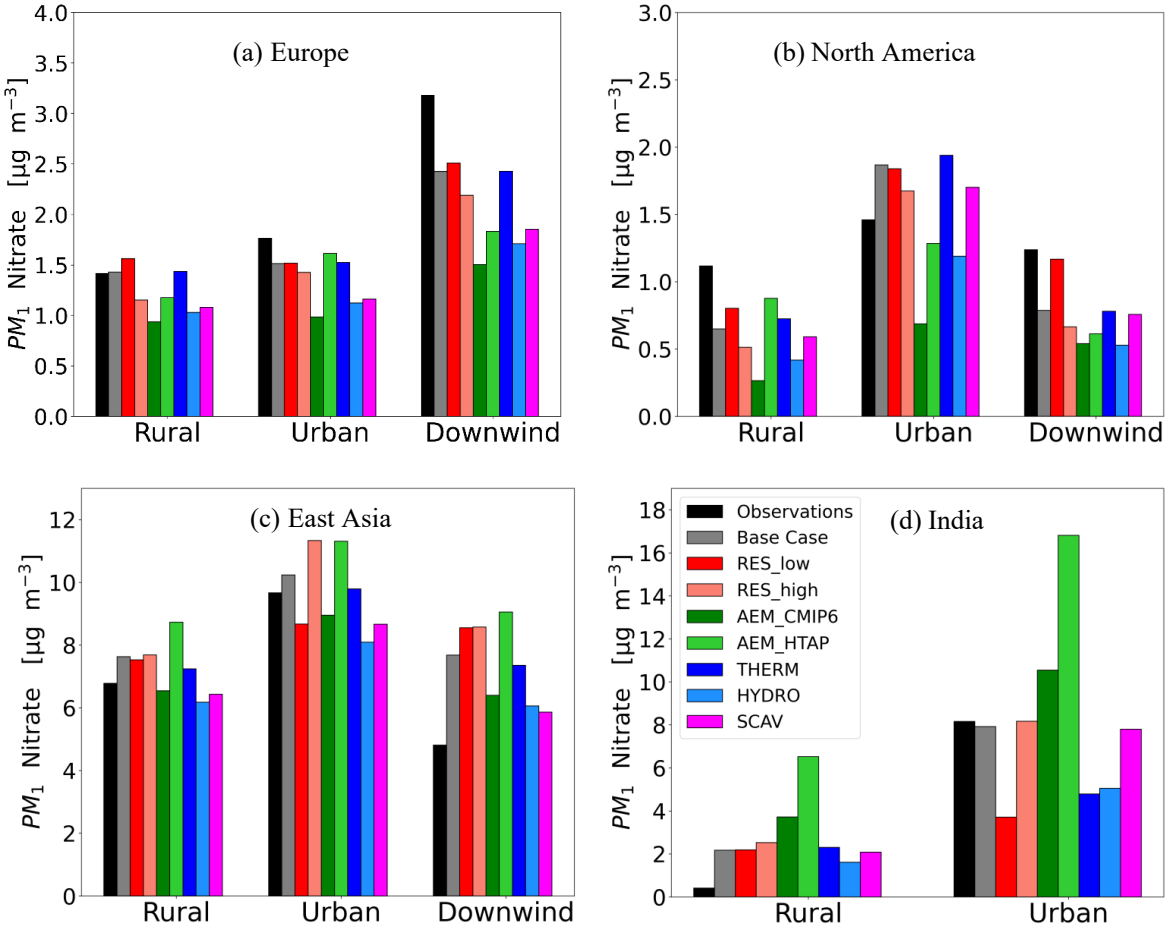

Figure 6: Average PM_1 NO_3^- surface concentrations measured by AMS instruments in field campaigns and predicted by the base case and all sensitivity cases for the regions of (a) Europe, (b) North America, (c) East Asia and (d) India divided into rural, urban and downwind locations.

4.3 Sensitivity to the model treatment of the aerosol thermodynamic state and chemistry

Metastable state: The simulation assuming a metastable thermodynamic state (aerosols do not precipitate into solid salts at low-humidity) indicates only minor discrepancies in surface $PM_{2.5}$ nitrate concentrations compared to the base case (Fig. 4b). Concentrations exhibit a 10–15% increase in North America and Europe, while in the Himalayan Plateau, they decrease by up to 30%, and in East Asia, they are slightly lower.

When evaluated against $PM_{2.5}$ observations, the 'THERM' case model run demonstrates a high degree of similarity to the base case model across all observational networks. However, slightly less accurate predictions (differences <5%) are observed for the EPA and IMPROVE networks, as reflected in the statistically insignificant differences between the metrics derived for the sensitivity and base case model runs.

For observations of PM_1 nitrate concentrations, the 'THERM' sensitivity results are nearly identical to the base case model run in Europe and North America for all location types. A similar behavior is observed in East Asia, where the 'THERM' case overpredicts observed concentrations by approximately 5% compared to the base case model run for all locations. In India, the 'THERM' and base case results show no difference in rural areas, but values are underpredicted by about 40% in urban areas due to the use of the metastable state assumption. This discrepancy is associated with the combination of moderate temperatures and low relative humidity at these locations, which hinder the partitioning of nitrate into the aerosol phase (Ansari and Pandis, 2000; Milousis et al., 2024). These factors contribute to the model-measurement discrepancies, particularly in urban areas with elevated nitrate aerosol concentrations. Statistically, this particular sensitivity performs marginally better than the base case model run for downwind sites in East Asia. However, it underestimates nitrate concentrations at urban sites in India, with only minor discrepancies to observed values elsewhere.

Lower N_2O_5 uptake coefficient for hydrolysis: The simulation that incorporated a lower uptake coefficient for N_2O_5 hydrolysis consistently yielded lower surface $PM_{2.5}$ nitrate concentrations in all regions when compared to the base case model (Fig. 5g). The simulation indicates a 20% decrease in East Asia and a 40% decrease in Europe and North America, reflecting the suppression of nitrate formation via the hydrolysis pathway.

A comparison of the 'HYDRO' model run with observations reveals a tendency to underpredict the concentrations of $PM_{2.5}$ nitrate by the EMEP network during winter and spring. The discrepancy between the 'HYDRO' model run and the observations is more pronounced in winter and spring (25% and 35%, respectively) compared to summer and autumn. For the EPA network, this sensitivity underpredicts winter values by approximately 30%, yet it demonstrates a higher degree of agreement with observations for all other seasons when compared to the other sensitivity cases. For IMPROVE observations, the 'HYDRO' case results in a lower overprediction in all seasons when compared to the base case model run. The model-measurement differences are within 30%. For EANET observations, the 'HYDRO' model run yielded values that more closely aligned with observations compared to the results of the other sensitivity model runs, with the exception of the 'CMIP' case during summer. Statistically, the 'HYDRO' case demonstrates enhanced performance in comparison to the base case across all observational networks and metrics, with the exception of the EANET observations during the autumn season. The most substantial enhancements compared to the base case are observed for the EPA network, as this scenario demonstrated the most improved metrics in comparison to the rest of the sensitivities, for values obtained in summer and autumn.

Notably, for PM_1 nitrate concentrations, the 'HYDRO' case exhibits the second highest underprediction among all sensitivity model runs, surpassed only by the 'CMIP' case, across all location types in Europe. A similar behavior was observed for North American values. However, the outcomes of the model-measurement comparison vary significantly for values in East Asia. Specifically, while the 'HYDRO' model run demonstrates the most significant underprediction for urban site values (approximately 15%) among all other sensitivity cases, it exhibits a lower overprediction bias compared to the base case for both rural and downwind locations, resulting in

a closer agreement with the measurements. In India, the 'HYDRO' case displays the least pronounced overprediction for rural values among all the sensitivity model runs, although these values are substantially lower (a factor of 4.5) than the observations. Notably, for urban areas, the 'HYDRO' case demonstrates a comparable underprediction to that observed in the 'RES_low' and 'THERM' cases. Statistically, the 'HYDRO' case demonstrates a lower performance than the base case in Europe, particularly for rural and downwind locations, as evidenced by the presence of stronger negative biases and higher error rates. In North America, the model's performance is suboptimal for rural locations but superior for urban sites, exhibiting comparable metrics for downwind predictions. In East Asia, the 'HYDRO' model run demonstrates more accurate predictions than the base case for rural and downwind locations for most metrics (with the exception of RMSE), yet predictions are less precise for urban sites. In India, the predictions in rural areas are improved compared to the base case model run by this sensitivity, but predictions in urban areas remain unchanged. This observation indicates that the 'HYDRO' model run performs better in capturing nighttime aerosol nitrate formation, which is predominant in rural areas. In contrast, daytime production pathways seem to be more significant in urban areas.

4.4 Sensitivity to the scavenging treatment

Simplified scavenging treatment: The implementation of a simplified scavenging treatment for the gas phase aerosol precursors in the model (Section 2.3) yields substantially reduced surface $PM_{2.5}$ nitrate concentrations compared to the base case (Fig. 4h). The most substantial disparities are evident in Europe and East Asia, where concentrations are reduced by approximately 60%. Comparatively, North America exhibits a reduction of approximately 30%, while India experiences a decline of around 10–20%. These lower concentrations can be attributed to the high wet deposition fluxes in the simplified mechanism, which neglects gas-phase diffusion limitations and assumes an equilibrium between the gas and aerosol phases (Tost et al., 2007b). Additionally, the assumed pH of 5 for clouds and precipitation is less acidic than typical for polluted regions, further enhancing nitrate scavenging.

A comparison of the 'SCAV' case with observations reveals the strongest underprediction for EMEP measurements in winter (~45%). Comparable estimates are obtained in the 'CMIP' case during the spring season. Overprediction biases are less by ~20% and ~30%, respectively, than in the base case model run during summer and autumn. For the EPA network, the 'SCAV' case demonstrates the most significant overprediction of observations in winter (~45%) among all sensitivity model runs. However, values are only marginally overpredicted in the other seasons (~10%), and even slightly underpredicted in spring. The IMPROVE observations demonstrate a closer alignment with the 'SCAV' case predictions in comparison to the base case predictions throughout the year, exhibiting notable reductions in model-measurement discrepancies by up to ~40% during winter and spring. For EANET observations, the 'SCAV' model run yielded smaller values than the base case, thereby reducing the overprediction bias by ~35% during winter. In all other seasons within the region, this particular sensitivity demonstrates the smallest discrepancies between model predictions and observations among the rest. Statistically, the 'SCAV' case demonstrates enhanced performance in comparison to the base case for EMEP and EPA observations across the majority of seasons, with the exception of winter, where the model exhibits a substantial underprediction tendency, as evidenced by both bias and error metrics. The model-measurement agreement for observations of the IMPROVE network exhibited enhancement in comparison to the base case model run across all seasons. The agreement for EANET observations

shows improvements only during winter and summer, while during spring and autumn the statistical metrics of the 'SCAV' case are worse compared to the base case.

For PM_1 nitrate, the 'SCAV' case demonstrates a higher underprediction of observations compared to the base case for all location types in Europe. The magnitude of the bias observed in the 'SCAV' case is comparable to that seen in the 'CMIP' and 'HYDRO' cases. In North America, the 'SCAV' case results in an underprediction of concentrations of approximately 50% for rural sites and 40% for downwind sites, though it is slightly smaller than the overprediction bias of the base case model for urban locations. In East Asia, the 'SCAV' case exhibits a smaller overprediction of observed values compared to the base case results for downwind locations (~25%), while this sensitivity provides nearly identical estimates for rural sites. Conversely, urban sites exhibit a slight underprediction (12%) in this sensitivity analysis. In India, the 'SCAV' sensitivity model run does not lead to substantial changes in the estimates compared to the base case results for both urban and rural locations. Statistically, the 'SCAV' case demonstrates suboptimal performance in comparison to the base case with regard to bias metrics for results in Europe, although the discrepancy in error metrics is less pronounced. In North America, the 'SCAV' case demonstrates poorer metrics for rural sites, yet it exhibits enhancements for urban sites. Downwind sites display elevated biases but reduced errors. In East Asia, the 'SCAV' case exhibits higher accuracy in capturing observations at rural and downwind sites compared to the base case, but performs less successfully at urban sites. A similar pattern is observed in the results for India. In summary, when evaluated against the metrics of the base case, the 'SCAV' case yielded enhancements for rural sites in Europe and India.

5. Temporal Variability and Tropospheric Burden of NO_3^-

With regard to the $PM_{2.5}$ size mode, the availability of continuous time series data from monitoring networks facilitates a comparison of seasonal patterns across different model sensitivities and regions. Conversely, the PM_1 measurements, which were campaign-based and characterized by varying durations, lack the capability to facilitate a comparable seasonal analysis. Consequently, a selection of stations measuring PM_1 concentrations in Europe was chosen for PM_1, given the considerable difficulties encountered by the model in this region for this size mode, regarding the replication of observation concentrations. These stations, which provide hourly measurements, facilitate a detailed comparison of the diurnal variation of modeled and observed data. Finally, this section includes an analysis of the total tropospheric burden of nitrate aerosols. This analysis compares estimates from all sensitivity cases to assess their global-scale implications. This multi-scale approach aims to highlight the temporal dynamics and atmospheric significance of nitrate aerosols in relation to different modeling configurations.

5.1 Seasonal variation of $PM_{2.5}$ concentrations

Figure 7 presents the seasonal patterns of $PM_{2.5}$ predictions from model sensitivity runs and measurements obtained from observational networks in the specified regions. For the EMEP network, all models consistently underpredicted the $PM_{2.5}$ concentrations from January to April, with the largest discrepancies observed in March, ranging from 35% for the 'RES_low' case to 55% for the 'SCAV' case. It is noteworthy that the 'HTAP' case is the sole model run that accurately replicates this period, including the peak concentration observed in the measurements in March. Conversely, from April to December, the majority of sensitivity cases exhibit an overprediction of observed concentrations, with the exception of the 'HTAP' case after October. The most pronounced overestimations are observed in the 'RES_low' and base cases, with concentrations

reaching up to twice the observed levels in October. In contrast, the 'CMIP' and 'HYDRO' cases exhibit smaller discrepancies between model and measurement, with model overestimations of approximately 40%. While all model cases captured the general seasonal cycle, the 'HTAP' case misaligned the timing of the second maximum, which was shifted to one month earlier and exhibited a stronger post-summer decline compared to the other model runs. The results of the 'CMIP' case, followed by the 'RES_high' and 'HYDRO' cases, demonstrate the closest agreement with observations, particularly at low nitrate concentrations. Overall, the magnitude of model overpredictions is most pronounced during summer and early autumn. The enhanced discrepancies between model projections and observations for this network can be partially attributed to the elevated evaporation of the semi-volatile nitrate aerosol species under warm conditions (Ames and Malm, 2001; Docherty et al., 2011), a process that is augmented by the utilization of nylon filters by the EMEP samplers (Yu et al., 2005).

A similar seasonal pattern is observed in the USA when comparing model outputs to EPA measurements, with underpredictions of observed values from January to April and overpredictions from April to December. The 'SCAV' case demonstrates the most significant underprediction of observations, exhibiting a 35% discrepancy in February. In contrast, the 'RES_low' case reveals the most substantial overprediction, with concentrations surpassing observations by a factor of 2 in August. The sensitivity model runs with different anthropogenic emission inventories demonstrate contrasting behaviors, with the 'HTAP' case consistently overpredicting the measured concentrations and the 'CMIP' case underpredicting them. Notwithstanding these biases, the seasonal variation is adequately captured in all model cases, with the 'RES_high' and 'HYDRO' model runs demonstrating the most optimal overall performance. A similar pattern to the European region was observed, where the warm months were characterized by the largest overprediction biases for this network as well. This phenomenon is attributed, at least in part, to biases associated with evaporation losses during that particular period of the year. Specifically, filter samples are found to be strongly influenced by ambient temperature and relative humidity. Under warmer weather conditions, the increased temperatures of the filters result in the increased evaporation of semi-volatile species like particulate nitrate (Ames and Malm, 2001; Docherty et al., 2011). For the IMPROVE network, all model cases exhibit overpredictions of $PM_{2.5}$ concentrations throughout the year, with more pronounced discrepancies observed during colder months. During these months, the 'HTAP' scenario demonstrates discrepancies of up to a factor of 2.5 in February and a factor of 2 in December, while the 'RES_low' scenario exhibits comparable deviations in spring and summer. Among the sensitivity cases, the 'CMIP' model run demonstrates the most robust agreement with observed data, followed by the 'SCAV' case during the early months of the year and the 'RES_high' and 'HYDRO' sensitivities during the remainder of the year.

The EANET network demonstrates a comparable seasonal variability to the IMPROVE network, with all model cases consistently predicting higher concentrations than observed throughout the year, while successfully reproducing the observed seasonality. The most pronounced overpredictions occur during the cold months, with the 'HTAP' model run exhibiting the most significant deviations of up to a factor of 3.5 in January. The 'SCAV' case demonstrates the most favorable agreement with observations, exhibiting deviations that remain constrained to a factor of 1.5 during the cold season. This suggests that the intricate aerosol scavenging process included in the base case may potentially underestimate the wet deposition fluxes of particulate nitrate in this region. The 'HYDRO' and 'CMIP' cases also demonstrate notable performance, particularly in cases of lower concentrations.

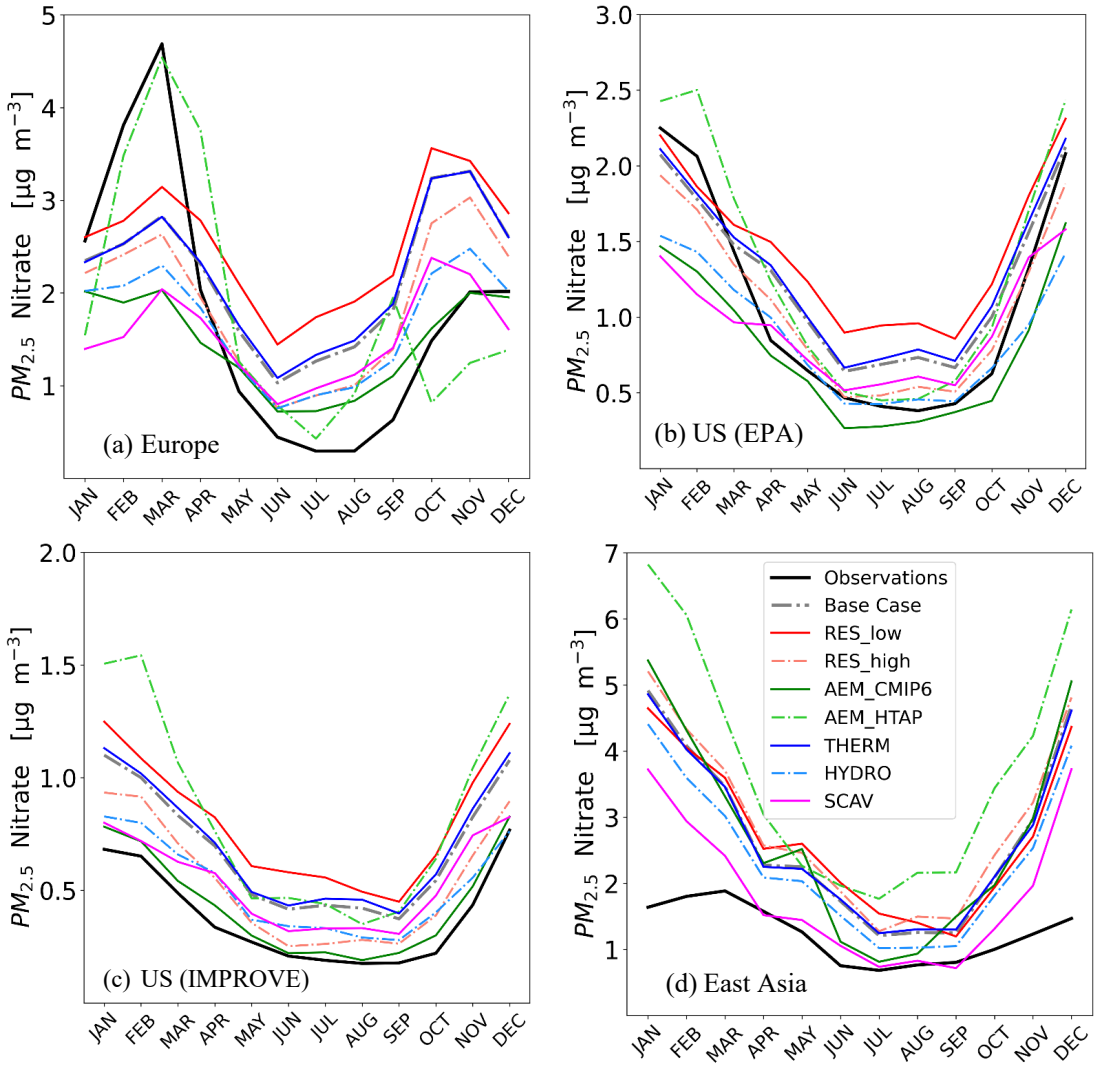

Figure 7: Seasonal variation of measured (black line) and predicted (colored lines) $PM_{2.5}$ NO_3^- surface concentrations from the base case and all sensitivity model cases and observations of the networks of (a) EMEP, (b) EPA, (c) IMPROVE and (d) EANET.

5.2 Diurnal variation of PM_1 concentrations

Figure 8 presents a comparison of the diurnal variation of PM_1 nitrate concentration predictions from the base case model and the sensitivity model runs against hourly observations from seven European stations. At Birkenes, the majority of model cases demonstrate the capacity to replicate the observed diurnal pattern, with concentrations peaking in the early morning and decreasing in the late evening. However, the 'RES_low' case demonstrates a substantial deviation, with concentrations that are twice the observed values. The 'RES_high' case provides the closest approximation to the observed concentrations, suggesting that a higher grid resolution is more effective in capturing the variations in aerosol nitrate concentrations induced by anthropogenic activities during the day. Conversely, the 'SCAV' model run exhibited the most significant underprediction, reaching a factor of 2.In Bucharest, the model sensitivities yielded a comparable morning peak, albeit smaller than the observed value, occurring approximately two hours earlier than the observed peak. While an evening minimum is predicted at a similar time, the model estimations overemphasize its peak, resulting in an underprediction that is twice as strong as the one exhibited for the morning values. The 'RES_high' scenario demonstrates superior performance compared to the other cases for this station, which exhibits a diurnal pattern analogous to the previous station, followed by the base and 'THERM' scenarios. The 'SCAV' case demonstrates the most significant diurnal variability among the rest of the sensitivities, exhibiting a pronounced decrease in concentrations during the transition from day to night.

At Hohenspeissenberg, the model results fail to reproduce the observed early morning minimum. Predicted late morning maxima and afternoon minima are higher than the observations in most cases, except for the 'RES_high', 'HYDRO', and 'CMIP' cases. During the early morning hours, these three cases demonstrate the smallest discrepancies with the observations, while the 'RES_low' model run exhibits a stronger agreement in the afternoon due to a less pronounced decline in the modeled concentrations. The station's elevation of 300 meters serves to mitigate the influence of anthropogenically influenced air masses, thereby reducing the variability observed in hourly values. This phenomenon is not reflected by the model's results.

At Melpitz, the observed diurnal pattern is well reproduced by the model results. In the majority of sensitivity cases, morning values are marginally higher than observed values, while evening values are slightly lower. The 'CMIP' case demonstrates the most accurate morning values among the diverse model runs, while the base and 'THERM' cases exhibit more precise evening concentration predictions compared to the others. The 'RES_low' model run demonstrates the most overall agreement with observations throughout the day, attributable to the less pronounced maximum and minimum peaks.

For the SIRTA station, the model results adequately capture the diurnal pattern, though the evening minimum values are predicted three hours later than observed. The 'RES_low' and 'RES_high' cases demonstrated an enhanced representation of the morning maximum compared to the other cases, while the 'RES_low' model run exhibited superior prediction of the evening minimum compared to all other sensitivities. This 'RES_low' case also demonstrated a less pronounced transition from daytime to nighttime values, similar to the previous comparison. The other model sensitivity cases underpredict the observations, with discrepancies ranging from 40% ('HTAP' case) to a factor of 3 ('CMIP' case).

At Puy De Dôme, the model results fail to reproduce the diurnal variation of the observations. The station's location on one of the highest peaks of the Chaîne des Puy renders it a representative point for conditions of the regional atmosphere. This characteristic is evidenced by the absence of a pronounced diurnal variation in the PM_1 values, in contrast to what is observed in stations more

characteristic of anthropogenically affected atmospheres, such as Bucharest and SIRTA. The morning values are marginally overpredicted by the 'RES_low' case; however, evening values are consistently underpredicted by all sensitivities, at a time when the observations showed nearly constant values. The 'RES_low' model run exhibits the least deviation from observations in the afternoon, while the base and 'THERM' cases demonstrate more accurate performance in the early morning.

At Villeneuve, the observed diurnal pattern is generally well reproduced by the model results, with the exception of a three-to-four-hour delay in the observed evening minimum. It is evident that all cases exhibit an underprediction of the observed concentrations, with the most pronounced discrepancies observed in the 'HTAP' case, reaching up to a factor of 3, and the least significant discrepancies observed in the base and 'THERM' cases, at approximately 60%.

The analysis indicates that the grid resolution is the most critical factor in reproducing the diurnal variability of PM_1 nitrate concentrations. For stations exhibiting regional characteristics (Hohenspeissenberg, Melpitz, and Puy De Dôme), the 'RES_high' model run provides optimal predictions during the day, while the 'RES_low' model run more accurately captures evening and nighttime values. The observed discrepancy during nighttime hours can be attributed to the distortion of NOx fields in the 'RES_low' case, resulting from the larger grid cells. This distortion leads to elevated nitrate radical concentrations and increased nitrate aerosol production during nighttime hours, a process that has the greatest impact on rural areas (Zakoura and Pandis, 2018). Consequently, the 'RES_low' case results in increased nighttime concentrations that approximate the observed values. The base and 'THERM' scenarios demonstrate satisfactory performance across all stations, while the 'HYDRO' case exhibits minimal enhancement. For the sensitivity model runs employing different emission inventories, the 'HTAP' case outperforms the 'CMIP' case; however, the agreement between modeled values and observations remains less than that for the base case. This outcome confirms the suitability of the CAMS database for modeling European PM_1 nitrate concentrations.

849
850 **Table 4**: Names, locations and data availability of the stations used for the comparison of diurnal
851 PM_1 NO_3^- concentrations. The location type of each station is also categorized as rural (RUR) or
852 downwind (DW) locations.
853

Station Name	Station Code	Longitude	Latitude	Availability of hourly data
Birkenes II (RUR)	NO0002R	58°23'19"N	008°15'07"E	8/2012 – 8/2018
Bucharest (DW)	RO0007R	44.344°N	26.012°E	8/2016 – 8/2018
Hohenspeissenberg (DW)	DE0043G	47°48'05"N	011°00'35"E	4/2015 – 10/2015 1/2017 – 9/2017 10/2017 – 11/2018
Melpitz (RUR)	DE0044R	51°31'49"N	012°56'02"E	7/2015 – 9/2015 5/2016 – 11/2017
Puy de Dôme (RUR)	FR0030R	45°46'00"N	002°57'00"E	3/2015 – 10/2016 1/2018 – 12/2018
SIRTA Atmospheric Research Observatory (DW)	FR0020R	48°42'31"N	002°09'32"E	10/2014 – 1/2016
Villeneuve d'Ascq (DW)	FR0027U	50.611°N	3.14°E	10/2016 – 11/2017 7/2018 – 12/2018

854
855

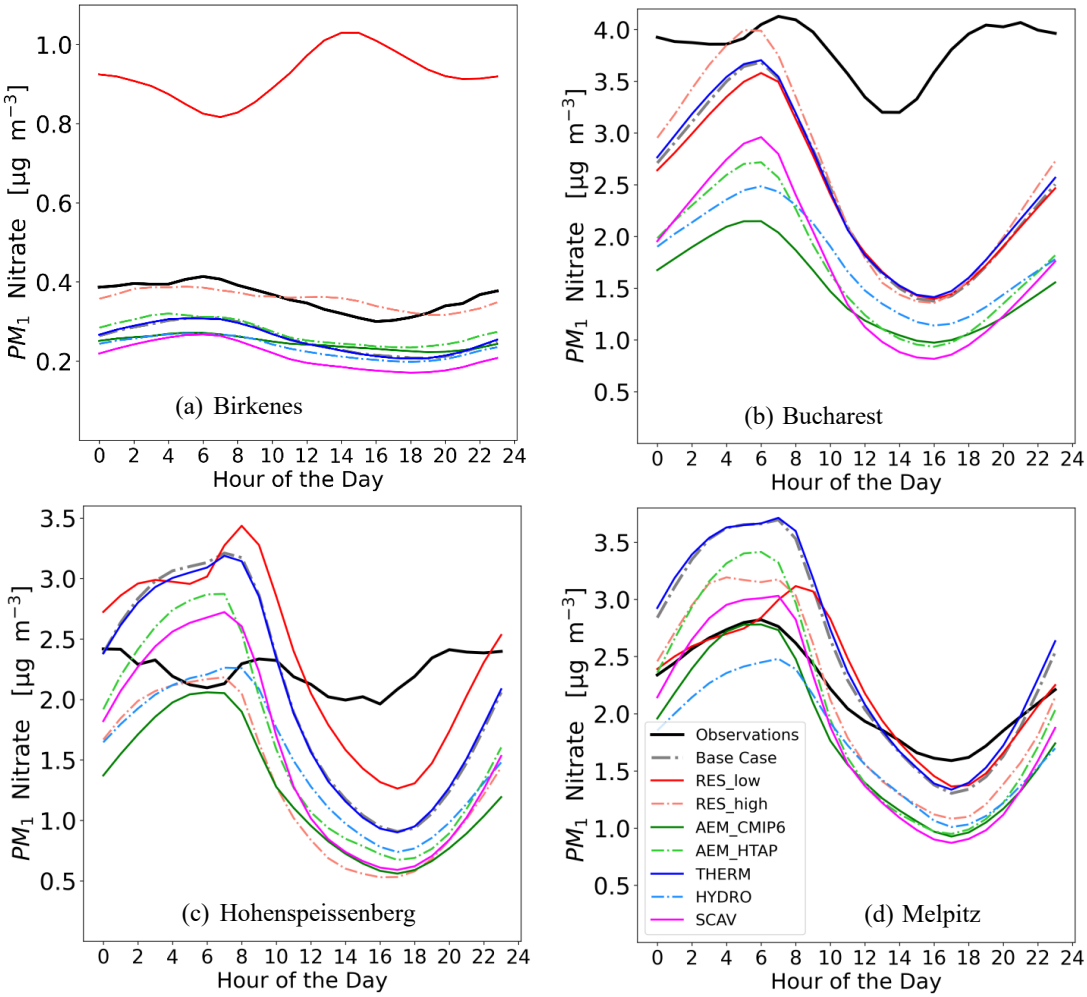

856
857 **Figure 8**: Diurnal evolution of measured (black line) and predicted (colored lines) PM_1 NO_3^-
858 surface concentrations from the base case model and all model sensitivity cases for the stations at
859 (a) Birkenes, (b) Bucharest, (c) Hohenspeissenberg and (d) Melpitz.
860

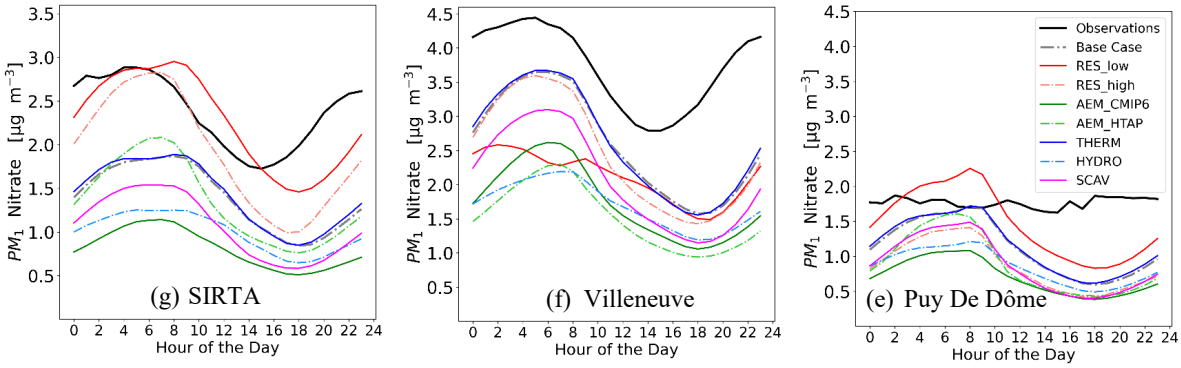

Figure 8 (cont): Diurnal evolution of measured (black line) and predicted (colored lines) PM_1 NO_3^- surface concentrations from the base case model and all model sensitivity cases for the stations at (e) SIRTA, (f) Villeneuve and (g) Puy De Dôme.

5.3 Tropospheric burden of particulate nitrate

The global tropospheric burden of aerosol nitrate, defined as the total tropospheric column mass concentration expressed in terms of teragrams (Tg) and averaged over the entire time period from 2008 to 2018, is outlined in Table 5 and Figure 9. This analysis encompasses the predictions from the base case as well as the sensitivity model runs. The base case estimates a burden of 0.7 Tg, closely matching the multi-model average of 0.63 Tg reported by Bian et al. (2017). The 'RES_low' case demonstrates the most substantial burden of 0.89 Tg, representing a 27% increase compared to the base case estimate. This is attributable to larger grid cells, which have a distorting effect on NOx concentration fields over broader regions, leading to elevated nocturnal production of particulate nitrate. Conversely, the 'RES_high' case exhibits the lowest burden of 0.53 Tg, a 24% decrease compared to the base case estimate, attributed to the more accurate reproduction of NOx concentration fields by this sensitivity and the reduced nocturnal production of particulate nitrate.

The 'CMIP' case estimates a burden value close to the base case one (0.74 Tg), while the 'HTAP' model run produces a higher burden of 0.88 Tg, driven by the elevated particulate nitrate differences compared to the base case, particularly over India and the Western US. The 'THERM' and 'HYDRO' cases both yielded burdens of 0.69 Tg, indicating a minimal impact of the aerosol thermodynamic state assumption, as well as the N_2O_5 uptake coefficient for hydrolysis on the nitrate aerosol burden. The 'SCAV' case estimates a lower burden of 0.53 Tg due to the increased wet deposition rates from the simplified scavenging approach. This outcome is consistent with the results reported by Tost et al. (2007b), who, employing analogous simplifications and assumptions, including a pH value of 5 for rain and clouds, also observed increased deposition rates.

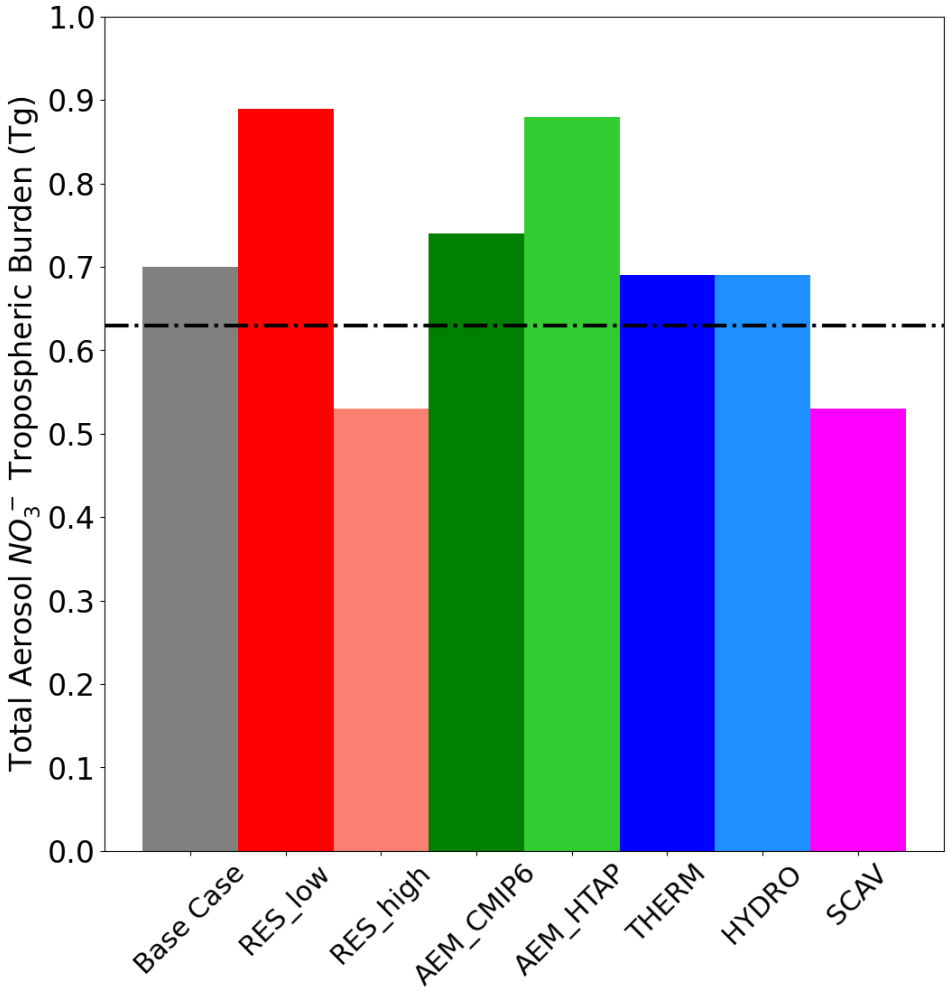

888 **Figure 9**: Bar chart showing the average tropospheric burden of total aerosol NO_3^- predicted from
889 the base case and all sensitivity cases for the period 2010-2018. Also shown is the respective
890 average burden from 9 models taken from Bian et al. (2017), equal to 0.63 Tg.
891

Table 5: Average tropospheric burden of aerosol NO_3^- for the period 2010-2018 for the base case and all sensitivity simulations.

	Tropospheric Burden (Tg)
Simulation Name	NO_3^-
Base Case	0.70
RES_low (T42)	0.89
RES_high (T106)	0.53
CMIP6	0.74
HTAP	0.88
THERM	0.69
HYDRO	0.69
SCAV	0.53

6. Conclusions

This study examined the impact of diverse atmospheric modeling components on the precision of predicted surface concentrations of nitrate aerosols. A series of sensitivity scenarios were developed to assess the impact of grid resolution, anthropogenic emission inventories, aerosol thermodynamic assumptions, uptake coefficient for N_2O_5 hydrolysis, and scavenging treatments on model predictions. A comparative analysis was conducted against $PM_{2.5}$ filter observations and PM_1 AMS measurements, focusing on polluted regions within the Northern Hemisphere. The findings indicated that accurately replicating observed $PM_{2.5}$ and PM_1 concentrations necessitates a nuanced approach, as no single model configuration consistently yielded the best results for all conditions and regions.

With respect to $PM_{2.5}$ observations, the model demonstrated the most optimal performance in the USA region, exhibiting the lowest overall bias and error metrics for all respective sensitivities. In East Asia, the model consistently overpredicted concentrations in all configurations, although percentage differences were often moderate. Despite the significant disparities in model-observations differences within this region, certain configurations demonstrated the capacity to enhance both the predicted concentrations and the statistical metrics. These configurations included higher grid resolution, a lower uptake coefficient for N_2O_5 hydrolysis, and a simplified aerosol scavenging treatment. Conversely, Europe emerged as a particularly challenging region for the model to replicate, exhibiting both under- and overpredictions of nitrate concentrations relative to observations, a pattern that exhibited significant seasonal variation. Specifically, the discrepancies between predictions and measurements, in terms of model overprediction, reached their zenith during the warmer period for this region. This phenomenon can be attributed to the enhanced evaporation of the semi-volatile nitrate aerosol species under warm conditions, a process that is amplified by the use of nylon filters. This phenomenon was also observed in the comparison with the EPA network values. Conversely, the model exhibited elevated discrepancies with observed values from the IMPROVE and EANET networks during the colder periods. Notwithstanding these challenges, the scenarios that demonstrated an enhancement in comparison to the base case predictions for East Asia were found to be equally effective in the other two regions, thereby underscoring their significance in enhancing the model's precision in replicating $PM_{2.5}$ nitrate observations.

With respect to PM_1 observations, the model demonstrated considerable variations in performance across different location types and regions. Generally, observations in urban areas exhibited the strongest correlation with model predictions across all regions within the sensitivity cases. However, observations in rural locations were either underpredicted or severely overpredicted in North America and India, respectively. In contrast, rural observations in Europe and East Asia were more accurately replicated by the base and 'CMIP' cases, respectively. In general, downwind locations posed the greatest challenge for the model, with underprediction biases being evident in Europe and North America. In contrast, a contrasting behavior was observed for East Asian values. Overall, the base case demonstrated a satisfactory agreement with most observations for the regions of Europe and East Asia. In contrast to the $PM_{2.5}$ comparison, it was challenging to identify specific model configurations that consistently outperformed the base case in terms of predicted nitrate concentrations or statistical metrics. However, the selection of emission inventory emerged as the most crucial factor in enhancing the model's estimation accuracy. Specifically, the model runs that used the CAMS database provided the best representation of particulate nitrate concentrations for Europe, the model runs that used the

HTAPv3 database were most accurate for observations in North America, while the model runs that used the CMIP6 database best captured values in East Asia.

An analysis of the diurnal variation of PM_1 nitrate concentrations observed at European stations revealed that the majority of model configurations effectively captured the overall diurnal patterns of the observations at most stations. However, there were exceptions, namely stations that exhibited characteristics more indicative of regional atmospheric conditions, and thus lacked significant diurnal variation concerning their maximum and minimum values. However, notable biases emerged, with the model results systematically overemphasizing the evening minima and exhibiting a sharp decline in concentrations after midday. This behavior was not mirrored in the observations, leading to underpredictions of the observed values in the afternoon and evening. The selection of the grid resolution proved to have the most significant impact on the predicted diurnal patterns. The high-resolution configuration demonstrated higher accuracy during the morning hours, while the lower-resolution configuration exhibited a stronger ability to capture afternoon and evening values. Among the emission inventories, utilization of the CAMS database yielded the most reliable estimates for PM_1 nitrate particle concentrations over Europe.

In regard to the tropospheric nitrate aerosol burden, the base case, the metastable aerosol state assumptions, the lower uptake coefficient for N_2O_5 hydrolysis, and the use of the CMIP6 emissions database yielded values that were the closest to the multi-model average value reported by Bian et al. (2017). Conversely, scenarios involving a reduced grid resolution and the HTAPv3 emissions database resulted in estimates that were approximately 25% higher than the base case. This outcome is attributed to the influence of augmented grid cells and expanded precursor fields. Conversely, the scenarios where a higher grid resolution and a simplified aerosol scavenging treatment were used estimated burdens approximately 25% lower compared to the base case, attributable to the finer spatial resolution and increased wet deposition, respectively.

In conclusion, this study underscores the complexity of accurately modeling nitrate aerosols. The findings underscore the necessity of selecting appropriate configurations based on regional and seasonal conditions, with high-resolution grids, CMIP6 emissions, and adjusted uptake coefficients for N_2O_5 hydrolysis being pivotal in enhancing the model's performance. However, the observed variability across regions and seasons underscores the necessity of a multifaceted, context-sensitive approach to further advance the field of atmospheric modeling of particulate nitrate concentrations.

Code and Data Availability

The usage of MESSy (Modular Earth Submodel System) and access to the source code is licensed to all affiliates of institutions which are members of the MESSy Consortium. Institutions can become a member of the MESSy Consortium by signing the "MESSy Memorandum of Understanding". More information can be found on the MESSy Consortium website: http://www.messy-interface.org (last access: 22 May 2024). The code used in this study has been based on MESSy version 2.55 and is archived with a restricted access DOI (https://doi.org/10.5281/zenodo.8379120, The MESSy Consortium, 2023). The data produced in the study is available from the authors upon request.

Acknowledgements

This work was supported by the project FORCeS funded from the European Union's Horizon 2020 research and innovation program under grant agreement No 821205. The work described in this paper has received funding from the Initiative and Networking Fund of the Helmholtz Association through the project "Advanced Earth System Modelling Capacity (ESM)". The authors gratefully acknowledge the Earth System Modelling Project (ESM) for funding this work by providing computing time on the ESM partition of the supercomputer JUWELS (Alvarez, 2021) at the Jülich Supercomputing Centre (JSC).

Competing Interests

The authors declare that no competing interests of any kind exist.

Author Contributions

AM and VAK wrote the paper with contributions from APT, HF and SS. VAK planned the research with contributions from APT. AM performed the simulations and analyzed the results, assisted by VAK and APT. APT and SS provided the observational data. All the authors discussed the results and contributed to the paper.

REFERENCES

Aksoyoglu, S., Ciarelli, G., El-Haddad, I., Baltensperger, U., and Prévôt, A. S. H.: Secondary inorganic aerosols in Europe: sources and the significant influence of biogenic VOC emissions, especially on ammonium nitrate, Atmospheric Chemistry and Physics, 17, 7757–7773, https://doi.org/10.5194/acp-17-7757-2017 , 2017.

Alvarez, D.: JUWELS cluster and booster: Exascale pathfinder with modular supercomputing architecture at juelich supercomputing Centre, Journal of large-scale research facilities JLSRF, 7, A183-A183, https://doi.org/10.17815/jlsrf-7-183, 2021.

Ames, R. B. and Malm, W. C.: Comparison of sulfate and nitrate particle mass concentrations measured by IMPROVE and the CDN, Atmospheric Environment, 35, 905-916, https://doi.org/10.1016/S1352-2310(00)00369-1 , 2001.

Ansari, A. S. and Pandis, S. N.: The effect of metastable equilibrium states on the partitioning of nitrate between the gas and aerosol phases, Atmospheric Environment, 34, 157-168, https://doi.org/10.1016/S1352-2310(99)00242-3, 2000.

Astitha, M., Lelieveld, J., Kader, M. A., Pozzer, A., and de Meij, A.: Parameterization of dust emissions in the global atmospheric chemistry-climate model EMAC: impact of nudging and soil properties, Atmospheric Chemistry and Physics, 12, 11057-11083, https://doi.org/10.5194/acp-12-11057-2012 , 2012.

Bacer, S., Sullivan, S. C., Karydis, V. A., Barahona, D., Kramer, M., Nenes, A., Tost, H., Tsimpidi, A. P., Lelieveld, J., and Pozzer, A.: Implementation of a comprehensive ice crystal formation parameterization for cirrus and mixed-phase clouds in the EMAC model (based on MESSy 2.53), Geoscientific Model Development , 11, https://doi.org/10.5194/gmd-11-4021-2018 , 2018.

Bellouin, N., Rae, J., Jones, A., Johnson, C., Haywood, J., and Boucher, O.: Aerosol forcing in the Climate Model Intercomparison Project (CMIP5) simulations by HadGEM2-ES and the role of ammonium nitrate, Journal of Geophysical Research: Atmospheres, 116, https://doi.org/10.1029/2011JD016074 , 2011.

Bertram, T. H., Thornton, J. A., Riedel, T. P., Middlebrook, A. M., Bahreini, R., Bates, T. S., Quinn, P. K., & Coffman, D. J.: Direct observations of N_2O_5 reactivity on ambient aerosol particles, Geophysical Research Letters, 36, https://doi.org/10.1029/2009GL040248 , 2009.

Bian, H., Chin, M., Hauglustaine, D. A., Schulz, M., Myhre, G., Bauer, S. E., Lund, M. T., Karydis, V. A., Kucsera, T. L., Pan, X., Pozzer, A., Skeie, R. B., Steenrod, S. D., Sudo, K., Tsigaridis, K., Tsimpidi, A. P., and Tsyro, S. G.: Investigation of global particulate nitrate from the AeroCom phase III experiment, Atmospheric Chemistry and Physics, 17, 12911–12940, https://doi.org/10.5194/acp-17-12911-2017 , 2017.

Bouwman, A. F., Lee, D. S., Asman, W. A., Dentener, F. J., Van Der Hoek, K. W., and Olivier, J. G. J.: A global high-resolution emission inventory for ammonia, Global biogeochemical cycles, 11, 561-587, https://doi.org/10.1029/97GB02266, 1997.

Bromley, L. A.: Thermodynamic properties of strong electrolytes in aqueous solutions, AIChE journal, 19, 313-320, https://doi.org/10.1002/aic.690190216, 1973.

Brown, S.S., Dubé, W.P., Fuchs, H., Ryerson, T.B., Wollny, A.G., Brock, C.A., Bahreini, R., Middlebrook, A.M., Neuman, J.A., Atlas, E. and Roberts, J.M.,: Reactive uptake coefficients for N_2O_5 determined from aircraft measurements during the Second Texas Air Quality Study: Comparison to current model parameterizations, Journal of Geophysical Research: Atmospheres, 114, https://doi.org/10.1029/2008JD011679 , 2009.

Chang, W. L., Bhave, P. V., Brown, S. S., Riemer, N., Stutz, J., & Dabdub, D.: Heterogeneous atmospheric chemistry, ambient measurements, and model calculations of N_2O_5: A review, Aerosol Science and Technology, 45, 665-695, https://doi.org/10.1080/02786826.2010.551672 , 2011.

Chang, W.L., Brown, S.S., Stutz, J., Middlebrook, A.M., Bahreini, R., Wagner, N.L., Dubé, W.P., Pollack, I.B., Ryerson, T.B. and Riemer, N.,: Evaluating N_2O_5 heterogeneous hydrolysis parameterizations for CalNex 2010, Journal of Geophysical Research: Atmospheres, 121, 5051-5070, https://doi.org/10.1002/2015JD024737 , 2016.

Chen, Y., Wolke, R., Ran, L., Birmili, W., Spindler, G., Schröder, W., Su, H., Cheng, Y., Tegen, I., and Wiedensohler, A.: A parameterization of the heterogeneous hydrolysis of N_2O_5 for mass-based aerosol models: improvement of particulate nitrate prediction, Atmospheric Chemistry and Physics, 18, 673–689, https://doi.org/10.5194/acp-18-673-2018 , 2018.

Chowdhury, S., Pozzer, A., Haines, A., Klingmueller, K., Münzel, T., Paasonen, P., Sharma, A., Venkataraman, C. and Lelieveld, J.,: Global health burden of ambient PM2. 5 and the contribution of anthropogenic black carbon and organic aerosols, Environment International, 159, 107020, https://doi.org/10.1016/j.envint.2021.107020 , 2022.

Crippa, M., Guizzardi, D., Butler, T., Keating, T., Wu, R., Kaminski, J., Kuenen, J., Kurokawa, J., Chatani, S., Morikawa, T., Pouliot, G., Racine, J., Moran, M. D., Klimont, Z., Manseau, P. M., Mashayekhi, R., Henderson, B. H., Smith, S. J., Suchyta, H., Muntean, M., Solazzo, E., Banja, M., Schaaf, E., Pagani, F., Woo, J.-H., Kim, J., Monforti-Ferrario, F., Pisoni, E., Zhang, J., Niemi, D., Sassi, M., Ansari, T., and Foley, K.: The HTAP_v3 emission mosaic: merging regional and global monthly emissions (2000–2018) to support air quality modelling and policies, Earth Sysem Science Data, 15, 2667–2694, https://doi.org/10.5194/essd-15-2667-2023 , 2023.

Dee, D. P., Uppala, S. M., Simmons, A. J., Berrisford, P., Poli, P., Kobayashi, S., Andrae, U., Balmaseda, M. A., Balsamo, G., Bauer, P., Bechtold, P., Beljaars, A. C. M., van de Berg, L., Bidlot, J., Bormann, N., Delsol, C., Dragani, R., Fuentes, M., Geer, A. J., Haimberger, L., Healy, S. B., Hersbach, H., Hólm, E. V., Isaksen, L., Kållberg, P., Köhler, M., Matricardi, M., McNally, A. P., Monge-Sanz, B. M., Morcrette, J. J., Park, B. K., Peubey, C., de Rosnay, P., Tavolato, C., Thépaut, J. N., and Vitart, F.: The ERA-Interim reanalysis: configuration and performance of the data assimilation system, Quarterly Journal of the Royal Meteorological Society, 137, 553-597, https://doi.org/10.1002/qj.828 , 2011.

Dentener, F., Kinne, S., Bond, T., Boucher, O., Cofala, J. and co-authors: Emissions of primary aerosol and precursor gases in the years 2000 and 1750 prescribed data-sets for AeroCom, Atmospheric Chemistry and Physics, 6, 4321-4344, https://doi.org/10.5194/acp-6-4321-2006, 2006.

Docherty, K. S., Aiken, A. C., Huffman, J. A., Ulbrich, I. M., DeCarlo, P. F., Sueper, D., Worsnop, D. R., Snyder, D. C., Peltier, R. E., Weber, R. J., Grover, B. D., Eatough, D. J., Williams, B. J., Goldstein, A. H., Ziemann, P. J., and Jimenez, J. L.: The 2005 Study of Organic Aerosols at Riverside (SOAR-1): instrumental intercomparisons and fine particle composition, Atmospheric Chemistry and Physics, 11, 12387–12420, https://doi.org/10.5194/acp-11-12387-2011 , 2011.

EMEP Programme Air Pollutant Monitoring Data, available at : https://projects.nilu.no/ccc/index.html

Evans, M. J. and Jacob, D. J.: Impact of new laboratory studies of N_2O_5 hydrolysis on global model budgets of tropospheric nitrogen oxides, ozone, and OH, Geophysical Research Letters, 32, https://doi.org/10.1029/2005GL022469 , 2005.

Fountoukis, C. and Nenes, A.: ISORROPIA II: a computationally efficient thermodynamic equilibrium model for K+–Ca 2+–Mg 2+–NH 4+–Na+–SO 4 2−–NO 3−–Cl−–H 2 O aerosols, Atmospheric Chemistry and Physics, 7, 4639-4659, https://doi.org/10.5194/acp-7-4639-2007, 2007.

Fountoukis, C., Nenes, A., Sullivan, A., Weber, R., Van Reken, T., Fischer, M., Matías, E., Moya, M., Farmer, D., and Cohen, R. C.: Thermodynamic characterization of Mexico City aerosol during MILAGRO 2006, Atmospheric Chemistry and Physics, 9, 2141-2156, https://doi.org/10.5194/acp-9-2141-2009, 2009.

Ge, X., Schaap, M., Kranenburg, R., Segers, A., Reinds, G. J., Kros, H., and de Vries, W.: Modeling atmospheric ammonia using agricultural emissions with improved spatial variability and temporal

dynamics, Atmospheric Chemistry and Physics, 20, 16055–16087, https://doi.org/10.5194/acp-20-16055-2020 , 2020.
Glantz, P., Fawole, O. G., Ström, J., Wild, M., & Noone, K. J.: Unmasking the effects of aerosols on greenhouse warming over Europe, Journal of Geophysical Research: Atmospheres, 127, e2021JD035889, https://doi.org/10.1029/2021JD035889 , 2022.
Grewe, V., Brunner, D., Dameris, M., Grenfell, J. L., Hein, R., Shindell, D., and Staehelin, J.: Origin and variability of upper tropospheric nitrogen oxides and ozone at northern mid-latitudes, Atmospheric Environment, 35, 3421-3433, https://doi.org/10.1016/S1352-2310(01)00134-0, 2001.
Guelle, W., Schulz, M., Balkanski, Y., & Dentener, F.: Influence of the source formulation on modeling the atmospheric global distribution of sea salt aerosol, Journal of Geophysical Research: Atmospheres, 106, 27509-27524, https://doi.org/10.1029/2001JD900249 , 2001.
Guo, H., Sullivan, A. P., Campuzano-Jost, P., Schroder, J. C., Lopez-Hilfiker, F. D., Dibb, J. E., Jimenez, J. L., Thornton, J. A., Brown, S. S., Nenes, A., and Weber, R. J.: Fine particle pH and the partitioning of nitric acid during winter in the northeastern United States, Journal of Geophysical Research: Atmospheres, 121, 10, 355-310, 376, https://doi.org/10.1002/2016JD025311 , 2016.
Hauglustaine, D. A., Balkanski, Y., and Schulz, M.: A global model simulation of present and future nitrate aerosols and their direct radiative forcing of climate, Atmospheric Chemistry and Physics, 14, 11031-11063, https://doi.org/10.5194/acp-14-11031-2014 , 2014.
Heald, C. L., Collett Jr., J. L., Lee, T., Benedict, K. B., Schwandner, F. M., Li, Y., Clarisse, L., Hurtmans, D. R., Van Damme, M., Clerbaux, C., Coheur, P.-F., Philip, S., Martin, R. V., and Pye, H. O. T.: Atmospheric ammonia and particulate inorganic nitrogen over the United States, Atmospheric Chemistry and Physics, 12, 10295–10312, https://doi.org/10.5194/acp-12-10295-2012 , 2012.
Hendriks, C., Kranenburg, R., Kuenen, J. J. P., Van den Bril, B., Verguts, V., & Schaap, M.: Ammonia emission time profiles based on manure transport data improve ammonia modelling across north western Europe. Atmospheric Environment, 131, 83-96, https://doi.org/10.1016/j.atmosenv.2016.01.043 , 2016.
Im, U., Bauer, S. E., Frohn, L. M., Geels, C., Tsigaridis, K., & Brandt, J.: Present-day and future PM2. 5 and O3-related global and regional premature mortality in the EVAv6. 0 health impact assessment model, Environmental Research, 216, 114702, https://doi.org/10.1016/j.envres.2022.114702 , 2023.
Inness, A., Ades, M., Agustí-Panareda, A., Barré, J., Benedictow, A., Blechschmidt, A.-M., Dominguez, J. J., Engelen, R., Eskes, H., Flemming, J., Huijnen, V., Jones, L., Kipling, Z., Massart, S., Parrington, M., Peuch, V.-H., Razinger, M., Remy, S., Schulz, M., and Suttie, M.: The CAMS reanalysis of atmospheric composition, Atmospheric Chemistry and Physics, 19, 3515–3556, https://doi.org/10.5194/acp-19-3515-2019 , 2019.
Interagency Monitoring of Protected Visual Environment (IMPROVE), available at : http://vista.cira.colostate.edu/Improve/improve-data/
Jockel, P., Sander, R., Kerkweg, A., Tost, H., and Lelieveld, J.: the modular earth submodel system (MESSy)-a new approach towards earth system modeling, Atmospheric Chemistry and Physics, 5, 433-444, https://doi.org/10.5194/acp-5-433-2005, 2005.
Jockel, P., Tost, H., Pozzer, A., Bruhl, C., Buchholz, J. and co-authors: The atmospheric chemistry general circulation model ECHAM5/MESSy1: consistent simulation of ozone from the surface to the mesosphere, Atmospheric Chemistry and Physics, 6, 5067-5104, https://doi.org/10.5194/acp-6-5067-2006, 2006.
Jockel, P., Tost, H., Pozzer, A., Kunze, M., Kirner, O. and co-authors: Earth system chemistry integrated modelling (ESCiMo) with the modular earth submodel system (MESSy) version 2.51, Geoscientific Model Development, 9, 1153-1200, https://doi.org/10.5194/gmd-9-1153-2016, 2016.

Jones, A. C., Hill, A., Remy, S., Abraham, N. L., Dalvi, M., Hardacre, C., Hewitt, A. J., Johnson, B., Mulcahy, J. P., and Turnock, S. T.: Exploring the sensitivity of atmospheric nitrate concentrations to nitric acid uptake rate using the Met Office's Unified Model, Atmospheric Chemistry and Physics, 21, 15901–15927, https://doi.org/10.5194/acp-21-15901-2021 , 2021.

Kakavas, S., & Pandis, S. N.: Effects of urban dust emissions on fine and coarse PM levels and composition, Atmospheric Environment, 246, 118006, https://doi.org/10.1016/j.atmosenv.2020.118006 , 2021.

Karydis, V. A., Tsimpidi, A. P., Fountoukis, C., Nenes, A., Zavala, M., Lei, W. F., Molina, L. T., and Pandis, S. N.: Simulating the fine and coarse inorganic particulate matter concentrations in a polluted megacity, Atmospheric Environment, 44, 608-620 , https://doi.org/10.1016/j.atmosenv.2009.11.023 , 2010.

Karydis, V. A., Tsimpidi, A. P., Pozzer, A., Astitha, M., and Lelieveld, J.: Effects of mineral dust on global atmospheric nitrate concentrations, Atmospheric Chemistry and Physics, 16, 1491-1509, https://doi.org/10.5194/acp-16-1491-2016, 2016.

Karydis, V. A., Tsimpidi, A. P., Bacer, S., Pozzer, A., Nenes, A., and Lelieveld, J.: Global impact of mineral dust on cloud droplet number concentration, Atmospheric Chemistry and Physics, 17, 5601-5621, https://doi.org/10.5194/acp-17-5601-2017, 2017.

Karydis, V. A., Tsimpidi, A. P., Pozzer, A., and Lelieveld, J.: How alkaline compounds control atmospheric aerosol particle acidity, Atmospheric Chemistry and Physics, 21, 14983-15001, https://doi.org/10.5194/acp-21-14983-2021, 2021.

Kerkweg, A., Sander, R., Tost, H., and Jöckel, P.: Technical note: Implementation of prescribed (OFFLEM), calculated (ONLEM), and pseudo-emissions (TNUDGE) of chemical species in the Modular Earth Submodel System (MESSy), Atmospheric Chemistry and Physics, 6, 3603–3609, https://doi.org/10.5194/acp-6-3603-2006 , 2006a.

Kerkweg, A., Buchholz, J., Ganzeveld, L., Pozzer, A., Tost, H., and Jöckel, P.: An implementation of the dry removal processes DRY DEPosition and SEDImentation in the Modular Earth Submodel System (MESSy), Atmospheric Chemistry and Physics, 6, 4617-4632, https://doi.org/10.5194/acp-6-4617-2006, 2006b.

Klingmüller, K., Metzger, S., Abdelkader, M., Karydis, V. A., Stenchikov, G. L., Pozzer, A., and Lelieveld, J.: Revised mineral dust emissions in the atmospheric chemistry-climate model EMAC (MESSy 2.52 DU_Astitha1 KKDU2017 patch), Geoscientific Model Development, 11, 989-1008, https://doi.org/10.5194/gmd-11-989-2018 , 2018.

Kusik, C. L. and Meissner H.P.: Electrolyte Activity Coefficients in Inorganic Processing, AIChE Symp. Series, 173, 14-20, 1978.

Lanz, V. A., Prévôt, A. S. H., Alfarra, M. R., Weimer, S., Mohr, C., DeCarlo, P. F., Gianini, M. F. D., Hueglin, C., Schneider, J., Favez, O., D'Anna, B., George, C., and Baltensperger, U.: Characterization of aerosol chemical composition with aerosol mass spectrometry in Central Europe: an overview, Atmospheric Chemistry and Physics, 10, 10453–10471, https://doi.org/10.5194/acp-10-10453-2010 , 2010.

Li, S., Zhang, F., Jin, X., Sun, Y., Wu, H., Xie, C., Chen, L., Liu, J., Wu, T., Jiang, S. and Cribb, M.,: Characterizing the ratio of nitrate to sulfate in ambient fine particles of urban Beijing during 2018–2019, Atmospheric environment, 237, 117662, https://doi.org/10.1016/j.atmosenv.2020.117662 , 2020.

Liu, L., Bei, N., Hu, B., Wu, J., Liu, S., Li, X., Wang, R., Liu, Z., Shen, Z. and Li, G.,: Wintertime nitrate formation pathways in the north China plain: Importance of N_2O_5 heterogeneous hydrolysis, Environmental Pollution, 266, 115287, https://doi.org/10.1016/j.envpol.2020.115287 , 2020.

Lohmann, U. and Ferrachat, S.: Impact of parametric uncertainties on the present-day climate and on the anthropogenic aerosol effect, Atmospheric Chemistry and Physics, 10, https://doi.org/10.5194/acp-10-11373-2010 , 2010.

Meissner, H. P. and Peppas, N. A.: Activity coefficients – aqueous solutions of polybasic acids and their salts, AIChE Journal,19, 806–809, https://doi.org/10.1002/aic.690190419, 1973.

Metzger, S., Dentener, F., Krol, M., Jeuken, A., & Lelieveld, J.: Gas/aerosol partitioning 2. Global modeling results, Journal of Geophysical Research: Atmospheres, 107, ACH-17, https://doi.org/10.1029/2001JD001103 , 2002.

Miao, R., Chen, Q., Zheng, Y., Cheng, X., Sun, Y., Palmer, P. I., Shrivastava, M., Guo, J., Zhang, Q., Liu, Y., Tan, Z., Ma, X., Chen, S., Zeng, L., Lu, K., and Zhang, Y.: Model bias in simulating major chemical components of $PM_{2.5}$ in China, Atmospheric Chemistry and Physics, 20, 12265–12284, https://doi.org/10.5194/acp-20-12265-2020 , 2020.

Milousis, A., Tsimpidi, A. P., Tost, H., Pandis, S. N., Nenes, A., Kiendler-Scharr, A., and Karydis, V. A.: Implementation of the ISORROPIA-lite aerosol thermodynamics model into the EMAC chemistry climate model (based on MESSy v2.55): implications for aerosol composition and acidity, Geoscientific Model Development, 17, 1111-1131, https://doi.org/10.5194/gmd-17-1111-2024 , 2024.

Milousis, A., Klingmüller, K., Tsimpidi, A. P., Kok, J. F., Kanakidou, M., Nenes, A., and Karydis, V. A.: Impact of mineral dust on the global nitrate aerosol direct and indirect radiative effect, EGUsphere [preprint], https://doi.org/10.5194/egusphere-2024-1579 , 2024.

Myhre, G., Samset, B. H., Schulz, M., Balkanski, Y., Bauer, S., Berntsen, T. K., Bian, H., Bellouin, N., Chin, M., Diehl, T., Easter, R. C., Feichter, J., Ghan, S. J., Hauglustaine, D., Iversen, T., Kinne, S., Kirkevåg, A., Lamarque, J. F., Lin, G., Liu, X., Lund, M. T., Luo, G., Ma, X., van Noije, T., Penner, J. E., Rasch, P. J., Ruiz, A., Seland, Ø., Skeie, R. B., Stier, P., Takemura, T., Tsigaridis, K., Wang, P., Wang, Z., Xu, L., Yu, H., Yu, F., Yoon, J. H., Zhang, K., Zhang, H., and Zhou, C.: Radiative forcing of the direct aerosol effect from AeroCom Phase II simulations, Atmospheric Chemistry and Physics, 13, 1853-1877, https://doi.org/10.5194/acp-13-1853-2013 , 2013.

Nair, A. A., & Yu, F.: Quantification of atmospheric ammonia concentrations: A review of its measurement and modeling, Atmosphere, 11, 1092, https://doi.org/10.3390/atmos11101092 , 2020.

Nair, H. R. C. R., Budhavant, K., Manoj, M. R., Andersson, A., Satheesh, S. K., Ramanathan, V., & Gustafsson, Ö.: Aerosol demasking enhances climate warming over South Asia, NPJ climate and atmospheric science, 6, 39, https://doi.org/10.1038/s41612-023-00367-6 , 2023.

Nenes, A., Pandis, S. N., Weber, R. J., and Russell, A.: Aerosol pH and liquid water content determine when particulate matter is sensitive to ammonia and nitrate availability, Atmospheric Chemistry and Physics, 20, 3249-3258, https://doi.org/10.5194/acp-20-3249-2020, 2020.

O'Neill, B. C., Tebaldi, C., van Vuuren, D. P., Eyring, V., Friedlingstein, P., Hurtt, G., Knutti, R., Kriegler, E., Lamarque, J.-F., Lowe, J., Meehl, G. A., Moss, R., Riahi, K., and Sanderson, B. M.: The Scenario Model Intercomparison Project (ScenarioMIP) for CMIP6, Geoscientific Model Development, 9, 3461–3482, https://doi.org/10.5194/gmd-9-3461-2016 , 2016.

Phillips, G. J., Thieser, J., Tang, M., Sobanski, N., Schuster, G., Fachinger, J., Drewnick, F., Borrmann, S., Bingemer, H., Lelieveld, J., and Crowley, J. N.: Estimating N_2O_5 uptake coefficients using ambient measurements of NO_3, N_2O_5, $ClNO_2$ and particle-phase nitrate, Atmospheric Chemistry and Physics, 16, 13231–13249, https://doi.org/10.5194/acp-16-13231-2016 , 2016.

Pinder, R. W., Adams, P. J., Pandis, S. N., & Gilliland, A. B.: Temporally resolved ammonia emission inventories: Current estimates, evaluation tools, and measurement needs, Journal of Geophysical Research: Atmospheres, 111, https://doi.org/10.1029/2005JD006603 , 2006.

Pozzer, A., Jöckel, P., Sander, R., Williams, J., Ganzeveld, L., and Lelieveld, J.: The MESSy-submodel AIRSEA calculating the air-sea exchange of chemical species, Atmospheric Chemistry and Physics, 6, 5435-5444, https://doi.org/10.5194/acp-6-5435-2006, 2006.

Pringle, K. J., Tost, H., Message, S., Steil, B., Giannadaki, D., Nenes, A., Fountoukis, C., Stier, P., Vignati, E., and Leieved, J.: Description and evaluation of GMXe: a new aerosol submodel for global simulations (v1), Geoscientific Model Development, 3, https://doi.org/10.5194/gmd-3-391-2010 , 2010a.

Pringle, K. J., Tost, H., Metzger, S., Steil, B., Giannadaki, D., Nenes, A., Fountoukis, C., Stier, P., Vignati, E., and Lelieveld, J.: Corrigendum to "Description and evaluation of GMXe: a new aerosol submodel for global simulations (v1)" published in Geoscientific Model Development, 3, 391–412, 2010, Geoscientific Model Development, 3(2), 413-413, https://doi.org/10.5194/gmd-3-413-2010 , 2010b.

Pye, H. O. T., Nenes, A., Alexander, B., Ault, A. P., Barth, M. C., Clegg, S. L., Collett Jr., J. L., Fahey, K. M., Hennigan, C. J., Herrmann, H., Kanakidou, M., Kelly, J. T., Ku, I.-T., McNeill, V. F., Riemer, N., Schaefer, T., Shi, G., Tilgner, A., Walker, J. T., Wang, T., Weber, R., Xing, J., Zaveri, R. A., and Zuend, A.: The acidity of atmospheric particles and clouds, Atmospheric Chemistry and Physics, 20, 4809–4888, https://doi.org/10.5194/acp-20-4809-2020 , 2020.

Qu, Y., Chen, Y., Liu, X., Zhang, J., Guo, Y., & An, J.: Seasonal effects of additional HONO sources and the heterogeneous reactions of N_2O_5 on nitrate in the North China Plain, Science of the Total Environment, 690, 97-107, https://doi.org/10.1016/j.scitotenv.2019.06.436 , 2019.

Randerson, J.T., G.R. van der Werf, L. Giglio, G.J. Collatz, and P.S. Kasibhatla: Global Fire Emissions Database, Version 4.1 (GFEDv4). ORNL DAAC, Oak Ridge, Tennessee, USA. https://doi.org/10.3334/ORNLDAAC/1293 , 2017.

Reis, S., Pinder, R. W., Zhang, M., Lijie, G., and Sutton, M. A.: Reactive nitrogen in atmospheric emission inventories, Atmospheric Chemistry and Physics, 9, 7657–7677, https://doi.org/10.5194/acp-9-7657-2009 , 2009.

Roeckner, E., Brokopf, R., Esch, M., Giorgetta, M., Hagemann, S., Kornblueh, L., Manzini, E., Schlese, U., and Schulzweida, U.: Sensitivity of simulated climate to horizontal and vertical resolution in the ECHAM5 atmosphere model, Journal of Climate, 19, 3771-3791, https://doi.org/10.1175/JCLI3824.1 , 2006.

Sander, R., Baumgaertner, A., Cabrera-Perez, D., Frank, F., Gromov, S., Grooss, J. U., Harder, H., Huijnen, V., Jockel, P., Karydis, V. A., Niemeyer, K. E., Pozzer, A., Hella, R. B., Schultz, M. G., Taraborrelli, D., and Tauer, S.: The community atmospheric chemistry box model CAABA/MECCA-4.0, Geoscientific Model Development, 12, 1365-1385, https://doi.org/10.5194/gmd-12-1365-2019 , 2019.

Schaap, M., van Loon, M., ten Brink, H. M., Dentener, F. J., and Builtjes, P. J. H.: Secondary inorganic aerosol simulations for Europe with special attention to nitrate, Atmospheric Chemistry and Physics, 4, 857–874, https://doi.org/10.5194/acp-4-857-2004 , 2004.

Seinfeld, J. H. and Pandis, S. N.: Atmospheric chemistry and physics: from air pollution to climate change. John Wiley & Sons, ISBN 1118947401, 2016.

Song, S., Gao, M., Xu, W., Shao, J., Shi, G., Wang, S. and co-authors: Fine-particle pH for Beijing winter haze as inferred from different thermodynamic equilibrium models, Atmospheric Chemistry and Physics, 18, 7423-7438, https://doi.org/10.5194/acp-18-7423-2018, 2018.

Stier, P., Feichter, J., Kinne, S., Kloster, S., Vignati, E., Wilson, J., Ganzeveld, L., Tegen, I., Werner, M., Balkanski, Y., Schulz, M., Boucher, O., Minikin, A., and Petzold, A.: The aerosol-climate model ECHAM5-HAM, Atmospheric Chemistry and Physics, 5, 1125–1156, https://doi.org/10.5194/acp-5-1125-2005 , 2005.

Storelvmo, T., Leirvik, T., Lohmann, U., Phillips, P. C., & Wild, M.: Disentangling greenhouse warming and aerosol cooling to reveal Earth's climate sensitivity, Nature Geoscience, 9, 286-289, https://doi.org/10.1038/ngeo2670 , 2016.

Sutton, M. A., Reis, S., Riddick, S. N., Dragosits, U., Nemitz, E., Theobald, M. R., Tang, Y. S., Braban, C. F., Vieno, M., Dore, A. J., Mitchell, R. F., Wanless, S., Daunt, F., Fowler, D., Blackall, T. D., Milford, C., Flechard, C. R., Loubet, B., Massad, R., Cellier, P., Personne, E., Coheur, P. F., Clarisse, L., Van Damme, M., Ngadi, Y., Clerbaux, C., Skjøth, C. A., Geels, C., Hertel, O., Wichink Kruit, R. J., Pinder, R. W., Bash, J. O., Walker, J. T., Simpson, D., Horváth, L., Misselbrook, T. H., Bleeker, A., Dentener, F., and de Vries, W.: Towards a climate-dependent paradigm of ammonia emission and deposition, Philosophical Transactions of the Royal Society B: Biological Sciences, 368, https://doi.org/10.1098/rstb.2013.0166 , 2013.

The Acid Deposition Monitoring Network in East Asia, available at : https://monitoring.eanet.asia/document/public/index

Tilgner, A., Schaefer, T., Alexander, B., Barth, M., Collett Jr., J. L., Fahey, K. M., Nenes, A., Pye, H. O. T., Herrmann, H., and McNeill, V. F.: Acidity and the multiphase chemistry of atmospheric aqueous particles and clouds, Atmospheric Chemistry and Physics, 21, 13483–13536, https://doi.org/10.5194/acp-21-13483-2021 , 2021.

Tost, H., Jockel, P. J., Kerkweg, A., Sander, R., and Lelieveld, J.: Technical note: A new comprehensive SCAVenging submodel for global atmospheric chemistry modelling, Atmospheric Chemistry and Physics, 6, 565-574, https://doi.org/10.5194/acp-6-565-2006 , 2006.

Tost, H., Jöckel, P., and Lelieveld, J.: Lightning and convection parameterisations - uncertainties in global modelling, Atmospheric Chemistry and Physics, 7, 4553-4568, https://doi.org/10.5194/acp-7-4553-2007 , 2007a.

Tost, H., Jockel, P., Kerkweg, A., Pozzer, A., Sander, R., and Lelieveld, J.: Global cloud and precipitation chemistry and wet deposition: tropospheric model simulations with ECHAM5/MESSy1, Atmospheric Chemistry and Physics, 7, 2733-2757, https://doi.org/10.5194/acp-7-2733-2007 , 2007b.

Tsimpidi, A. P., Karydis, V. A., Pozzer, A., Pandis, S. N., and Lelieveld, J.: ORACLE (v1. 0): module to simulate the organic aerosol composition and evolution in the atmosphere, Geoscientific Model Development, 7, 3153-3172, https://doi.org/10.5194/gmd-7-3153-2014, 2014.

Tsimpidi, A. P., Karydis, V. A., Pandis, S. N., and Lelieveld, J.: Global combustion sources of organic aerosols: model comparison with 84 AMS factor-analysis data sets, Atmospheric Chemistry and Physics, 16, 8939–8962, https://doi.org/10.5194/acp-16-8939-2016 , 2016.

Tsimpidi, A. P., Karydis, V. A., Pozzer, A., Pandis, S. N., and Lelieveld, J.: ORACLE 2-D (v2.0): an efficient module to compute the volatility and oxygen content of organic aerosol with a global chemistry–climate model, Geoscientific Model Development, 11, 3369-3389, https://doi.org/10.5194/gmd-11-3369-2018 , 2018.

Tsimpidi, A. P., Scholz, S. M. C., Milousis, A., Mihalopoulos, N., and Karydis, V. A.: Aerosol Composition Trends during 2000–2020: In depth insights from model predictions and multiple worldwide observation datasets, EGUsphere [preprint], https://doi.org/10.5194/egusphere-2024-3590 , 2024.

U.S. Environmental Protection Agency Clean Air Markets Division Clean Air Status and Trends Network (CASTNET), available at *:* https://www.epa.gov/castnet

Vignati, E., Wilson, J., and Stier, P.: M7: An efficient size-resolved aerosol microphysics module for large-scale aerosol transport models, Journal of Geophysical Research: Atmospheres, 109, https://doi.org/10.1029/2003JD004485, 2004.

Walker, J. M., Philip, S., Martin, R. V., and Seinfeld, J. H.: Simulation of nitrate, sulfate, and ammonium aerosols over the United States, Atmospheric Chemistry and Physics, 12, 11213–11227, https://doi.org/10.5194/acp-12-11213-2012 , 2012.

Wang, H., Chen, X., Lu, K., Tan, Z., Ma, X., Wu, Z., Li, X., Liu, Y., Shang, D., Wu, Y. and Zeng, L.,: Wintertime N_2O_5 uptake coefficients over the North China Plain, Science bulletin, 65, 765-774, https://doi.org/10.1016/j.scib.2020.02.006 , 2020.

Wang, Y., Zhang, Q. Q., He, K., Zhang, Q., and Chai, L.: Sulfate-nitrate-ammonium aerosols over China: response to 2000–2015 emission changes of sulfur dioxide, nitrogen oxides, and ammonia, Atmospheric Chemistry and Physics, 13, 2635–2652, https://doi.org/10.5194/acp-13-2635-2013 , 2013.

Xie, X., Hu, J., Qin, M., Guo, S., Hu, M., Wang, H., Lou, S., Li, J., Sun, J., Li, X. and Sheng, L.,: Modeling particulate nitrate in China: Current findings and future directions, Environment International, 166, 107369, https://doi.org/10.1016/j.envint.2022.107369 , 2022.

Yienger, J. J. and Levy, H.: Empirical model of global soil-biogenic NOx emissions, Journal of Geophysical Research: Atmospheres, 100, 11447-11464, https://doi.org/10.1029/95JD00370, 1995.

Yu, X. Y., Lee, T., Ayres, B., Kreidenweis, S. M., Collett, J. L., & Malm, W.: Particulate Nitrate Measurement Using Nylon Filters, Journal of the Air & Waste Management Association, 55, 1100–1110. https://doi.org/10.1080/10473289.2005.10464721 , 2005.

Zakoura, M. and Pandis, S. N.: Overprediction of aerosol nitrate by chemical transport models: The role of grid resolution, Atmospheric Environment, 187, 390-400, https://doi.org/10.1016/j.atmosenv.2018.05.066, 2018.

Zakoura, M., & Pandis, S. N.: Improving fine aerosol nitrate predictions using a Plume-in-Grid modeling approach, Atmospheric Environment, 215, 116887, https://doi.org/10.1016/j.atmosenv.2019.116887 , 2019.

Zhang, X., Wu, Y., Liu, X., Reis, S., Jin, J., Dragosits, U., Van Damme, M., Clarisse, L., Whitburn, S., Coheur, P.F. and Gu, B.,: Ammonia emissions may be substantially underestimated in China, Environmental Science & Technology, 51, 12089-12096, https://doi.org/10.1021/acs.est.7b02171 , 2017.

4 Dust-Nitrate interactions and their importance in the radiative effects of NO_3^- aerosols

The content of this chapter was accepted for publication as : “Impact of mineral dust on the global nitrate aerosol direct and indirect radiative effect” by A. Milousis, K. Klingmüller, A. P. Tsimpidi, J. F. Kok, M. Kanakidou, A. Nenes, and V. A. Karydis in Atmospheric Chemistry and Physics, 2024, DOI: https://doi.org/10.5194/egusphere-2024-1579 under the Creative Commons 4.0 License (https://creativecommons.org/licenses/by/4.0/deed.en).

The supplementary material is provided in Appendix A.4. The data produced in the study are available from the authors upon request. The authors contributed to the article as follows:

AM and VAK wrote the paper with contributions from KK, APT, JFK, MK, and AN. VAK planned the research with contributions from APT, MK and AN. AM, KK and VAK designed the methodology for the radiative effect calculations. AM performed the simulations and analyzed the results, assisted by VAK and APT. All the authors discussed the results and contributed to the paper.

Impact of mineral dust on the global nitrate aerosol direct and indirect radiative effect

Alexandros Milousis[1], Klaus Klingmüller[2], Alexandra P. Tsimpidi[1], Jasper F. Kok[3], Maria Kanakidou[4,5,6], Athanasios Nenes[5,7], and Vlassis A. Karydis[1]

[1]Institute for Energy and Climate Research, IEK-8 Troposphere, Forschungszentrum Jülich GmbH, Jülich, Germany
[2]Max Planck Institute for Chemistry, Mainz, Germany
[3]Department of Atmospheric and Oceanic Sciences, University of California Los Angeles, Los Angeles, CA, USA.
[4]Environmental Chemical Processes Laboratory, Department of Chemistry, University of Crete, Heraklion, Greece
[5]Center for the Study of Air Quality and Climate Change, Foundation for Research & Technology Hellas, Patras, Greece
[6]Institute of Environmental Physics, University of Bremen, Bremen, Germany
[7]Laboratory of Atmospheric Processes and Their Impacts, Ecole Polytechnique Fédérale de Lausanne, Switzerland

Correspondence to: Vlassis A. Karydis (v.karydis@fz-juelich.de)

Abstract

Nitrate (NO_3^-) aerosol is projected to increase dramatically in the coming decades and may become the dominant inorganic particle species. This is due to the continued strong decrease in SO_2 emissions, which is not accompanied by a corresponding decrease in NO_x and especially NH_3 emissions. Thus, the radiative effect (RE) of NO_3^- aerosol may become more important than that of SO_4^{2-} aerosol in the future. The physicochemical interactions of mineral dust particles with gas and aerosol tracers play an important role in influencing the overall RE of dust and non-dust aerosols but can be a major source of uncertainty due to their lack of representation in many global climate models. Therefore, this study investigates how and to what extent dust affects the current global NO_3^- aerosol radiative effect through both radiation (RE_{ari}) and cloud interactions (RE_{aci}) at the top of the atmosphere (TOA). For this purpose, multi-year simulations nudged towards the observed atmospheric circulation were performed with the global atmospheric chemistry and climate model EMAC, while the thermodynamics of the interactions between inorganic aerosols and mineral dust were simulated with the thermodynamic equilibrium model ISORROPIA-lite. The emission flux of the mineral cations Na^+, Ca^{2+}, K^+ and Mg^{2+} is calculated as a fraction of the total aeolian dust emission based on the unique chemical composition of the major deserts worldwide. Our results reveal positive and negative shortwave and longwave radiative effects in different regions of the world via aerosol-radiation interactions and cloud adjustments. Overall, the NO_3^- aerosol direct effect contributes a global cooling of -0.11 W/m^2, driven by fine-mode particle cooling at short wavelengths. Regarding the indirect effect, it is noteworthy that NO_3^- aerosol exerts a global mean warming of +0.17 W/m^2. While the presence of NO_3^- aerosol enhances the ability of mineral dust particles to act as cloud condensation nuclei (CCN), it simultaneously inhibits the formation of cloud droplets from the smaller anthropogenic particles. This is due to the coagulation of fine anthropogenic CCN particles with the larger nitrate-coated mineral dust particles, which leads to a reduction in total aerosol number concentration. This mechanism results in an overall reduced cloud albedo effect and is thus attributed as warming.

Keywords: direct radiative effect, indirect radiative effect, nitrate aerosols, mineral dust

1. Introduction

Atmospheric aerosols are among the most complex components of the Earth's climate system. This is due not only to the diversity of their origins, with many natural and anthropogenic emission sources, but also to their extremely varied chemical composition and properties. The many mechanisms by which they interact with each other and with physical entities such as radiation, clouds, land, and oceans add to their complexity and play a critical role in the energy balance of the planet (Arias et al., 2021). The most direct way in which aerosols affect the Earth's energy balance is through their interactions with solar shortwave (SW) and terrestrial longwave (LW) radiation (IPCC, 2013). Overall, the radiative effect due to aerosol-radiation interactions (RE_{ari}) is mainly dominated by the scattering of SW radiation back to space (negative radiative effect, generating a cooling of the climate system) and the absorption of LW radiation (positive radiative effect, generating a warming of the climate system) (Gao et al., 2018; Tsigaridis and Kanakidou, 2018). Aerosols belonging to the black and/or brown carbon family, together with mineral dust particles, contribute to absorption (Kanakidou et al., 2005; Zhang et al., 2017; Wong et al., 2019), while the main inorganic aerosol components, such as sulfate and nitrate, as well as a significant amount of organic carbon contribute mainly to scattering (Kirchstetter et al., 2004; (Bond and Bergstrom, 2006; Klingmüller et al., 2019; Zhang, 2020). However, mineral dust can also influence the behavior of the RE_{ari} of anthropogenic pollution. Dust particles alter the anthropogenic radiative effect of aerosol-radiation interactions by reducing the loading of anthropogenic aerosols (either by coagulating with them or by adsorption of their precursor inorganic trace gases), leading to less scattering of solar radiation and thus a warming effect (Kok et al., 2023).

Atmospheric aerosols can also indirectly affect the Earth's energy balance by forming clouds, controlling cloud optical thickness and scattering properties, and altering their precipitation and lifetime (IPCC, 2013). Atmospheric aerosols act as cloud condensation nuclei (CCN), providing a suitable surface for water vapor to condense, leading to the formation of liquid droplets that develop into a corresponding liquid cloud (Lance et al., 2004). Such clouds are referred to as warm clouds and are typically found in the lower troposphere (Khain and Pinsky, 2018). However, there is constant competition between small and large particles for the available amount of water vapor (Barahona et al., 2010; Morales and Nenes, 2014). Under the same humidity conditions, the presence of small particles will lead to the formation of small droplets with high number concentrations, while the presence of larger particles will lead to the formation of large droplets but with lower number concentrations. Depending on the size characteristics of its particle population, a warm cloud will exhibit different optical properties, with a population dominated by smaller particles generally being more reactive in the SW spectrum. The change in cloud reflectivity due to the presence of aerosols is referred to as the first radiative effect due to aerosol-cloud interactions (RE_{aci}) and was first described by Twomey (1977). The small size of anthropogenic aerosols results in an overall smaller cloud droplet size, which reduces precipitation efficiency and thus increases cloud lifetime. This contributes to cloud reflectivity and is referred to as the second radiative effect of aerosol cloud-interactions, first described by Albrecht (1989). These two indirect effects are considered equally important for the total indirect radiative effect of aerosols (Lohmann and Feichter, 2005). Atmospheric aerosols exert a net cooling effect that can partially mask the warming effect of greenhouse gases, therefore, the recent decline in

anthropogenic aerosol concentrations may accelerate global warming (Urdiales-Flores et al., 2023). Overall, the radiative effect due to aerosol-cloud interactions is considered the main source of existing uncertainty in the effective (total) radiative effect of aerosols in the atmosphere (Myhre et al., 2014; Seinfeld et al., 2016).

Mineral dust influences the anthropogenic radiative effect through aerosol-cloud interactions in several ways that can result in either a net warming or net cooling effect. Dust particles can increase the of cloud droplet number concentrations (CDNC) in remote areas since through chemical aging by pollutants (Nenes et al., 2014; Karydis et al., 2017), dust particles become more hygroscopic and require lower supersaturation thresholds for activation (Karydis et al., 2011). This is caused by the transfer of anthropogenic pollutants towards remote desert regions which enhances the solubility of dust particles. In such regions, this mostly results in increased cloud albedo and a net cooling effect. However, dust particles also tend to reduce the availability of smaller anthropogenic CCN. This is due to intrusions of aged dust particles into polluted environments which reduce the numbers of smaller aerosols through increased coagulation with them. This results in lower cloud reflectivity (albedo) and thus a net warming effect (Klingmüller et al., 2020). Furthermore, when dust is above or below low-level clouds, the resulting effect of local heating is an increase in total cloud cover due to enhanced temperature inversion or enhanced upward vertical motion, respectively (Kok et al., 2023). On the other hand, when dust is present inside low-level clouds, local heating enhances in-cloud evaporation, resulting in an overall decrease in cloud cover. Kok et al. (2023) showed that the amount of desert dust in the atmosphere has increased since the mid-19th century, causing an overall cooling effect on the Earth that masks up to 8% of the warming caused by greenhouse gases. If the increase in dust were halted, the previously hidden additional warming potential of greenhouse gases could lead to slightly faster climate warming.

NO_3^- is expected to dominate the global aerosol composition in the coming decades due to the predicted limited availability of SO_4^{-2} following the abrupt decline in SO_2 emissions, which will not necessarily be accompanied by proportional reductions in NO_x and NH_3 emissions (Bellouin et al., 2011; Hauglustaine et al., 2014). Excess NO_3^- is expected to exert a cooling RE_{ari} by scattering SW radiation (Bauer et al., 2007a; Xu and Penner, 2012; Myhre et al., 2013; IPCC, 2013; Li et al., 2015), but the RE_{aci} is much more complex and complicated and can lead to both cooling and warming. Mineral dust thus becomes a key factor, as it is one of the main promoters of NO_3^- aerosol formation, providing a very suitable surface for gaseous HNO_3 condensation to the aerosol phase (Karydis et al., 2011; Trump et al., 2015). In addition to HNO_3 adsorption, heterogeneous reactions on the surface of dust particles are known to promote nitrate formation (Krueger et al.,2004; Hodzic et al.,2006). The most important pathway through which this occurs is N_2O_5 hydrolysis with a yield for aerosol nitrate of ~2 (Seisel et al.,2005; Tang et al.,2012). At the same time, other reactions, such as NO_2 oxidation, contribute to much slower nitrate production and are of major importance mainly during short periods of dust pollution events (Li et al., 2024). These processes affect not only the optical properties of dust aerosols, which will influence their overall RE_{ari}, but also how they can alter cloud formation and microphysics. NO_3^- aerosols increase the hygroscopicity of mineral dust (Kelly et al., 2007) by providing layers of soluble material on their surface, thus increasing their ability to act as CCN (Karydis et al., 2017). In doing so, they also increase the size of dust particles through hygroscopic growth and therefore their coagulation efficiency. Thus, nitrate-dust interactions are a complex mechanism that ultimately affects

climatology in a variety of ways. The role of mineral dust in modifying the influence of NO_3^- aerosols in the global RE_{aci} is not yet well understood. This study aims to focus on the extent of the RE_{ari} and RE_{aci} of NO_3^- aerosols and on how interactions with mineral dust regulate both on a global scale.

This study is organized as follows: in Section 2, details of the modeling setup for conducting the global simulations as well as the treatment of dust-nitrate interactions in the model are discussed and the methodology for calculating the global RE_{ari} and RE_{aci} of NO_3^- aerosols is explained. Section 3 presents the main results for the global RE_{ari} for coarse and fine NO_3^- aerosols for the base case simulation and the sensitivity cases listed in Table 1. Section 4 presents the results for the global RE_{aci} of total NO_3^- aerosols, while section 5 includes the feedback mechanism of dust-nitrate interactions with cloud microphysics. Finally, the main conclusions and a general discussion on the scope of the study are presented in section 6.

2. Methodology

2.1 Model Setup

The simulations were performed with the global atmospheric chemistry and climate model EMAC (ECHAM/MESSy) (Jockel et al., 2006), which includes several submodels describing atmospheric processes and their interactions with oceans, land, and human influences. These submodels are linked through the Modular Earth Submodel System (MESSy) (Jockel et al., 2005) to a base model, the 5th Generation European Center Hamburg General Circulation Model (ECHAM) (Roeckner et al., 2006). The submodel system used in this work includes the MECCA submodel, which performs the gas phase chemistry calculations (Sander et al., 2019). The SCAV submodel is responsible for the in-cloud liquid-phase chemistry and wet deposition processes (Tost et al., 2006; Tost et al., 2007b), while DRYDEP and SEDI are used to compute the dry deposition of gases and aerosols and gravitational settling, respectively (Kerkweg et al., 2006). All aerosol microphysical processes are calculated by the GMXe submodel (Pringle et al., 2010a; Pringle et al., 2010b), where aerosols are divided into 4 lognormal size modes (nucleation, Aitken, accumulation and coarse). Each mode is defined in terms of aerosol number concentration, number mean dry radius, and geometric standard deviation (sigma). The mean dry radius for each mode is allowed to vary within fixed bounds (0.5 nm – 6 nm for nucleation, 6 nm - 60 nm for Aitken, 60 nm - 700 nm for accumulation, and above 700 for coarse) and the sigma is fixed and equal to 1.59 for the first three size modes and 2 for the coarse mode. The coagulation of aerosols is also handled by GMXe, following Vignati et al. (2004) and the coagulation coefficients for Brownian motion are calculated according to Fuchs and Davies (1964). The partitioning between the gas and aerosol phases is calculated using the ISORROPIA-lite thermodynamic module (Kakavas et al., 2022) as implemented in EMAC by Milousis et al. (2024). The optical properties of the aerosols and the radiative transfer calculations are simulated by the submodels AEROPT (Dietmuller et al., 2016) and RAD (Dietmuller et al., 2016), respectively. AEROPT can be called several times within a model time step with different settings for the aerosol properties. More details are given in section 2.3.1. All cloud properties and microphysical processes are simulated by the CLOUD submodel (Roeckner et al., 2006) using the two-moment microphysical scheme of Lohmann and Ferrachat (2010) for liquid and ice clouds. The activation processes of liquid cloud droplets and ice crystals follow the physical treatment of Morales and Nenes (2014) and Barahona and Nenes (2009),

respectively, as described by Karydis et al. (2017) and Bacer et al. (2018). More details are given in Section 2.3.2.

The meteorology for each of the simulations was nudged by ERA5 reanalysis data (C3S, 2017), thus this study estimates the radiative effect of nitrate aerosols with respect to RE_{ari} and RE_{aci} separately, rather than the effective (total) radiative effect, as this would require multiple free-run simulations with prescribed sea surface temperatures for each case separately. The spectral resolution used for each simulation was T63L31, which corresponds to a grid resolution of $1.875° \times 1.875°$ and 31 vertical layers up to 25 km in height. The period covered by the simulations is from 2007 to 2018, with the first year representing the model spin-up period.

Anthropogenic aerosol and trace gas emissions were taken from the CMIP6 database (O'Neill et al., 2016) according to the SSP370 scenario. Natural NH_3 emissions (from land and ocean) were based on the GEIA database (Bouwman et al., 1997), and natural volcanic SO_2 emissions were taken from the AEROCOM database (Dentener et al., 2006). Biogenic NO emissions from soils were calculated online according to the algorithm of Yienger and Levy (1995), while lightning-produced NO_x was also calculated online by the LNOx submodel (Tost et al., 2007a) using the parameterization of Grewe et al. (2001). DMS emissions from the oceans are calculated online by the AIRSEA submodel (Pozzer et al., 2006). Sea salt emissions are based on the AEROCOM database (Dentener et al., 2006) following the chemical composition reported by Seinfeld and Pandis (2016), i.e. 30.6% Na^+, 3.7% Mg^+, 1.2% Ca^{2+}, 1.1% K^+, and 55% Cl^-. Dust emissions are calculated online using the parameterization of Astitha et al. (2012). In this scheme, while the surface friction velocity is the most important parameter for the amount of the emitted dust flux, the meteorological information for each grid cell is also taken into account. Dust particles are emitted in the accumulation and coarse size modes of the insoluble fraction but can be transferred to the soluble fraction after either coagulation with other soluble species and/or by condensation of soluble material on their surface. Both processes are treated and calculated by GMXe and ISORROPIA-lite. The emissions of mineral ions (Ca^{2+}, Mg^{2+}, K^+, and Na^+) are estimated as a fraction of the total dust emission flux based on the soil chemical composition of each grid cell. This is done using desert soil composition maps from Klingmüller et al. (2018) which are based on the mineral ion fractions from Karydis et al. (2016). These mineral ions are treated as individual species that are part of the aerosol in each size mode and are assumed to be well mixed with the rest of the aerosol species considered (i.e., dust, black carbon, organics, inorganic ions). The aerosol composition within each of the seven modes considered is uniform in size (internally mixed), but may vary between modes (externally mixed).

To assess the impact of changes in mineral dust chemistry and emissions on the global NO_3^- aerosol RE_{ari} and RE_{aci}, four additional sensitivity simulations were performed (Table 1). In the first sensitivity simulation, mineral dust is described only by a bulk, chemically inert species. In this case, there is no uptake of HNO_3 by the dust particles due to acid-base interactions with the non-volatile cations (NVCs), and so it remains in the gas phase. In the second sensitivity case, the chemical composition of the mineral dust was assumed to be spatially uniform, with a percentage distribution for bulk dust, Na^+, K^+, Ca^{2+} and Mg^{2+} particles assumed to be 94%, 1.2%, 1.5%, 2.4% and 0.9% respectively according to Sposito (1989). Finally, two additional simulations were performed to assess the impact of the global mineral dust budget on the results, where the dust emission fluxes were first halved and then increased by 50% to account for the historical increase

in global dust mass load since pre-industrial times, as reconstructed by Kok et al. (2023). The particle size distribution of the emitted dust mass remained unchanged in all sensitivity simulations.

Overall, the EMAC model is well established in the literature for its ability to accurately predict organic and inorganic aerosol concentrations and compositions, aerosol optical depth, acid deposition, gas-phase mixing ratios, cloud properties, and meteorological parameters (de Meij et al., 2012; Pozzer et al., 2012, 2022; Tsimpidi et al., 2016, 2017; Karydis et al., 2016, 2017; Bacer et al., 2018; Milousis et al., 2024), factually replicate dust emissions (Astitha et al., 2012; Abdelkader et al., 2015; Klingmüller et al., 2018), and provide realistic estimates for CCN and CDNC (Chang et al., 2017; Karydis et al., 2017; Fanourgakis et al., 2019). Here, a comparison of the performance of the model in estimating the surface mass concentrations of $PM_{2.5}$ NO_3^- and total PM_{10} aerosols is provided in the supplemental material (Figures S2, S3 and Tables S1, S2). In addition, the ability of the model to estimate CDNCs is evaluated (Figure S4 and Table S3). The comparison is made with observations of $PM_{2.5}$ nitrate aerosols from regional networks in the polluted northen hemisphere covering the regions of East Asia (EANET, The Acid Deposition Monitoring Network in East Asia), Europe (EMEP, European Monitoring and Evaluation Programme) and the USA for urban (EPA-CASTNET, U.S. Environmental Protection Agency Clean Air Status and Trends Network) and rural (IMPROVE, Interagency Monitoring of Protected Visual Environments) locations. The comparison with observations of surface mass PM_{10} aerosols also covers the above mentioned monitoring networks, with the exception of the EPA. Finally, the CDNCs estimated by the base case simulation are compared with the CDNCs observed in different regions of the planet (continental, polluted and clean marine) over different time periods, but also altitudes, as found in Karydis et al., (2017) and all relevant references therein.

Table 1: Differences between the base case and all sensitivity simulations performed.

Simulation Name	Conditions Applied
Base Case	Mineral dust ion composition according to Karydis et al. (2016)[1]
Sensitivity 1: Chemically Inert Dust	Mineral dust emitted exclusively as a chemically inert bulk particle
Sensitivity 2: Homogeneous Ion Composition	Global homogeneous ionic composition of mineral dust particles according to Sposito (1989)[2]
Sensitivity 3: Half Dust Scenario	50% reduced dust emission flux
Sensitivity 4: Increased Dust Scenario	50% increased dust emission flux

2.2 Treatment of Dust-Nitrate Interactions

The interactions between mineral dust and nitrate aerosols play a crucial role in altering the size distribution and optical properties of both species and can also strongly influence cloud microphysical processes (Fig. 1). Therefore, these interactions affect both the RE_{ari} and the RE_{aci} of both nitrate and dust aerosols. First, the adsorption of HNO_3 onto the surface of dust particles is a process that strongly promotes the formation of nitrate aerosols on dust (Karydis et al., 2016). We treat this condensation process using the GMXe submodel. Specifically, the amount of gas phase species that kinetically condenses within a model time step (equal to 10 minutes in this study) is calculated according to the diffusion-limited condensation theory of Vignati et al. (2004). The diffusive flux of gas on a single particle surface for each size mode *i* is described by the

[1] The ionic composition of the dust particles with respect to the mineral ions Ca^{2+}, Mg^{2+}, K^{+}, and Na^{+} depends on the chemical composition of the soil in each grid cell, which is estimated from the desert soil composition maps of Klingmüller et al. (2018) based on the fraction of mineral ions present found in Karydis et al. (2016).

[2] The ionic composition of the dust particles is homogeneous and held constant in all grid cells where dust is present. The dust particles are a mixture of bulk species and the mineral ions Na^{+}, K^{+}, Ca^{2+} and Mg^{2+} with mass fraction of 94%, 1.2%, 1.5%, 2.4% and 0.9% respectively.

condensation coefficient C_i according to Fuchs and Davies (1964) and is estimated from the following function as found in Vignati et al. (2004).

$$C_i = \frac{4\pi D r_{gi}}{\frac{4D}{svr_{gi}} + \frac{r_{gi}}{r_{gi} + \Delta}}$$

Where r_{gi} is the geometric mean radius of the size mode *i*, D is the diffusion coefficient, s is an accommodation coefficient for each gas species treated and has the assigned values of 1 for H_2SO_4 (Vignati et al. 2004), 0.1 for HNO_3, 0.064 for HCl and 0.09 for NH_3 (Pringle et al., 2010a; Pringle et al., 2010b). v is the mean thermal velocity of the molecule and Δ is the mean free path length of the gas molecule (the distance from which the kinetic regime applies with respect to the particle).This information is then passed to the ISORROPIA-lite thermodynamic module to calculate the gas/aerosol partitioning. Specifically, the module receives as input the ambient temperature and humidity along with the diffusion-limited concentrations of H_2SO_4, NH_3, HNO_3, and HCl, the concentrations of the non-volatile cations (NVCs) Na^+, K^+, Ca^{2+} and Mg^{2+}, and the concentrations of the ions SO_4^{2-}, NO_3^-, NH_4^+, and Cl^- present in the aerosol phase from the previous time step. The module then calculates the equilibrium reactions of the NO_3^- anion with the NVCs, depending on their abundance with respect to the SO_4^{2-} anion, taking into account mass conservation, electroneutrality, water activity equations and precalculated activity coefficients for specific ionic pairs (Fountoukis and Nenes, 2007; Kakavas et al., 2022). Therefore, in all cases where mineral dust is considered chemically active, all reactions of nitrate aerosols with NVC are treated. The salts that may be formed are assumed to be completely deliquesced as follows:

$$Ca(NO_3)_2 \rightarrow Ca^{2+}_{(aq)} + 2NO^-_{3(aq)}$$

$$NaNO_3 \rightarrow Na^+_{(aq)} + NO^-_{3(aq)}$$

$$KNO_3 \rightarrow K^+_{(aq)} + NO^-_{3(aq)}$$

$$Mg(NO_3)_2 \rightarrow Mg^{2+}_{(aq)} + 2NO^-_{3(aq)}$$

Salt deliquescence over a range of relative humidities is treated by the Mutual Deliquescence Relative Humidity (MDRH) approach of Wexler and Seinfeld (1991). In a multicomponent salt mixture, the MDRH determines the humidity value above which all salts are considered to be saturated. In this study, if the wet aerosol is below the MDRH, it does not crystalize and remains in a supersaturated aqueous solution (Kakavas et al., 2022), with all salts completely deliquesced. More information on equilibrium reactions and equilibrium constants as well as the corresponding thermodynamic equilibrium calculations can be found in Fountoukis and Nenes (2007). It should be noted that in this study nitrate production on dust particles does not only occur via the thermodynamic equilibrium between gas-phase HNO_3 and particulate nitrate, but also via heterogeneous chemistry by hydrolysis of N_2O_5 on the dust surface. This chemical formation pathway is the most dominant for heterogeneous nitrate production (Seisel et al., 2005; Tang et al., 2012), while others, such as NO_2 oxidation during dust pollution events over polluted regions (Li et al., 2024), do not show such high yields under normal conditions. On the other hand, consideration of sulphate production by heterogeneous chemistry on dust would theoretically result in slightly reduced amounts of particulate nitrate in some cases due to acidification of dust

particles inhibiting partitioning of HNO_3 to the aerosol phase (Nenes et al., 2020). Overall, full consideration of heterogeneous chemistry on dust could change simulated nitrate aerosol concentrations only slightly and episodically, and therefore changes to radiative effect estimates are not expected to be critical.

The coating of dust particles by nitrate aerosols during gas/aerosol partitioning calculations is an important process that leads to an increase in dust solubility and hygroscopicity (Laskin et al., 2005). Therefore, after these processes have taken place, a large fraction of the originally insoluble dust particles has become soluble (Fig. 1a), which leads to changes in their optical properties, as their increased ability to absorb water makes them more efficient in extinguishing SW radiation and absorbing and emitting LW radiation (Fig. 1a, 1b) (Kok et al., 2023). The transfer to the soluble fraction after coating with soluble material is handled by the GMXe submodel, which also provides key aerosol attributes necessary for the calculation of the dust optical properties (see Section 2.3).

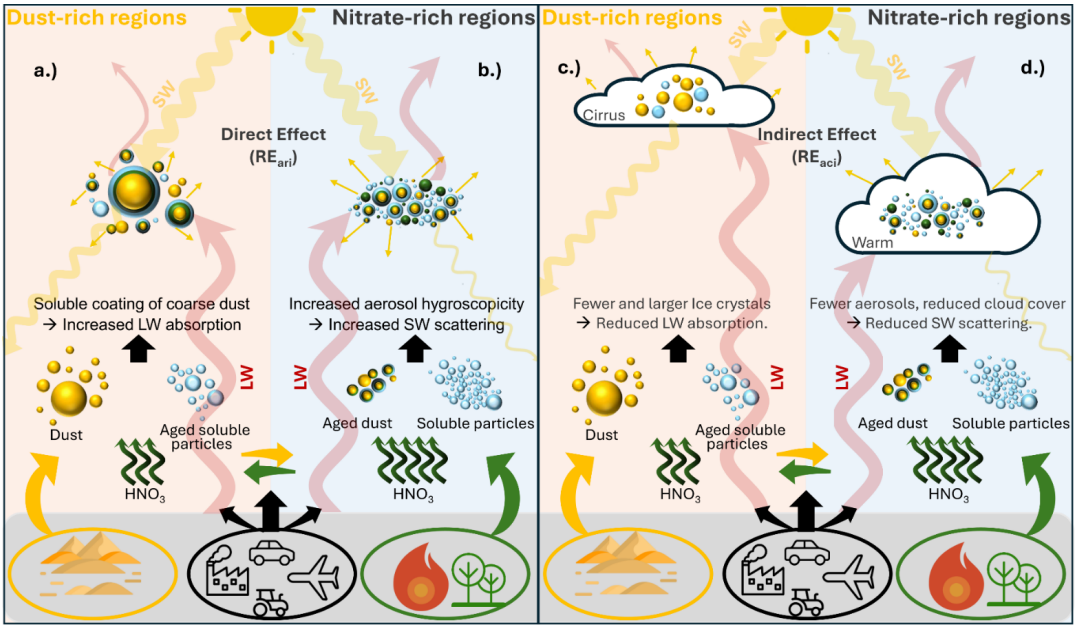

Figure 1: Conceptual illustration of how dust-nitrate interactions affect the total NO_3^- (left) RE_{ari} and (right) RE_{aci}. **a)** In dust-rich environments, nitric acid transported from anthropogenic pollution and biomass burning regions interacts with mineral cations to form a soluble coating on the surface of dust particles. The dominant effect of these interactions is an enhanced LW absorption (warming RE_{ari}) by the coarse dust particles. **b.)** In nitrate-rich environments, the intrusion of dust particles and their subsequent interaction with freshly formed nitric acid leads to an overall increase in aerosol hygroscopicity and thus a stronger SW reflection (cooling RE_{ari}). **c.)** In dust-rich environments, the number of ice crystals in cirrus clouds is reduced while their size is increased due to the interaction of dust particles with the transported HNO_3. This results in an optical thinning of the ice clouds, which leads to less trapping of outgoing LW radiation (cooling RE_{aci}). **d.)** In nitrate-rich environments, the increased wet radius of aged dust particles leads to enhanced coagulation with smaller particles, resulting in a decrease in the number of smaller aerosols and,

in turn, a decrease in the number of activated particles in cloud droplets by smaller aerosols, which ultimately leads to a reduction in the backscattering of SW radiation by warm clouds (warming RE_{ari}).

In general, the changes in the properties of dust particles through their interactions with nitrate aerosols will result in more efficient removal rates, mainly through wet deposition, due to their higher hygroscopicity and increased size (Fan et al., 2004). The reduced number of dust particles that can act as ice nuclei (IN) and their increased size can lead to an optical thinning of cirrus clouds (Fig. 1c) (Kok et al., 2023). Furthermore, the changes induced by dust-nitrate interactions reduce the activation of smaller aerosols in warm clouds (Fig. 1d). In particular, the enhanced hygroscopicity of dust particles will lead to a faster depletion of the available supersaturation, as they act as giant CCN that absorb large amounts of water vapor to activate into cloud droplets (Karydis et al., 2017). In addition, the population of smaller aerosols will also be depleted by increased coagulation with the large dust particles. As a consequence of the different degrees of complexity of the dust-nitrate interactions, it is very important to note that they do not always result in a linear response in terms of how they affect climate through their subsequent interactions with radiation, clouds, or both.

2.3 Radiative Effect Calculation

To calculate the global RE_{ari} and RE_{aci} of NO_3^- aerosols, the optical properties from the AEROPT submodel and the radiative transfer calculations from the RAD submodel were used. First, AEROPT provides the aerosol extinction (absorption and scattering) coefficients, the single scattering albedo, and the aerosol asymmetry factor for each grid cell with a vertical distribution analogous to the vertical resolution used. The GMXe submodel is used to provide input of aerosol attributes for the calculation of aerosol optical properties, which is done online using 3D look-up tables. The tables provide information on the real and imaginary parts of the refractive index and the Mie size parameter per size mode (Dietmuller et al., 2016). Then, the radiative scheme of RAD uses the particle number weighted average of the extinction cross section, the single scattering albedo, and the asymmetry factor as input for the radiative transfer calculations. In addition to AEROPT, RAD takes input from the submodels ORBIT (Earth orbital parameters), CLOUDOPT (cloud optical properties) (Dietmuller et al., 2016), and IMPORT (import of external datasets) to calculate the radiative transfer properties for longwave and shortwave radiation fluxes separately. Both the AEROPT and RAD submodels can be invoked multiple times within a model time step, each time with different settings for the aerosol optical properties, allowing radiative transfer estimates for identical climatological conditions. This is of paramount importance for the calculation of the RE_{ari} of aerosols since any effects due to possibly different climatological conditions must be eliminated. Henceforth, all references to RE estimates, as well as net, longwave, and shortwave flux quantities, will refer to the top of the atmosphere (TOA) only.

2.3.1 Radiative Effect from Aerosol-Radiation Interactions (RE_{ari})

To estimate the global RE_{ari} of all aerosols as well as that of total, coarse, and fine NO_3^- aerosols, 3 simulations were performed for each sensitivity case in Table 1. In the first simulation all aerosol species are present. In the second simulation NO_3^- aerosols are completely removed by turning off their formation by removing the pathway of HNO_3 formation through both NO_2 oxidation and

N_2O_5 hydrolysis, leaving no available HNO_3 to condense on the aerosol via equilibrium partitioning and form nitrate. In the third simulation, coarse mode NO_3^- aerosols are removed by allowing HNO_3 to condense only on the fine mode (i.e., the sum of the three smaller lognormal size modes: nucleation, Aitken, and accumulation). For each of these three simulations, the radiative transfer routines are called twice for each time step. One call uses the normal aerosol optical properties of the existing population, and the other call uses an aerosol optical depth equal to 0 to emulate an atmosphere without aerosols. Essentially, the global RE_{ari} of each simulation can be calculated by taking the difference between the net fluxes between the two calls. More specifically, the first simulation will yield the RE_{ari} of the total aerosol load ($F_{1,ari}$ hereafter), the second simulation will yield the RE_{ari} of all aerosols except NO_3^- ($F_{2,ari}$ below), and the third simulation will yield the RE_{ari} of all aerosols except the coarse mode NO_3^- ($F_{3,ari}$ below). Since the above estimates of the radiative effect were computed using the exact same climatology, its effect was effectively eliminated. However, in order to isolate the NO_3^- aerosol radiative effect, it is also essential to disable any aerosol-cloud interactions, otherwise the cooling effect would be severely underestimated because cloud scattering would make aerosol scattering less relevant (Ghan et al., 2012). For this purpose, the simplest cloud scheme available in the EMAC model is used, which calculates the cloud microphysics according to Lohmann and Roeckner (1996) who empirically relate the cloud droplet number concentration to the sulfate aerosol mass (Boucher and Lohmann 1995) and specifically to its monthly mean values as derived from the sulfur cycle of the ECHAM5 circulation model (Feichter et al., 1996). The cloud coverage is estimated according to Tompkins (2002) with the use of prognostic equations for the water phases and the distribution moments. To disable aerosol-cloud interactions, no aerosol activation routines are used to avoid coupling with the activation schemes. Overall, the global RE_{ari} of total, coarse, and fine NO_3^- aerosols are obtained as follows:

- $F_{NO3,ari}(F_{N,ari}) = F_{1,ari} - F_{2,ari}$
- $F_{coarseNO3,ari}(F_{cN,ari}) = F_{1,ari} - F_{3,ari}$
- $F_{fineNO3,ari}(F_{fN,ari}) = F_{3,ari} - F_{2,ari}$

2.3.2 Radiative Effect from Aerosol-Cloud Interactions (RE_{aci})

In this work we estimate the effect of total NO_3^- aerosols on the calculated global RE_{aci}. Climatology plays a crucial role in aerosol-cloud interactions and simulating a "fine-only NO_3^- atmosphere", as done for the RE_{ari} calculations, would produce an unrealistic climatological scenario, since coarse-mode NO_3^- is strongly associated with cations in mineral dust particles (Karydis et al., 2016), making them quite effective as CCN (Karydis et al., 2017). Therefore, the RE_{aci} calculations require 2 additional simulations for each sensitivity case separately: one with all aerosols present and one with the entire NO_3^- aerosol load removed by turning off their formation as described in the previous section. The global RE_{aci} is then given by:

- $F_{NO3,aci}(F_{N,aci}) = FF_N - F_{N,ari}$

where FF_N is the total NO_3^- aerosol feedback radiative effect. Since $F_{N,ari}$ is calculated using the methodology described in Section 2.3.1, it is only necessary to estimate FF_N. This is equal to the difference in net fluxes between the two additional simulations. There is no need to emulate an aerosol-free atmosphere here since any differences induced by different climatologies must be

included. The two simulations performed for the calculation of FF_N use the cloud formation scheme as described in Lohmann and Ferrachat (2010), which uses prognostic equations for the water phases and the bulk cloud microphysics. In addition, the empirical cloud cover scheme of Sundqvist et al. (1989) is used. For aerosol activation, the CDNC activation scheme of Morales and Nenes (2014) is used, which includes the adsorption activation of mineral dust as described in Karydis et al. (2017). The effect of dust-nitrate interactions on clouds presented here refers to the lowest level of cloud formation at 940 hPa. For the ICNC activation, the scheme of Barahona and Nenes (2009) is used, which calculates the ice crystal size distribution through heterogeneous and homogeneous freezing as well as ice crystal growth.

3. Radiative Effect from Aerosol-Radiation Interactions (RE_{ari})

3.1 Base Case

The global average RE_{ari} of total NO_3^- aerosols at the top of the atmosphere was found to be -0.11 W/m^2, which is within the reported range of the estimated present day all-sky direct radiative effect of total NO_3^- aerosols by other studies (Liao et al., 2004; Bauer et al., 2007a; Bauer et al., 2007b; Bellouin et al., 2011; Xu and Penner, 2012; Heald et al., 2014) (Table S4). The NO_3^- cooling of the RE_{ari} calculated by EMAC is driven by the scattering of SW radiation (equal to -0.34 W/m^2), which outweighs the warming due to absorption of LW radiation (equal to +0.23 W/m^2) (Table 2). The RE_{ari} of the total NO_3^- aerosol shows a clearly contrasting behavior with respect to the size mode considered (Table 2; Figure 2).

In particular, the coarse particles show a net warming effect of +0.17 W/m^2 (Fig. 2i) and contribute to 96% of the LW warming of the total nitrate, while only contributing 15% of the radiative cooling in the SW spectrum (-0.05 W/m^2). The LW warming is strongest over the dust belt zone and especially over the Sahara, the Middle East and the northern face of the Himalayan plateau, while the contribution over other arid regions such as the Atacama, Gobi, Taklimakan and Mojave deserts is significant. These regions are characterized by moderate to high concentrations of coarse NO_3^- aerosols due to the adsorption of HNO_3 on desert soil particles (Karydis et al., 2016; Milousis et al., 2024). Therefore, the warming due to absorption of terrestrial LW radiation by coarse-mode nitrates interacting with mineral dust is the strongest over these areas (see Fig. 1a), ranging from +1.5 W/m^2 to +5 W/m^2 (Fig. 2iii). On the other hand, the cooling exerted by coarse nitrate aerosol through the SW RE_{ari} is more pronounced over areas where it interacts strongly with high concentrations of mineral dust particles (see Fig. 1b). Such areas include the Congo Basin, where HNO_3 from tropical forest biomass burning interacts with Saharan mineral dust particles; the Middle East and North Indian regions, where anthropogenic HNO_3 emissions interact with mineral dust particles from the Sahara and Taklimakan deserts, respectively; and the East Asian region, where HNO_3 emissions from Chinese megacities interact with mineral dust particles from the Gobi Desert. These regions can lead to an average cooling of up to -3.5 W/m^2 (Fig. 2v).

Interestingly, there is no significant cooling from SW interactions over the Sahara for the coarse mode. This phenomenon can be attributed to two factors, the first related to nitrate-dust interactions and the second related to the characteristics of the region. Specifically, because the underlying desert surface is very bright, its absorption in this part of the spectrum is less than that of the particles above it, which means that the desert surface can scatter radiation more effectively than the particles above it. This is further enhanced by the growth of coarse mode particles there

(see Fig. 4x and section 5.1) which increases the absorption cross section of the particles. All this leads to an overall attenuation of the cooling effect over this region and sometimes even to local warming (Fig. 2v).

In contrast to the radiative effect of coarse NO_3^- particles, the RE_{ari} of fine NO_3^- particles is an overall cooling of -0.28 W/m^2 (Fig. 2ii). Fine nitrates have a negligible 4 % contribution to the warming in the LW spectrum (Fig. 2iv) but account for 85 % of the net cooling of the total nitrate aerosols (Fig. 2vi). The cooling induced by fine NO_3^- aerosols from scattering of SW radiation is stronger (up to -5 W/m^2) over regions of high anthropogenic activity, particularly the East Asian and Indian regions, where fine nitrates dominate the total nitrate aerosol load. The regions of West Africa and the Amazon Basin are characterized by moderate fine nitrate concentrations, and the cooling observed there is enhanced by HNO_3 associated with biomass burning interacting with fresh and aged Saharan dust particles, respectively, which are dominated by accumulation mode sizes in the absence of coarse mode nitrates. Finally, other polluted regions such as North America and Europe also show SW cooling up to -2 W/m^2.

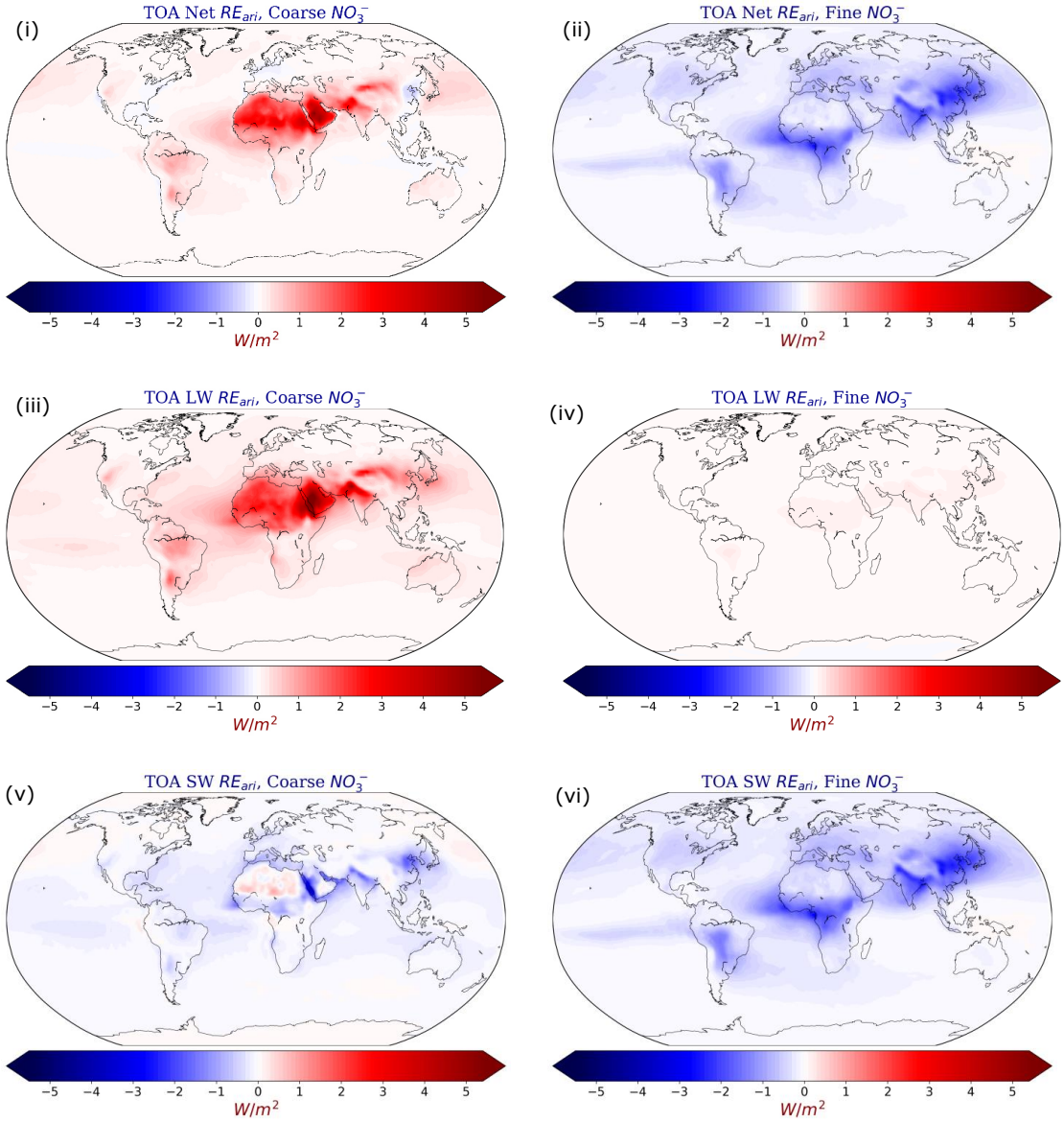

452

453 **Figure 2:** Global mean TOA net RE_{ari} for (i) coarse and (ii) fine $NO3^-$ aerosols; longwave RE_{ari} for (iii)
454 coarse and (iv) fine $NO3^-$ aerosols; shortwave RE_{ari} for (v) coarse and (vi) fine $NO3^-$ aerosols, as calculated
455 by EMAC from the base case simulation.

456 **Table 2:** Net, longwave, and shortwave global mean TOA RE_{ari} of total, coarse, and fine NO_3^-
457 aerosols for the base case and each sensitivity case simulations.

458
459

Simulation	Aerosol Component	TOA RE_{ari} (W/m^2)		
		Net	**LW**	**SW**
Base Case	Total NO_3^-	- 0.11	+ 0.23	- 0.34
	Coarse NO_3^-	+ 0.17	+ 0.22	- 0.05
	Fine NO_3^-	- 0.28	+0.01	- 0.29
Chemically Inert Dust	Total NO_3^-	- 0.09	+ 0.11	- 0.20
	Coarse NO_3^-	+ 0.07	+ 0.10	- 0.03
	Fine NO_3^-	- 0.16	+ 0.01	- 0.17
Homogeneous Ion Composition	Total NO_3^-	- 0.09	+ 0.18	- 0.27
	Coarse NO_3^-	+ 0.13	+ 0.17	- 0.04
	Fine NO_3^-	- 0.22	+ 0.01	- 0.23
Half Dust Scenario	Total NO_3^-	- 0.08	+ 0.19	- 0.27
	Coarse NO_3^-	+ 0.15	+ 0.18	- 0.03
	Fine NO_3^-	- 0.23	+ 0.01	- 0.24
Increased Dust Scenario	Total NO_3^-	- 0.10	+ 0.27	- 0.37
	Coarse NO_3^-	+ 0.20	+ 0.26	- 0.06
	Fine NO_3^-	- 0.30	+ 0.01	- 0.31

460

3.2 Sensitivity of RE_{ari} Estimates

The comparison of the calculated total NO_3^- radiative effect due to interactions with net, LW, and SW radiation for the sensitivity cases listed in Table 1 can be found in Table 2, which shows each of the estimates. Consideration of nitrate interactions with mineral dust cations can greatly affect the NO_3^- RE_{ari} estimates. Assuming that mineral dust particles are inert, the estimated warming due to LW radiation interactions for total nitrate aerosols is 52% weaker than in the base case where dust reactivity is considered. Similarly, the cooling effect exerted by all nitrate aerosols through interactions with SW radiation is estimated to be 41% weaker under the assumption that mineral dust is non-reactive. Both estimates are lower when mineral dust is assumed to be chemically inert, since HNO_3 is no longer effectively adsorbed on dust particles. However, since both the estimated warming and cooling are weaker, the effects partially cancel each other out, resulting in a net cooling effect (-0.09 W/m^2) that is 18% weaker compared to the base case calculations. Assuming a homogeneous ionic composition for the dust, results in SW cooling and LW warming for total nitrate aerosols being 21% and 22% lower, respectively, weakening the estimate for the net cooling RE_{ari} by 18% (-0.09 W/m^2). The net direct radiative effect of total NO_3^- is the same for the cases where dust is assumed to have a homogeneous chemical composition and where it has no chemical identity, indicating the importance of both aspects for the impact of dust-nitrate interactions on the direct radiative effect.

In the Half Dust scenario, the total nitrate aerosol LW warming estimate is 17% weaker than in the base case, while the total nitrate aerosol SW estimate is even more so (21%), resulting in a lower net cooling estimate of -0.08 W/m^2. Finally, the Increased Dust scenario shows the strongest total nitrate aerosol LW warming effect (17% increase over the base case) due to an increase in coarse mode nitrate. At the same time, the cooling effect of total nitrate aerosols due to interactions with SW radiation shows a smaller increase of 9%. Thus, accounting for the historical increase in mineral dust emissions results in a net cooling estimate of -0.10 W/m^2, which is smaller than the base case. Interestingly, the behavior of the global total NO_3^- RE_{ari} does not exhibit linearity with respect to the global dust load. This is not surprising since the nitrate-dust interactions themselves are not linearly correlated, and a given increase or decrease in dust emissions does not lead to an analogous change in nitrate aerosol levels. For example, Karydis et al. (2016) have shown that moving from a scenario in which nitrate-dust chemistry is not considered to one in which it is, but with half dust emissions, resulted in a 39% increase in the tropospheric burden of nitrate aerosols. However, moving from a scenario with half to full dust emissions, the corresponding increase was only 9%. In our case, moving from the chemically inert dust scenario to the half dust scenario led to an 18% increase in atmospheric nitrate aerosol burden, while moving from the half dust scenario to the base case led to an additional 8% increase, and finally moving from the base case to the increased dust scenario led to an even smaller increase of 5%.

There are several reasons for this non-linearity between changes in dust load and nitrate production. Firstly, since the adsorption of HNO_3 onto dust particles is the main driver of nitrate production on dust, over desert areas (where the change in dust load takes place) the amount of nitric acid present is the limiting factor for such production, rather than the amount of dust itself. Secondly, when more dust is present in the atmosphere, the combination of its increased coating with the higher aerosol numbers, tends to result in its more efficient removal by wet deposition as

well as coagulation. This inherently affects nitrate production, which does not increase in proportion to the increase in dust.

4 Radiative Effect from Aerosol-Cloud Interactions (RE_{aci})

4.1 Base Case

The global average RE_{aci} of total NO_3^- aerosols at the top of the atmosphere was found to be +0.17 W/m^2. In contrast, an estimate of the RE_{aci} of nitrate aerosols by Xu and Penner (2012) showed only a trivial cooling effect for particulate NO_3^- (-0.01 W/m^2). Similar to the RE_{ari}, the net RE_{aci} estimated by EMAC is driven by the effect on the SW part of the spectrum, which causes a warming effect of +0.27 W/m^2, while the effect on the LW radiation causes an average cooling of -0.10 W/m^2 (Table 3). Overall, the net RE_{aci} of total NO_3^- aerosols is reversed compared to the net RE_{ari}, i.e. RE_{aci} exerts a strong cooling effect over regions where RE_{ari} exerts a warming effect and vice versa (Fig. 3i). The reason for this is that the regions contributing to a cooling RE_{ari} are dominated by smaller sized nitrate aerosols and vice versa. Therefore, the size characteristics of the dominant nitrate aerosol population lead to different effects on the cloud optical properties as discussed in section 1. For example, as the dominance of smaller nitrate aerosols decreases over a particular region, the optical thinning of low-level clouds will have an opposite effect on the RE_{aci} (Fig. 1d). Details of the mechanism by which nitrate-dust interactions affect cloud microphysical processes are discussed in section 5. Over North America and Europe, RE_{aci} causes a warming effect of up to +3 W/m^2, driven solely by the effect on SW radiation (Fig. 3iii). Over the regions of East Asia and the Amazon and Congo basins, RE_{aci} reaches a maximum of +5 W/m^2, driven by both the effect on the SW (up to +4 W/m^2) and LW (up to +1.5 W/m^2) parts of the radiation spectrum. The cooling effect of RE_{aci} (up to -2 W/m^2) extends mainly between the equatorial line and the Tropic of Cancer, mainly due to the interaction of nitrate aerosols with desert dust particles (e.g. from the Sahara) and their effect on the terrestrial spectrum (LW) (Figs. 1c & 3ii). The cooling effect of dust interactions with anthropogenic particles in the LW spectrum corroborates the findings of Klingmüller et al. (2020) and is attributed to the reduced ice-water path due to the depletion of small aerosols, which in turn leads to less trapped outgoing terrestrial radiation. In addition, Kok et al. (2023) note how the presence of dust particles leads to an optical thinning of cirrus clouds by reducing the number of ice crystals while increasing their size, which also leads to less trapping of outgoing LW radiation and thus a cooling effect (Fig. 1c). On the other hand, the warming effect of dust interactions with anthropogenic particles in the SW spectrum requires further investigation and is therefore discussed in more detail in Section 5.

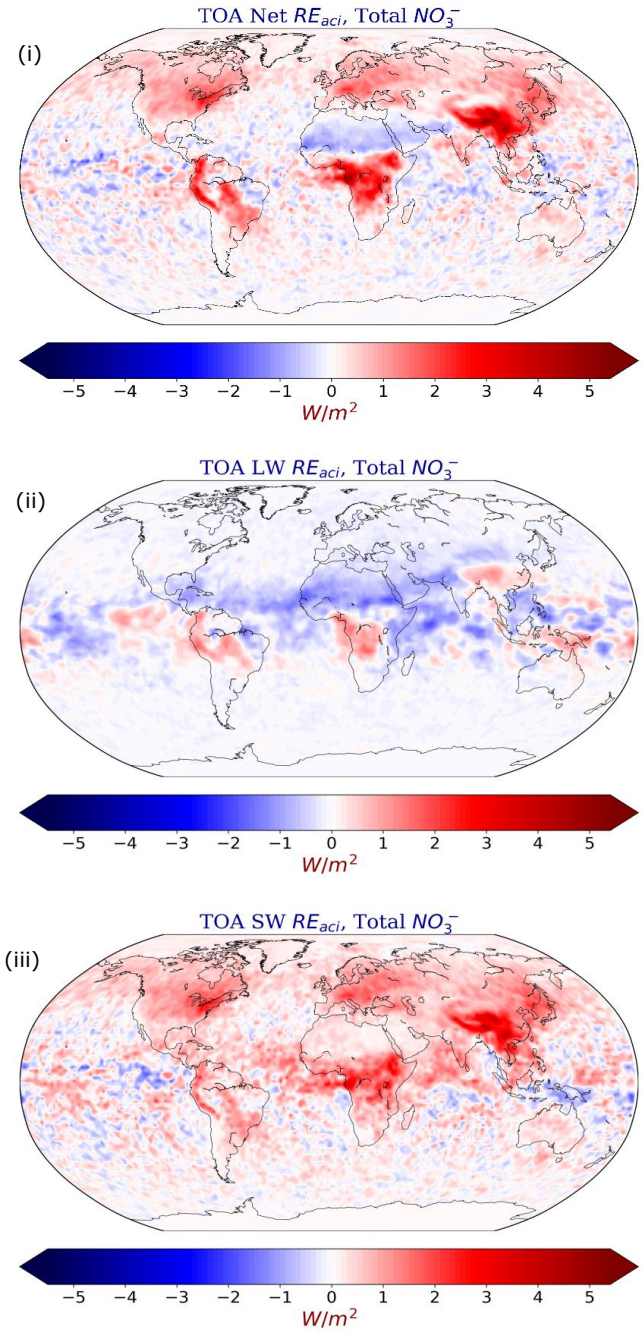

535 **Figure 3:** Global mean TOA RE_{aci} for total NO_3^- aerosols. Estimates for (i) net, (ii) longwave, and (iii)
536 shortwave, as calculated by EMAC from the base case simulation.

Table 3: Net, longwave, and shortwave global mean TOA RE_{aci} of total NO_3^- aerosols for the base case and each sensitivity case simulations.

Simulation	TOA RE_{aci} (W/m^2)		
	Net	**LW**	**SW**
Base Case	+ 0.17	- 0.10	+ 0.27
Chemically Inert Dust	+ 0.11	- 0.06	+ 0.17
Homogeneous Ion Composition	+ 0.13	- 0.09	+ 0.22
Half Dust Scenario	+ 0.15	- 0.08	+ 0.23
Increased Dust Scenario	+ 0.14	- 0.11	+ 0.25

4.2 Sensitivity of RE_{aci} Estimates

Table 3 shows the comparison of the net, LW, and SW contributions of total NO_3^- to the RE_{aci} at the top of the atmosphere as calculated by the base case simulation and all sensitivity cases considered. By assuming a chemically inert dust, the calculated net RE_{aci} of nitrate decreases by 35%, resulting in a net warming of +0.11 W/m^2. As with the RE_{ari} estimate, this sensitivity case produces the largest deviation from the base case among all sensitivity simulations, for both the SW (37% less warming) and LW (40% less cooling) estimates. This is due to the fact that the absence of dust-nitrate interactions does not have such a large impact on the population of both aerosols and activated particles (see also Section 5). The assumption of a homogeneous ionic composition of the mineral dust leads to a weakened LW cooling estimate of 10% and a weakened SW warming estimate of 19% resulting in a net NO_3^- RE_{aci} of +0.13 W/m^2 (24% lower than in the base case).

The reduced dust emissions result in a 15% weaker warming in the SW spectrum and a 20% weaker cooling in the LW spectrum, leading to an overall NO_3^- RE_{aci} of +0.15 W/m^2 (12% weaker than the base case scenario). This is because the reduced loading of nitrate aerosols, especially in the coarse mode, in the half dust scenario results in less absorption of LW radiation (Fig. 1c) (hence less cooling). Similarly, the effect of dust-nitrate interactions on the activation of smaller particles (Fig. 1d) is less drastic and results in a weaker inhibition of SW radiation scattering (hence less warming, see also Section 5). Finally, increased dust emissions in the increased dust scenario show a 10% increase in the LW cooling and an 8% decrease in the SW warming effect, surprisingly resulting in a net warming (+0.14 W/m^2) that is lower than in the half dust scenario. The reason that this scenario results in more LW cooling than the base case is that the increased amount of dust particles leads to even more optical thinning of the ice clouds, and therefore even less trapping of LW radiation (more cooling). However, the reason why the SW warming estimate is lower than the base case is more complicated. First, the transition from the half dust scenario to the base case and then to the increased dust scenario does not lead to an analogous increase in the nitrate aerosol

burden (see Section 3.2). Moreover, since the number of aerosols has increased from the increased dust scenario to the base case, but the relative humidity has remained largely the same, there is more competition for water vapor because it is now distributed over a larger population. As a result, the wet radius increase in the presence of nitrates is not as strong in the increased dust scenario compared to the base case, and the depletion of smaller sized particles is also not as strong (not shown). The implications of the depletion of the aerosol population in the presence of nitrate aerosols on the microphysical processes of warm clouds, and consequently on SW warming, are discussed in the next section.

5 Effect Of NO_3^- Aerosols on Cloud Microphysics

5.1 Maximum Supersaturation, Hygroscopicity and Wet Radius

To further investigate the cause of the positive RE_{aci} induced by the NO_3^- aerosols, their effect on the aerosol population characteristics as well as on the cloud microphysics is investigated, with respect to the lowest forming cloud level of 940 hPa. For this purpose, a sensitivity simulation is performed assuming a 'nitrate aerosol free' (NAF) atmosphere, in which the formation of NO_3^- aerosols has been switched off, but an advanced cloud scheme is considered which is the same as the one described in Section 2.3.2. Essentially the same setup that was used for the estimation of the total nitrate aerosol feedback radiative effect. This simulation is used to determine whether the presence of NO_3^- aerosols has a significant effect on the hygroscopicity and size of atmospheric aerosols and ultimately on the maximum supersaturation developed during cloud formation. Over polluted areas affected by transported dust air masses from surrounding arid areas, the presence of NO_3^- aerosols can increase the CCN activity of the large mineral dust particles, resulting in a reduction of the maximum supersaturation and inhibiting the activation of the small anthropogenic particles into cloud droplets (Klingmüller et al., 2020). Results from the NAF sensitivity simulation support this hypothesis over parts of Eastern and Central Asia, where the maximum supersaturation decreases by up to 0.05%. In contrast, the presence of NO_3^- aerosols increases maximum supersaturation by up to 0.2% over North America, Europe, the Middle East, and parts of southern Asia (Fig. 4ii). Therefore, changes in maximum supersaturation caused by the presence of NO_3^- aerosols cannot explain their warming effect through the RE_{aci}.

The presence of NO_3^- has a significant effect on the hygroscopicity of both fine and coarse aerosols and consequently on their wet radius, as shown in Figures 1a,b & 4. This is most evident for coarse desert dust particles, which mix with NO_3^- aerosols from urban and forest regions, increasing their hygroscopicity by an order of magnitude (up to 0.1), especially over the African-Asian dust belt and the Atacama Desert in South America (Fig. 4vi). Aerosol hygroscopicity is similarly increased for the fine mode particles both near arid regions and over the highly industrialized region of Southeast Asia (Fig. 4iv). The low values of the hygroscopic parameter of the fine aerosol population, especially over the dust belt zone, are largely due to the higher proportion of insoluble fine particles present over these regions (Figure S5). This is also observed over other regions with similarly low fine aerosol hygroscopicity (South Africa, South America and Western U.S). Nevertheless, the estimates of aerosol kappa values at 940 hPa are broadly consistent with the results of Pringle et al., (2010c). On the other hand, the aerosol hygroscopicity for the two size modes is only slightly reduced, by up to 0.06 (or <10%) over the oceans and coasts of Europe and East Asia, due to interactions of NO_3^- with sea salt particles, reducing their

hygroscopicity. The increased ability of both coarse dust aerosols and smaller aerosols to absorb water leads to an increase in their wet radius, but in different parts of the world. For example, fine particle sizes increase by up to 0.04 μm (up to 40%) mostly over regions of high anthropogenic activity (North America, Europe, and East Asia) (Fig. 4viii). On the other hand, coarse mode particle sizes are increased by up to 0.1 μm (up to 10%) over the forests of central Africa and the African-Asian dust belt zone (Fig. 4x), while showing a similar decrease near the coasts of the polluted northern hemisphere due to the effect of NO_3^- on the hygroscopicity of sea salt.

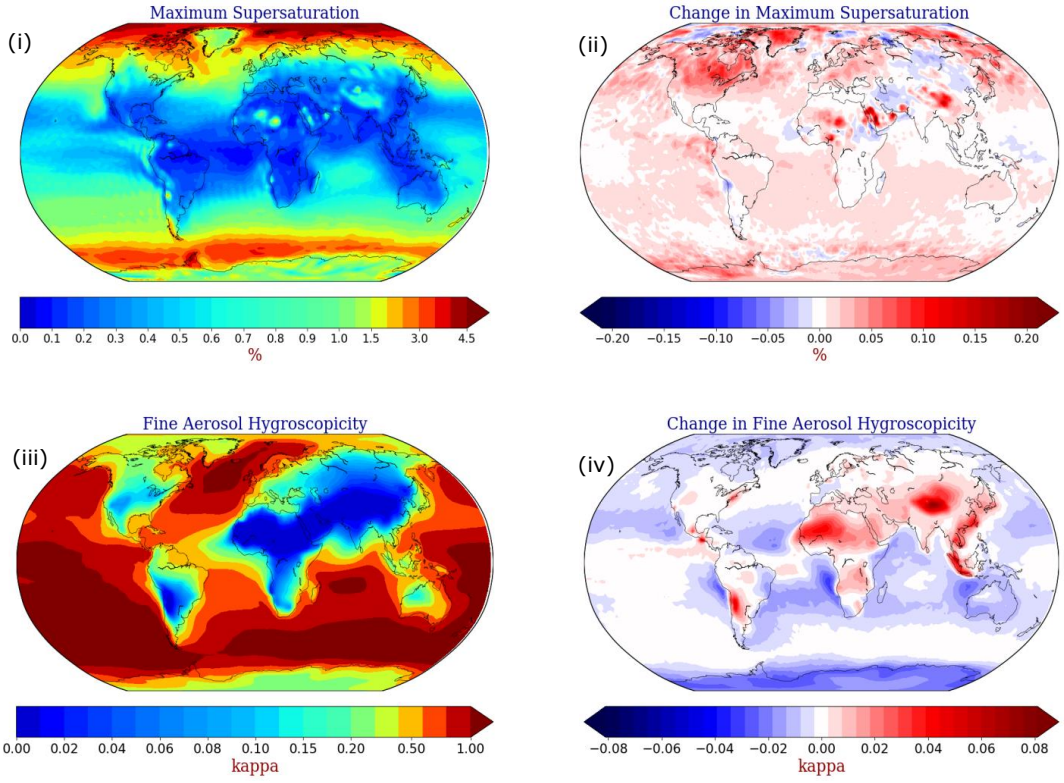

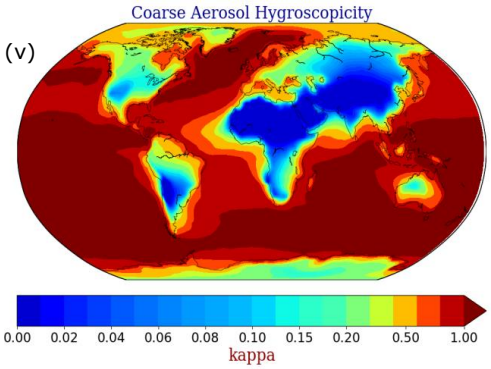
Coarse Aerosol Hygroscopicity
(v)
0.00 0.02 0.04 0.06 0.08 0.10 0.15 0.20 0.50 1.00
kappa

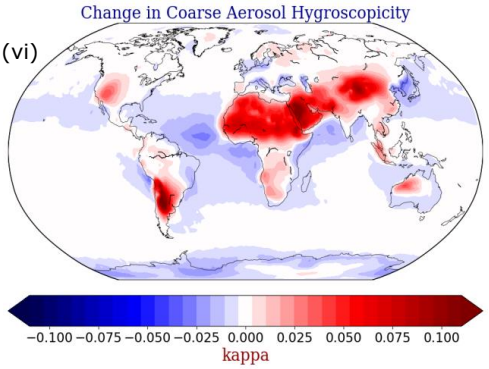
Change in Coarse Aerosol Hygroscopicity
(vi)
−0.100 −0.075 −0.050 −0.025 0.000 0.025 0.050 0.075 0.100
kappa

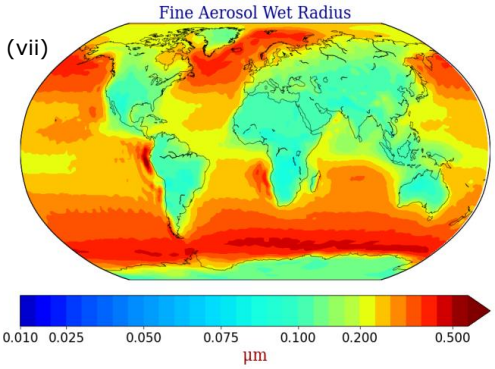
Fine Aerosol Wet Radius
(vii)
0.010 0.025 0.050 0.075 0.100 0.200 0.500
µm

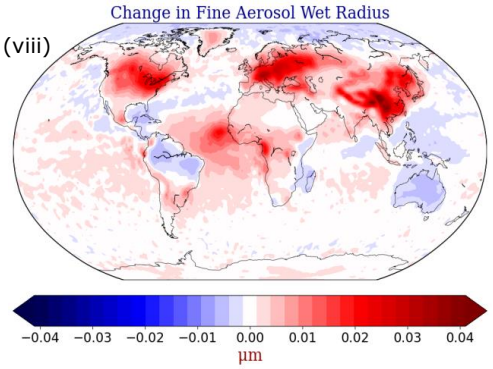
Change in Fine Aerosol Wet Radius
(viii)
−0.04 −0.03 −0.02 −0.01 0.00 0.01 0.02 0.03 0.04
µm

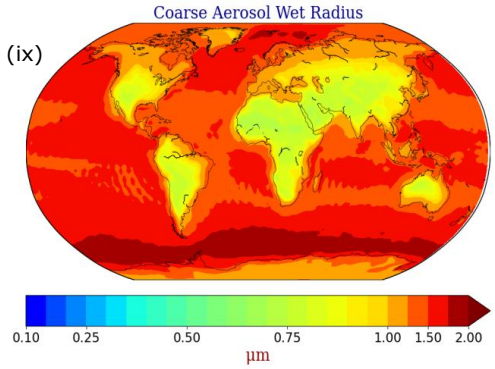
Coarse Aerosol Wet Radius
(ix)
0.10 0.25 0.50 0.75 1.00 1.50 2.00
µm

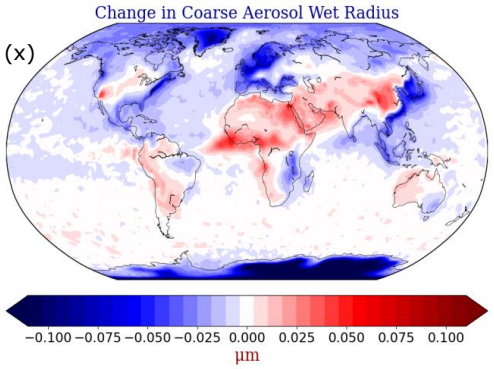
Change in Coarse Aerosol Wet Radius
(x)
−0.100 −0.075 −0.050 −0.025 0.000 0.025 0.050 0.075 0.100
µm

616

Figure 4: (i) Global mean maximum supersaturation, fine aerosol (iii) hygroscopicity and (v) wet radius, and coarse aerosol (vii) hygroscopicity and (ix) wet radius, as calculated by EMAC from the base case simulation at the altitude of 940 hPa. Absolute difference between base case and Nitrate Aerosol Free (NAF) sensitivity simulation in (ii) maximum supersaturation, fine aerosol (iv) hygroscopicity and (vi) wet radius, and coarse aerosol (viii) hygroscopicity and (x) wet radius at the altitude of 940 hPa. Red indicates higher values calculated by the base case simulation in the presence of NO_3^- aerosols.

5.2 Number Concentrations of Aerosol and Activated Particles

Figure 5 shows the effect of NO_3^- on the number concentration of fine and coarse aerosols between the base case and the 'NAF' sensitivity simulation, as well as the total aerosol population. The presence of NO_3^- aerosols decreases the total aerosol number concentration over forests and polluted regions (see also Fig. 1d). This behavior is driven solely by the decrease in smaller particle sizes, as the effect is minimal for the coarser particles (Figs. 5ii & 5iv). The largest decrease is calculated over East and South Asia (up to 1000 cm^{-3} or 10%), while decreases of up to 200 cm^{-3} on average (~10%) are found over Europe, the USA, and Central Africa. This effect is directly related to the increased wet radius of the aerosol population (Fig. 4viii) over these regions and thus to its depositional efficiency. In addition, coarse dust particles become more hygroscopic due to interactions with NO_3^- aerosols that increase in size, resulting in increased coagulation with the smaller anthropogenic particles, which reduces their abundance.

The reduced aerosol number concentration in the presence of NO_3^- can lead to a reduction of particles that are also activated into cloud droplets. Such behavior can be seen in Figure 6, which shows the effect of NO_3^- on the number concentration of activated fine and coarse particles in cloud droplets between the base case and the 'NAF' sensitivity simulation. The reduction in the total number of activated cloud droplets is almost entirely due to the reduction in smaller size particles (Figs. 6ii & 6iv). A reduction in the total number of activated droplets of up to 30 cm^{-3} or 10% is observed over the USA, Amazon, Europe, Central Africa, and parts of the Middle East, while this reduction reaches up to 100 cm^{-3} (10%) over Southeast Asia, where the largest reductions in aerosol numbers are also calculated (Fig. 4ii). In turn, these are the regions where the warming effect of NO_3^- aerosols on the calculated mean RE_{aci} is strongest (Figure 3i). The small increase in activated droplets (~ 10 cm^{-3} or 1%) over Beijing, which concerns the fine mode particles, is most likely because their number concentration decreases with increasing size. The high aerosol number concentration there, which is the global maximum (Figure 5i), results in a hotspot of more readily activated particles in the presence of NO_3^-. On the other hand, the CDNC decreases slightly over the Sahara due to the more efficient deposition capacity of coarse dust particles due to their interactions with nitrate aerosols, which is also reflected in the decrease in aerosol number (Fig. 6iv). Overall, the lower particle number in the presence of NO_3^- aerosols hinders the ability of the smaller anthropogenic particles to activate into cloud droplets, leading to a reduced cloud cover and thus a reduced cloud albedo effect. Therefore, not only less LW radiation is absorbed, but more importantly, less SW radiation is scattered back to space, resulting in an overall warming of the net average RE_{aci} for total NO_3^- aerosols.

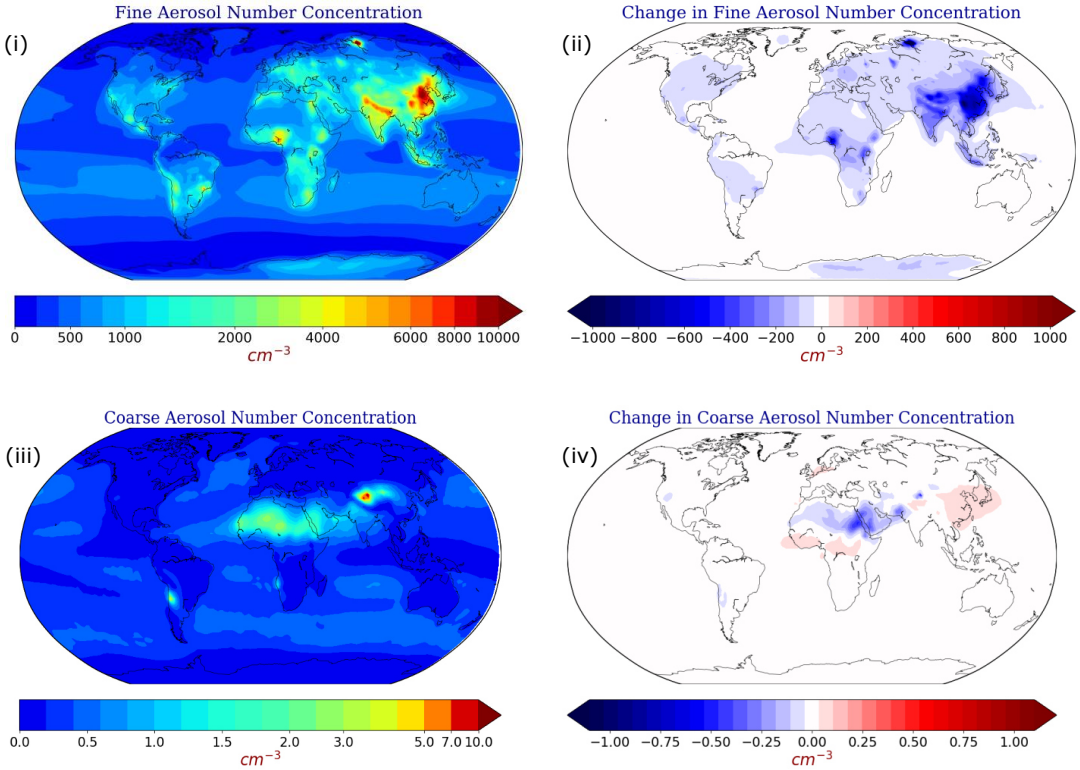

Figure 5: Global mean number concentration of (i) fine and (iii) coarse aerosols as calculated by EMAC from the base case simulation at the altitude of 940 hPa. Absolute difference between the base case and the Nitrate Aerosol Free (NAF) sensitivity simulation in the number concentration of (ii) fine and (iv) coarse aerosols at the altitude of 940 hPa. Blue indicates that number concentrations are lower in the presence of NO_3^- aerosols.

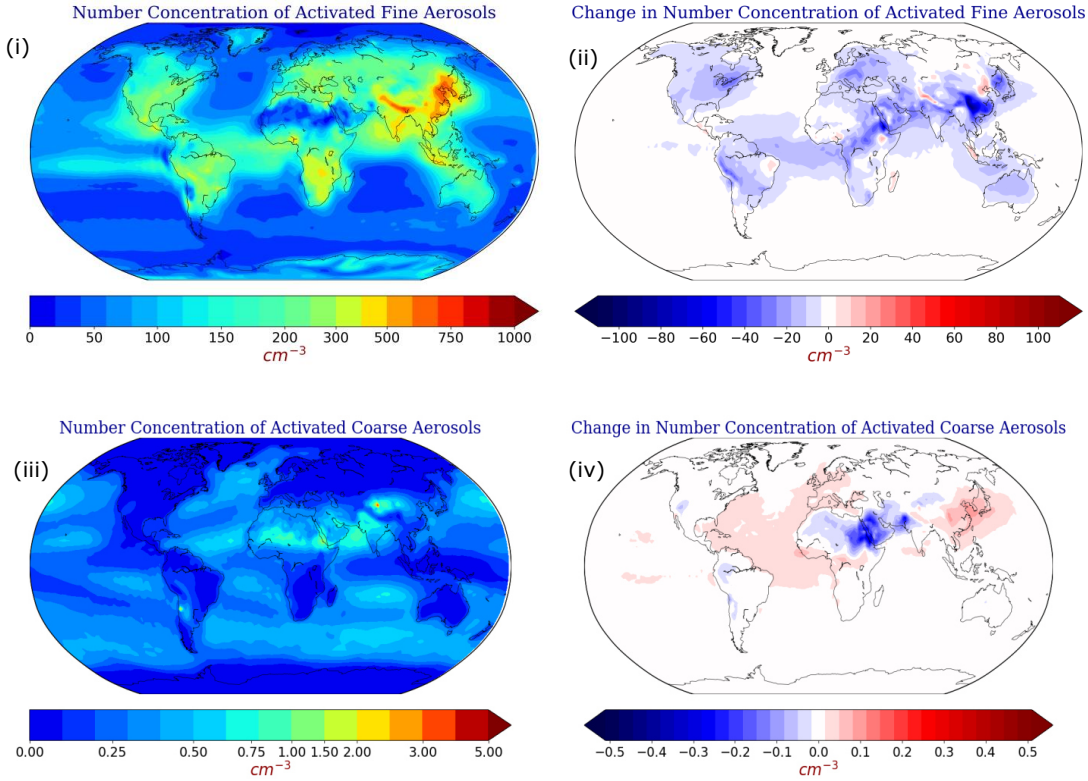

Figure 6: Global mean number concentration of activated (i) fine and (iii) coarse aerosols as calculated by EMAC from the base case simulation at the altitude of 940 hPa. Absolute difference between the base case and the Nitrate Aerosol Free (NAF) sensitivity simulation in the number concentration of activated (ii) fine and (iv) coarse aerosols at the altitude of 940 hPa. Blue indicates that number concentrations are lower in the presence of NO_3^- aerosols.

6. Conclusions and Discussion

This study presents the effects of interactions between mineral dust and NO_3^- aerosols on the present-day global TOA radiative effect of the latter. We investigate how the presence of dust affects the radiative effect of NO_3^- aerosols, both through aerosol interactions with radiation and separately with clouds (RE_{ari} and RE_{aci}, respectively). Sensitivity simulations are also performed, varying both the mineral dust composition and its emissions, to assess their effect on the calculated NO_3^- aerosol radiative effect.

It was found that the global average net RE_{ari} of total NO_3^- aerosols is -0.11 W/m^2, which is mainly due to the cooling from the shortwave part of the radiation spectrum due to scattering,

equal to -0.34 W/m^2. A warming from the longwave part of the spectrum due to absorption was found to be +0.23 W/m^2 on global average and was mainly located over regions with high concentrations of coarse NO_3^- aerosols. SW cooling was also observed in these regions, but also over regions of high anthropogenic activity, mainly over the polluted northern hemisphere. The behavior of the RE_{ari} was opposite when considering different sizes of NO_3^- aerosols. Specifically, the coarse mode was responsible for 96% of the estimated warming in the LW part of the spectrum, but 15% of the estimated cooling in the SW part of the spectrum. On the other hand, the contribution of the fine mode to the LW warming was negligible, but it was the main contributor to the SW cooling, accounting for 85% of the net estimate. The sensitivity experiments revealed that the chemistry of the mineral dust is the most important factor in changing the estimated RE_{ari} of the total NO_3^- aerosols. In particular, LW warming is most affected by this assumption, being 52% weaker after assuming chemically inert dust emissions, while the SW cooling is reduced by 41% compared to the base case simulation, amounting to a net cooling of -0.09 W/m^2. A globally homogeneous ionic composition for mineral dust had a smaller effect in LW (22% decrease) and SW (21% decrease) but resulted in the same net estimate of -0.09 W/m^2. Halving the dust emissions resulted in weaker estimates for LW and SW by 17% and 21%, respectively, and the lowest overall net RE_{ari} of -0.08 W/m^2. On the other hand, a 50% increase in dust emissions increased both LW warming and SW cooling by 17% and 9% respectively, resulting in a net cooling RE_{ari} of -0.10 W/m^2, indicating the strong non-linear relationship of nitrate-dust interactions and how they affect the radiative effect estimates.

The global average net RE_{aci} of total NO_3^- aerosols was +0.17 W/m^2 due to the effect on the shortwave portion of the spectrum. This was found to be +0.27 W/m^2, while the cooling from the longwave part was -0.10 W/m^2. Spatially, the net RE_{aci} is reversed compared to the net RE_{ari} for total NO_3^- aerosols, where regions responsible for a strong SW cooling of the RE_{ari} contribute to a strong SW warming of the RE_{aci} and vice versa. This is due to the fact that nitrate-dust interactions challenge the dominance of smaller particles over heavily polluted regions, reducing the reflectivity of warm cloud and thus having an opposite effect on the RE_{aci}. The sensitivity experiments again showed that the consideration of the mineral dust chemistry is the most important aspect for the calculation of the RE_{aci} of the total NO_3^- aerosols. When the dust was assumed to be chemically inert, the LW and SW estimates were up to 40% weaker, resulting in a net warming of +0.11 W/m^2. Assuming a homogeneous ion composition resulted in a smaller weakening of the estimates (up to 18%) and a net warming of +0.13 W/m^2. When dust emissions were halved, the LW cooling was reduced slightly more than in the base case, resulting in a net warming of +0.15 W/m^2. The 50% increase in dust emissions had the largest effect on LW behavior (10% increase), but surprisingly the net estimate (+0.14 W/m^2) was smaller than in the half-dust scenario. The reason for this is that the SW estimate did not increase but decreased by 8% due to the fact that in this scenario the increased nitrate burden causes increased competition for the available supersaturation and the effect of dust-nitrate interactions on the smaller aerosol populations is not as emphasized as in the base case.

The total NO_3^- aerosol RE_{aci} shows a positive sign, which is attributed to a reduced cloud albedo effect. More specifically, although the presence or absence of NO_3^- aerosol in the atmosphere did not significantly affect the total available maximum supersaturation, it did alter both the hygroscopicity and wet radii of the aerosols. In the presence of NO_3^-, the hygroscopicity of aerosols

over deserts was increased by up to an order of magnitude, leading to an increase in their wet radius of up to 10%, with an even larger increase of up to 40% for smaller particles over urban regions. Therefore, in the presence of NO_3^- aerosols, the depletion of fine particles by coagulation with coarser particles (i.e., mineral dust) is enhanced and further increases the size of the coarse particles. The reduction in the number of aerosols is up to 10% in some regions, with maximum reductions calculated over Southeast Asia. This reduction in the number of fine aerosols leads to a reduction in the number of cloud droplets activated by fine aerosols (also up to 10%), which would otherwise have absorbed more outgoing longwave radiation and, more importantly, scattered more incoming shortwave radiation. Thus, the reduced cloud albedo effect leads to a cooling in the longwave part of the spectrum, which is offset by a strong warming in the shortwave part, overall resulting in a net warming of the atmosphere.

The chemistry-climate model simulations presented here suggest that NO_3^- aerosol-radiation interactions lead to a net effect of -0.11 W/m^2 (cooling) driven by fine NO_3^- aerosol, while NO_3^- aerosol-cloud interactions lead to a net effect of +0.17 W/m^2 (warming) driven mainly by coarse mode NO_3^- aerosol.

Code and Data Availability

The usage of MESSy (Modular Earth Submodel System) and access to the source code is licensed to all affiliates of institutions which are members of the MESSy Consortium. Institutions can become a member of the MESSy Consortium by signing the "MESSy Memorandum of Understanding". More information can be found on the MESSy Consortium website: http://www.messy-interface.org (last access: 22 May 2024). The code used in this study has been based on MESSy version 2.55 and is archived with a restricted access DOI (https://doi.org/10.5281/zenodo.8379120, The MESSy Consortium, 2023). The data produced in the study is available from the authors upon request.

Acknowledgements

This work was supported by the project FORCeS funded from the European Union's Horizon 2020 research and innovation program under grant agreement No 821205. JFK was funded by the National Science Foundation (NSF) Directorate for Geosciences grants 1856389 and 2151093. The work described in this paper has received funding from the Initiative and Networking Fund of the Helmholtz Association through the project "Advanced Earth System Modelling Capacity (ESM)". The authors gratefully acknowledge the Earth System Modelling Project (ESM) for funding this work by providing computing time on the ESM partition of the supercomputer JUWELS (Alvarez, 2021) at the Jülich Supercomputing Centre (JSC).

Competing Interests

At least one of the (co-)authors is a member of the editorial board of Atmospheric Chemistry and Physics.

Author Contributions

AM and VAK wrote the paper with contributions from KK, APT, JFK, MK, and AN. VAK planned the research with contributions from APT, MK and AN. AM, KK and VAK designed the methodology for the radiative effect calculations. AM performed the simulations and analyzed the results, assisted by VAK and APT. All the authors discussed the results and contributed to the paper.

REFERENCES

Abdelkader, M., Metzger, S., Mamouri, R. E., Astitha, M., Barrie, L., Levin, Z., and Lelieveld, J.: Dust–air pollution dynamics over the eastern Mediterranean, Atmos. Chem. Phys., 15, 9173–9189, https://doi.org/10.5194/acp-15-9173-2015 , 2015.

Albrecht, B. A.: Aerosols, Cloud Microphysics, and Fractional Cloudiness, Science, 245(4923), 1227-1230, https://doi.org/10.1126/science.245.4923.1227 , 1989.

Alvarez, D.: JUWELS cluster and booster: Exascale pathfinder with modular supercomputing architecture at juelich supercomputing Centre. *Journal of large-scale research facilities JLSRF*, *7*, A183-A183, https://doi.org/10.17815/jlsrf-7-183, 2021.

Arias, P.A., N. Bellouin, E. Coppola, R.G. Jones, G. Krinner, J. Marotzke, V. Naik, M.D. Palmer, G.-K. Plattner, J. Rogelj, M. Rojas, J. Sillmann, T. Storelvmo, P.W. Thorne, B. Trewin, K. Achuta Rao, B. Adhikary, R.P. Allan, K. Armour, G. Bala, R. Barimalala, S. Berger, J.G. Canadell, C. Cassou, A. Cherchi, W. Collins, W.D. Collins, S.L. Connors, S. Corti, F. Cruz, F.J. Dentener, C. Dereczynski, A. Di Luca, A. Diongue Niang, F.J. Doblas-Reyes, A. Dosio, H. Douville, F. Engelbrecht, V. Eyring, E. Fischer, P. Forster, B. Fox-Kemper, J.S. Fuglestvedt, J.C. Fyfe, N.P. Gillett, L. Goldfarb, I. Gorodetskaya, J.M. Gutierrez, R. Hamdi, E. Hawkins, H.T. Hewitt, P. Hope, A.S. Islam, C. Jones, D.S. Kaufman, R.E. Kopp, Y. Kosaka, J. Kossin, S. Krakovska, J.-Y. Lee, J. Li, T. Mauritsen, T.K. Maycock, M. Meinshausen, S.-K. Min, P.M.S. Monteiro, T. Ngo-Duc, F. Otto, I. Pinto, A. Pirani, K. Raghavan, R. Ranasinghe, A.C. Ruane, L. Ruiz, J.-B. Sallée, B.H. Samset, S. Sathyendranath, S.I. Seneviratne, A.A. Sörensson, S. Szopa, I. Takayabu, A.-M. Tréguier, B. van den Hurk, R. Vautard, K. von Schuckmann, S. Zaehle, X. Zhang, and K. Zickfeld, 2021: Technical Summary. In *Climate Change 2021: The Physical Science Basis. Contribution of Working Group I to the Sixth Assessment Report of the Intergovernmental Panel on Climate Change* [Masson-Delmotte, V., P. Zhai, A. Pirani, S.L. Connors, C. Péan, S. Berger, N. Caud, Y. Chen, L. Goldfarb, M.I. Gomis, M. Huang, K. Leitzell, E. Lonnoy, J.B.R. Matthews, T.K. Maycock, T. Waterfield, O. Yelekçi, R. Yu, and B. Zhou (eds.)]. Cambridge University Press, Cambridge, United Kingdom and New York, NY, USA, https://doi.org/10.1017/9781009157896.002 , 2021.

Astitha, M., Lelieveld, J., Kader, M. A., Pozzer, A., and de Meij, A.: Parameterization of dust emissions in the global atmospheric chemistry-climate model EMAC: impact of nudging and soil properties, Atmospheric Chemistry and Physics , 12(22), 11057-11083, https://doi.org/10.5194/acp-12-11057-2012 , 2012.

Bacer, S., Sullivan, S. C., Karydis, V. A., Barahona, D., Kramer, M., Nenes, A., Tost, H., Tsimpidi, A. P., Lelieveld, J., and Pozzer, A.: Implementation of a comprehensive ice crystal formation parameterization for cirrus and mixed-phase clouds in the EMAC model (based on MESSy 2.53), Geoscientific Model Development , 11(10), https://doi.org/10.5194/gmd-11-4021-2018 , 2018.

Barahona, D. and Nenes, A.: Parameterizing the competition between homogeneous and heterogeneous freezing in cirrus cloud formation - monodisperse ice nuclei, Atmospheric Chemistry and Physics , 9(16), 369-381, https://doi.org/10.5194/acp-9-5933-2009 , 2009.

Barahona, D., West, R., Stier, P., Romakkaniemi, S., Kokkola, H., and Nenes, A.: Comprehensively accounting for the effect of giant CCN in cloud activation parameterizations, Atmospheric Chemistry and Physics , 10(5) , 2467-2473, https://doi.org/10.5194/acp-10-2467-2010 , 2010.

Bauer, S. E., Koch, D., Unger, N., Metzger, S. M., Shindell, D. T., and Streets, D. G.: Nitrate aerosols today and in 2030: a global simulation including aerosols and tropospheric ozone, Atmospheric Chemistry and Physics , 7(19) , https://doi.org/10.5194/acp-7-5043-2007 , 2007a.

Bauer, S. E., Mishchenko, M. I., Lacis, A. A., Zhang, S., Perlwitz, J., and Metzger, S. M.: Do sulfate and nitrate coatings on mineral dust have important effects on radiative properties and climate modeling?, Journal of Geophysical Research: Atmospheres, 112(D6), https://doi.org/10.1029/2005JD006977, 2007b.

Bellouin, N., Rae, J., Jones, A., Johnson, C., Haywood, J., and Boucher, O.: Aerosol forcing in the Climate Model Intercomparison Project (CMIP5) simulations by HadGEM2-ES and the role of ammonium nitrate, Journal of Geophysical Research: Atmospheres, 116(D20) , https://doi.org/10.1029/2011JD016074 , 2011.

Bond, T. C. and Bergstrom, R. W.: Light absorption by carbonaceous particles: An investigative review, Aerosol Science and Technology, 40(1), 27-67, https://doi.org/10.1080/02786820500421521 , 2006.

Boucher, O., & Lohmann, U.: The sulfate-CCN-cloud albedo effect. *Tellus B: Chemical and Physical Meteorology*, *47*(3), 281-300, https://doi.org/10.3402/tellusb.v47i3.16048, 1995.

Bouwman, A. F., Lee, D. S., Asman, W. A. H., Dentener, F. J., VanderHoek, K. W., and Olivier, J. G. J.: A global high-resolution emission inventory for ammonia, Global Biogeochemical Cycles , 11(4) , https://doi.org/10.1029/97GB02266 , 1997.

Chang, D. Y., Lelieveld, J., Tost, H., Steil, B., Pozzer, A., & Yoon, J.: Aerosol physicochemical effects on CCN activation simulated with the chemistry-climate model EMAC, *Atmospheric Environment*, *162*, 127-140, https://doi.org/10.1016/j.atmosenv.2017.03.036, 2017.

De Meij, A., Pozzer, A., Pringle, K. J., Tost, H., & Lelieveld, J.: EMAC model evaluation and analysis of atmospheric aerosol properties and distribution with a focus on the Mediterranean region, *Atmospheric research*, *114*, 38-69, https://doi.org/10.1016/j.atmosres.2012.05.014, 2012.

Dentener, F., Kinne, S., Bond, T., Boucher, O., Cofala, J., Generoso, S., Ginoux, P., Gong, S., Hoelzemann, J. J., Ito, A., Marelli, L., Penner, J. E., Putaud, J. P., Textor, C., Schulz, M., van der Werf, G. R., and Wilson, J.: Emissions of primary aerosol and precursor gases in the years 2000 and 1750 prescribed data-sets for AeroCom, Atmospheric Chemistry and Physics , 6(12) , 4321-4344, https://doi.org/10.5194/acp-6-4321-2006 , 2006.

Dietmuller, S., Jockel, P., Tost, H., Kunze, M., Gellhorn, C., Brinkop, S., Fromming, C., Ponater, M., Steil, B., Lauer, A., and Hendricks, J.: A new radiation infrastructure for the Modular Earth Submodel System (MESSy, based on version 2.51), Geoscientific Model Development, 9(6) , 2209-2222, https://doi.org/10.5194/gmd-9-2209-2016 , 2016.

European Monitoring and Evaluation Programme (EMEP): EBAS database online, https://projects.nilu.no/ccc/index.html , last access: 3 September 2024.

Fan, S.-M., Horowitz, L. W., Levy Ii, H., and Moxim, W. J.: Impact of air pollution on wet deposition of mineral dust aerosols, Geophysical Research Letters, 31(2), https://doi.org/10.1029/2003GL018501 , 2004.

Fanourgakis, G. S., Kanakidou, M., Nenes, A., Bauer, S. E., Bergman, T., Carslaw, K. S., Grini, A., Hamilton, D. S., Johnson, J. S., Karydis, V. A., Kirkevåg, A., Kodros, J. K., Lohmann, U., Luo, G., Makkonen, R., Matsui, H., Neubauer, D., Pierce, J. R., Schmale, J., Stier, P., Tsigaridis, K., van Noije, T., Wang, H., Watson-Parris, D., Westervelt, D. M., Yang, Y., Yoshioka, M., Daskalakis, N., Decesari, S., Gysel-Beer, M., Kalivitis, N., Liu, X., Mahowald, N. M., Myriokefalitakis, S., Schrödner, R., Sfakianaki, M., Tsimpidi, A. P., Wu, M., and Yu, F.: Evaluation of global simulations of aerosol particle and cloud condensation nuclei number, with implications for cloud droplet formation, Atmos. Chem. Phys., 19, 8591–8617, https://doi.org/10.5194/acp-19-8591-2019 , 2019.

Feichter, J., Kjellström, E., Rodhe, H., Dentener, F., Lelieveldi, J., & Roelofs, G. J.: Simulation of the tropospheric sulfur cycle in a global climate model. *Atmospheric Environment*, *30*(10-11), 1693-1707, https://doi.org/10.1016/1352-2310(95)00394-0, 1996.

Fountoukis, C. and Nenes, A.: ISORROPIA II: a computationally efficient thermodynamic equilibrium model for K^+–Ca^{2+}–Mg^{2+}–NH_4^+–Na^+–SO_4^{2-}–NO_3^-–Cl^-–H_2O aerosols, Atmos. Chem. Phys., 7, 4639–4659, https://doi.org/10.5194/acp-7-4639-2007 , 2007.

Fuchs, N. A. and Davies, C. N.: The mechanics of aerosols, Pergamon Press, Oxford, ISBN 9780486660554, 1964.

Gao, M., Ji, D., Liang, F., and Liu, Y.: Attribution of aerosol direct radiative forcing in China and India to emitting sectors, Atmospheric Environment, 190, 35-42, https://doi.org/10.1016/j.atmosenv.2018.07.011 , 2018.

Ghan, S. J., Liu, X., Easter, R. C., Zaveri, R., Rasch, P. J., Yoon, J. H., and Eaton, B.: Toward a Minimal Representation of Aerosols in Climate Models: Comparative Decomposition of Aerosol Direct, Semidirect, and Indirect Radiative Forcing, Journal of Climate, 25(19), 6461-6476, https://doi.org/10.1175/JCLI-D-11-00650.1, 2012.

Grewe, V., Brunner, D., Dameris, M., Grenfell, J. L., Hein, R., Shindell, D., and Staehelin, J.: Origin and variability of upper tropospheric nitrogen oxides and ozone at northern mid-latitudes, Atmospheric Environment, 35(20), 3421-3433, https://doi.org/10.1016/S1352-2310(01)00134-0 , 2001.

Hauglustaine, D. A., Balkanski, Y., and Schulz, M.: A global model simulation of present and future nitrate aerosols and their direct radiative forcing of climate, Atmospheric Chemistry and Physics, 14(20), 11031-11063, https://doi.org/10.5194/acp-14-11031-2014 , 2014.

Heald, C. L., Ridley, D. A., Kroll, J. H., Barrett, S. R. H., Cady-Pereira, K. E., Alvarado, M. J., and Holmes, C. D.: Contrasting the direct radiative effect and direct radiative forcing of aerosols, Atmos. Chem. Phys., 14, 5513–5527, https://doi.org/10.5194/acp-14-5513-2014 , 2014.

Hodzic, A., Bessagnet, B., & Vautard, R.: A model evaluation of coarse-mode nitrate heterogeneous formation on dust particles. *Atmospheric Environment*, *40*(22), 4158-4171, https://doi.org/10.1016/j.atmosenv.2006.02.015, 2006.

Interagency Monitoring of Protected Visual Environment (IM-PROVE): Federal Land Manager Environmental Database, https://vista.cira.colostate.edu/Improve/improve-data/ ,last access: 3 September 2024.

IPCC, 2013: *Climate Change 2013:* The Physical Science Basis. Contribution of Working Group I to the Fifth Assessment Report of the Intergovernmental Panel on Climate Change [Stocker, T.F., D. Qin, G.-K. Plattner, M. Tignor, S.K. Allen, J. Boschung, A. Nauels, Y. Xia, V. Bex and P.M. Midgley (eds.)]. Cambridge University Press, Cambridge, United Kingdom and New York, NY, USA.

Jockel, P., Sander, R., Kerkweg, A., Tost, H., and Lelieveld, J.: Technical note: The Modular Earth Submodel System (MESSy) - a new approach towards Earth System Modeling, Atmospheric Chemistry and Physics, 5(2), 433-444, https://doi.org/10.5194/acp-5-433-2005 , 2005.

Jockel, P., Tost, H., Pozzer, A., Bruhl, C., Buchholz, J., Ganzeveld, L., Hoor, P., Kerkweg, A., Lawrence, M. G., Sander, R., Steil, B., Stiller, G., Tanarhte, M., Taraborrelli, D., Van Aardenne, J., and Lelieveld, J.: The atmospheric chemistry general circulation model ECHAM5/MESSy1: consistent simulation of ozone from the surface to the mesosphere, Atmospheric Chemistry and Physics, 6(12), 5067-5104, https://doi.org/10.5194/acp-6-5067-2006 , 2006.

Kakavas, S., Pandis, S. N., and Nenes, A.: ISORROPIA-Lite: A Comprehensive Atmospheric Aerosol Thermodynamics Module for Earth System Models, Tellus Series B-Chemical and Physical Meteorology, 74(1), 1-23, https://doi.org/10.16993/tellusb.33 , 2022.

Kanakidou, M., Seinfeld, J. H., Pandis, S. N., Barnes, I., Dentener, F. J., Facchini, M. C., Van Dingenen, R., Ervens, B., Nenes, A., Nielsen, C. J., Swietlicki, E., Putaud, J. P., Balkanski, Y., Fuzzi, S., Horth, J., Moortgat, G. K., Winterhalter, R., Myhre, C. E. L., Tsigaridis, K., Vignati, E., Stephanou, E. G., and Wilson, J.: Organic aerosol and global climate modelling: a review, Atmospheric Chemistry and Physics, 5(4), 1053-1123, https://doi.org/10.5194/acp-5-1053-2005 , 2005.

Karydis, V. A., Kumar, P., Barahona, D., Sokolik, I. N., and Nenes, A.: On the effect of dust particles on global cloud condensation nuclei and cloud droplet number, Journal of Geophysical Research: Atmospheres, 116, https://doi.org/10.1029/2011JD016283, 2011.

Karydis, V. A., Tsimpidi, A. P., Pozzer, A., Astitha, M., and Lelieveld, J.: Effects of mineral dust on global atmospheric nitrate concentrations, Atmospheric Chemistry and Physics, 16(3), 1491-1509, https://doi.org/10.5194/acp-16-1491-2016 , 2016.

Karydis, V. A., Tsimpidi, A. P., Bacer, S., Pozzer, A., Nenes, A., and Lelieveld, J.: Global impact of mineral dust on cloud droplet number concentration, Atmospheric Chemistry and Physics, 17(9), 5601-5621, https://doi.org/10.5194/acp-17-5601-2017 , 2017.

Kelly, J. T., Chuang, C. C., and Wexler, A. S.: Influence of dust composition on cloud droplet formation, Atmospheric Environment, 41(14), 2904-2916, https://doi.org/10.1016/j.atmosenv.2006.12.008 , 2007.

Kerkweg, A., Buchholz, J., Ganzeveld, L., Pozzer, A., Tost, H., and Jockel, P.: Technical note: An implementation of the dry removal processes DRY DEPosition and SEDImentation in the modular earth submodel system (MESSy), Atmospheric Chemistry and Physics, 6(12), 4617-4632, https://doi.org/10.5194/acp-6-4617-2006 , 2006.

Khain, A. P. and Pinsky, M.: Physical Processes in Clouds and Cloud Modeling, Cambridge University Press, ISBN 9781139049481, 2018.

Kirchstetter, T. W., Novakov, T., and Hobbs, P. V.: Evidence that the spectral dependence of light absorption by aerosols is affected by organic carbon, Journal of Geophysical Research: Atmospheres, 109(D21), https://doi.org/10.1029/2004JD004999 , 2004.

Klingmüller, K., Metzger, S., Abdelkader, M., Karydis, V. A., Stenchikov, G. L., Pozzer, A., and Lelieveld, J.: Revised mineral dust emissions in the atmospheric chemistry-climate model EMAC (MESSy 2.52 DU_Astitha1 KKDU2017 patch), Geoscientific Model Development, 11(3), 989-1008, https://doi.org/10.5194/gmd-11-989-2018 , 2018.

Klingmüller, K., Lelieveld, J., Karydis, V. A., and Stenchikov, G. L.: Direct radiative effect of dust–pollution interactions, Atmospheric Chemistry and Physics, 19(11), 7397-7408, https://doi.org/10.5194/acp-19-7397-2019 , 2019.

Klingmüller, K., Karydis, V. A., Bacer, S., Stenchikov, G. L., and Lelieveld, J.: Weaker cooling by aerosols due to dust–pollution interactions, Atmospheric Chemistry and Physics, 20(23), 15285-15295, https://doi.org/10.5194/acp-20-15285-2020 , 2020.

Kok, J. F., Storelvmo, T., Karydis, V. A., Adebiyi, A. A., Mahowald, N. M., Evan, A. T., He, C., and Leung, D. M.: Mineral dust aerosol impacts on global climate and climate change, Nature Reviews Earth & Environment, 4(2), 71-86, https://doi.org/10.1038/s43017-022-00379-5 , 2023.

Krueger, B. J., Grassian, V. H., Cowin, J. P., & Laskin, A.: Heterogeneous chemistry of individual mineral dust particles from different dust source regions: the importance of particle mineralogy. *Atmospheric Environment*, *38*(36), 6253-6261, https://doi.org/10.1016/j.atmosenv.2004.07.010, 2004.

Lance, S., Nenes, A., and Rissman, T. A.: Chemical and dynamical effects on cloud droplet number: Implications for estimates of the aerosol indirect effect, Journal of Geophysical Research: Atmospheres, 109(D22), https://doi.org/10.1029/2004JD004596 , 2004.

Laskin, A., Wietsma, T. W., Krueger, B. J., and Grassian, V. H.: Heterogeneous chemistry of individual mineral dust particles with nitric acid: A combined CCSEM/EDX, ESEM, and ICP-MS study, Journal of Geophysical Research: Atmospheres, 110(D10), https://doi.org/10.1029/2004JD005206 , 2005.

Li, J., Wang, W.-C., Liao, H., and Chang, W.: Past and future direct radiative forcing of nitrate aerosol in East Asia, Theoretical and Applied Climatology, 121, 445-458, https://doi.org/10.1007/s00704-014-1249-1 , 2015.

Li, X., Yu, Z., Yue, M., Liu, Y., Huang, K., Chi, X., ... & Wang, M.: Impact of mineral dust photocatalytic heterogeneous chemistry on the formation of the sulfate and nitrate: A modelling study over East Asia. *Atmospheric Environment*, *316*, 120166, https://doi.org/10.1016/j.atmosenv.2023.120166, 2024.

Liao, H., Seinfeld, J. H., Adams, P. J., and Mickley, L. J.: Global radiative forcing of coupled tropospheric ozone and aerosols in a unified general circulation model, Journal of Geophysical Research: Atmospheres, 109(D16), https://doi.org/10.1029/2003JD004456 , 2004.

Lohmann, U. and Roeckner, E.: Design and performance of a new cloud microphysics scheme developed for the ECHAM general circulation model, Climate Dynamics, 12, 557-572, https://doi.org/10.1007/BF00207939 , 1996.
Lohmann, U. and Feichter, J.: Global indirect aerosol effects: a review, Atmospheric Chemistry and Physics, 5(3), https://doi.org/10.5194/acp-5-715-2005 , 2005.
Lohmann, U. and Ferrachat, S.: Impact of parametric uncertainties on the present-day climate and on the anthropogenic aerosol effect, Atmospheric Chemistry and Physics, 10(23), https://doi.org/10.5194/acp-10-11373-2010 , 2010.
Milousis, A., Tsimpidi, A. P., Tost, H., Pandis, S. N., Nenes, A., Kiendler-Scharr, A., and Karydis, V. A.: Implementation of the ISORROPIA-lite aerosol thermodynamics model into the EMAC chemistry climate model (based on MESSy v2.55): implications for aerosol composition and acidity, Geoscientific Model Development, 17(3), 1111-1131, https://doi.org/10.5194/gmd-17-1111-2024 , 2024.
Morales Betancourt, R. and Nenes, A.: Understanding the contributions of aerosol properties and parameterization discrepancies to droplet number variability in a global climate model, Atmospheric Chemistry and Physics, 14(9), 4809-4826, https://doi.org/10.5194/acp-14-4809-2014 , 2014.
Myhre, G., Samset, B. H., Schulz, M., Balkanski, Y., Bauer, S., Berntsen, T. K., Bian, H., Bellouin, N., Chin, M., Diehl, T., Easter, R. C., Feichter, J., Ghan, S. J., Hauglustaine, D., Iversen, T., Kinne, S., Kirkevåg, A., Lamarque, J. F., Lin, G., Liu, X., Lund, M. T., Luo, G., Ma, X., van Noije, T., Penner, J. E., Rasch, P. J., Ruiz, A., Seland, Ø., Skeie, R. B., Stier, P., Takemura, T., Tsigaridis, K., Wang, P., Wang, Z., Xu, L., Yu, H., Yu, F., Yoon, J. H., Zhang, K., Zhang, H., and Zhou, C.: Radiative forcing of the direct aerosol effect from AeroCom Phase II simulations, Atmospheric Chemistry and Physics, 13(4), 1853-1877, https://doi.org/10.5194/acp-13-1853-2013 , 2013.
Myhre, G., Shindell, D., and Pongratz, J.: Anthropogenic and natural radiative forcing, Climate Change 2013-The Physical Science Basis, 659-740, https://dx.doi.org/10.1017/CBO9781107415324.018 , 2014.
Nenes, A., Murray, B., Bougiatioti, A. (2014). Mineral Dust and its Microphysical Interactions with Clouds. In: Knippertz, P., Stuut, JB. (eds) Mineral Dust. Springer, Dordrecht. https://doi.org/10.1007/978-94-017-8978-3_12 , 2014.
Nenes, A., Pandis, S. N., Weber, R. J., and Russell, A.: Aerosol pH and liquid water content determine when particulate matter is sensitive to ammonia and nitrate availability, Atmos. Chem. Phys., 20, 3249–3258, https://doi.org/10.5194/acp-20-3249-2020 , 2020.
Pozzer, A., Jockel, P. J., Sander, R., Williams, J., Ganzeveld, L., and Lelieveld, J.: Technical note: the MESSy-submodel AIRSEA calculating the air-sea exchange of chemical species, Atmospheric Chemistry and Physics, 6(12), 5435-5444, https://doi.org/10.5194/acp-6-5435-2006 , 2006.
Pozzer, A., de Meij, A., Pringle, K. J., Tost, H., Doering, U. M., van Aardenne, J., and Lelieveld, J.: Distributions and regional budgets of aerosols and their precursors simulated with the EMAC chemistry-climate model, Atmos. Chem. Phys., 12, 961–987, https://doi.org/10.5194/acp-12-961-2012 , 2012.
Pozzer, A., Reifenberg, S. F., Kumar, V., Franco, B., Kohl, M., Taraborrelli, D., Gromov, S., Ehrhart, S., Jöckel, P., Sander, R., Fall, V., Rosanka, S., Karydis, V., Akritidis, D., Emmerichs, T., Crippa, M., Guizzardi, D., Kaiser, J. W., Clarisse, L., Kiendler-Scharr, A., Tost, H., and Tsimpidi, A.: Simulation of organics in the atmosphere: evaluation of EMACv2.54 with the Mainz Organic Mechanism (MOM) coupled to the ORACLE (v1.0) submodel, Geosci. Model Dev., 15, 2673–2710, https://doi.org/10.5194/gmd-15-2673-2022 , 2022.
Pringle, K. J., Tost, H., Message, S., Steil, B., Giannadaki, D., Nenes, A., Fountoukis, C., Stier, P., Vignati, E., and Leieved, J.: Description and evaluation of GMXe: a new aerosol submodel for global simulations (v1), Geoscientific Model Development, 3(2), https://doi.org/10.5194/gmd-3-391-2010 , 2010a.

Pringle, K. J., Tost, H., Metzger, S., Steil, B., Giannadaki, D., Nenes, A., Fountoukis, C., Stier, P., Vignati, E., and Lelieveld, J.: Corrigendum to "Description and evaluation of GMXe: a new aerosol submodel for global simulations (v1)" published in Geosci. Model Dev., 3, 391–412, 2010, Geoscientific Model Development, 3(2), 413-413, https://doi.org/10.5194/gmd-3-413-2010 , 2010b.

Pringle, K. J., Tost, H., Pozzer, A., Pöschl, U., and Lelieveld, J.: Global distribution of the effective aerosol hygroscopicity parameter for CCN activation, Atmos. Chem. Phys., 10, 5241–5255, https://doi.org/10.5194/acp-10-5241-2010 , 2010c.

Roeckner, E., Brokopf, R., Esch, M., Giorgetta, M., Hagemann, S., Kornblueh, L., Manzini, E., Schlese, U., and Schulzweida, U.: Sensitivity of simulated climate to horizontal and vertical resolution in the ECHAM5 atmosphere model, Journal of Climate, 19(16), 3771-3791, https://doi.org/10.1175/JCLI3824.1 , 2006.

Sander, R., Baumgaertner, A., Cabrera-Perez, D., Frank, F., Gromov, S., Grooss, J. U., Harder, H., Huijnen, V., Jockel, P., Karydis, V. A., Niemeyer, K. E., Pozzer, A., Hella, R. B., Schultz, M. G., Taraborrelli, D., and Tauer, S.: The community atmospheric chemistry box model CAABA/MECCA-4.0, Geoscientific Model Development, 12(4), 1365-1385, https://doi.org/10.5194/gmd-12-1365-2019 , 2019.

Seinfeld, J. H. and Pandis, S. N.: Atmospheric chemistry and physics from air pollution to climate change, John Wiley & Sons, ISBN 1118947401, 2016.

Seinfeld, J. H., Bretherton, C., Carslaw, K. S., Coe, H., DeMott, P. J., Dunlea, E. J., Feingold, G., Ghan, S., Guenther, A. B., Kahn, R., Kraucunas, I., Kreidenweis, S. M., Molina, M. J., Nenes, A., Penner, J. E., Prather, K. A., Ramanathan, V., Ramaswamy, V., Rasch, P. J., Ravishankara, A. R., Rosenfeld, D., Stephens, G., and Wood, R.: Improving our fundamental understanding of the role of aerosol−cloud interactions in the climate system, Proceedings of the National Academy of Sciences, 113(21), 5781-5790, https://doi.org/10.1073/pnas.1514043113 , 2016.

Seisel, S., Börensen, C., Vogt, R., & Zellner, R.: Kinetics and mechanism of the uptake of N 2 O 5 on mineral dust at 298 K. *Atmospheric Chemistry and Physics*, *5*(12), 3423-3432, https://doi.org/10.5194/acp-5-3423-2005 , 2005.

Sposito, G.: The Chemistry of Soils, Oxford University Press, New York, ISBN 9780190630881, 1989.

Sundqvist, H., Berge, E., and Kristjánsson, J. E.: Condensation and Cloud Parameterization Studies with a Mesoscale Numerical Weather Prediction Model, Monthly Weather Review, 117(8), 1641-1657, https://doi.org/10.1175/1520-0493(1989)117%3C1641:CACPSW%3E2.0.CO;2 , 1989.

Tang, M. J., Thieser, J., Schuster, G., & Crowley, J. N.: Kinetics and mechanism of the heterogeneous reaction of N 2 O 5 with mineral dust particles. *Physical Chemistry Chemical Physics*, *14*(24), 8551-8561, https://doi.org/10.1039/C2CP40805H, 2012.

The Acid Deposition Monitoring Network in East Asia: EANET Data on the Acid Deposition in the East Asian Region, https://monitoring.eanet.asia/document/public/index , last access: 3 September 2024.

Tompkins, A. M.: A Prognostic Parameterization for the Subgrid-Scale Variability of Water Vapor and Clouds in Large-Scale Models and Its Use to Diagnose Cloud Cover, Journal of the Atmospheric Sciences, 59(12), 1917-1942, https://doi.org/10.1175/1520-0469(2002)059%3C1917:APPFTS%3E2.0.CO;2 , 2002.

Tost, H., Jockel, P. J., Kerkweg, A., Sander, R., and Lelieveld, J.: Technical note: A new comprehensive SCAVenging submodel for global atmospheric chemistry modelling, Atmospheric Chemistry and Physics, 6(3), 565-574, https://doi.org/10.5194/acp-6-565-2006 , 2006.

Tost, H., Jöckel, P., and Lelieveld, J.: Lightning and convection parameterisations - uncertainties in global modelling, Atmospheric Chemistry and Physics, 7(17), 4553-4568, https://doi.org/10.5194/acp-7-4553-2007 , 2007a.

Tost, H., Jockel, P., Kerkweg, A., Pozzer, A., Sander, R., and Lelieveld, J.: Global cloud and precipitation chemistry and wet deposition: tropospheric model simulations with ECHAM5/MESSy1, Atmospheric Chemistry and Physics, 7(10), 2733-2757, https://doi.org/10.5194/acp-7-2733-2007 , 2007b.
Trump, E. R., Fountoukis, C., Donahue, N. M., and Pandis, S. N.: Improvement of simulation of fine inorganic PM levels through better descriptions of coarse particle chemistry, Atmospheric Environment, 102, 274-281, https://doi.org/10.1016/j.atmosenv.2014.11.059 , 2015.
Tsigaridis, K. and Kanakidou, M.: The present and future of secondary organic aerosol direct forcing on climate, Current Climate Change Reports, 4, 84-98, https://doi.org/10.1007/s40641-018-0092-3 , 2018.
Tsimpidi, A. P., Karydis, V. A., Pandis, S. N., and Lelieveld, J.: Global combustion sources of organic aerosols: model comparison with 84 AMS factor-analysis data sets, Atmos. Chem. Phys., 16, 8939–8962, https://doi.org/10.5194/acp-16-8939-2016 , 2016.
Tsimpidi, A. P., Karydis, V. A., Pandis, S. N., and Lelieveld, J.: Global-scale combustion sources of organic aerosols: sensitivity to formation and removal mechanisms, Atmos. Chem. Phys., 17, 7345–7364, https://doi.org/10.5194/acp-17-7345-2017 , 2017.
Twomey, S.: The Influence of Pollution on the Shortwave Albedo of Clouds, Journal of Atmospheric Sciences, 34, 1149-1152, https://doi.org/10.1175/1520-0469(1977)034%3C1149:TIOPOT%3E2.0.CO;2 , 1977.
Urdiales-Flores, D., Zittis, G., Hadjinicolaou, P., Osipov, S., Klingmüller, K., Mihalopoulos, N., Kanakidou, M., Economou, T., and Lelieveld, J.: Drivers of accelerated warming in Mediterranean climate-type regions, npj Climate and Atmospheric Science, 6(1), 97, https://doi.org/10.1038/s41612-023-00423-1 , 2023.
U.S. Environmental Protection Agency Clean Air Markets Division Clean Air Status and Trends Network (CASTNET): CASTNET Data, https://www.epa.gov/castnet , last access: 3 September 2024.
Vignati, E., Wilson, J., and Stier, P.: M7: An efficient size-resolved aerosol microphysics module for large-scale aerosol transport models, Journal of Geophysical Research: Atmospheres, 109(D22), https://doi.org/10.1029/2003JD004485 , 2004.
Wexler, A. S., & Seinfeld, J. H.: Second-generation inorganic aerosol model. *Atmospheric Environment. Part A. General Topics*, *25*(12), 2731-2748, https://doi.org/10.1016/0960-1686(91)90203-J, 1991**.**
Wong, J. P. S., Tsagkaraki, M., Tsiodra, I., Mihalopoulos, N., Violaki, K., Kanakidou, M., Sciare, J., Nenes, A., and Weber, R. J.: Atmospheric evolution of molecular-weight-separated brown carbon from biomass burning, Atmospheric Chemistry and Physics, 19(11), 7319-7334, https://doi.org/10.5194/acp-19-7319-2019 , 2019.
Xu, L. and Penner, J. E.: Global simulations of nitrate and ammonium aerosols and their radiative effects, Atmospheric Chemistry and Physics, 12(20), https://doi.org/10.5194/acp-12-9479-2012 , 2012.
Yienger, J. J. and Levy, H.: EMPIRICAL-MODEL OF GLOBAL SOIL-BIOGENIC NOX EMISSIONS, Journal of Geophysical Research: Atmospheres, 100(D6), https://doi.org/10.1029/95JD00370 , 1995.
Zhang, Y., Forrister, H., Liu, J., Dibb, J., Anderson, B., Schwarz, J. P., Perring, A. E., Jimenez, J. L., Campuzano-Jost, P., Wang, Y., Nenes, A., and Weber, R. J.: Top-of-atmosphere radiative forcing affected by brown carbon in the upper troposphere, Nature Geoscience, 10(7), https://doi.org/10.1038/ngeo2960 , 2017.
Zhang, B.: The effect of aerosols to climate change and society, Journal of Geoscience and Environment Protection, 8(08), 55, https://doi.org/10.4236/gep.2020.88006 , 2020.

5 Conclusions

A central objective of this thesis was to investigate a variety of aspects associated with nitrate aerosol formation over a range of geographic locations and how different conditions affect that process in a global model. Furthermore, the impact of the aerosol physical state assumption and the inorganic aerosol acidity on nitrate aerosol global concentrations was also studied. The findings of this study indicate that employing a stable or a metastable assumption is more advantageous over specific regions, although the selection of a particular assumption should not be regarded as a straightforward decision on a global scale (Ansari and Pandis, 2000; Fountoukis et al., 2009; Karydis et al., 2010; Cheng et al., 2022). Furthermore, this thesis aims to suggest optimal global and/or regional model setups in order to minimize the bias between predictions and observations regarding fine mode nitrate aerosol. This is due to the fact that many models exhibit an overprediction bias when estimating PM_1 and $PM_{2.5}$ NO_3^- concentrations (Fountoukis et al., 2011; Heald et al., 2012; Ciarelli et al., 2016; Bian et al., 2017; Chen et al., 2018; Zakoura and Pandis, 2019; Tan et al., 2020; Jones et al., 2021; Miao et al., 2022). The suggestions pertain to the most polluted regions of the Northern Hemisphere, characterized by elevated average concentrations of fine-mode NO_3^- (namely, East Asia, India, Europe, and North America). A pivotal element of this thesis is the examination of the implications that dust-nitrate interactions have on the radiative effect of coarse, fine, and total NO_3^-. While the impact of dust-pollution interactions on the radiative effects of both has been the aim of recent studies (Klingmüller et al., 2018, 2019; Kok et al., 2023), not a lot of focus has been given specifically to nitrate aerosols. This thesis places particular emphasis on the radiative effect of NO_3^- due to aerosol-cloud interactions, as it is identified as the source of the greatest uncertainty in estimating the radiative forcing of this species, a common issue across various aerosols (Myhre et al., 2014; Seinfeld et al., 2016).

With respect to the initial research objective, following the successful implementation of the inorganic aerosol thermodynamics module, designated ISORROPIA-lite, within the global chemistry and climate model EMAC, a comparative analysis of its outcomes with the prior version, designated ISRORROPIA II, was conducted. A notable distinction between the two versions pertains to the assumptions made about the physical state of the aerosols. In the ISORROPIA II framework, the aerosols are capable of undergoing solidification at low levels of humidity, indicating a stable state. Conversely, in the ISORROPIA-lite approach, the aerosols always persist in a supersaturated state, characterized as a metastable condition. Despite employing divergent approaches, the two versions demonstrated minimal differences on a global scale. However, discrepancies emerged over regions characterized by intermediate humidity values ranging from 20% to 60%. In such conditions, the metastable assumption does not favor the partition of nitrate towards the aerosol phase, consequently resulting in slightly lower fine mode NO_3^- concentrations (up to 1.5 $\mu g/m^3$ or ~25%). This behavior was observed in regions such as the Himalayan Plateau and the Amazon Basin, in proximity to the Atacama Desert. East Asia was also a region that resulted in lower fine mode NO_3^- concentrations by the metastable assumption, as the low

sulfate/nitrate ratio of that area results in higher fractions of partitioning to the aerosol phase by the stable assumption. Conversely, in other arid regions such as the Middle East and the general dust belt zone, the metastable assumption led to elevated concentrations of coarse mode NO_3^- (up to 1 $\mu g/m^3$ or ~15%), attributable to the augmented water content of aerosols in these regions relative to the stable assumption. This heightened water content resulted in increased HNO_3 adsorption on dust particles, consequently elevating coarse mode NO_3^- concentrations.

Furthermore, the metastable assumption yielded, on average, more acidic coarse, but especially accumulation mode inorganic aerosols, over regions within the humidity range of 20% - 60%. This phenomenon can be attributed to the stable assumption, wherein, under conditions of low humidity, non-volatile cations (NVCs) present in the aerosols of these regions precipitate out of the aqueous phase, thereby precluding their inclusion in acidity calculations. Conversely, within the metastable assumption, the NVCs persist in the aqueous phase, irrespective of the humidity values. This phenomenon results in a reduction of inorganic aerosol acidity. However, the differences between these assumptions remained within a range of 1 pH unit. Accumulation mode particles were found to have more acidic values than coarse mode particles in regions with high NH_3 concentrations. A sensitivity analysis, in which the global NH_3 emissions were reduced by 50%, revealed a robust buffering mechanism that governs the pH of accumulation mode particles, which exhibited differences up to 3 pH units in the absence of typical NH_3 concentrations. This effect was less pronounced in coarse mode particles, which exhibited a tendency to exhibit higher alkalinity in these regions.

Finally, it was observed that ISORROPIA-lite led to a computational speed enhancement of up to 5% in comparison to ISORROPIA II, in terms of the number of time steps that the global model was capable of executing per second. This enhancement can be attributed to the utilization of pre-calculated look-up tables for the ionic activity coefficients, as opposed to their online computation during runtime, as implemented in ISORROPIA-lite. Given the negligible differences between the two versions, especially on a global scale, ISORROPIA-lite emerges as a reliable alternative for multi-decadal global-scale climate simulations..

With regard to the second research objective, the results from the global model were compared with surface measurements of PM_1 and $PM_{2.5}$ NO_3^- concentrations in the polluted North Hemisphere. Specifically, filter measurements of $PM_{2.5}$ NO_3^- were utilized from prominent observation networks in East Asia (EANET), Europe (EMEP), and the USA (EPA and IMPROVE). Concurrently, AMS measurements of PM_1 NO_3^- were utilized from campaigns conducted in East Asia, India, Europe, and North America, encompassing urban, rural, and downwind measurement locations.

The findings revealed a tendency of the model to overpredict $PM_{2.5}$ NO_3^- concentrations across all regions, with biases ranging from 1-2 ug/m^3 (Europe and US) up to a factor of 3 (East Asia). The discrepancy between model predictions and observations can be partly attributed to nitrate evaporation in filters during warmer periods, a phenomenon that is particularly evident in the cases of Europe and the US (EPA). East Asia exhibited a constant overprediction bias by the model throughout the year. The findings indicate that the adoption of either a higher model grid

resolution (specifically $1.125^o x\ 1.125^o$ instead of $1.875^o x\ 1.875^o$) or a lower uptake coefficient for N_2O_5 hydrolysis (namely, 0.002 instead of 0. 02), or the utilization of the CMIP6 anthropogenic emissions database, resulted in enhanced agreement between model predictions and $PM_{2.5}$ observations across all regions, as evidenced by their augmented statistical performance.

Additionally, it was observed that the model demonstrated a tendency to perform more effectively in estimating PM_1 NO3 concentrations, exhibiting generally higher levels of agreement when compared to AMS measurements. This was particularly evident in the regions of Europe and East Asia, where substantial agreement was observed, particularly in rural and urban locations. Conversely, the regions of North America and India exhibited higher model biases, characterized by underprediction of PM_1 values in rural and downwind locations in the former (~ factor of 2) and overprediction of PM_1 values in rural locations in the latter (~ factor of 4). In general, the downwind measurement locations were the most challenging for the model to replicate. Nevertheless, the use of a higher model grid resolution as well as a lower uptake coefficient for N_2O_5 hydrolysis, emerged as the most effective approaches to reduce this bias between model predictions and observations. Furthermore, it was observed that the utilization of distinct anthropogenic emissions databases yielded enhanced correlation across various regions. Specifically, the CAMS database exhibited reduced biases in regions such as Europe and India, while the HTAPv3 database demonstrated similar performance in North America and the CMIP6 database exhibited optimal performance in East Asia.

Finally, with regard to the third research objective, the impact of the interactions between dust and nitrate particles on the latter's radiative effects was assessed. Specifically, the present-day direct radiative effect (from aerosol-radiation interactions) of coarse and fine NO_3^- and the present-day indirect radiative effect (from aerosol-cloud interactions) of total NO_3^- were estimated at the top of the atmosphere. The findings revealed that coarse NO_3^- contributes to a positive direct effect (warming) of + 0.17 W/m^2 on average. This positive direct effect is driven by the absorption of LW radiation, which is enhanced by the increased coating of nitrate-containing dust particles after they interact with transported pollutants in desert regions. Conversely, fine NO_3^- exerts a negative direct effect (cooling) of – 0.28 W/m^2 on average, driven by the scattering of SW radiation, which is enhanced by the increased aerosol hygroscopicity of fine nitrate particles, after they interact with aged dust particles in regions with high anthropogenic activity. This results in the present day net direct radiative effect of total NO_3^- being -0.11 W/m^2 on average.

The study further unveils that total NO_3^- contributes to a positive indirect radiative effect of + 0.17 W/m^2 on average, driven by a + 0.27 W/m^2 warming in the SW part of the spectrum (less scattered radiation), outweighing a – 0.10 W/m^2 cooling in the LW part of the spectrum (less absorbed radiation). The negative indirect radiative effect in the LW spectrum is attributed to the fact that dust-nitrate interactions result in dust particles becoming more efficient ice nucleating particles. However, the ice clouds that are formed by these particles contain ice crystals that are larger in size but fewer in number. This phenomenon leads to the optical thinning of ice clouds, which are capable of absorbing less LW radiation, particularly within the dust belt zone where this behavior is most pronounced. Conversely, the positive indirect radiative effect in the SW spectrum

is attributable to the nitrate-induced enhancement in the hygroscopicity of fine and coarse mode aerosols, which can reach up to one order of magnitude. This, in turn, leads to an increase in the wet radius of these aerosols by up to 40% and 10%, respectively. Consequently, the presence of nitrates leads to an augmentation in the size of aerosols, thereby enhancing their efficacy as coagulators. The increased rates of coagulation result in a depletion of fine mode aerosol numbers (up to 10%), and in turn, an analogous decrease in the numbers of activated droplets by fine aerosols. The net effect of these processes is a reduction in the cloud albedo effect over regions where fine nitrate populations are dominant. This reduction in backscattered SW radiation, attributed to a warming indirect effect, is a key finding of this thesis.

A pivotal discovery in this study was the realization that the chemistry of mineral dust emerges as the most crucial factor influencing both radiative estimates and SW and LW estimates. This is evident by the fact that the exclusion of dust-nitrate interactions led to SW and LW estimates that were 40–50% weaker. A notable finding is the non-linear relationship between changes in global dust loading and global nitrate aerosol levels. This non-linearity is also reflected in the changes in radiative estimates.

The findings of this thesis build on and support the most recent findings of atmospheric and climate research while concurrently posing new research queries. Given the growing significance of nitrate aerosol, it is imperative that global models strive to minimize their biases and enhance the precision of NO_3^- concentration estimations. This approach would serve to reduce the uncertainty surrounding the estimation of the present day, as well as the anthropogenic radiative effects of the species. A crucial element in this regard is the incorporation of heterogeneous chemistry within global models to account for nitrate production on dust particles.

Bibliography

Adams, P. J., Seinfeld, J. H., and Koch, D. M.: Global concentrations of tropospheric sulfate, nitrate, and ammonium aerosol simulated in a general circulation model, Journal of Geophysical Research: Atmospheres, 104(D11), 13791-13823, https://doi.org/10.1029/1999JD900083, 1999.

Adams, P. J., Seinfeld, J. H., Koch, D., Mickley, L., and Jacob, D.: General circulation model assessment of direct radiative forcing by the sulfate-nitrate-ammonium-water inorganic aerosol system, Journal of Geophysical Research: Atmospheres, 106(D1), 1097-1111, https://doi.org/10.1029/2000JD900512, 2001.

Aksoyoglu, S., Ciarelli, G., El-Haddad, I., Baltensperger, U., and Prévôt, A. S. H.: Secondary inorganic aerosols in Europe: sources and the significant influence of biogenic VOC emissions, especially on ammonium nitrate, Atmospheric Chemistry and Physics, 17, 7757–7773, https://doi.org/10.5194/acp-17-7757-2017 , 2017.

Albrecht, B. A.: Aerosols, Cloud Microphysics, and Fractional Cloudiness, Science, 245(4923), 1227-1230, https://doi.org/10.1126/science.245.4923.1227 , 1989.

An, Q., Zhang, H., Wang, Z., Liu, Y., Xie, B., Liu, Q., Wang, Z., & Gong, S.: The development of an atmospheric aerosol/chemistry-climate model, BCC_AGCM_CUACE2. 0, and simulated effective radiative forcing of nitrate aerosols, Journal of Advances in Modeling Earth Systems, *11*(11), 3816-3835, https://doi.org/10.1029/2019MS001622, 2019.

Andreae, M. O. and Gelencsér, A.: Black carbon or brown carbon? The nature of light-absorbing carbonaceous aerosols, Atmospheric Chemistry and Physics, 6, 3131–3148, https://doi.org/10.5194/acp-6-3131-2006 , 2006.

Andreae, M. O., Jones, C. D., and Cox, P. M.: Strong present-day aerosol cooling implies a hot future, Nature, *435*(7046), 1187-1190, https://doi.org/10.1038/nature03671, 2005.

Ansari, A. S. and Pandis, S. N.: The effect of metastable equilibrium states on the partitioning of nitrate between the gas and aerosol phases, Atmospheric Environment, *34*(1), 157-168, https://doi.org/10.1016/S1352-2310(99)00242-3, 2000.

Arias, P.A., N. Bellouin, E. Coppola, R.G. Jones, G. Krinner, J. Marotzke, V. Naik, M.D. Palmer, G.-K. Plattner, J. Rogelj, M. Rojas, J. Sillmann, T. Storelvmo, P.W. Thorne, B. Trewin, K. Achuta Rao, B. Adhikary, R.P. Allan, K. Armour, G. Bala, R. Barimalala, S. Berger, J.G. Canadell, C. Cassou, A. Cherchi, W. Collins, W.D. Collins, S.L. Connors, S. Corti, F. Cruz, F.J. Dentener, C. Dereczynski, A. Di Luca, A. Diongue Niang, F.J. Doblas-Reyes, A. Dosio, H. Douville, F. Engelbrecht, V. Eyring, E. Fischer, P. Forster, B. Fox-Kemper, J.S. Fuglestvedt, J.C. Fyfe, N.P. Gillett, L. Goldfarb, I. Gorodetskaya, J.M. Gutierrez, R. Hamdi, E. Hawkins, H.T. Hewitt, P. Hope, A.S. Islam, C. Jones, D.S. Kaufman, R.E. Kopp, Y. Kosaka, J. Kossin, S. Krakovska, J.-Y. Lee, J. Li, T. Mauritsen, T.K. Maycock, M. Meinshausen, S.-K. Min, P.M.S. Monteiro, T. Ngo-Duc, F. Otto, I. Pinto, A. Pirani, K. Raghavan, R. Ranasinghe, A.C. Ruane, L. Ruiz, J.-B. Sallée, B.H. Samset, S. Sathyendranath, S.I. Seneviratne, A.A. Sörensson, S. Szopa, I. Takayabu, A.-M. Tréguier, B. van den Hurk, R. Vautard, K. von Schuckmann, S. Zaehle, X. Zhang, and K. Zickfeld, 2021: Technical Summary. In *Climate Change 2021:* The Physical Science Basis. Contribution of Working Group I to the Sixth Assessment Report of the Intergovernmental Panel on Climate Change [Masson-Delmotte, V., P. Zhai, A. Pirani, S.L. Connors, C. Péan, S. Berger,

N. Caud, Y. Chen, L. Goldfarb, M.I. Gomis, M. Huang, K. Leitzell, E. Lonnoy, J.B.R. Matthews, T.K. Maycock, T. Waterfield, O. Yelekçi, R. Yu, and B. Zhou (eds.)]. Cambridge University Press, Cambridge, United Kingdom and New York, NY, USA, https://doi.org/10.1017/9781009157896.002 , 2021.

Bauer, S. E., Koch, D., Unger, N., Metzger, S. M., Shindell, D. T., and Streets, D. G.: Nitrate aerosols today and in 2030: a global simulation including aerosols and tropospheric ozone, Atmospheric Chemistry and Physics , 7(19) , https://doi.org/10.5194/acp-7-5043-2007 , 2007a.

Bauer, S. E., Mishchenko, M. I., Lacis, A. A., Zhang, S., Perlwitz, J., and Metzger, S. M.: Do sulfate and nitrate coatings on mineral dust have important effects on radiative properties and climate modeling?, Journal of Geophysical Research: Atmospheres, 112(D6), https://doi.org/10.1029/2005JD006977, 2007b.

Bellouin, N., Rae, J., Jones, A., Johnson, C., Haywood, J., and Boucher, O.: Aerosol forcing in the Climate Model Intercomparison Project (CMIP5) simulations by HadGEm^2-ES and the role of ammonium nitrate, Journal of Geophysical Research: Atmospheres, 116(D20) , https://doi.org/10.1029/2011JD016074 , 2011.

Bian, H., Chin, M., Hauglustaine, D. A., Schulz, M., Myhre, G., Bauer, S. E., Lund, M. T., Karydis, V. A., Kucsera, T. L., Pan, X., Pozzer, A., Skeie, R. B., Steenrod, S. D., Sudo, K., Tsigaridis, K., Tsimpidi, A. P., and Tsyro, S. G.: Investigation of global particulate nitrate from the AeroCom phase III experiment, Atmospheric Chemistry and Physics, 17, 12911–12940, https://doi.org/10.5194/acp-17-12911-2017 , 2017.

Bougiatioti, A., Nikolaou, P., Stavroulas, I., Kouvarakis, G., Weber, R., Nenes, A., Kanakidou, M., and Mihalopoulos, N.: Particle water and pH in the eastern Mediterranean: source variability and implications for nutrient availability, Atmospheric Chemistry and Physics, 16, 4579–4591, https://doi.org/10.5194/acp-16-4579-2016 , 2016.

Brooks, S. D., Garland, R. M., Wise, M. E., Prenni, A. J., Cushing, M., Hewitt, E., and Tolbert, M. A.: Phase changes in internally mixed maleic acid/ammonium sulfate aerosols, Journal of Geophysical Research: Atmospheres, 108(D15), https://doi.org/10.1029/2002JD003204 , 2003.

Carslaw, K. S. (Ed): Aerosols and climate. Elsevier, ISBN 9780128197660 , 2022.

Chen, L., Gao, Y., Zhang, M., Fu, J. S., Zhu, J., Liao, H., Li, J., Huang, K., Ge, B., Wang, X., Lam, Y. F., Lin, C.-Y., Itahashi, S., Nagashima, T., Kajino, M., Yamaji, K., Wang, Z., and Kurokawa, J.: MICS-Asia III: multi-model comparison and evaluation of aerosol over East Asia, Atmospheric Chemistry and Physics, 19, 11911–11937, https://doi.org/10.5194/acp-19-11911-2019 , 2019a.

Chen, Y., Wolke, R., Ran, L., Birmili, W., Spindler, G., Schröder, W., Su, H., Cheng, Y., Tegen, I., and Wiedensohler, A.: A parameterization of the heterogeneous hydrolysis of N_2O_5 for mass-based aerosol models: improvement of particulate nitrate prediction, Atmospheric Chemistry and Physics, 18, 673–689, https://doi.org/10.5194/acp-18-673-2018 , 2018.

Chen, Y. L., Shen, H. Z., and Russell, A. G.: Current and Future Responses of Aerosol pH and Composition in the US to Declining SO_2 Emissions and Increasing NH_3 Emissions, Environmental Science & Technology, 53(16), 9646-9655, https://doi.org/10.1021/acs.est.9b02005 , 2019b.

Cheng, B., Wang-Li, L., Classen, J., and Bloomfield, P.: Performance of a Thermodynamic Model for Predicting Inorganic Aerosols in the Southeastern U.S, Atmosphere, 13, 1977, https://doi.org/10.3390/atmos13121977 , 2022.

Ciarelli, G., Aksoyoglu, S., Crippa, M., Jimenez, J.-L., Nemitz, E., Sellegri, K., Äijälä, M., Carbone, S., Mohr, C., O'Dowd, C., Poulain, L., Baltensperger, U., and Prévôt, A. S. H.: Evaluation of European air quality modelled by CAMx including the volatility basis set scheme, Atmospheric Chemistry and Physics, 16, 10313–10332, https://doi.org/10.5194/acp-16-10313-2016 , 2016.

Ciarelli, G., Theobald, M. R., Vivanco, M. G., Beekmann, M., Aas, W., Andersson, C., Bergström, R., Manders-Groot, A., Couvidat, F., Mircea, M., Tsyro, S., Fagerli, H., Mar, K., Raffort, V., Roustan, Y., Pay, M.-T., Schaap, M., Kranenburg, R., Adani, M., Briganti, G., Cappelletti, A., D'Isidoro, M., Cuvelier, C., Cholakian, A., Bessagnet, B., Wind, P., and Colette, A.: Trends of inorganic and organic aerosols and precursor gases in Europe: insights from the EURODELTA multi-model experiment over the 1990–2010 period, Geoscientific Model Development, 12, 4923–4954, https://doi.org/10.5194/gmd-12-4923-2019 , 2019.

Cunningham, E.: On the velocity of steady fall of spherical particles through fluid medium, Proceedings of the Royal Society of London. Series A, Containing Papers of a Mathematical and Physical Character, 83, 357-365, 1910.

Curtius, J.: Nucleation of atmospheric aerosol particles, Comptes Rendus Physique, *7*(9-10), 1027-1045, 2006.

Fountoukis, C., Nenes, A., Sullivan, A., Weber, R., Van Reken, T., Fischer, M., Matías, E., Moya, M., Farmer, D., and Cohen, R. C.: Thermodynamic characterization of Mexico City aerosol during MILAGRO 2006, Atmospheric Chemistry and Physics, 9, 2141–2156, https://doi.org/10.5194/acp-9-2141-2009 , 2009.

Fountoukis, C., Racherla, P. N., Denier van der Gon, H. A. C., Polymeneas, P., Charalampidis, P. E., Pilinis, C., Wiedensohler, A., Dall'Osto, M., O'Dowd, C., and Pandis, S. N.: Evaluation of a three-dimensional chemical transport model (PMCAMx) in the European domain during the EUCAARI May 2008 campaign, Atmospheric Chemistry and Physics, 11, 10331–10347, https://doi.org/10.5194/acp-11-10331-2011 , 2011.

Fu, X., Wang, S., Xing, J., Zhang, X., Wang, T., and Hao, J.: Increasing ammonia concentrations reduce the effectiveness of particle pollution control achieved via SO_2 and NO X emissions reduction in east China, Environmental Science & Technology Letters, *4*(6), 221-227, https://doi.org/10.1021/acs.estlett.7b00143, 2017.

Fuchs, N. A. and Davies, C. N.: The mechanics of aerosols, Pergamon Press, Oxford, ISBN 9780486660554, 1964.

Guo, H., Xu, L., Bougiatioti, A., Cerully, K. M., Capps, S. L., Hite Jr., J. R., Carlton, A. G., Lee, S.-H., Bergin, M. H., Ng, N. L., Nenes, A., and Weber, R. J.: Fine-particle water and pH in the southeastern United States, Atmospheric Chemistry and Physics, 15, 5211–5228, https://doi.org/10.5194/acp-15-5211-2015 , 2015.

Guo, H., Sullivan, A. P., Campuzano-Jost, P., Schroder, J. C., Lopez-Hilfiker, F. D., Dibb, J. E., Jimenez, J. L., Thornton, J. A., Brown, S. S., Nenes, A., and Weber, R. J.: Fine particle pH and the partitioning of

nitric acid during winter in the northeastern United States, Journal of Geophysical Research: Atmospheres, 121, 10, 355-310, 376, https://doi.org/10.1002/2016JD025311 , 2016.

Guo, H., Otjes, R., Schlag, P., Kiendler-Scharr, A., Nenes, A., and Weber, R. J.: Effectiveness of ammonia reduction on control of fine particle nitrate, Atmospheric Chemistry and Physics, 18, 12241–12256, https://doi.org/10.5194/acp-18-12241-2018 , 2018.

Galindo, N., Nicolás, J. F., Yubero, E., Caballero, S., Pastor, C., & Crespo, J.: Factors affecting levels of aerosol sulfate and nitrate on the Western Mediterranean coast, Atmospheric Research, *88*(3-4), 305-313, https://doi.org/10.1016/j.atmosres.2007.11.024, 2008.

Hand, J. L., Schichtel, B. A., Malm, W. C., and Pitchford, M. L.: Particulate sulfate ion concentration and SO_2 emission trends in the United States from the early 1990s through 2010, Atmospheric Chemistry and Physics, 12, 10353–10365, https://doi.org/10.5194/acp-12-10353-2012 , 2012.

Hauglustaine, D. A., Balkanski, Y., and Schulz, M.: A global model simulation of present and future nitrate aerosols and their direct radiative forcing of climate, Atmospheric Chemistry and Physics, 14(20), 11031-11063, https://doi.org/10.5194/acp-14-11031-2014 , 2014.

He, K., Yang, F., Ma, Y., Zhang, Q., Yao, X., Chan, C. K., Cadle, S., Chan, T., and Mulawa, P.: The characteristics of Pm^2. 5 in Beijing, China, Atmospheric Environment, 35(29), 4959-4970, https://doi.org/10.1016/S1352-2310(01)00301-6, 2001.

Heald, C. L., Collett Jr., J. L., Lee, T., Benedict, K. B., Schwandner, F. M., Li, Y., Clarisse, L., Hurtmans, D. R., Van Damme, M., Clerbaux, C., Coheur, P.-F., Philip, S., Martin, R. V., and Pye, H. O. T.: Atmospheric ammonia and particulate inorganic nitrogen over the United States, Atmospheric Chemistry and Physics, 12, 10295–10312, https://doi.org/10.5194/acp-12-10295-2012 , 2012.

Heald, C. L., Ridley, D. A., Kroll, J. H., Barrett, S. R. H., Cady-Pereira, K. E., Alvarado, M. J., and Holmes, C. D.: Contrasting the direct radiative effect and direct radiative forcing of aerosols, Atmospheric Chemistry and Physics, 14, 5513–5527, https://doi.org/10.5194/acp-14-5513-2014 , 2014.

Hidy, G.: Aerosols: an industrial and environmental science, Elsevier, ISBN 9780124123366, 2012.

IPCC, 2013: Climate Change 2013*:* The Physical Science Basis. Contribution of Working Group I to the Fifth Assessment Report of the Intergovernmental Panel on Climate Change [Stocker, T.F., D. Qin, G.-K. Plattner, M. Tignor, S.K. Allen, J. Boschung, A. Nauels, Y. Xia, V. Bex and P.M. Midgley (eds.)]. Cambridge University Press, Cambridge, United Kingdom and New York, NY, USA.

Jacobson, M. Z.: Fundamentals of atmospheric modeling, Cambridge university press, ISBN 9781139165389, 1999.

Jimenez, J. L., Canagaratna, M. R., Donahue, N. M., Prevot, A. S. H., Zhang, Q., Kroll, J. H., DeCarlo, P. F., Allan, J. D., Coe, H., Ng, N. L., Aiken, A. C., Docherty, K. S., Ulbrich, I. M., Grieshop, A. P., Robinson, A. L., Duplissy, J., Smith, J. D., Wilson, K. R., Lanz, V. A., Hueglin, C., Sun, Y. L., Tian, J., Laaksonen, A., Raatikainen, T., Rautiainen, J., Vaattovaara, P., Ehn, M., Kulmala, M., Tomlinson, J. M., Collins, D. R., Cubison, M. J., E, Dunlea, J., Huffman, J. A., Onasch, T. B., Alfarra, M. R., Williams, P. I., Bower, K., Kondo, Y., Schneider, J., Drewnick, F., Borrmann, S., Weimer, S., Demerjian, K., Salcedo, D., Cottrell, L., Griffin, R., Takami, A., Miyoshi, T., Hatakeyama, S., Shimono, A., Sun, J. Y., Zhang, Y. M., Dzepina, K., Kimmel, J. R., Sueper, D., Jayne, J. T., Herndon, S. C., Trimborn, A. M., Williams, L. R., Wood, E. C., Middlebrook, A. M., Kolb, C. E., Baltensperger, U., and Worsnop, D. R.: Evolution

of organic aerosols in the atmosphere, Science, 326(5959), 1525-1529, https://doi.org/10.1126/science.1180353, 2009.

Jones, A. C., Hill, A., Remy, S., Abraham, N. L., Dalvi, M., Hardacre, C., Hewitt, A. J., Johnson, B., Mulcahy, J. P., and Turnock, S. T.: Exploring the sensitivity of atmospheric nitrate concentrations to nitric acid uptake rate using the Met Office's Unified Model, Atmospheric Chemistry and Physics, 21, 15901–15927, https://doi.org/10.5194/acp-21-15901-2021 , 2021.

Kai, Z., Yuesi, W., Tianxue, W., Yousef, M., & Frank, M.: Properties of nitrate, sulfate and ammonium in typical polluted atmospheric aerosols (PM_{10}) in Beijing, Atmospheric Research, *84*(1), 67-77, https://doi.org/10.1016/j.atmosres.2006.05.004 , 2007.

Kajino, M., & Aikawa, M.: A model validation study of the washout/rainout contribution of sulfate and nitrate in wet deposition compared with precipitation chemistry data in Japan, Atmospheric Environment, *117*, 124-134, https://doi.org/10.1016/j.atmosenv.2015.06.042 , 2015.

Kanakidou, M., Seinfeld, J. H., Pandis, S. N., Barnes, I., Dentener, F. J., Facchini, M. C., Van Dingenen, R., Ervens, B., Nenes, A., Nielsen, C. J., Swietlicki, E., Putaud, J. P., Balkanski, Y., Fuzzi, S., Horth, J., Moortgat, G. K., Winterhalter, R., Myhre, C. E. L., Tsigaridis, K., Vignati, E., Stephanou, E. G., and Wilson, J.: Organic aerosol and global climate modelling: a review, Atmospheric Chemistry and Physics, 5(4), 1053-1123, https://doi.org/10.5194/acp-5-1053-2005 , 2005.

Karydis, V. A., Tsimpidi, A. P., Fountoukis, C., Nenes, A., Zavala, M., Lei, W., Molina, L. T., and Pandis, S. N.: Simulating the fine and coarse inorganic particulate matter concentrations in a polluted megacity, Atmospheric Environment, 44(5), 608-620, https://doi.org/10.1016/j.atmosenv.2009.11.023 , 2010.

Karydis, V. A., Kumar, P., Barahona, D., Sokolik, I. N., and Nenes, A.: On the effect of dust particles on global cloud condensation nuclei and cloud droplet number, Journal of Geophysical Research: Atmospheres, 116, https://doi.org/10.1029/2011JD016283, 2011.

Karydis, V. A., Tsimpidi, A. P., Pozzer, A., Astitha, M., and Lelieveld, J.: Effects of mineral dust on global atmospheric nitrate concentrations, Atmospheric Chemistry and Physics, 16(3), 1491-1509, https://doi.org/10.5194/acp-16-1491-2016 , 2016.

Karydis, V. A., Tsimpidi, A. P., Bacer, S., Pozzer, A., Nenes, A., and Lelieveld, J.: Global impact of mineral dust on cloud droplet number concentration, Atmos. Chem. Phys., 17, 5601–5621, https://doi.org/10.5194/acp-17-5601-2017 , 2017.

Kim, J. Y., Song, C. H., Ghim, Y. S., Won, J. G., Yoon, S. C., Carmichael, G. R., and Woo, J. H.: An investigation on NH_3 emissions and particulate NH_4^+–NO3− formation in East Asia, Atmospheric Environment, 40(12), 2139-2150, https://doi.org/10.1016/j.atmosenv.2005.11.048 , 2006.

Klingmüller, K., Lelieveld, J., Karydis, V. A., and Stenchikov, G. L.: Direct radiative effect of dust–pollution interactions, Atmospheric Chemistry and Physics, 19(11), 7397-7408, https://doi.org/10.5194/acp-19-7397-2019 , 2019.

Klingmüller, K., Karydis, V. A., Bacer, S., Stenchikov, G. L., and Lelieveld, J.: Weaker cooling by aerosols due to dust–pollution interactions, Atmospheric Chemistry and Physics, 20(23), 15285-15295, https://doi.org/10.5194/acp-20-15285-2020 , 2020.

Köhler, H.: The nucleus in and the growth of hygroscopic droplets, Transactions of the Faraday Society, *32*, 1152-1161, ISBN , 1936.

Kok, J. F., Storelvmo, T., Karydis, V. A., Adebiyi, A. A., Mahowald, N. M., Evan, A. T., He, C., and Leung, D. M.: Mineral dust aerosol impacts on global climate and climate change, Nature Reviews Earth & Environment, 4(2), 71-86, https://doi.org/10.1038/s43017-022-00379-5 , 2023.

Krzyzanowski, B., Mullan, A. F., Turcano, P., Camerucci, E., Bower, J. H., & Savica, R.: Air Pollution and Parkinson Disease in a Population-Based Study, JAMA Network Open, *7(9):e2433602*, https://doi.org/10.1001/jamanetworkopen.2024.33602, 2024.

Kumar, P., Sokolik, I. N., and Nenes, A.: Parameterization of cloud droplet formation for global and regional models: including adsorption activation from insoluble CCN, Atmospheric Chemistry and Physics, 9, 2517–2532, https://doi.org/10.5194/acp-9-2517-2009 , 2009.

Kumar, P., Sokolik, I. N., and Nenes, A.: Cloud condensation nuclei activity and droplet activation kinetics of wet processed regional dust samples and minerals, Atmospheric Chemistry and Physics, 11, 8661–8676, https://doi.org/10.5194/acp-11-8661-2011 , 2011.

Laaksonen, A., Talanquer, V., & Oxtoby, D. W.: Nucleation: Measurements, theory, and atmospheric applications, Annual Review of Physical Chemistry, *46*(1), 489-524, https://doi.org/10.1146/annurev.pc.46.100195.002421 , 1995.

Lajtha, K., Jones, J.: Trends in cation, nitrogen, sulfate and hydrogen ion concentrations in precipitation in the United States and Europe from 1978 to 2010: a new look at an old problem, Biogeochemistry, 116, 303–334, https://doi.org/10.1007/s10533-013-9860-2, 2013.

Lamarque, J.-F., Bond, T. C., Eyring, V., Granier, C., Heil, A., Klimont, Z., Lee, D., Liousse, C., Mieville, A., Owen, B., Schultz, M. G., Shindell, D., Smith, S. J., Stehfest, E., Van Aardenne, J., Cooper, O. R., Kainuma, M., Mahowald, N., McConnell, J. R., Naik, V., Riahi, K., and van Vuuren, D. P.: Historical (1850–2000) gridded anthropogenic and biomass burning emissions of reactive gases and aerosols: methodology and application, Atmospheric Chemistry and Physics, 10, 7017–7039, https://doi.org/10.5194/acp-10-7017-2010 , 2010.

Lanz, V. A., Prévôt, A. S. H., Alfarra, M. R., Weimer, S., Mohr, C., DeCarlo, P. F., Gianini, M. F. D., Hueglin, C., Schneider, J., Favez, O., D'Anna, B., George, C., and Baltensperger, U.: Characterization of aerosol chemical composition with aerosol mass spectrometry in Central Europe: an overview, Atmospheric Chemistry and Physics, 10, 10453–10471, https://doi.org/10.5194/acp-10-10453-2010 , 2010.

Leibensperger, E. M., Mickley, L. J., Jacob, D. J., Chen, W.-T., Seinfeld, J. H., Nenes, A., Adams, P. J., Streets, D. G., Kumar, N., and Rind, D.: Climatic effects of 1950–2050 changes in US anthropogenic aerosols – Part 1: Aerosol trends and radiative forcing, Atmospheric Chemistry and Physics, 12, 3333–3348, https://doi.org/10.5194/acp-12-3333-2012 , 2012.

Li, J., Wang, W. C., Liao, H., & Chang, W.: Past and future direct radiative forcing of nitrate aerosol in East Asia, Theoretical and Applied Climatology, *121*, 445-458, https://doi.org/10.1007/s00704-014-1249-1 , 2015.

Li, J. and Han, Z.: Seasonal Variation of Nitrate Concentration and Its Direct Radiative Forcing over East Asia, Atmosphere, 7(8), 105, https://doi.org/10.3390/atmos7080105 , 2016.

Li, S., Zhang, F., Jin, X., Sun, Y., Wu, H., Xie, C., Chen, L., Liu, J., Wu, T., Jiang, S., Cribb, M., and Li, Z.: Characterizing the ratio of nitrate to sulfate in ambient fine particles of urban Beijing during 2018–

2019, Atmospheric Environment, 237, 117662, https://doi.org/10.1016/j.atmosenv.2020.117662 , 2020.

Liao, H., Seinfeld, J. H., Adams, P. J., and Mickley, L. J.: Global radiative forcing of coupled tropospheric ozone and aerosols in a unified general circulation model, Journal of Geophysical Research: Atmospheres, 109(D16), https://doi.org/10.1029/2003JD004456 , 2004.

Lin, Y. C., Cheng, M. T., Lin, W. H., Lan, Y. Y., & Tsuang, B. J.: Causes of the elevated nitrate aerosol levels during episodic days in Taichung urban area, Taiwan, Atmospheric Environment, 44(13), 1632-1640, https://doi.org/10.1016/j.atmosenv.2010.01.039 , 2010.

Marticorena, B., and Bergametti G.: Modeling the atmospheric dust cycle: 1. Design of a soil-derived dust emission scheme, Journal of Geophysical Research: Atmospheres, 100(D8), 16415–16430, 10.1029/95JD00690 , 1995.

Metzger, S., Dentener, F., Pandis, S., and Lelieveld, J., Gas/aerosol partitioning, 1, A computationally efficient model, Journal of Geophysical Research: Atmospheres, 107(D16), https://doi.org/10.1029/2001JD001102 , 2002.

Miao, R., Chen, Q., Zheng, Y., Cheng, X., Sun, Y., Palmer, P. I., Shrivastava, M., Guo, J., Zhang, Q., Liu, Y., Tan, Z., Ma, X., Chen, S., Zeng, L., Lu, K., and Zhang, Y.: Model bias in simulating major chemical components of $PM_{2.5}$ in China, Atmospheric Chemistry and Physics, 20, 12265–12284, https://doi.org/10.5194/acp-20-12265-2020 , 2020.

Monahan, E. C.: The ocean as a source for atmospheric particles, in: The role of air-sea exchange in geochemical cycling, Springer, 129-163, 1986.

Moss, R. H., Edmonds, J. A., Hibbard, K. A., Manning, M. R., Rose, S. K., van Vuuren, D. P., Carter, T. R., Emori, S., Kainuma, M., Kram, T., Meehl, G. A., Mitchell, J. F. B., Nakicenovic, N., Riahi, K., Smith, S. J., Stouffer, R. J., Thomson, A. M., Weyant, J. P., and Wilbanks, T. J.: The next generation of scenarios for climate change research and assessment, Nature, 463(7282), 747-756, https://doi.org/10.1038/nature08823 , 2010.

Myhre, G., Myhre, C. L., Samset, B. H., & Storelvmo, T.: Aerosols and their relation to global climate and climate sensitivity, Nature Education Knowledge, *4*(5), 7, 2013.

Myhre, G., Shindell, D., and Pongratz, J.: Anthropogenic and natural radiative forcing, Climate Change 2013-The Physical Science Basis, 659-740, https://dx.doi.org/10.1017/CBO9781107415324.018 , 2014.

Nenes, A., Pandis, S. N., Weber, R. J., and Russell, A.: Aerosol pH and liquid water content determine when particulate matter is sensitive to ammonia and nitrate availability. Atmospheric Chemistry and Physics, *20*(5), 3249-3258, https://doi.org/10.5194/acp-20-3249-2020, 2020.

Parsons, M. T., Knopf, D. A., and Bertram, A. K.: Deliquescence and Crystallization of Ammonium Sulfate Particles Internally Mixed with Water-Soluble Organic Compounds, The Journal of Physical Chemistry A, 108(52), https://doi.org/10.1021/jp0462862 , 2004.

Petters, M. D. and Kreidenweis, S. M.: A single parameter representation of hygroscopic growth and cloud condensation nucleus activity, Atmospheric Chemistry and Physics, 7, 1961–1971, https://doi.org/10.5194/acp-7-1961-2007 , 2007.

Pope, C. A.: What do epidemiologic findings tell us about health effects of environmental aerosols? Journal of Aerosol Medicine, *13*(4), 335-354, https://doi.org/10.1089/jam.2000.13.335 , 2000.

Pope, C. A., & Dockery, D. W.: Health Effects of Fine Particulate Air Pollution: Lines that Connect, Journal of the Air & Waste Management Association, *56*(6), 709–742. https://doi.org/10.1080/10473289.2006.10464485, 2006.

Pruppacher, H. R. and Klett, J. D.: Microphysics of Clouds and Precipitation, Reidel, Dordrecht, ISBN 978-90-277-1106-9, 1979.

Pye, H. O. T., Nenes, A., Alexander, B., Ault, A. P., Barth, M. C., Clegg, S. L., Collett Jr., J. L., Fahey, K. M., Hennigan, C. J., Herrmann, H., Kanakidou, M., Kelly, J. T., Ku, I.-T., McNeill, V. F., Riemer, N., Schaefer, T., Shi, G., Tilgner, A., Walker, J. T., Wang, T., Weber, R., Xing, J., Zaveri, R. A., and Zuend, A.: The acidity of atmospheric particles and clouds, Atmospheric Chemistry and Physics, 20, 4809–4888, https://doi.org/10.5194/acp-20-4809-2020 , 2020.

Schaap, M., van Loon, M., ten Brink, H. M., Dentener, F. J., and Builtjes, P. J. H.: Secondary inorganic aerosol simulations for Europe with special attention to nitrate, Atmospheric Chemistry and Physics, 4, 857–874, https://doi.org/10.5194/acp-4-857-2004 , 2004.

Seinfeld, J. H. and Pandis, S. N.: *Atmospheric chemistry and physics: from air pollution to climate change*. John Wiley & Sons, ISBN 1118947401, 2016.

Seinfeld, J. H., Bretherton, C., Carslaw, K. S., Coe, H., DeMott, P. J., Dunlea, E. J., Feingold, G., Ghan, S., Guenther, A. B., Kahn, R., Kraucunas, I., Kreidenweis, S. M., Molina, M. J., Nenes, A., Penner, J. E., Prather, K. A., Ramanathan, V., Ramaswamy, V., Rasch, P. J., Ravishankara, A. R., Rosenfeld, D., Stephens, G., and Wood, R.: Improving our fundamental understanding of the role of aerosol−cloud interactions in the climate system, Proceedings of the National Academy of Sciences, 113(21), 5781-5790, https://doi.org/10.1073/pnas.1514043113 , 2016.

Shah, V., Jaeglé, L., Thornton, J. A., Lopez-Hilfiker, F. D., Lee, B. H., Schroder, J. C., Campuzano-Jost, P., Jimenez, J. L., Guo, H., Sullivan, A. P., Weber, R. J., Green, J. R., Fiddler, M. N., Bililign, S., Campos, T. L., Stell, M., Weinheimer, A. J., Montzka, D. D., and Brown, S. S.: Chemical feedbacks weaken the wintertime response of particulate sulfate and nitrate to emissions reductions over the eastern United States, Proceedings of the National Academy of Sciences, 115, 8110-8115, https://doi.org/10.1073/pnas.1803295115 , 2018.

Silva, P. J., Vawdrey, E. L., Corbett, M., and Erupe, M.: Fine particle concentrations and composition during wintertime inversions in Logan, Utah, USA, Atmospheric Environment, 41(26), 5410-5422, https://doi.org/10.1016/j.atmosenv.2007.02.016, 2007.

Slinn, W. G.: Precipitation scavenging: some problems, approximate solutions and suggestions for future research, Battelle Pacific Northwest Labs., Richland, Wash.(USA), 1974.

Slinn, S. A. and Slinn, W. G. N.: Predictions for particle deposition on natural waters, Atmospheric Environment (1967), 14, 1013-1016, https://doi.org/10.1016/0004-6981(80)90032-3 , 1980.

Slinn, W. G. N.: Predictions for particle deposition to vegetative canopies, Atmospheric Environment (1967), 16, 1785-1794, https://doi.org/10.1016/0004-6981(82)90271-2 , 1982.

Smith, S. J., Andres, R., Conception, E., & Lurz, J.: Historical sulfur dioxide emissions 1850-2000: Methods and results, Pacific Northwest National Lab., Richland, WA (USA), https://doi.org/10.2172/15020102 , 2004.

Sorjamaa, R. and Laaksonen, A.: The effect of H_2O adsorption on cloud drop activation of insoluble particles: a theoretical framework, Atmospheric Chemistry and Physics, 7, 6175–6180, https://doi.org/10.5194/acp-7-6175-2007 , 2007.

Sposito, G.: The Chemistry of Soils, Oxford University Press, New York, ISBN 9780190630881, 1989.

Stokes, R. H., & Robinson, R. A.: Interactions in aqueous nonelectrolyte solutions. I. Solute-solvent equilibria. *The Journal of Physical Chemistry*, *70*(7), https://doi.org/10.1021/j100879a010 , 1966.

Suslick, K. S.: Encyclopedia of physical science and technology, Sonoluminescence and sonochemistry, 3rd edn. Elsevier Science Ltd, Massachusetts, 1-20, ISBN 9780122274107**,** 2001.

Tan, J., Fu, J. S., Carmichael, G. R., Itahashi, S., Tao, Z., Huang, K., Dong, X., Yamaji, K., Nagashima, T., Wang, X., Liu, Y., Lee, H.-J., Lin, C.-Y., Ge, B., Kajino, M., Zhu, J., Zhang, M., Liao, H., and Wang, Z.: Why do models perform differently on particulate matter over East Asia? A multi-model intercomparison study for MICS-Asia III, Atmospheric Chemistry and Physics, 20, 7393–7410, https://doi.org/10.5194/acp-20-7393-2020 , 2020.

Tang, Y. S., Flechard, C. R., Dammgen, U., Vidic, S., Djuricic, V. and co-authors: Pan-European rural monitoring network shows dominance of NH 3 gas and NH 4 NO 3 aerosol in inorganic atmospheric pollution load, Atmospheric Chemistry and Physics, 21(2), 875-914, https://doi.org/10.5194/acp-21-875-2021, 2021.

Tilgner, A., Schaefer, T., Alexander, B., Barth, M., Collett Jr., J. L., Fahey, K. M., Nenes, A., Pye, H. O. T., Herrmann, H., and McNeill, V. F.: Acidity and the multiphase chemistry of atmospheric aqueous particles and clouds, Atmos. Chem. Phys., 21, 13483–13536, https://doi.org/10.5194/acp-21-13483-2021 , 2021.

Trump, E. R., Fountoukis, C., Donahue, N. M., and Pandis, S. N.: Improvement of simulation of fine inorganic PM levels through better descriptions of coarse particle chemistry, Atmospheric Environment, 102, 274-281, https://doi.org/10.1016/j.atmosenv.2014.11.059 , 2015.

Tuccella, P., Curci, G., Visconti, G., Bessagnet, B., Menut, L., and Park, R. J.: Modeling of gas and aerosol with WRF/Chem over Europe: Evaluation and sensitivity study, Journal of Geophysical Research: Atmospheres, 117(D3), https://doi.org/10.1029/2011JD016302 , 2012.

Twomey, S.: The Influence of Pollution on the Shortwave Albedo of Clouds, Journal of Atmospheric Sciences, 34, 1149-1152, https://doi.org/10.1175/1520-0469(1977)034%3C1149:TIOPOT%3E2.0.CO;2 , 1977.

Urdiales-Flores, D., Zittis, G., Hadjinicolaou, P., Osipov, S., Klingmüller, K., Mihalopoulos, N., Kanakidou, M., Economou, T., and Lelieveld, J.: Drivers of accelerated warming in Mediterranean climate-type regions, npj Climate and Atmospheric Science, 6(1), 97, https://doi.org/10.1038/s41612-023-00423-1 , 2023.

van Vuuren, D. P., Edmonds, J., Kainuma, M., Riahi, K., Thomson, A., Hibbard, K., Hurtt, G. C., Kram, T., Krey, V., Lamarque, J.-F., Masui, T., Meinshausen, M., Nakicenovic, N., Smith, S. J., and Rose, S. K.: The representative concentration pathways: an overview, Climatic Change, 109, 5, https://doi.org/10.1007/s10584-011-0148-z , 2011.

Vehkamäki, H., Kulmala, M., Napari, I., Lehtinen, K. E., Timmreck, C., Noppel, M., & Laaksonen, A.: An improved parameterization for sulfuric acid–water nucleation rates for tropospheric and stratospheric conditions, Journal of Geophysical Research: Atmospheres, 107(D22), AAC-3, https://doi.org/10.1029/2002JD002184 , 2002.

Walker, J. M., Philip, S., Martin, R. V., and Seinfeld, J. H.: Simulation of nitrate, sulfate, and ammonium aerosols over the United States, Atmospheric Chemistry and Physics, 12, 11213–11227, https://doi.org/10.5194/acp-12-11213-2012 , 2012.

Wang, Y., Zhang, Q. Q., He, K., Zhang, Q., and Chai, L.: Sulfate-nitrate-ammonium aerosols over China: response to 2000–2015 emission changes of sulfur dioxide, nitrogen oxides, and ammonia, Atmospheric Chemistry and Physics, 13, 2635–2652, https://doi.org/10.5194/acp-13-2635-2013 , 2013.

Weagle, C. L., Snider, G., Li, C., Van Donkelaar, A., Philip, S., Bissonnette, P., Burke, J., Jackson, J., Latimer, R., and Stone, E.: Global sources of fine particulate matter: interpretation of Pm^2. 5 chemical composition observed by SPARTAN using a global chemical transport model, Environmental science & technology, 52(20), 11670-11681, https://doi.org/10.1021/acs.est.8b01658, 2018.

Wen, L., Xue, L., Wang, X., Xu, C., Chen, T., Yang, L., Wang, T., Zhang, Q., and Wang, W.: Summertime fine particulate nitrate pollution in the North China Plain: increasing trends, formation mechanisms and implications for control policy, Atmospheric Chemistry and Physics, 18, 11261–11275, https://doi.org/10.5194/acp-18-11261-2018 , 2018.

Wexler, A. S., & Seinfeld, J. H.: Second-generation inorganic aerosol model, Atmospheric Environment Part A. General Topics, 25(12), 2731-2748, https://doi.org/10.1016/0960-1686(91)90203-J, 1991.

Xu, L. and Penner, J. E.: Global simulations of nitrate and ammonium aerosols and their radiative effects, Atmospheric Chemistry and Physics, 12(20), https://doi.org/10.5194/acp-12-9479-2012 , 2012.

Xu, G., Zhang, Q., Yao, Y., and Zhang, X.: Changes in Pm^2. 5 sensitivity to NO x and NH_3 emissions due to a large decrease in SO_2 emissions from 2013 to 2018, Atmospheric and Oceanic Science Letters, 13(3), 210-215, https://doi.org/10.1080/16742834.2020.1738009, 2020.

Yang, Y., Lou, S., Wang, H., Wang, P., and Liao, H.: Trends and source apportionment of aerosols in Europe during 1980–2018, Atmospheric Chemistry and Physics, 20, 2579–2590, https://doi.org/10.5194/acp-20-2579-2020 , 2020.

Yu, S., Dennis, R., Roselle, S., Nenes, A., Walker, J., Eder, B., Schere, K., Swall, J., and Robarge, W.: An assessment of the ability of three-dimensional air quality models with current thermodynamic equilibrium models to predict aerosol NO3−, Journal of Geophysical Research: Atmospheres, 110(D7), https://doi.org/10.1029/2004JD004718 , 2005.

Zakoura, M. and Pandis, S. N.: Overprediction of aerosol nitrate by chemical transport models: The role of grid resolution, Atmospheric Environment, *187*, 390-400, https://doi.org/10.1016/j.atmosenv.2018.05.066, 2018.

Zakoura, M. and Pandis, S. N.: Improving fine aerosol nitrate predictions using a Plume-in-Grid modeling approach, Atmospheric Environment, 215, 116887, https://doi.org/10.1016/j.atmosenv.2019.116887 , 2019.

Zdanovskii, A. B.: New methods for calculating solubilities of electrolytes in multicomponent systems, Zhur. Fiz. Kim., 22, 1475-1485, 1948.

Zhang, L., Gong, S., Padro, J., and Barrie, L.: A size-segregated particle dry deposition scheme for an atmospheric aerosol module, Atmospheric Environment, 35(3), 549-560, https://doi.org/10.1016/S1352-2310(00)00326-5 , 2001.

Acknowledgements

Many people have shown their support towards me during my time in Forschungszentrum Jülich and without them this work would never have been possible. I would like to take the opportunity now and thank them.

First of all, I would like to thank Prof. Dr. Andreas Wahner who, along with our beloved Prof. Dr. Astrid Kiendler-Scharr, have allowed me to carry out my doctoral studies at the ICE-3 Institute of the Forschungszentrum.

I would like to express my gratitude towards Prof. Dr. Hendrik Fuchs who, after the tragic loss of Astrid 2 years ago, has stepped up to take the position of acting as my Doktorvater. He was always there whenever I needed to ask him any questions no matter if they were of organizational matter or related to the thesis content. He was instrumental in helping me appoint my Thesis Advisory Committee.

I am very grateful towards Prof. Dr. Dirk Witthaut for accepting the position of being the chairperson in the committee and Prof. Dr. Andrea Pozzer for accepting to be the second reviewer of my thesis.

A special thank you goes to Dr. Vlassis Karydis and Dr. Alexandra Tsimpidi. They were always available every time I felt the need to bother them with any question I could think of. Thank you for guiding me and being my mentors, thank you for making me aware of so many things regarding to the nature of this work, thank you for believing in me to complete a PhD in climate science modelling when I was barely even knowledgeable of a Linux environment in the beginning. But also thank you for not being afraid to act as friends in many moments too. It was truly a pleasure working in your team.

I want to say a warm thank you to the entire modelling group of ICE-3 for making me feel welcome as a part of them from the very beginning. A special thanks goes to Dr. Astrid Kerkweg who never once failed to ask my numerous questions about all the technical details of the EMAC model, always providing assistance in all matters regarding that.

I have to give special thanks to Apostolos Koumparos, Susanne Scholz, Xurong Wang, Jan Kraayvanger and Xiao Li for always providing a fun and friendly atmosphere to the office.

I am especially grateful to my family and friends for their unwavering support and understanding. To my wife Kira, who I am to this day convinced has no complete knowledge of the topic of my thesis, thank you for always being by my side and succeeding in picking me up during the most difficult days and for always being my anchor. To my Dad, Mum, Grandpa and Grandma I know it was never easy being away from you, and for that thank you so much for never failing to show me your love and always tell me how proud you are. To both my sisters, thank you for coming to visit any change you had and making me feel like home every time. Last but definitely not least, a special thank you to my Mother in Law and my late Father in Law for taking me with open arms into their family and for showing me so many great aspects of the life here in Germany.

A Appendix

A.1 Supplementary material to Chapter 1 – Parameterizations of aerosol deposition processes

Dry Deposition

The process of particle dry deposition is based on the big leaf model, where the air resistance is interpreted in the same way as a layout of linear resistances in an electrical circuit. Thus the total particle deposition velocity u_d is given as such :

$$u_d = \frac{1}{r_a + r_b + r_a r_b u_s} + u_s \qquad \text{(A1.1)}$$

Where r_a is the aerodynamic resistance, r_b is the quasi-laminar resistance (a metric of molecular diffusion) and u_s is the gravitational settling velocity of the particle, which is a metric of the sedimentation flux. The first two parameters are calculated according to the following equations :

$$r_a = \int_{z_0}^{z} \frac{\Phi(\zeta)}{\kappa u_* z} dz \qquad \text{(A1.2)}$$

Where z_0 is the roughness length, z is the reference height, κ is the dimensionless von Karman constant, u_* is the friction velocity and $\Phi(\zeta)$ is a dimensionless stability function that depends on the Monin-Obukhov length L and is equal to $\zeta = {}^{z}/_{L}$, as well as the profiles of the horizontal wind speed and temperature.

$$r_b = \frac{1}{3u_* \left[S_c^{-\gamma} + \left(\frac{S_t}{a+S_t}\right)^2 + \frac{1}{2}\left(\frac{Dp}{A}\right)^2 \right] R_1} \qquad \text{(A1.3)}$$

Where, D_p is the particle diameter, S_c is the Schmidt number (a metric of particle Brownian diffusion), S_t is the Stokes number and along with the parameter $R_1 = \exp\left(-S_t^{1/2}\right)$, they represent the fraction of particles that directly stick to a given surface on first contact. Finally, A corresponds to the characteristic radius of collectors and along with the parameters γ and α, they depend on different land-use specifications. The equations (A1.1) to (A1.3) can be found in Seinfeld and Pandis (2016), the equation for the calculation of R_1 is based on Slinn (1982), while typical values for A, α and γ are adopted from Zhang et al. (2001).

Gravitational Sedimentation

As stated the gravitational sedimentation flux for aerosol particles is given by the settling velocity according to Pruppacher and Klett (1979) as :

$$u_s = u_{Stokes} * f_{Slinn} * f_{Csf} \tag{A1.4}$$

Where, the Stokes velocity represents the sedimentation velocity of spheres and is given as :

$$u_{Stokes} = \frac{2}{9}\left(\rho_p(i) - \rho_{air}\right)\frac{g}{\eta_d} r_p(i)^2 \tag{A1.5}$$

With i referring to the respective aerosol size mode, $\rho_p(i)$ is the aerosol density, ρ_{air} is the density of air, $r_p(i)$ is the particle radius, g denotes the gravitational acceleration and η_d the dynamic viscosity of the air. The parameter f_{Slinn} is a correction factor that is applied to an aerosol population that follows the lognormal size distribution. It is a necessary correction to account for the fact that in a specific size mode, the sedimentation velocity of all particles is larger than the one of a particle having the mean mode radius, and is given according to Slinn and Slinn (1980) as :

$$f_{Slinn} = \sigma_p(i)^{2 \ln \sigma_p(i)} \tag{A1.6}$$

With $\sigma_p(i)$ being the standard deviation of the aerosol radius in the size mode i. Finally, the parameter f_{Csf} is a correction factor to account for aerodynamical differences between ideal spheres and real non-spherical particles. It is called the Cunningham-slip-flow factor (Cunningham, 1910) and is calculated as :

$$f_{Csf} = 1 + 1.257\frac{\lambda_{air}}{r_p(i)} + 0.4\frac{\lambda_{air}}{r_p(i)}\exp\left(\frac{-1.1 r_p(i)}{\lambda_{air}}\right) \tag{A1.7}$$

Where λ_{air} is the mean free path of air molecules.

Wet Deposition – In Cloud Scavenging

To account for the change in number concentration n, of aerosols after in-cloud scavenging by cloud droplets has taken place, the following equation is most commonly used (Pruppacher and Klett, 1979; Seinfeld and Pandis, 2016) :

$$n\left(D_p, t\right) = n\left(D_p, t_0\right)\exp\left(-\Lambda_{ic}\left(D_p\right) * t\right) \tag{A1.8}$$

Where D_p is the particle diameter and $\Lambda_{ic}(D_p)$ is the in-cloud scavenging coefficient which is given as :

$$\Lambda_{ic}(D_p) = N_d K(D_p, x) \quad \text{(A1.9)}$$

Here N_d is the number concentration of cloud droplets and $K(D_p, x)$ is the collection coefficient between a particle with diameter D_p and a rain droplet with diameter x, and is estimated according to the coagulation theory of Fuks and Davies (1964) as :

$$K_{D_p,x} = \frac{2kT}{3\mu}\frac{x}{D_p} \quad \text{(A1.10)}$$

Where k is the Boltzmann constant, T is the temperature and μ is the viscosity of air.

Wet Deposition – Below Cloud Scavenging

Similarly, the change in aerosol number concentration n, of aerosols after below-cloud scavenging by cloud droplets is given as (Pruppacher and Klett, 1979; Seinfeld and Pandis, 2016):

$$\frac{dn(D_p)}{dt} = -\Lambda_{bc}(D_p)n(D_p) \quad \text{(A1.11)}$$

Here, $\Lambda_{bc}(D_p)$ is the below-cloud scavenging coefficient which is calculated by :

$$\Lambda_{bc}(D_p) = \int_0^\infty \frac{\pi}{4} * D_d^2 * u_t(D_d) * E(D_d, D_p) * N(D_d) dD_d \quad \text{(A1.12)}$$

Where D_d is the cloud droplet radius, $u_t(D_d)$ is the cloud droplet falling velocity, $N(D_d)$ is the cloud droplet size distribution and $E(D_d, D_p)$ is the particle-droplet collision efficiency parameter which denotes the ratio of total number of particle-droplet collisions occurring in an area that is equal to the effective cross-section of the cloud droplet. It is estimated according to Slinn (1974):

$$E(D_d, D_p) = \frac{4}{R_e S_c}\left[1 + 0.4R_e^{1/2}S_c^{1/3} + 0.16R_e^{1/2}S_c^{1/2}\right] + 4\varphi\left[\omega^{-1} + \left(1 + 2R_e^{1/2}\right)\varphi\right] + \left(\frac{S_t - S^*}{S_t - S^* + \frac{2}{3}}\right)^{3/2} \quad \text{(A1.13)}$$

Where, R_e is the Reynolds number, $\varphi = \frac{D_p}{D_d}$ is the ratio of particle-to-droplet diameters, $\omega = \frac{\mu_w}{\mu_a}$ is the ratio of water-to-air viscosity and S^* is a parameter that is dependent on R_e and is calculated as :

$$S^* = \frac{1.2+\frac{1}{12}\ln(1+R_e)}{1+\ln(1+R_e)} \qquad \text{(A1.14)}$$

The first term of equation (A1.14) refers to the contribution of from Brownian diffusion, the second term to the contribution of interception and the third term to the contribution of impaction.

A.2 Supplementary material to Chapter 2

Supplement of Geosci. Model Dev., 17, 1111–1131, 2024
https://doi.org/10.5194/gmd-17-1111-2024-supplement

Geoscientific Model Development
Open Access
EGU

Supplement of

Implementation of the ISORROPIA-lite aerosol thermodynamics model into the EMAC chemistry climate model (based on MESSy v2.55): implications for aerosol composition and acidity

Alexandros Milousis et al.

Correspondence to: Vlassis A. Karydis (v.karydis@fz-juelich.de)

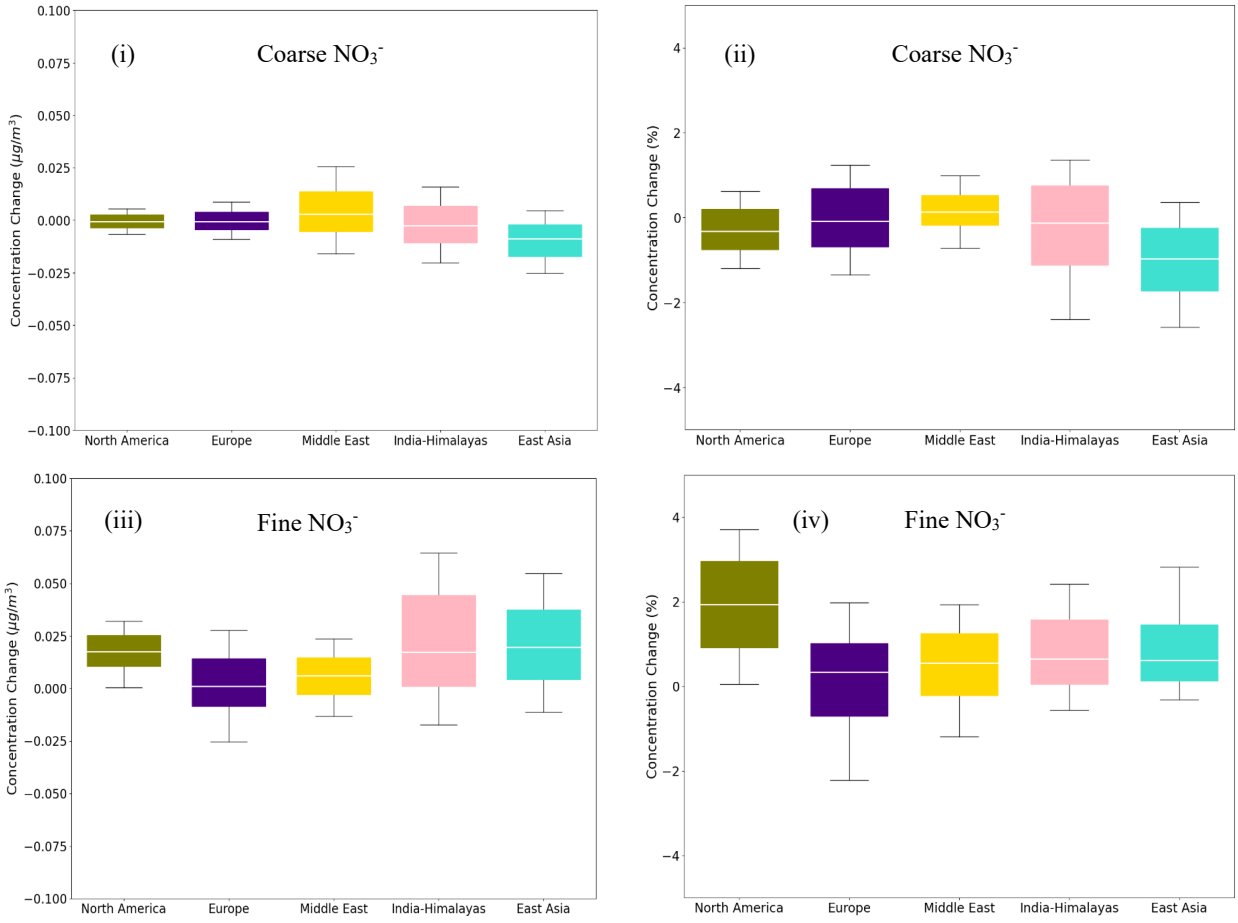

Figure S1: Bar chart plots depicting the 25th, 50th and 75th percentiles (box) of the difference in the global daily mean surface concentrations of i) coarse and ii) fine aerosol NO_3^- for the regions of North America, Europe, Middle East, India-Himalayas and East Asia, as predicted by EMAC using ISORROPIA II v1 and ISORROPIA II v2.3. The fractional differences in global daily mean surface concentrations of iii) coarse and iv) fine aerosol NO_3^- for the same regions are also shown. Both models assume that the aerosol is at its stable state at low RH and a positive change corresponds to higher concentrations by ISORROPIA II v1.

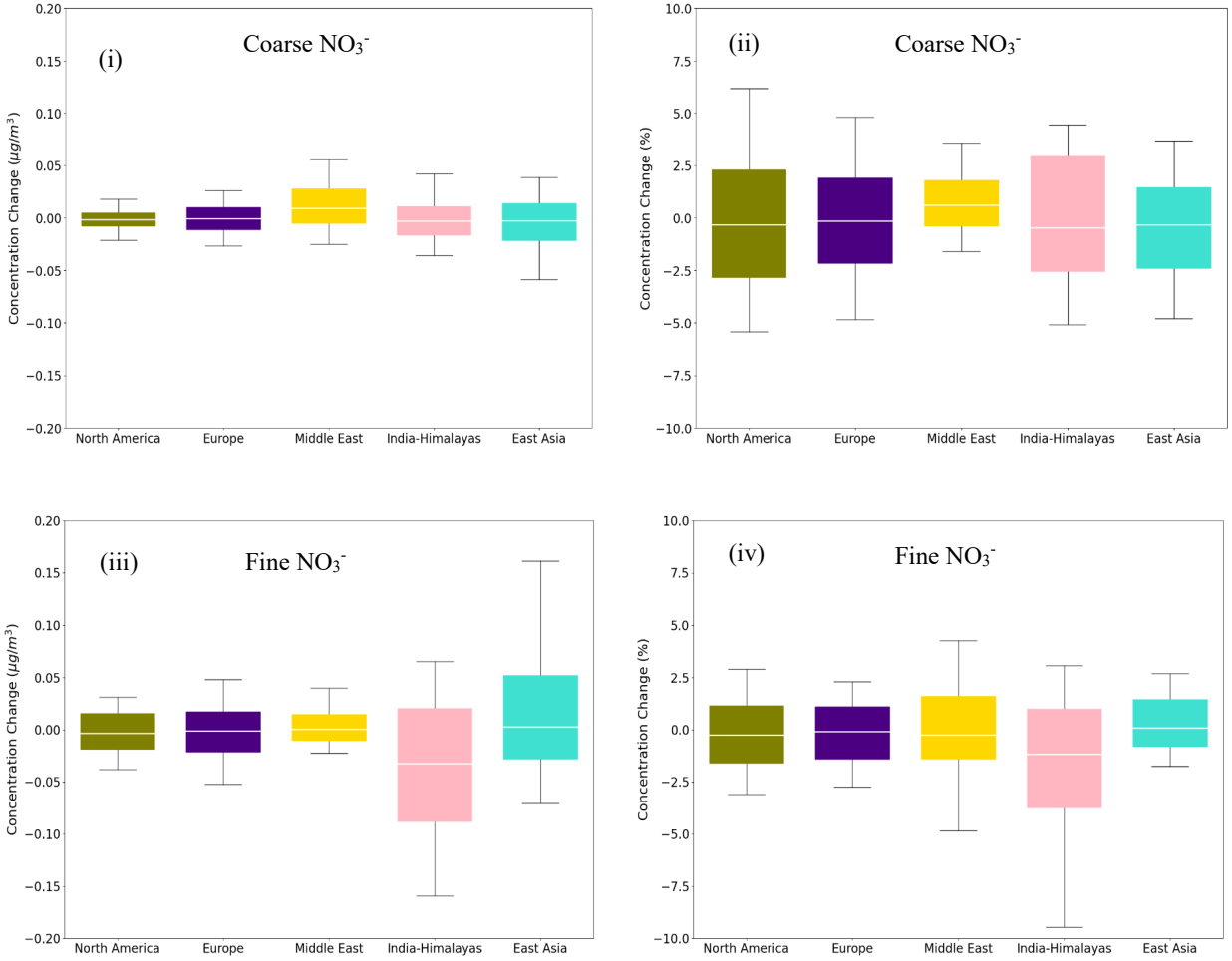

Figure S2: Bar chart plots depicting the 25th, 50th and 75th percentiles (box) of the difference in the global daily mean surface concentrations of i) coarse and ii) fine aerosol NO_3^- for the regions of North America, Europe, Middle East, India-Himalayas and East Asia, as predicted by EMAC using ISORROPIA-lite and ISORROPIA II. The fractional differences in global daily mean surface concentrations of iii) coarse and iv) fine aerosol NO_3^- for the same regions are also shown. Both models assume that the aerosol is at its metastable state at low RH and a positive change corresponds to higher concentrations by ISORROPIA-lite.

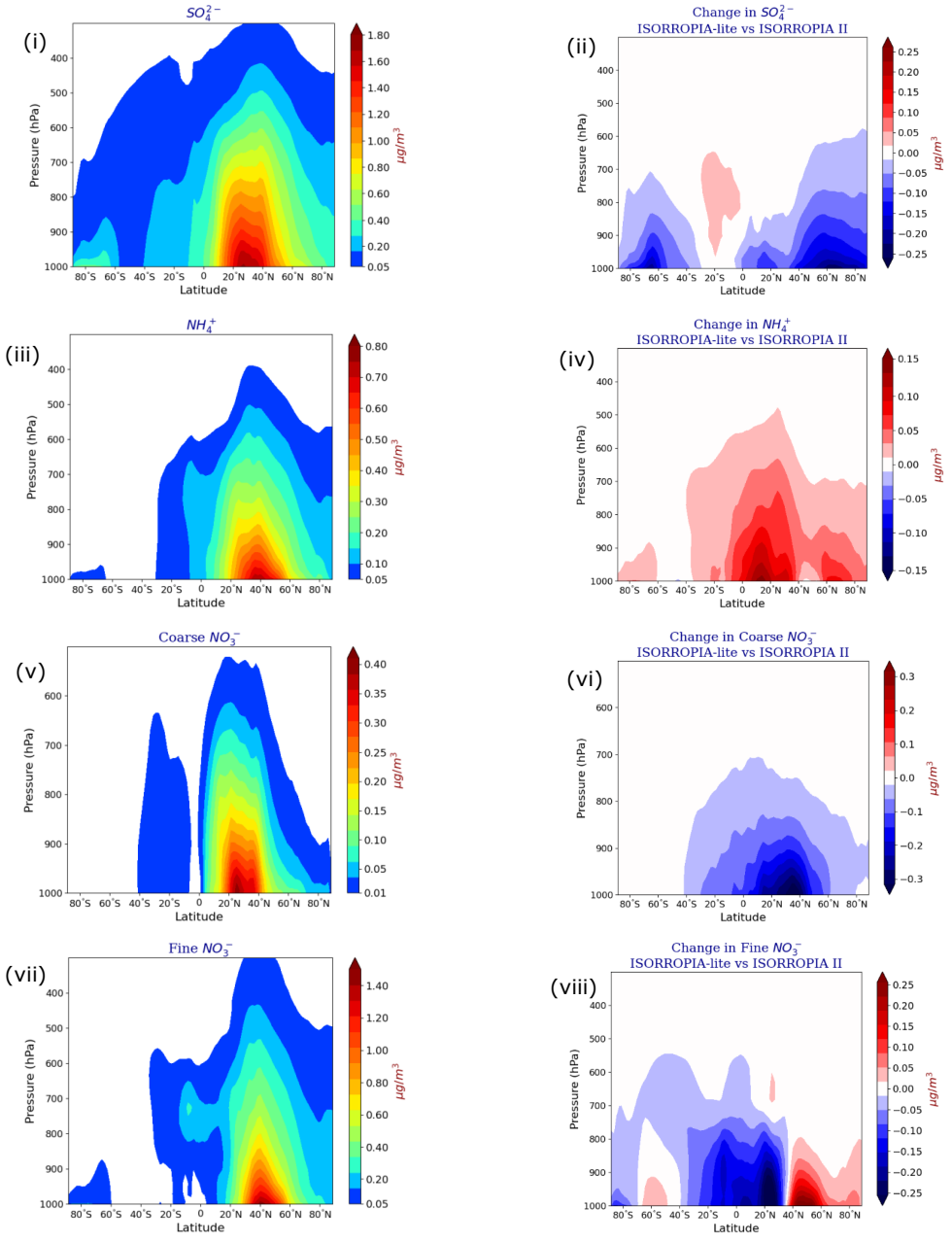

Figure S3 : Annually averaged zonal concentrations of i) SO_4^{2-} and ii) NH_4^+ in TSP, iii) coarse and iv) fine aerosol NO_3^- as predicted by EMAC using ISORROPIA-lite. Change of the annually averaged EMAC-simulated zonal concentration of v) NH_4^+ and vi) SO_4^{2-} in TSP, vii) coarse and viii) fine aerosol NO_3^- after employing ISORROPIA II. Positive values in red indicate higher concentrations by ISORROPIA-lite. The models assume different aerosol states.

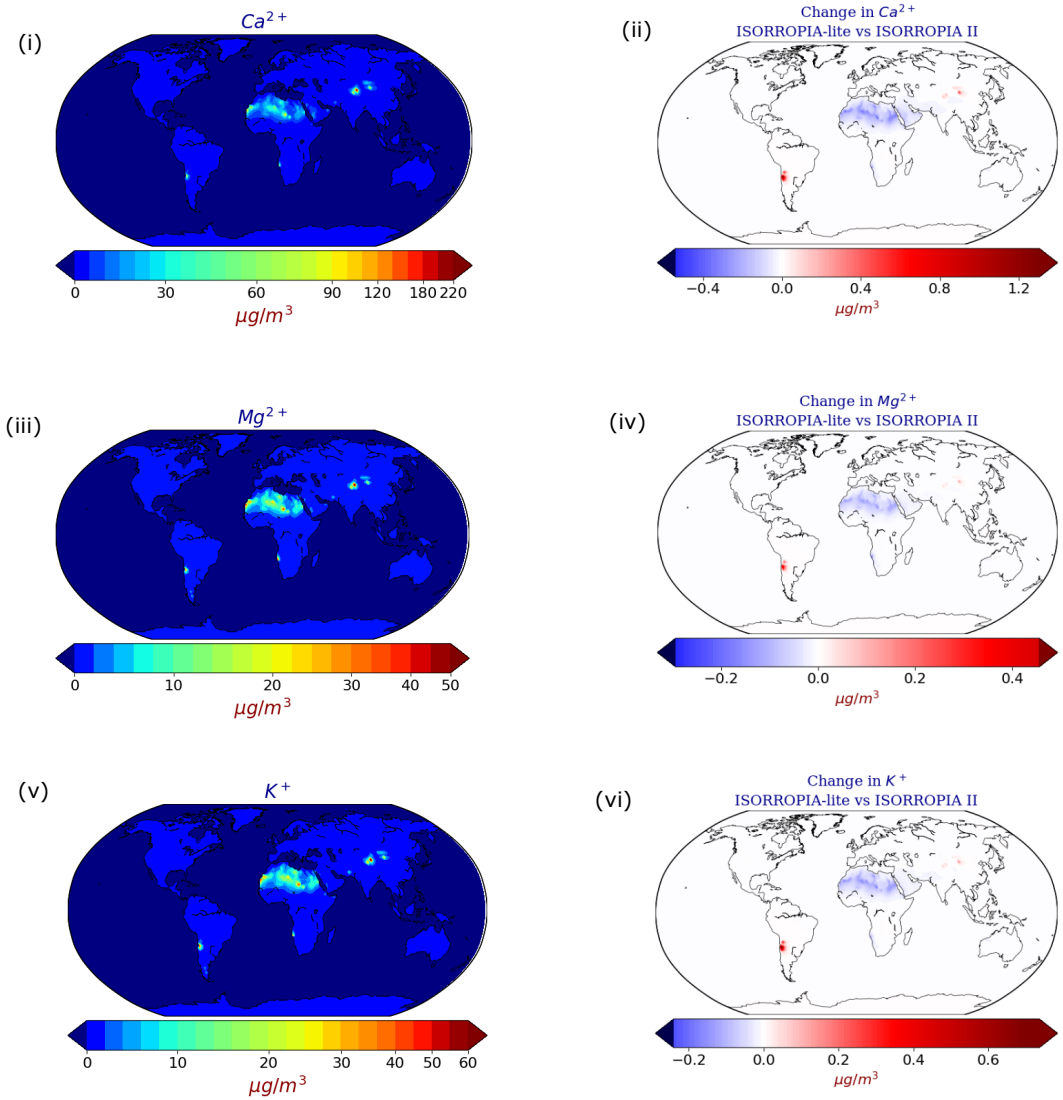

Figure S4: Annual mean surface concentrations of i) Ca^{2+}, ii) Mg^{2+} and iii) K^+ in TSP as predicted by EMAC using ISORROPIA-lite. Change of the annual mean EMAC-simulated surface concentration of iv) Ca^{2+}, v) Mg^{2+} and vi) K^+ in TSP after employing ISORROPIA II. Positive values in red indicate higher concentrations by ISORROPIA-lite. The models assume different aerosol states.

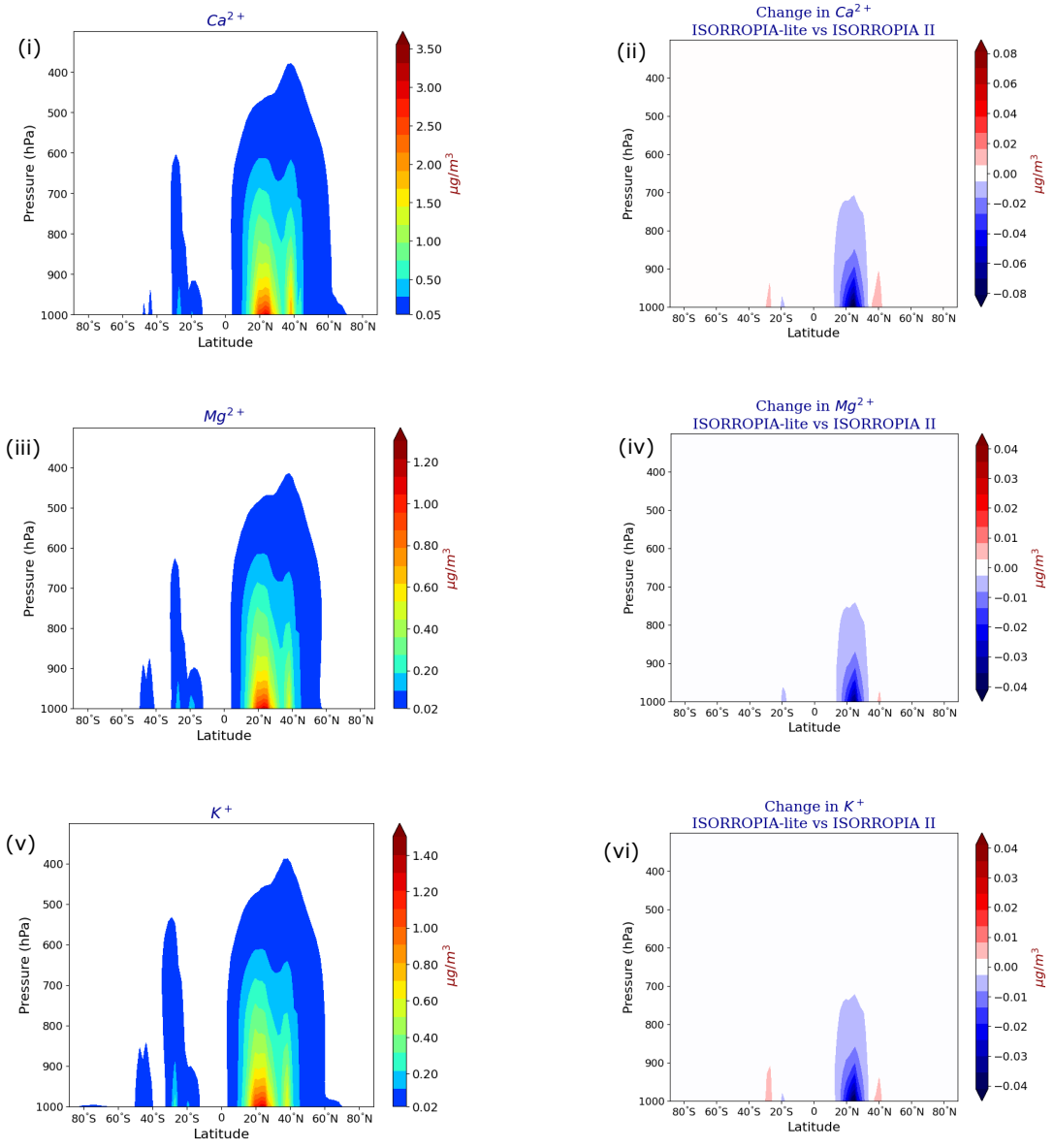

Figure S5: Annually averaged zonal concentrations of i) Ca^{2+}, ii) Mg^{2+} and iii) K^+ in TSP as predicted by EMAC using ISORROPIA-lite. Change of the annually averaged EMAC-simulated zonal concentration of iv) Ca^{2+}, v) Mg^{2+} and vi) K^+ in TSP after employing ISORROPIA II. Positive values in red indicate higher concentrations by ISORROPIA-lite. The models assume different aerosol states.

Table S1: Seasonal statistical evaluation of EMAC predicted surface concentrations of $PM_{2.5}$ SO_4^{2-} using ISORROPIA II in stable mode against observations during 2010.

Network	Season	Number of datasets	Mean Observed ($\mu g\ m^{-3}$)	Mean Predicted ($\mu g\ m^{-3}$)	MAGE ($\mu g\ m^{-3}$)	MB ($\mu g\ m^{-3}$)	NME (%)	NMB (%)	RMSE ($\mu g\ m^{-3}$)
EPA	Winter	148	2.15	1.08	1.11	-1.06	51.73	-49.52	1.57
	Spring	290	1.99	1.68	0.57	-0.31	28.52	-15.44	0.73
	Summer	287	2.64	1.18	1.48	-1.46	55.88	-55.33	1.76
	Autumn	294	1.87	1.49	0.49	-0.37	26.33	-19.9	0.63
IMPROVE	Winter	116	0.92	0.72	0.57	-0.2	61.48	-21.67	1.26
	Spring	233	0.99	1.09	0.38	0.1	38.11	10.16	0.5
	Summer	193	1.35	0.79	0.68	-0.56	50.41	-41.55	1.05
	Autumn	214	0.94	0.99	0.31	0.04	33.1	4.61	0.42
EMEP	Winter	7	2.82	1.74	1.08	-1.08	38.28	-38.28	1.42
	Spring	18	1.62	1.2	0.75	-0.42	46.52	-25.74	0.88
	Summer	18	2.24	1.15	1.09	-1.09	48.62	-48.44	1.28
	Autumn	17	1.73	1.21	0.76	-0.53	43.91	-30.4	0.89
EANET	Winter	30	3.72	1.27	2.68	-2.45	72.04	-65.83	4.0
	Spring	60	3.79	1.77	2.3	-2.02	60.73	-53.34	3.42
	Summer	61	2.66	1.38	1.56	-1.28	58.7	-48.17	2.15
	Autumn	61	2.28	1.27	1.31	-1.01	57.49	-44.16	1.92

Table S2: Seasonal statistical evaluation of EMAC predicted surface concentrations of $PM_{2.5}$ NH_4^+ using ISORROPIA II in stable mode against observations during 2010.

Network	Season	Number of datasets	Mean Observed (μg m^{-3})	Mean Predicted (μg m^{-3})	MAGE (μg m^{-3})	MB (μg m^{-3})	NME (%)	NMB (%)	RMSE (μg m^{-3})
EPA	Winter	137	1.52	1.56	0.57	0.04	37.73	2.66	0.94
	Spring	269	0.98	1.69	0.79	0.71	80.17	72.58	0.97
	Summer	265	0.82	0.41	0.43	-0.41	51.71	-49.8	0.56
	Autumn	273	0.65	0.55	0.19	-0.11	29.33	-16.39	0.29
EMEP	Winter	6	2.07	2.8	0.84	0.74	40.56	35.63	1.27
	Spring	14	1.24	2.17	0.99	0.93	79.77	74.9	1.19
	Summer	14	0.84	0.43	0.41	-0.41	48.61	-48.61	0.45
	Autumn	13	0.83	1.16	0.41	0.34	49.7	40.67	0.53
EANET	Winter	27	1.39	1.38	0.94	-0.02	67.29	-1.12	1.81
	Spring	59	1.07	1.7	1.22	0.63	114.5	58.75	1.78
	Summer	58	0.69	0.56	0.33	-0.14	47.43	-19.85	0.47
	Autumn	58	0.54	0.48	0.38	-0.06	69.24	-11.74	0.58

Table S3: Seasonal statistical evaluation of EMAC predicted surface concentrations of $PM_{2.5}$ NO_3^- using ISORROPIA II in stable mode against observations during 2010.

Network	Season	Number of datasets	Mean Observed (μg m^{-3})	Mean Predicted (μg m^{-3})	MAGE (μg m^{-3})	MB (μg m^{-3})	NME (%)	NMB (%)	RMSE (μg m^{-3})
EPA	Winter	144	2.82	3.83	1.97	1.01	70.0	35.87	2.61
	Spring	291	1.41	3.2	1.9	1.79	135.16	127.11	2.35
	Summer	280	0.5	0.28	0.28	-0.22	55.11	-44.42	0.69
	Autumn	290	0.66	0.54	0.36	-0.12	54.07	-18.01	0.58
IMPROVE	Winter	116	0.81	2.16	1.41	1.34	173.76	164.76	1.77
	Spring	233	0.5	1.81	1.35	1.32	272.05	266.11	1.78
	Summer	193	0.2	0.29	0.18	0.09	89.7	48.07	0.25
	Autumn	214	0.21	0.37	0.25	0.16	119.85	77.91	0.35
EMEP	Winter	7	3.35	5.27	2.81	1.92	83.9	57.38	4.13
	Spring	18	1.63	2.47	1.56	0.83	95.71	50.94	2.14
	Summer	18	0.27	0.58	0.43	0.31	158.9	114.1	0.63
	Autumn	17	0.8	1.5	0.85	0.7	106.94	87.44	1.35
EANET	Winter	30	2.03	2.88	2.01	0.85	99.01	41.67	3.03
	Spring	59	1.85	2.43	1.97	0.58	106.59	31.6	3.05
	Summer	59	0.63	0.64	0.61	0.01	96.31	1.3	0.91
	Autumn	59	0.77	0.83	0.69	0.06	89.49	7.92	1.08

Table S4: Seasonal statistical evaluation of EMAC predicted surface concentrations of $PM_{2.5}$ SO_4^{2-} using ISORROPIA-lite against observations during 2010.

Network	Season	Number of datasets	Mean Observed ($\mu g\ m^{-3}$)	Mean Predicted ($\mu g\ m^{-3}$)	MAGE ($\mu g\ m^{-3}$)	MB ($\mu g\ m^{-3}$)	NME (%)	NMB (%)	RMSE ($\mu g\ m^{-3}$)
EPA	Winter	148	2.15	1.05	1.14	-1.09	52.91	-50.9	1.59
	Spring	290	1.99	1.68	0.57	-0.31	28.53	-15.67	0.73
	Summer	287	2.64	1.19	1.47	-1.46	55.7	-55.16	1.75
	Autumn	294	1.87	1.48	0.49	-0.38	26.53	-20.53	0.64
IMPROVE	Winter	116	0.92	0.7	0.57	-0.22	61.55	-24.25	1.26
	Spring	233	0.99	1.09	0.38	0.1	38.04	9.99	0.49
	Summer	193	1.35	0.79	0.68	-0.56	50.32	-41.67	1.04
	Autumn	214	0.94	0.99	0.31	0.04	33.1	4.61	0.42
EMEP	Winter	7	2.82	1.72	1.1	-1.1	39.06	-39.06	1.44
	Spring	18	1.62	1.2	0.74	-0.42	45.99	-25.96	0.87
	Summer	18	2.24	1.15	1.1	-1.09	48.93	-48.83	1.29
	Autumn	17	1.73	1.2	0.77	-0.54	44.58	-30.91	0.91
EANET	Winter	30	3.72	1.24	2.7	-2.48	72.49	-66.6	4.03
	Spring	60	3.79	1.79	2.28	-1.99	60.18	-52.68	3.4
	Summer	61	2.66	1.38	1.56	-1.28	58.74	-48.13	2.15
	Autumn	61	2.28	1.28	1.3	-1.0	57.08	-43.97	1.91

Table S5: Seasonal Statistical evaluation of EMAC predicted surface concentrations of $PM_{2.5}$ NH_4^+ using ISORROPIA-lite against observations during 2010.

Network	Season	Number of datasets	Mean Observed (μg m^{-3})	Mean Predicted (μg m^{-3})	MAGE (μg m^{-3})	MB (μg m^{-3})	NME (%)	NMB (%)	RMSE (μg m^{-3})
EPA	Winter	137	1.52	1.54	0.56	0.02	37.09	1.47	0.93
	Spring	269	0.98	1.72	0.8	0.74	81.38	74.93	0.98
	Summer	265	0.82	0.42	0.42	-0.4	50.71	-48.66	0.56
	Autumn	273	0.65	0.58	0.19	-0.07	29.08	-10.72	0.28
EMEP	Winter	6	2.07	2.77	0.82	0.71	39.47	34.09	1.25
	Spring	14	1.24	1.97	0.84	0.73	67.16	58.72	1.02
	Summer	14	0.84	0.46	0.38	-0.38	44.76	-44.76	0.42
	Autumn	13	0.83	1.18	0.43	0.35	51.57	42.76	0.54
EANET	Winter	27	1.39	1.35	0.93	-0.05	66.56	-3.36	1.81
	Spring	59	1.07	1.56	1.07	0.49	100.22	45.52	1.63
	Summer	58	0.69	0.59	0.32	-0.1	45.81	-14.62	0.46
	Autumn	58	0.54	0.52	0.37	-0.02	67.43	-4.4	0.56

Table S6: Seasonal statistical evaluation of EMAC predicted surface concentrations of $PM_{2.5}$ NO_3^- using ISORROPIA-lite against observations during 2010.

Network	Season	Number of datasets	Mean Observed (μg m^{-3})	Mean Predicted (μg m^{-3})	MAGE (μg m^{-3})	MB (μg m^{-3})	NME (%)	NMB (%)	RMSE (μg m^{-3})
EPA	Winter	144	2.82	3.76	1.91	0.94	67.68	33.49	2.54
	Spring	291	1.41	3.26	1.96	1.85	139.4	131.61	2.36
	Summer	280	0.5	0.29	0.27	-0.21	54.12	-41.95	0.69
	Autumn	290	0.66	0.63	0.38	-0.03	56.94	-4.81	0.6
IMPROVE	Winter	116	0.81	2.15	1.41	1.34	172.65	164.36	1.74
	Spring	233	0.5	1.86	1.39	1.36	279.62	275.01	1.79
	Summer	193	0.2	0.3	0.18	0.1	92.3	53.19	0.26
	Autumn	214	0.21	0.42	0.28	0.21	137.09	102.38	0.39
EMEP	Winter	7	3.35	5.22	2.79	1.87	83.37	55.94	4.09
	Spring	18	1.63	2.55	1.58	0.92	96.88	56.11	2.1
	Summer	18	0.27	0.64	0.48	0.37	174.65	134.53	0.69
	Autumn	17	0.8	1.6	0.92	0.8	115.23	100.3	1.42
EANET	Winter	30	2.03	2.88	2.01	0.85	98.65	41.9	3.03
	Spring	59	1.85	2.38	1.9	0.53	103.14	28.86	2.98
	Summer	59	0.63	0.69	0.64	0.06	100.43	8.81	0.95
	Autumn	59	0.77	0.87	0.69	0.1	89.82	13.14	1.08

A.3 Supplementary material to Chapter 3

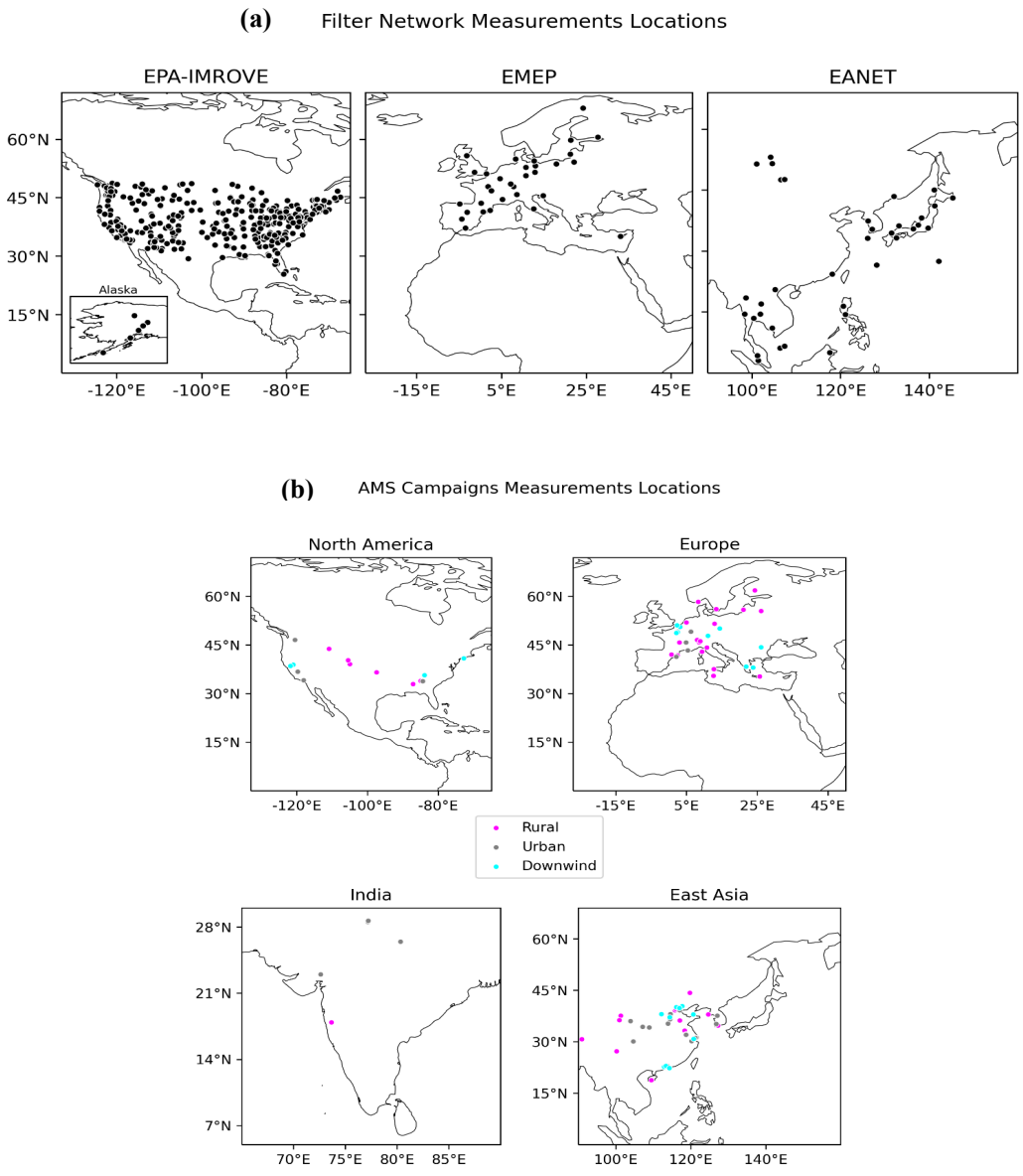

Figure S1: Locations of (a) $PM_{2.5}$ NO_3^- filter measurements from observation networks and (b) PM_1 NO_3^- AMS measurements from observation campaigns in (magenta) rural, (grey) urban and (cyan) downwind locations.

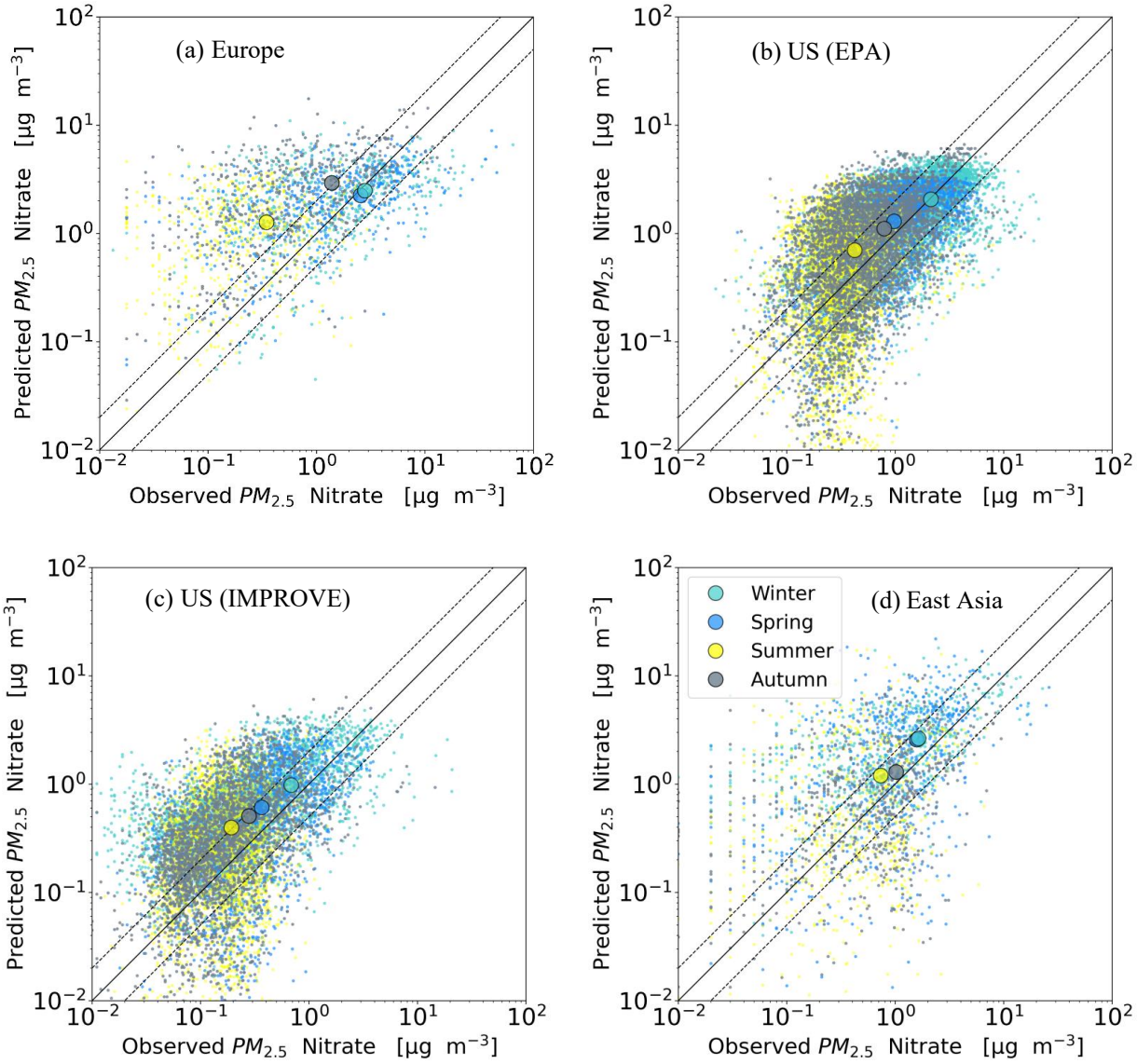

Figure S2: Scatterplots comparing the seasonal mean surface concentrations of $PM_{2.5}$ NO_3^- as simulated by EMAC from the Base Case with observations from the networks of (i) EMEP, (ii) EPA, (iii) IMPROVE and (iv) EANET. The enlarged dots indicate the mean seasonal values. Also shown are the 1:1 lines (solid) as well as the 2:1 and 1:2 lines (dashed).

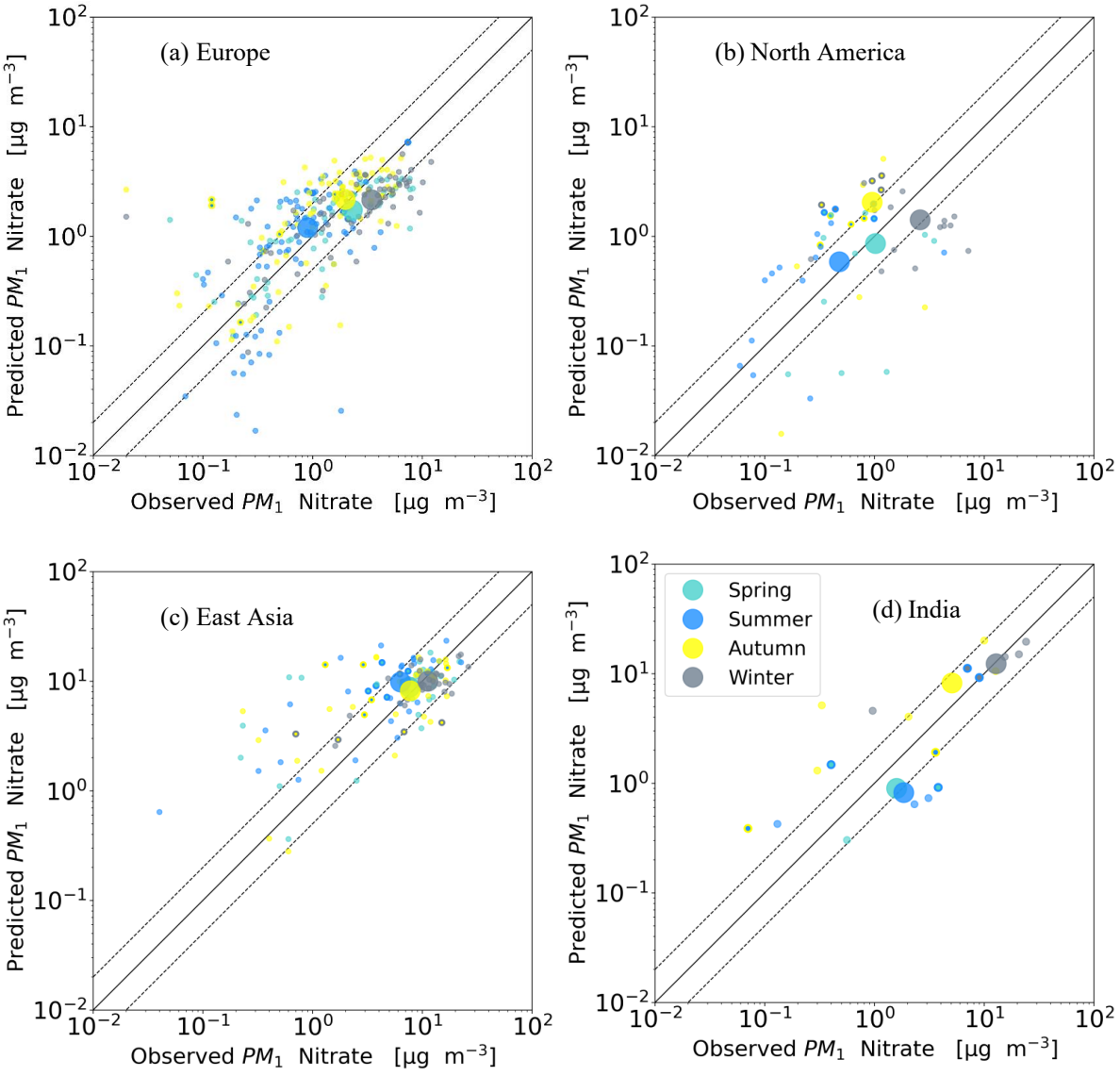

Figure S3: Scatterplots comparing the seasonal mean surface concentrations of PM_1 NO_3^- as simulated by EMAC from the Base Case with observations from campaigns in (i) Europe, (ii) North America, (iii) East Asia and (iv) India in all locations types (urban, rural and downwind). The enlarged dots indicate the mean seasonal values. Also shown are the 1:1 lines (solid) as well as the 2:1 and 1:2 lines (dashed).

Table S1: Seasonal statistical evaluation of EMAC predicted surface concentrations of $PM_{2.5}$ NO_3^- from the RES_low sensitivity against observations during 2010-2018. The used metrics include the Mean Absolute Gross Error (MAGE), Mean Bias (MB), Normalized Mean Error (NME), Normalized Mean Bias (NMB) and Root Mean Square Error (RMSE).

Network	**Season**	**Number of datasets**	**Mean Observed** (μg m^{-3})	**Mean Predicted** (μg m^{-3})	**MAGE** (μg m^{-3})	**MB** (μg m^{-3})	**NME** (%)	**NMB** (%)	**RMSE** (μg m^{-3})
EPA	Winter	144	2.8	2.6	1.4	-0.3	49	-9	2.2
	Spring	291	1.4	2.3	1.3	0.9	95	66	1.6
	Summer	280	0.5	1.1	0.8	0.6	160	121	1.2
	Autumn	290	0.7	1.2	0.7	0.5	112	74	1.0
IMPROVE	Winter	116	0.8	1.4	0.8	0.6	94	75	1.0
	Spring	233	0.5	1.2	0.8	0.7	154	141	1.1
	Summer	193	0.2	0.6	0.4	0.4	222	194	0.7
	Autumn	214	0.2	0.6	0.4	0.4	208	173	0.7
EMEP	Winter	7	3.4	4.2	2.4	0.9	71	26	3.3
	Spring	18	1.6	3.4	2.0	1.8	122	111	2.8
	Summer	18	0.3	1.9	1.6	1.6	591	591	2.0
	Autumn	17	0.8	3.1	2.3	2.3	281	281	3.0
EANET	Winter	30	2.0	2.3	1.7	0.8	81	14	2.9
	Spring	59	1.9	2.2	1.9	0.4	100	19	3.2
	Summer	59	0.6	2.0	2.0	1.4	308	217	3.7
	Autumn	59	0.8	0.6	0.7	-0.2	90	-23	1.2

Table S2: Statistical evaluation of EMAC predicted surface concentrations of PM_1 NO_3^- from the RES_low sensitivity against observations during 2010-2018. The used metrics include the Mean Absolute Gross Error (MAGE), Mean Bias (MB), Normalized Mean Error (NME), Normalized Mean Bias (NMB) and Root Mean Square Error (RMSE).

Network	**Season**	**Number of datasets**	**Mean Observed** (μg m^{-3})	**Mean Predicted** (μg m^{-3})	**MAGE** (μg m^{-3})	**MB** (μg m^{-3})	**NME** (%)	**NMB** (%)	**RMSE** (μg m^{-3})
USA	Rural	31	1.1	0.8	1.0	-0.3	81	-29	1.3
	Urban	22	1.5	1.8	1.6	0.3	108	21	2.1
	Downwind	5	1.2	1.2	1.4	-0.1	117	-6	2.0
East Asia	Rural	40	6.8	7.6	3.8	0.9	55	13	4.9
	Urban	78	9.7	8.7	4.0	-1.0	41	-10	5.3
	Downwind	15	4.9	8.6	4.1	3.8	85	77	5.0
Europe	Rural	163	1.4	1.6	1.0	0.2	67	11	1.5
	Urban	28	1.8	1.6	1.1	-0.2	61	-8	1.6
	Downwind	99	3.2	2.6	1.8	-0.6	57	-20	2.6
India	Rural	5	0.4	2.0	1.7	1.6	408	380	2.2
	Urban	14	8.2	3.3	5.2	-4.8	63	-59	7.9

Table S3: Seasonal statistical evaluation of EMAC predicted surface concentrations of $PM_{2.5}$ NO_3^- from the RES_high sensitivity against observations during 2010-2018. The used metrics include the Mean Absolute Gross Error (MAGE), Mean Bias (MB), Normalized Mean Error (NME), Normalized Mean Bias (NMB) and Root Mean Square Error (RMSE).

Network	Season	Number of datasets	Mean Observed (μg m^{-3})	Mean Predicted (μg m^{-3})	MAGE (μg m^{-3})	MB (μg m^{-3})	NME (%)	NMB (%)	RMSE (μg m^{-3})
EPA	Winter	144	2.8	2.3	1.4	-0.5	50	-18	2.3
	Spring	291	1.4	1.9	1.1	0.5	75	36	1.3
	Summer	280	0.5	0.6	0.4	0.1	86	26	0.8
	Autumn	290	0.7	0.7	0.5	0.0	76	3	0.8
IMPROVE	Winter	116	0.8	1.1	0.6	0.3	68	33	0.8
	Spring	233	0.5	0.9	0.5	0.4	105	72	0.8
	Summer	193	0.2	0.3	0.2	0.1	97	7	0.3
	Autumn	214	0.2	0.3	0.2	0.1	96	9	0.4
EMEP	Winter	7	3.4	3.7	2.3	0.4	68	11	3.1
	Spring	18	1.6	2.7	1.5	1.0	90	63	1.9
	Summer	18	0.3	1.5	1.2	1.2	445	444	1.6
	Autumn	17	0.8	2.3	1.6	1.5	193	193	2.2
EANET	Winter	30	2.0	2.5	1.8	0.4	88	21	3.2
	Spring	59	1.9	2.1	1.72	0.2	93	13	3.0
	Summer	59	0.6	1.5	1.4	0.9	217	141	3.1
	Autumn	59	0.8	1.0	0.9	0.7	122	33	1.5

Table S4: Statistical evaluation of EMAC predicted surface concentrations of PM_1 NO_3^- from the RES_high sensitivity against observations during 2010-2018. The used metrics include the Mean Absolute Gross Error (MAGE), Mean Bias (MB), Normalized Mean Error (NME), Normalized Mean Bias (NMB) and Root Mean Square Error (RMSE).

Network	**Season**	**Number of datasets**	**Mean Observed** (μg m^{-3})	**Mean Predicted** (μg m^{-3})	**MAGE** (μg m^{-3})	**MB** (μg m^{-3})	**NME** (%)	**NMB** (%)	**RMSE** (μg m^{-3})
USA	Rural	31	1.1	0.5	1.0	-0.6	86	-54	1.5
	Urban	22	1.5	1.7	1.5	0.2	102	14	2.0
	Downwind	5	1.2	0.7	1.2	-0.6	96	-46	2.0
East Asia	Rural	40	6.8	7.8	4.3	1.0	64	15	5.5
	Urban	78	9.7	11.3	4.1	1.6	42	17	5.5
	Downwind	15	4.9	8.6	4.4	3.8	90	77	6.5
Europe	Rural	163	1.4	1.2	0.8	-0.3	57	-18	1.4
	Urban	28	1.8	1.5	1.2	-0.3	66	-17	1.7
	Downwind	99	3.2	2.2	1.4	-0.9	43	-30	2.1
India	Rural	5	0.4	2.5	2.1	2.1	505	500	3.1
	Urban	14	8.2	8.5	2.9	0.4	36	4	3.7

Table S5: Seasonal statistical evaluation of EMAC predicted surface concentrations of $PM_{2.5}$ NO_3^- from the CMIP6 sensitivity against observations during 2010-2018. The used metrics include the Mean Absolute Gross Error (MAGE), Mean Bias (MB), Normalized Mean Error (NME), Normalized Mean Bias (NMB) and Root Mean Square Error (RMSE).

Network	Season	Number of datasets	Mean Observed (μg m^{-3})	Mean Predicted (μg m^{-3})	MAGE (μg m^{-3})	MB (μg m^{-3})	NME (%)	NMB (%)	RMSE (μg m^{-3})
EPA	Winter	144	2.8	1.9	1.4	-0.9	49	-32	2.3
	Spring	291	1.4	1.4	0.7	0.0	52	-2	1.0
	Summer	280	0.5	0.3	0.3	-0.2	58	-36	0.7
	Autumn	290	0.7	0.4	0.4	-0.2	65	-36	0.6
IMPROVE	Winter	116	0.8	0.9	0.6	0.1	77	15	0.9
	Spring	233	0.5	0.7	0.4	0.2	87	35	0.6
	Summer	193	0.2	0.2	0.2	0.0	81	18	0.2
	Autumn	214	0.2	0.3	0.2	0.0	103	22	0.4
EMEP	Winter	7	3.4	3.6	2.6	0.2	77	7	3.6
	Spring	18	1.6	1.6	1.0	0.0	61	-3	1.2
	Summer	18	0.3	0.6	0.5	0.4	186	129	0.7
	Autumn	17	0.8	1.3	0.8	0.5	94	59	1.1
EANET	Winter	30	2.0	3.0	2.0	0.9	96	46	2.9
	Spring	59	1.9	2.0	1.6	0.1	86	8	2.8
	Summer	59	0.6	0.8	0.8	0.2	126	32	1.2
	Autumn	59	0.8	0.9	0.7	0.1	88	12	1.1

Table S6: Statistical evaluation of EMAC predicted surface concentrations of PM_1 NO_3^- from the CMIP6 sensitivity against observations during 2010-2018. The used metrics include the Mean Absolute Gross Error (MAGE), Mean Bias (MB), Normalized Mean Error (NME), Normalized Mean Bias (NMB) and Root Mean Square Error (RMSE).

Network	**Season**	**Number of datasets**	**Mean Observed** (μg m^{-3})	**Mean Predicted** (μg m^{-3})	**MAGE** (μg m^{-3})	**MB** (μg m^{-3})	**NME** (%)	**NMB** (%)	**RMSE** (μg m^{-3})
USA	Rural	31	1.1	0.3	1.0	-0.9	85	-77	1.6
	Urban	22	1.5	0.6	0.9	-0.8	62	-57	1.8
	Downwind	5	1.2	0.5	1.0	-0.7	79	-56	1.8
East Asia	Rural	40	6.8	6.5	4.	-0.3	60	-4	5.1
	Urban	78	9.7	8.9	3.7	-0.8	39	-8	4.9
	Downwind	15	4.9	6.7	3.5	1.8	71	38	4.6
Europe	Rural	163	1.4	1.0	0.8	-0.5	53	-33	1.4
	Urban	28	1.8	1.0	1.0	-0.8	56	-42	1.7
	Downwind	99	3.2	1.5	1.8	-1.7	57	-52	2.6
India	Rural	5	0.4	4.3	4.0	3.9	975	952	7.0
	Urban	14	8.2	10.3	4.1	2.2	50	27	7.0

Table S7: Seasonal statistical evaluation of EMAC predicted surface concentrations of $PM_{2.5}$ NO_3^- from the HTAP sensitivity against observations during 2010-2018. The used metrics include the Mean Absolute Gross Error (MAGE), Mean Bias (MB), Normalized Mean Error (NME), Normalized Mean Bias (NMB) and Root Mean Square Error (RMSE).

Network	Season	Number of datasets	Mean Observed (μg m^{-3})	Mean Predicted (μg m^{-3})	MAGE (μg m^{-3})	MB (μg m^{-3})	NME (%)	NMB (%)	RMSE (μg m^{-3})
EPA	Winter	144	2.8	2.6	1.3	-0.2	44	-8	2
	Spring	291	1.4	2.2	1.0	0.8	73	55	1.2
	Summer	280	0.5	0.5	0.3	0.0	64	6	0.7
	Autumn	290	0.7	0.9	0.5	0.2	76	31	0.7
IMPROVE	Winter	116	0.8	1.7	1	0.9	122	110	1.2
	Spring	233	0.5	1.3	0.8	0.8	166	159	1.0
	Summer	193	0.2	0.5	0.3	0.3	173	151	0.5
	Autumn	214	0.2	0.6	0.4	0.4	201	169	0.6
EMEP	Winter	7	3.4	2.0	2.9	-1.3	87	-39	4.0
	Spring	18	1.6	4.2	2.7	2.6	166	159	3.6
	Summer	18	0.3	0.5	0.4	0.2	153	85	0.6
	Autumn	17	0.8	1.1	1.2	0.3	154	38	1.8
EANET	Winter	30	2.0	3.8	2.7	1.8	130	89	3.5
	Spring	59	1.9	2.8	2.0	0.9	109	49	3.1
	Summer	59	0.6	1.3	1.0	0.6	157	99	1.8
	Autumn	59	0.8	1.3	0.9	0.6	121	73	1.9

Table S8: Statistical evaluation of EMAC predicted surface concentrations of PM_1 NO_3^- from the HTAP sensitivity against observations during 2010-2018. The used metrics include the Mean Absolute Gross Error (MAGE), Mean Bias (MB), Normalized Mean Error (NME), Normalized Mean Bias (NMB) and Root Mean Square Error (RMSE).

Network	**Season**	**Number of datasets**	**Mean Observed** (μg m^{-3})	**Mean Predicted** (μg m^{-3})	**MAGE** (μg m^{-3})	**MB** (μg m^{-3})	**NME** (%)	**NMB** (%)	**RMSE** (μg m^{-3})
USA	Rural	31	1.1	0.9	0.7	-0.2	66	-21	1.1
	Urban	22	1.5	1.2	1.1	-0.2	76	-15	1.8
	Downwind	5	1.2	0.6	0.9	-0.6	75	-51	1.7
East Asia	Rural	40	6.8	8.9	5.5	2.2	81	32	7.4
	Urban	78	9.7	11.3	4.5	1.6	47	167	5.9
	Downwind	15	4.9	8.9	4.2	4.0	87	83	5.9
Europe	Rural	163	1.4	1.2	0.9	-0.2	66	-17	1.5
	Urban	28	1.8	1.6	1.1	-0.1	60	-7	1.5
	Downwind	99	3.2	1.8	1.9	-1.4	60	-43	2.6
India	Rural	5	0.4	6.9	6.5	6.5	593	574	11.8
	Urban	14	8.2	16.6	9.3	8.4	114	103	13.6

Table S9: Seasonal statistical evaluation of EMAC predicted surface concentrations of $PM_{2.5}$ NO_3^- from the THERM sensitivity against observations during 2010-2018. The used metrics include the Mean Absolute Gross Error (MAGE), Mean Bias (MB), Normalized Mean Error (NME), Normalized Mean Bias (NMB) and Root Mean Square Error (RMSE).

Network	Season	Number of datasets	Mean Observed (μg m^{-3})	Mean Predicted (μg m^{-3})	MAGE (μg m^{-3})	MB (μg m^{-3})	NME (%)	NMB (%)	RMSE (μg m^{-3})
EPA	Winter	144	2.8	2.4	1.4	-0.5	50	-17	2.2
	Spring	291	1.4	2.2	1.2	0.8	89	55	1.5
	Summer	280	0.5	0.8	0.6	0.3	111	67	0.9
	Autumn	290	0.7	0.9	0.6	0.3	90	40	0.9
IMPROVE	Winter	116	0.8	1.2	0.7	0.4	80	51	0.9
	Spring	233	0.5	1.1	0.7	0.6	132	114	0.9
	Summer	193	0.2	0.5	0.3	0.3	167	136	0.5
	Autumn	214	0.2	0.4	0.3	0.2	150	110	0.5
EMEP	Winter	7	3.4	3.9	2.6	0.5	77	16	3.4
	Spring	18	1.6	2.2	1.6	1.2	97	72	2.1
	Summer	18	0.3	1.6	1.3	1.3	487	480	1.8
	Autumn	17	0.8	2.7	1.9	1.9	243	238	2.8
EANET	Winter	30	2.0	2.4	1.6	0.3	79	17	2.7
	Spring	59	1.9	2.0	1.6	0.1	85	7	2.8
	Summer	59	0.6	1.6	1.3	0.9	212	144	2.5
	Autumn	59	0.8	0.8	0.7	0.1	84	8	1.1

Table S10: Statistical evaluation of EMAC predicted surface concentrations of PM_1 NO_3^- from the THERM sensitivity against observations during 2010-2018. The used metrics include the Mean Absolute Gross Error (MAGE), Mean Bias (MB), Normalized Mean Error (NME), Normalized Mean Bias (NMB) and Root Mean Square Error (RMSE).

Network	**Season**	**Number of datasets**	**Mean Observed** (μg m^{-3})	**Mean Predicted** (μg m^{-3})	**MAGE** (μg m^{-3})	**MB** (μg m^{-3})	**NME** (%)	**NMB** (%)	**RMSE** (μg m^{-3})
USA	Rural	31	1.1	0.7	1.0	-0.4	85	-35	1.4
	Urban	22	1.5	1.9	1.7	0.4	114	30	2.2
	Downwind	5	1.2	0.7	1.1	-0.5	88	-37	1.8
East Asia	Rural	40	6.7	7.4	4.5	0.6	67	9	5.8
	Urban	78	9.7	9.8	4.0	0.1	42	1	5.2
	Downwind	15	4.9	7.4	3.0	2.6	61	53	4.6
Europe	Rural	163	1.4	1.4	0.8	0.0	63	2	1.4
	Urban	28	1.8	1.6	1.0	-0.2	56	-12	1.5
	Downwind	99	3.2	2.4	1.5	-0.7	48	-23	2.2
India	Rural	5	0.4	2.2	1.8	1.8	447	442	2.7
	Urban	14	8.2	4.7	4.9	-3.5	60	-43	7.2

Table S11: Seasonal statistical evaluation of EMAC predicted surface concentrations of $PM_{2.5}$ NO_3^- from the SCAV sensitivity against observations during 2010-2018. The used metrics include the Mean Absolute Gross Error (MAGE), Mean Bias (MB), Normalized Mean Error (NME), Normalized Mean Bias (NMB) and Root Mean Square Error (RMSE).

Network	**Season**	**Number of datasets**	**Mean Observed** (μg m^{-3})	**Mean Predicted** (μg m^{-3})	**MAGE** (μg m^{-3})	**MB** (μg m^{-3})	**NME** (%)	**NMB** (%)	**RMSE** (μg m^{-3})
EPA	Winter	144	2.8	1.2	1.8	-1.7	64	-59	2.6
	Spring	291	1.4	1.4	1.0	0.0	71	78	1.3
	Summer	280	0.5	0.7	0.4	0.2	88	35	0.8
	Autumn	290	0.7	0.9	0.6	0.2	83	28	0.8
IMPROVE	Winter	116	0.8	0.7	0.5	-0.1	60	-11	0.8
	Spring	233	0.5	0.8	0.5	0.3	101	63	0.7
	Summer	193	0.2	0.3	0.2	0.2	111	76	0.4
	Autumn	214	0.2	0.4	0.3	0.2	122	76	0.5
EMEP	Winter	7	3.4	2.3	3.0	-1.1	89	-32	4.0
	Spring	18	1.6	2.0	1.2	0.4	72	23	1.5
	Summer	18	0.3	1.2	1.0	1.0	366	350	1.3
	Autumn	17	0.8	2.1	1.4	1.3	172	164	2.1
EANET	Winter	30	2.0	1.9	1.4	-0.1	71	-4	2.7
	Spring	59	1.9	1.6	1.5	-0.2	79	-13	2.9
	Summer	59	0.6	1.0	1.0	0.4	154	64	1.9
	Autumn	59	0.8	0.6	0.6	-0.2	83	-19	1.0

Table S12: Statistical evaluation of EMAC predicted surface concentrations of PM_1 NO_3^- from the SCAV sensitivity against observations during 2010-2018. The used metrics include the Mean Absolute Gross Error (MAGE), Mean Bias (MB), Normalized Mean Error (NME), Normalized Mean Bias (NMB) and Root Mean Square Error (RMSE).

Network	**Season**	**Number of datasets**	**Mean Observed** (μg m^{-3})	**Mean Predicted** (μg m^{-3})	**MAGE** (μg m^{-3})	**MB** (μg m^{-3})	**NME** (%)	**NMB** (%)	**RMSE** (μg m^{-3})
USA	Rural	31	1.1	0.6	1.0	-0.5	85	-47	1.4
	Urban	22	1.5	1.7	1.4	0.2	98	15	2.0
	Downwind	5	1.2	0.8	1.0	-0.5	81	-39	1.7
East Asia	Rural	40	6.8	6.6	4.3	-0.2	63	-3	5.5
	Urban	78	9.7	8.7	3.7	-1.0	38	-10	4.9
	Downwind	15	4.9	6.1	2.6	1.3	54	26	3.7
Europe	Rural	163	1.4	1.1	0.9	-0.3	61	-23	1.5
	Urban	28	1.8	1.2	1.0	-0.6	54	-33	1.7
	Downwind	99	3.2	1.9	1.8	-1.3	55	-41	2.6
India	Rural	5	0.4	2.0	1.7	1.6	407	378	2.4
	Urban	14	8.2	7.5	4.1	-0.6	50	-8	5.2

Table S13: Seasonal statistical evaluation of EMAC predicted surface concentrations of $PM_{2.5}$ NO_3^- from the HYDRO sensitivity against observations during 2010-2018. The used metrics include the Mean Absolute Gross Error (MAGE), Mean Bias (MB), Normalized Mean Error (NME), Normalized Mean Bias (NMB) and Root Mean Square Error (RMSE).

Network	Season	Number of datasets	Mean Observed (μg m^{-3})	Mean Predicted (μg m^{-3})	MAGE (μg m^{-3})	MB (μg m^{-3})	NME (%)	NMB (%)	RMSE (μg m^{-3})
EPA	Winter	144	2.8	2.0	1.4	-0.8	51	-30	2.3
	Spring	291	1.4	1.7	0.9	0.3	67	20	1.2
	Summer	280	0.5	0.5	0.3	0.0	64	-20	0.7
	Autumn	290	0.7	0.5	0.5	-0.2	70	-23	0.7
IMPROVE	Winter	116	0.8	1.0	0.6	0.2	68	20	0.8
	Spring	233	0.5	0.9	0.5	0.4	101	71	0.7
	Summer	193	0.2	0.4	0.2	0.2	117	77	0.3
	Autumn	214	0.2	0.3	0.2	0.1	98	38	0.4
EMEP	Winter	7	3.4	3.3	2.5	0.0	76	-1	3.3
	Spring	18	1.6	2.2	1.3	0.6	80	35	1.6
	Summer	18	0.3	1.0	0.8	0.8	298	274	1.1
	Autumn	17	0.8	1.8	1.1	1.0	138	128	1.7
EANET	Winter	30	2.0	2.2	1.5	0.2	75	9	2.7
	Spring	59	1.9	1.8	1.5	0.0	82	-2	2.8
	Summer	59	0.6	1.4	1.2	0.7	192	113	2.1
	Autumn	59	0.8	0.7	0.6	-0.1	82	-14	1.0

Table S14: Statistical evaluation of EMAC predicted surface concentrations of PM_1 NO_3^- from the HYDRO sensitivity against observations during 2010-2018. The used metrics include the Mean Absolute Gross Error (MAGE), Mean Bias (MB), Normalized Mean Error (NME), Normalized Mean Bias (NMB) and Root Mean Square Error (RMSE).

Network	**Season**	**Number of datasets**	**Mean Observed** (μg m^{-3})	**Mean Predicted** (μg m^{-3})	**MAGE** (μg m^{-3})	**MB** (μg m^{-3})	**NME** (%)	**NMB** (%)	**RMSE** (μg m^{-3})
USA	Rural	31	1.1	0.4	1.0	-0.7	87	-63	1.6
	Urban	22	1.5	1.2	1.1	-0.3	75	-20	1.9
	Downwind	5	1.2	0.5	1.1	-0.7	87	-57	2.0
East Asia	Rural	40	6.8	6.3	4.2	-0.5	62	-8	5.4
	Urban	78	9.7	8.1	4.1	-1.6	43	-16	5.3
	Downwind	15	4.9	6.1	2.3	1.2	47	25	3.6
Europe	Rural	163	1.4	1.0	0.8	-0.4	56	-27	1.4
	Urban	28	1.8	1.2	0.9	-0.6	53	-35	1.6
	Downwind	99	3.2	1.8	1.7	-1.5	54	-46	2.5
India	Rural	5	0.4	1.6	1.3	1.2	320	293	1.8
	Urban	14	8.2	4.9	4.7	-3.2	58	-40	6.6

A.4 Supplementary material to Chapter 4

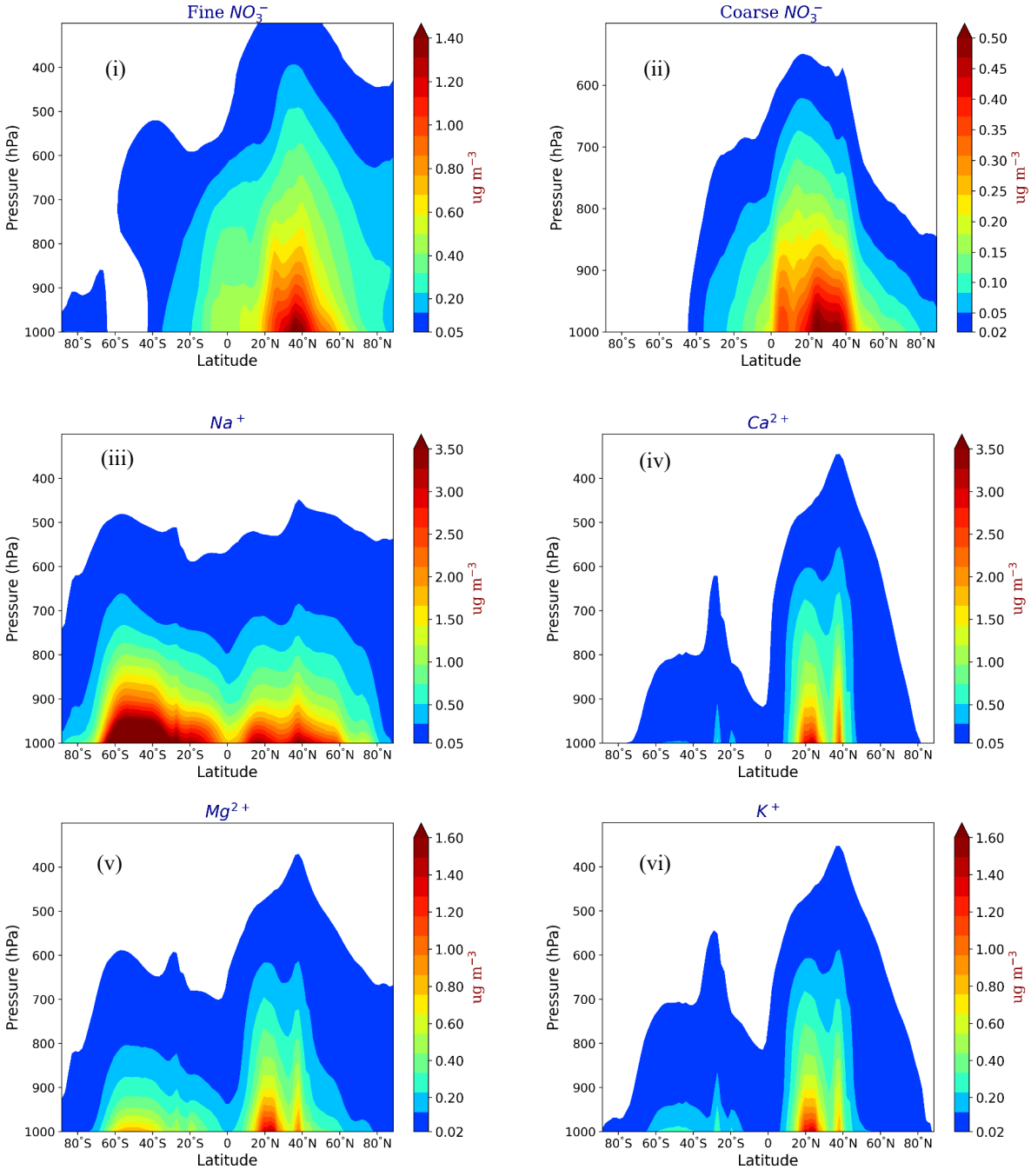

Figure S1 : Time averaged zonal concentrations of i) fine and ii) coarse aerosol NO_3^- , iii) Na^+ , iv) Ca^{2+}, v) Mg^{2+} and vi) K^+ in TSP as predicted by EMAC from the Base Case simulation.

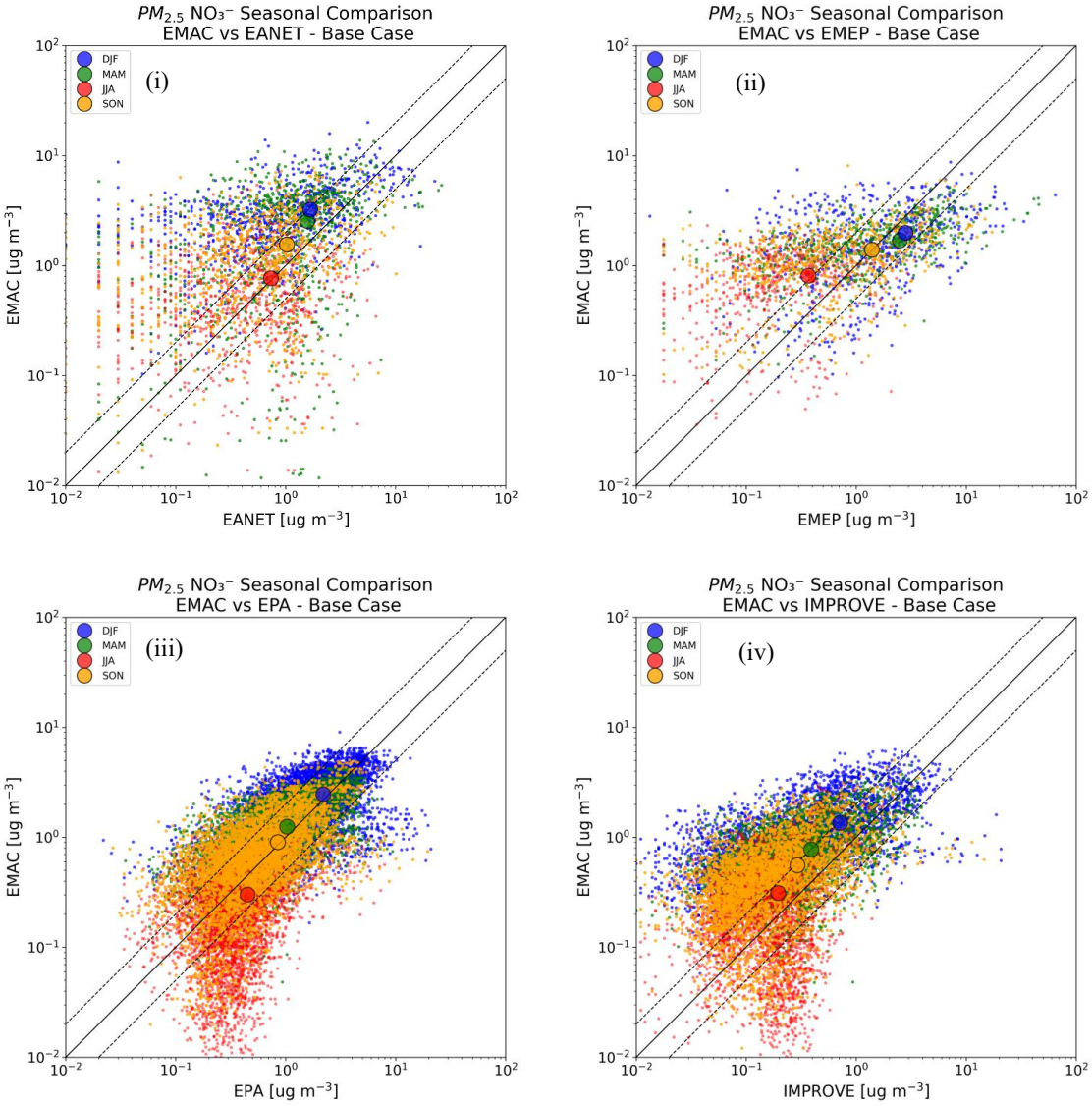

Figure S2: Scatterplots comparing the seasonal mean surface mass concentrations of $PM_{2.5}$ NO_3^- as simulated by EMAC from the Base Case simulation with observations from the networks of (i) EANET, (ii) EMEP, (iii) EPA and (iv) IMPROVE. Blue points indicate values in winter, green points in spring, red points in summer and yellow points in autumn. Enlarged dots indicate seasonal means. Also shown are the 1:1, 2:1, and 1:2 lines.

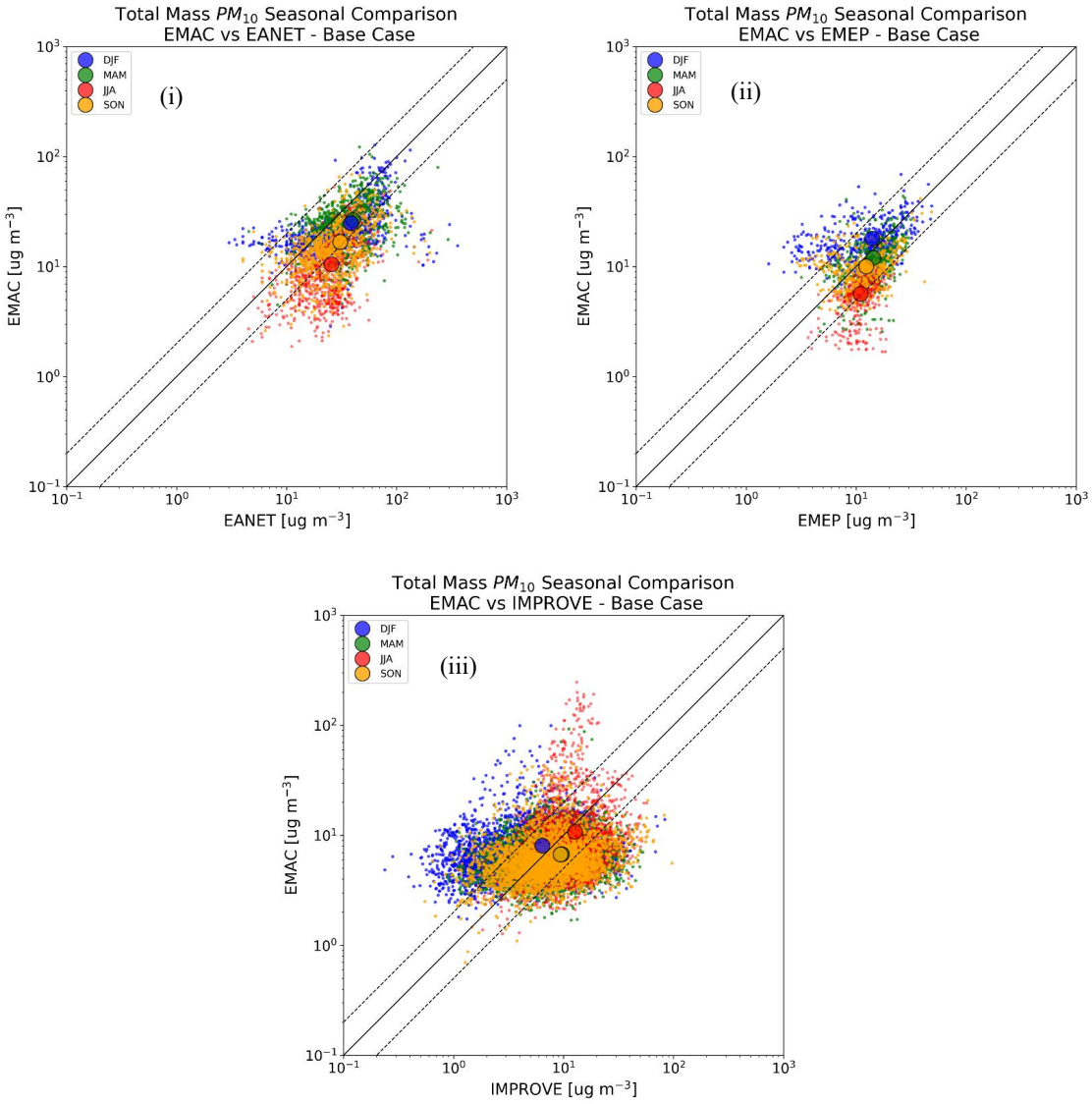

Figure S3: Scatterplots comparing the seasonal mean surface mass concentrations of PM_{10} aerosols as simulated by EMAC from the Base Case simulation with observations from the networks of (i) EANET, (ii) EMEP and (iii) IMPROVE. Blue points indicate values in winter, green points in spring, red points in summer and yellow points in autumn. Enlarged dots indicate seasonal means. Also shown are the 1:1, 2:1, and 1:2 lines.

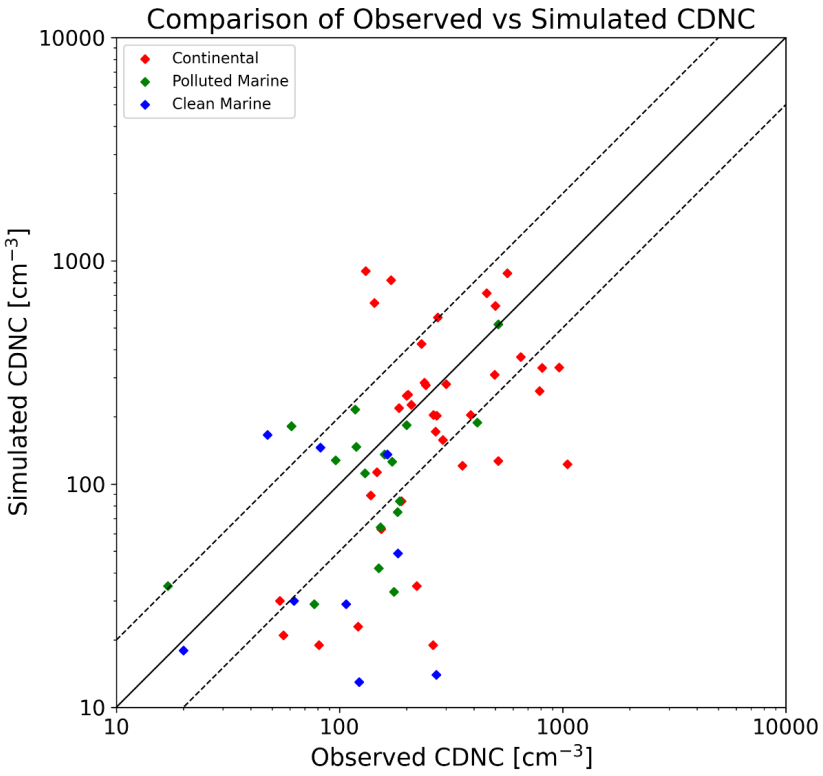

Figure S4: Comparison of global cloud droplet number concentrations as simulated by EMAC from the Base Case simulation and observed across different types of environments (continental, polluted and clean marine). The exact locations, altitudes and time periods of the measurements are shown in Table S3. Also shown are the 1:1, 2:1, and 1:2 lines.

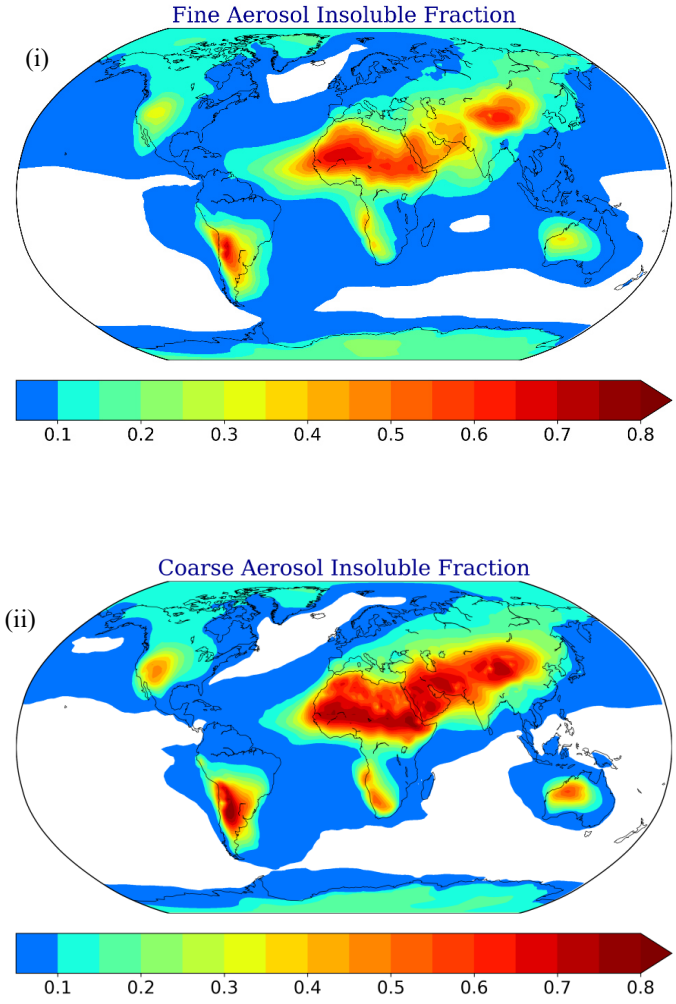

Figure S5 : Global mean insoluble fraction of (i) fine and (ii) coarse aerosols as predicted by EMAC from the Base Case simulation.

Table S1: Seasonal statistical evaluation of the EMAC predicted surface mass concentrations of $PM_{2.5}$ NO_3^- from the Base Case simulation against observations for the period 2008 - 2018.

Network	Season	Number of datasets	Mean Observed (μg m^{-3})	Mean Predicted (μg m^{-3})	MAGE (μg m^{-3})	MB (μg m^{-3})	NME (%)	NMB (%)	RMSE (μg m^{-3})
EPA	Winter	144	2.86	2.93	1.43	0.07	49.83	2.39	2.09
	Spring	291	1.63	1.78	0.71	0.14	43.54	8.84	1.09
	Summer	280	0.69	0.31	0.41	-0.38	59.5	-54.87	0.8
	Autumn	290	0.79	0.63	0.37	-0.16	46.88	-19.66	0.62
IMPROVE	Winter	116	0.92	1.52	1.03	0.6	111.16	64.6	1.48
	Spring	233	0.61	1.0	0.59	0.39	97.73	64.09	0.81
	Summer	193	0.24	0.37	0.26	0.13	107.85	52.94	0.39
	Autumn	214	0.26	0.44	0.29	0.18	111.35	67.43	0.44
EMEP	Winter	7	2.61	1.92	1.47	-0.68	56.4	-26.19	2.2
	Spring	18	1.99	1.72	0.69	-0.27	34.75	-13.47	1.05
	Summer	18	0.68	0.69	0.43	0.01	62.25	1.23	0.5
	Autumn	17	1.55	1.15	0.61	-0.4	39.12	-25.94	0.97
EANET	Winter	30	2.11	2.95	2.11	0.84	100.11	39.91	2.86
	Spring	59	1.74	2.67	1.84	0.92	105.65	53.04	2.8
	Summer	59	0.68	0.7	0.72	0.02	105.87	2.38	1.09
	Autumn	59	0.77	1.11	0.77	0.34	99.97	43.4	1.12

Table S2: Seasonal statistical evaluation of EMAC predicted PM_{10} aerosol surface mass concentrations from the Base Case simulation against observations for the period 2008 – 2018.

Network	Season	Number of datasets	Mean Observed (μg m^{-3})	Mean Predicted (μg m^{-3})	MAGE (μg m^{-3})	MB (μg m^{-3})	NME (%)	NMB (%)	RMSE (μg m^{-3})
IMPROVE	Winter	89	7.16	8.36	4.94	1.2	68.9	16.74	6.96
	Spring	222	10.8	7.89	5.48	-2.91	50.77	-26.92	8.64
	Summer	203	14.27	12.85	10.88	-1.42	76.22	-9.98	18.24
	Autumn	207	10.61	6.79	5.45	-3.82	51.33	-35.98	8.67
EMEP	Winter	17	15.2	13.4	6.46	-1.8	42.48	-11.84	7.88
	Spring	34	12.23	10.36	3.8	-1.86	31.06	-15.23	4.98
	Summer	35	12.74	4.92	7.82	-7.82	61.35	-61.35	8.74
	Autumn	36	13.78	8.91	5.13	-4.87	37.21	-35.31	6.22
EANET	Winter	20	38.98	21.49	19.48	-17.49	49.98	-44.87	31.46
	Spring	42	44.52	25.96	20.19	-18.56	45.35	-41.69	27.79
	Summer	41	27.94	9.38	18.56	-18.56	66.43	-66.43	22.73
	Autumn	42	30.43	13.23	17.32	-17.2	56.91	-56.52	21.52

Table S3: Comparison between cloud droplet number concentrations calculated by the Base Case simulation and global observations (Karydis et al., 2017 and references therein).

Location	Latitude	Longitude	Altitude	Time Period	Observed CDNC(cm^{-3})	Simulated CDNC(cm^{-3})
S. Pacific Ocean	20–35°S	135–175°W	PBL	Annual	82	146
E. Pacific Ocean	29–32°N	120–123°W	450–850 m	July	49–279	136
N. Pacific Ocan	41°N	131°W	< 1500 m	April	21–74	166
W. Canary Islands	32°N	25°W	PBL	July	17	35
W. Australia	30–40°S	88–103°E	PBL	Annual	107	29
Beaufort Sea	72–78°N	154–159°W	202–1017 m	June	178–365	14
Beaufort Sea	70.5–73°N	145–147°W	300–3000 m	June	20–225	13
Beaufort Sea	65–75°N	130–170°W	400–4600 m	April	48–77	30
NE. Alaska Coast	69–71°N	150–158°W	400–4000 m	October	10–30	18
Yellow Sea	28–31°N	127–131°E	PBL	Annual	30–1000	520
SE Asia Coast	10–40°N	105–150°E	PBL	Annual	186 (100–250)	84
N. American Coast	15–35°N	115–140°W	PBL	Annual	159 (150–300)	136
S. American Coast	8–28°S	70–90°W	PBL	Annual	182 (100–300)	75

S. African Coast	5–25°S	10–15°E	PBL	Annual	153 (130–300)	64
NE. Atlantic Ocean	50–55°N	25–30°W	800–2200 m	April	65–300	49
Santa Maria, Azores	37°N	25°W	550–1000 m	June	150 (74–192)	42
Canary Islands Vicinity	28°N	16.5°W	PBL	June – July	51–300	33
W. Moroccan Coast	34°N	11°W	PBL	July	77	29
Oregon Coast	45.5°N	124.5°W	PBL	August	25–210	216
Key West, FL	24.5°N	82°W	PBL	July	268–560	189
Fundy Bay, Nova Scotia	44°N	66°W	20–290 m	August	61 (59–97)	182
Cornwall Coast	50°N	5.5°W	450–800 m	February	130	112
British Isles, UK	55°N	2.5°W	Surface	April	172	126
British Isles, UK	51°N	6°W	Surface	October	119	147
British Isles, UK	53°N	9.5°W	Surface	December	96	128
SE. England Coast	51.5–52°N	1.5–2.5°E	380–750 m	September	151–249	184
SW. Indian Coast	10°N	65–75°E	50–550 m	February – March	100–500	280
Qinghai Province	34–37°N	98–103°E	PBL	Annual	30–700	219

Beijing	37–41°N	113–120°E	PBL	Annual	30–1100	880
NE. China	39–40°N	117.5 – 118.5°E	1719–1931 m	April – May	200–800	630
Hebei Province	35–40°N	112–119°E	PBL	Annual	30–400	819
Cumbria, England	54.5°N	2.5°W	Surface	March – April	100–2000	123
Cumbria, England	54.5°N	2.5°W	Surface	May	482–549	127
Koblenz, Germany	50°N	7.5°E	901–914 hPa	May	675–900	261
Koblenz, Germany	50°N	7.5°E	945 hPa	October	965	333
N. Finland	68°N	24°E	342–572 m	Annual	154 (30–610)	63
N. Finland	68°N	24°E	342–572 m	October – November	55–470	19
Kuopio, Finland	62.5°N	27.5°E	306 m	August – November	138	89
Cabauw, Netherlands	51°N	4.5°E	PBL	May	180–360	172
Jungfraujoch, Switzerland	46.5°N	7.5°E	Surface	July – August	112–416	204
Barrow, AK	71.5°N	156.5°W	389–830 m	August	56	21
Barrow, AK	71.5°N	156.5°W	431–736 m	May	222	35
Barrow, AK	71.5°N	156.5°W	297–591 m	June	121	23

Barrow, AK	71.5°N	156.5°W	393–762 m	July	54	30
Barrow, AK	71.5°N	156.5°W	1059–1608 m	September	81	19
Southern Great Plains, OK	36.5°N	97.5°W	795–1450 m	Winter	265–281	203
Southern Great Plains, OK	36.5°N	97.5°W	343–1241 m	Winter	244	277
Southern Great Plains, OK	36.5°N	97.5°W	985–1885 m	Spring	200–219	227
Southern Great Plains, OK	36.5°N	97.5°W	671–1475 m	Spring	203	252
Southern Great Plains, OK	36.5°N	97.5°W	1280–2200 m	Summer	128–159	648
Southern Great Plains, OK	36.5°N	97.5°W	756–1751 m	Summer	131	899
Southern Great Plains, OK	36.5°N	97.5°W	1030–1770m	Autumn	217-249	425
Southern Great Plains, OK	36.5°N	97.5°W	404–1183 m	Autumn	276	557
Southern Great Plains, OK	36.5°N	97.5°W	900–800 hPa	March	200 (100–320)	249
Southern Great Plains, OK	36.5°N	97.5°W	300–600 m	April	650	371
Southern Great Plains, OK	36.5°N	97.5°W	700–1200 m	September – October	457	717
Cleveland, OH ; Detroit, MI	40–42.5°N	80.5–85°W	300–1000 m	August	320–1300	332
Central Ontario	50°N	85°W	< 2500 m	October	147 (119–173)	113

Central Ontario	50°N	85°W	2000–2100 m	Summer	350–360	121
Central Ontario	50°N	85°W	1300 m	Winter	190	84
Upper NY State	44°N	75°W	1500 m	Autumn	240	285
State College, PA	41°N	78°W	1000–1600 m	October	388	204
Mount Gibbes, NC	35.5°N	82°W	Surface	Annual	238–754	309
Cape Kennedy, FL	28.5°N	80.5°W	600–2800 m	August	250–330	158

Table S4 : Comparison of estimates for the direct radiative effect (RE_{ari}) of total NO_3^- aerosols from this study and other studies referenced within.

Reference Study	RE_{ari} Estimate (W/m^2)	Time Period
Liao et al., 2004	-0.14	Present Day 2000
Bauer et al., 2007a	-0.11 -0.14	Present Day 2000 Present Day 2030
Bauer et al., 2007b	-0.11	Present Day 2000
Bellouin et al., 2011	-0.12	Present Day 2000
Xu and Penner 2012	-0.12	Present Day 2000
Heald et al., 2014	-0.10	Present Day 2010
This Study	-0.11	Present Day (2008 - 2018)

Band / Volume 650
Assimilation of groundwater level and cosmic-ray neutron sensor soil moisture measurements into integrated terrestrial system models for better predictions
F. Li (2024), xvii, 172 pp
ISBN: 978-3-95806-796-7

Band / Volume 651
Integration of a rib-channel design to improve air-side contacting in solid oxide cell (SOC) stacks
Y. S. Ayhan (2024), 82 pp
ISBN: 978-3-95806-797-4

Band / Volume 652
Modelling Secondary Circulation in Convective Boundary Layer Using Large Eddy Simulation
L. Zhang (2024), 84 pp
ISBN: 978-3-95806-799-8

Band / Volume 653
Optionen zur Umsetzung der Klimaschutzziele im Verkehrssektor
S. Kraus (2025), XI, 317 pp
ISBN: 978-3-95806-802-5

Band / Volume 654
Modellierung der flächendifferenzierten Grundwasserneubildung für Schleswig-Holstein im Beobachtungszeitraum 1961 – 2021 und für Klimaszenarien bis 2100
I. McNamara, B. Tetzlaff, F. Wendland, T. Wolters (2025), 191 pp
ISBN: 978-3-95806-803-2

Band / Volume 655
Entwicklung alternativer Brenngaselektroden für die Hochtemperatur-Elektrolyse
F. E. Winterhalder (2025), vii, 161 pp
ISBN: 978-3-95806-805-6

Band / Volume 656
Oxide-based All-Solid-State Batteries for and from Recycling Processes
V. M. Kiyek (2025), viii, 128 pp, xix
ISBN: 978-3-95806-806-3

Band / Volume 657
Investigation of current and future anthropogenic chemical regimes in simulation chamber experiments
M. Färber (2025), 213 pp
ISBN: 978-3-95806-809-4

Band / Volume 658
Dynamischer Betrieb von Polymer-Elektrolyt-Membran Wasserelektrolyseuren
E. Rauls (2025), XIV, 239 pp
ISBN: 978-3-95806-811-7

Band / Volume 659
Pore-scale reactive transport modeling in cementitious materials: Development and application of a high-performance computing code based on the Lattice-Boltzmann method
S. Rohmen (2025), X, 295 pp
ISBN: 978-3-95806-812-4

Band / Volume 660
Recyclingmöglichkeiten für die Keramikkomponenten einer Festoxidzelle
S. Sarner (2025), VIII, 122 pp
ISBN: 978-3-95806-816-2

Band / Volume 661
Methodological Approach Enabling the Two-phase Flow Investigation in Alkaline Electrolysis under Demanding Conditions
S. Renz (2025), IX, 252 pp
ISBN: 978-3-95806-821-6

Band / Volume 662
Variable renewable energy potential estimates based on high-resolution regional atmospheric modelling over southern Africa
S. Chen (2025), XIII, 141 pp
ISBN: 978-3-95806-822-3

Band / Volume 663
Advances in Understanding Nitrate Aerosol Formation and the Implications for Atmospheric Radiative Balance
A. Milousis (2025), 195 pp
ISBN: 978-3-95806-823-0

Energie & Umwelt / Energy & Environment
Band / Volume 663
ISBN 978-3-95806-823-0

Mitglied der Helmholtz-Gemeinschaft

JÜLICH
Forschungszentrum